Mechanisms of plastic deformation in amorphous silicon by atomistic simulation using the Stillinger-Weber potential

by

Michael J. Demkowicz

Submitted to the Department of Mechanical Engineering on March 31, 2005
in partial fulfillment of the requirements for the degree of
Doctor of Philosophy in Mechanical Engineering

at the

Massachusetts Institute of Technology

June, 2005

Signature of Author.....
Department of Mechanical Engineering
March 31, 2005

Certified by.....
Ali S. Argon
eering
rvisor

Accepted by.....
nand
Professor of Mechanical Engineering
Chairman, Department Committee on Graduate Students

Mechanisms of plastic deformation in amorphous silicon by atomistic simulation using the Stillinger-Weber potential

by

MICHAEL J. DEMKOWICZ

Submitted to the Department of Mechanical Engineering on March 31, 2005
in partial fulfillment of the requirements for the degree of
Doctor of Philosophy in Mechanical Engineering

ABSTRACT

Molecular dynamics simulation of amorphous silicon (a-Si) using the Stillinger-Weber potential reveals the existence of two distinct atomic environments: one solidlike and the other liquidlike. The mechanical behavior of a-Si when plastically deformed to large strain can be completely described by the mass fraction ϕ of liquidlike material in it. Specifically, samples with higher ϕ are more amenable to plastic flow, indicating that liquidlike atomic environments act as plasticity "carriers" in a-Si. When deformed under constant pressure, all a-Si samples converge to a unique value of ϕ characteristic of steady state flow.

Discrete stress relaxations were found to be the source of low-temperature plastic flow in a-Si in deformation simulations by potential energy minimization. These relaxations are triggered when a local yielding criterion is satisfied in a small cluster of atoms. The atomic rearrangements accompanying discrete stress relaxations are describable as autocatalytic avalanches of unit shearing events. Every such unit event centers on a clearly identifiable change in bond length between the two split peaks of the second nearest neighbor shell in the radial distribution function (RDF) of bulk a-Si in steady-state flow.

Thesis Supervisor: Ali S. Argon
Title: Quentin Berg Professor Emeritus, Mechanical Engineering

Table of contents

1. Introduction

The goal of the research presented here is to investigate the mechanisms of plastic flow in amorphous silicon (a-Si) using atomistic simulation. This section explains how the ultrahardness of nc-TiN/a-Si_3N_4 nanostructured ceramic composite coatings motivated this study as well as the modeling assumptions that made using a-Si as a model system attractive. It concludes with a brief overview of the remaining sections.

1.1 Ultrahardness of nanocrystalline ceramic composite coatings

The motivation for this study originates in a desire to explain the unusually high resistance to plastic flow exhibited by a series of recently created nc-TiN/a-Si_3N_4 nanostructured ceramic composite coatings, some of which have shown indentation hardnesses in excess of that of nanocrystalline diamond thin films [Veprek, 1999]. The excellent mechanical behavior and thermal stability of these materials has made them highly attractive candidates for application as coatings for high-speed, high-temperature machine tools [Argon *et al.*, 2004]. In this context they hold a significant advantage over carbon-based coatings because the latter tend to dissolve easily into the substrate upon which they were deposited if that substrate is iron-based (e.g. low carbon steel). Today, nc-(AlTi)N/a-Si_3N_4 composite ceramic coatings—whose structure is similar to the nc-TiN/a-Si_3N_4 coatings that motivated this work—are commercially available through a joint venture between PLATIT AG[1] and SHM Ltd.[2].

Aside from their technological significance, nc-TiN/a-Si_3N_4 composite ceramic coatings pose a challenge to the current understanding of the processes governing plastic flow behavior of covalently bonded nanocrystalline materials. Detailed investigation has indicated that these coatings are made up of crystalline TiN grains 2-5nm in diameter while the Si_3N_4 component is thought to exist in disordered intergranular layers of 1-3

[1] http://www.platit.com/
[2] http://www.shm-cz.cz/

atomic diameter thickness [Argon, Veprek, 2002]. It has been suggested that at the appropriate proportions of these two components, the TiN grains are completely wetted by a monolayer of Si_3N_4 [Niederhofer *et al.*, 2001]. Due to the small size of the TiN grains and the typically high lattice resistance of covalently bonded solids [Ren *et al.*, 1995], dislocation-mediated plasticity is not expected to play an important role in the mechanical behavior of nc-TiN/a-Si_3N_4 coatings. The plastic deformation behavior of the assemblage is therefore governed by the component whose ideal shear strength is lower.

The rise in plastic resistance associated with the increasing difficulty of nucleating and propagating dislocations as grain sizes decrease is a well-known effect in the study of polycrystalline metals [Hall, 1951; Petch, 1953] and has recently received considerable attention in large-scale atomistic simulation studies of metals [Yamakov *et al.*, 2001; Yamakov *et al.*, 2002; Schiotz, Jacobsen, 2003; Schiotz, 2004]. Below grain sizes of about 10-20 nm, however, polycrystalline metals exhibit a reversal in the trend of increasing plastic resistance [Yip, 1998; Schiotz, 2004] as the rising proportion of intergranular regions makes large scale plastic deformation by grain boundary shear processes ever more favorable [Schiotz *et al.*, 1998]. Therefore, the fact that— even at TiN grain sizes of 3.5nm —nc-TiN/a-Si_3N_4 coatings do not show a reversal in the trend of rising plastic resistance with decreasing grain sizes [Veprek, Reiprich, 1995] indicates that the intergranular regions in these materials are less amenable to plastic flow than the intergranular regions found in nanocrystalline metals. The reason for this difference likely arises because of the covalent bonding environment of intergranular regions in nc-TiN/a-Si_3N_4 as well as the difficulty in propagation of dislocations that might nucleate from the grain boundaries.

1.2 Modeling assumptions

The first step towards understanding plasticity in disordered intergranular layers is to develop insight into the plastic flow behavior of the intergranular material in its bulk amorphous or glassy form. The necessity of doing so has already been realized in the case of deformation of nanocrystalline metals, where deformation in intergranular layers is

explicitly compared with deformation in metallic glasses [Lund, Schuh, 2004]. Investigators of deformation in nanocrystalline metals benefit from a large body of knowledge that has been developed on plastic flow of metallic glasses [Argon, Kuo, 1979; Maeda, Takeuchi, 1981; Srolovitz *et al.*, 1983; Argon, Shi, 1983; Deng *et al.*, 1989; Bulatov, Argon, 1994; Falk, Langer, 1998]. A similarly large amount of research has been conducted on plastic deformation in glassy polymers [Theodorou, Suter, 1985b; Theodorou, Suter, 1986; Hutnik *et al.*, 1991; Mott *et al.*, 1993]. By comparison, however, the current state of knowledge on plasticity of covalent network materials is markedly deficient. This information, however, is needed to explain the behavior of nanostructured ceramics.

Covalent network glasses—such as a-Si, a-Ge, SiO_2, B_2O_3, or alkali modified glasses—should be studied separately from metallic glasses and glassy polymers because of fundamental differences in the type of atomic bonding environments envisioned in these three cases. Metallic glasses are usually modeled by collections of atoms interacting with spherically symmetric potentials that do not exhibit any directional nature [Deng *et al.*, 1989]. Glassy polymers, on the other hand, exhibit strong directional bonds along polymer backbones, but the interactions of atoms not joined in this way (e.g. of atoms from different polymer chains) are once again modeled by relatively weaker spherically symmetric potentials [Theodorou, Suter, 1985b]. Bonding between all atoms in covalent network glasses is of a strong and directional nature and so is qualitatively different from the two cases described above. To the best of the authors' knowledge, the research presented here is the first computer investigation of plastic deformation to strains much larger than the yield strain (i.e. to "large strain") in a system that incorporates the atomic binding characteristics appropriate for covalent network glasses [Demkowicz, Argon, 2004b; Demkowicz, Argon, 2005a; Demkowicz, Argon, 2005b].

A faithful investigation of plasticity in nc-TiN/a-Si_3N_4 coatings would have to take into account a range of complex chemical interactions between all the elements that make up the material. Current *ab initio* methods are not yet capable of rapidly simulating atomic configurations of sufficient size (~10^3-10^4 atoms) and on sufficiently long time scales (~1-10 ns) to address questions of fully developed low-temperature plasticity. On the other hand, well-tested empirical potentials for all the possible constituents of

nanocrystalline ceramic coatings (e.g. for TiN) are largely unavailable. It is therefore convenient to conceive of a single-component model system capable of existing in disordered form as well as a nanocrystalline form similar to that described for nc-TiN/a-Si_3N_4. This model system should also have a well-tested empirical potential that explicitly incorporates the effects of directional bonding, as discussed above. A clear choice for such a model system is silicon (Si). This material has a well-known amorphous form [Tanaka, 1999] and has been observed to form disordered intergranular layers [Furukawa *et al.*, 1986] as well as nanocrystalline configurations that resemble those that are thought to describe nc-TiN/a-Si_3N_4 [Veprek *et al.*, 1981; Shen *et al.*, 1995]. Furthermore, several empirical potentials to model it have been constructed and tested [Stillinger, Weber, 1985; Tersoff, 1986; Balamane *et al.*, 1992; Bazant *et al.*, 1997].

The goal of this study, therefore, is to investigate the mechanical behavior of amorphous silicon (a-Si) using atomistic simulations in order to:

- Characterize its plastic flow behavior
- Find the mechanisms that govern inelastic relaxation in it
- Exhibit the role it plays in plastic flow of nanocrystalline silicon (nc-Si)

1.3 Scope

Remarkably little is known about the plastic flow behavior of covalently bonded network glasses, including a-Si: both experimental and theoretical (computational) investigations are scarce. Nevertheless, a number of studies have been undertaken on relevant related topics, such as plasticity in glassy metals and polymers or the behavior of covalent network glasses under pressurization. Chapter 2 (Background) reviews these studies.

Chapter 3 (Simulation methods) details the investigated a-Si system. It also discusses the two simulation techniques that were used in this study: molecular dynamics (MD) and potential energy minimization (PEM). Chapter 4 (Analysis methods) discusses the specialized analysis methods that were used to analyze the results from both types of simulations.

Chapter 5 (Creating a-Si by melting and quenching) describes the MD simulations that were used to create a-Si systems of differing densities. It also presents characterizations of these structures by standard techniques—such as radial and angular distribution function (RDFs and ADFs)—as well as some of the specialized ones explained in chapter 4.

Chapter 6 (Structure of atomic environments in a-Si) presents a method of unambiguously distinguishing between two qualitatively different atomic environments of a-Si. Due to the nature of their structure and properties, these environments were named "solidlike" and "liquidlike." The properties of variously quenched a-Si structures (chapter 5) are shown to be predicted from the mass fraction ϕ of liquidlike atomic environments by the rule of mixtures.

Chapter 7 (Deformation of a-Si at T=300K by MD) presents simulations of large strain plastic flow in a-Si systems of differing initial densities. The spectrum of mechanical behaviors exhibited is shown to correlate to the liquidlike mass fraction ϕ defined in chapter 6. Based on the simulations in chapter 7, it is concluded that ϕ can be viewed as a plasticity carrier in a-Si by analogy to the role of dislocation densities in crystalline silicon (c-Si).

The MD simulations presented in chapter 7 served as a good mesoscopic description of plasticity in a-Si, but they do not yield much insight into the intimate details of its governing mechanisms. Chapter 8 (Study of mechanisms of stress relaxation by PEM) addresses these mechanisms through the analysis of simulations conducted using the effectively zero temperature method of potential energy minimization (PEM). Overall plastic behavior in a-Si is shown there to arise from a series of stress relaxations associated with autocatalytic avalanches of unit inelastic shearing events triggered when a local yielding criterion is met somewhere inside the system. The recurring features of the structure and kinematics of unit inelastic shearing events are described in chapter 9 (Structure and kinematics of unit shearing events).

Finally, chapter 10 (Role of a-Si in plastic deformation of nanocrystalline Si) relates the findings from the previous sections to the plastic flow behavior of nc-Si. This goal is achieved through the study of a model quasi-columnar nc-Si structure. It is shown that the emergence of a liquidlike zone of easily flowing material governs large-scale

plasticity in this setting. The high relative density of this easily flowing material is shown to account for microvoid nucleation given a high initial negative pressure.

The remaining chapters are devoted to conclusions, acknowledgements, and references.

2. Background

This section reports on the work done to date on inelastic deformation in a-Si. Since the volume of available material is small, it also summarizes the development of mechanistic understanding of plasticity in metallic glasses and glassy polymers and several other issues of interest to the study of structure and stability of disordered covalently bonded network solids. A discussion of the current state of knowledge on a-Si as it exists in intergranular layers is also presented.

2.1 Amorphous silicon

Amorphous silicon (a-Si) is a form of silicon lacking in long-range crystalline order. First produced in 1969 by growth under plasma discharge [Chattick *et al.*, 1969], it has been applied to the production of inexpensive photovoltaics [Carison, Wronsky, 1976] and field-effect transistors used in LCD flat panel displays [Snell *et al.*, 1981]. Its optical and electronic properties [Staebler, Wronsky, 1977] and well as its response to various degrees of hydrogenation [Kaplan *et al.*, 1978] have been extensively studied over the past four decades. Tanaka *et al.* recently summarized the work done on a-Si to date [Tanaka *et al.*, 1999]. Nevertheless, only a few experimental studies (discussed in sections 2.3 and 2.4) on its inelastic deformation behavior have been carried out. No atomistic simulation work on plastic flow was reported prior to the author's research [Demkowicz, Argon, 2004b].

2.2 Structure and rigidity of covalent network materials

As was pointed out in the introduction, metallic systems can be seen as interacting with simple spherical potentials while polymers involve strong covalent bonding along backbones and weak bonding between individual chains. Purely covalently bonded

materials such as amorphous silicon—also known as covalent network materials—involve only strong atomic interactions of the kind found along polymer backbones. Thus, such materials represent a state of local atomic constraint more extreme than that found in either metals or polymers. For this reason, network materials could be expected to exhibit some particularities in their structure and plastic flow behavior.

Although few previous investigations have focused on elucidating the details of plasticity in disordered covalently bonded solids, there have been investigations into how the bonding structure of such materials affects their rigidity. A simple local constraint model may be used to elucidate the effect of the average number of covalent bonds between neighboring atoms on the rigidity of a random network material [Thorpe *et al.*, 2000]. This approach—first proposed as a means to finding compositions for optimal glass formability in chalcogenides [Phillips, 1979; Phillips, 1981a; Phillips, 1981b]—predicts a linear dependence of the concentration f of zero frequency eigenmodes on the average coordination $\langle C \rangle$:

$$f = 2 - \tfrac{5}{6}\langle C \rangle . \tag{2.1}$$

In particular, according to this treatment there are no more such modes above an average coordination of 2.4. Therefore, above this critical value the potential energy of a well-relaxed covalently bonded system is likely to be "stiff" in all eigendirections. These predictions have been verified by simulations performed on random bond network models [Thorpe *et al.*, 2000] and fall into a general class of problems often referred to as "rigidity percolation" [Kantor, Webman, 1984].

Materials with average coordination higher than 2.4 can be considered covalent network materials. The amorphous Si_3N_4 intercrystalline layers in nc-TiN/a-Si_3N_4 materials that motivated this research (section 1.1) have an average coordination of 3.5>2.4, i.e. they can be thought of as covalent network materials. Silicon—whose average coordination is usually not below 4—results in a level of local atomic constraint that also classifies it as a covalent network material.

The best-known model of the structure of well relaxed four-fold coordinated random network materials was proposed by Zachariasen [Zachariasen, 1932]. His view holds that nearest neighbor covalent bonds between atoms are so stiff that any change in their equilibrium length would incur a heavy energy penalty. Thus, energy would be minimized in a disordered covalently bonded material if lack of long-range order were accommodated through structural features other than changes in bond lengths, in particular through bond angle distortions [Zallen, 1979]. This structural model is called the continuous random network (CRN). Its radial distribution function is clearly distinguishable from that of disordered materials interacting through spherical potentials as the latter give evidence of significant variability in nearest-neighbor bond lengths as well as of ill-defined second nearest neighbor positions [Zallen, 1979].

2.3 Experimental investigations of inelastic relaxation in network glasses

There are, unfortunately, few experiments that directly address plasticity of amorphous network glasses. One exception is the work of Witvrouw and Spaepen [Witvrouw, Spaepen, 1993] who conducted detailed analyses of the mechanisms of viscoelastic relaxation in a-Si. Based on the noticeable deviation of stress relaxation rate from the predications of unimolecular rate theory, they concluded that activation of every viscoelastic relaxation requires the presence of more than one structural component like a bonding environment. Their investigation, however, did not reach levels of steady-state flow, having achieved initial strains only on the order of a few percent (i.e. within the elastic range of a-Si as predicted in this study; chapter 7). Part of the reason for the relatively low strains attained in these experiments is that bulk a-Si—like most ceramics—is intrinsically brittle: application of higher strains would likely have caused fracture in the samples under investigation. This limitation can in principle be circumvented if enough care is taken to reduce the number of possible crack nucleation sites and prevent the development of high tensile stresses under loading.

One approach that fulfills both criteria is to carry out an indentation study. Clarke *et al.* pursued this avenue [Clarke *et al.*, 1988] by using indentation of initially perfect c-

Si to create fully dense a-Si. They then once again indented the amorphized region causing a measurable increment of plastic flow under the indenter. In the course of indentation, the conductivity of a-Si under the indenter was observed to increase, indicating that the easily flowing state of a-Si is metallic. Upon unloading, however, the conductivity returned to its initial value and the structure of a-Si in the indented region could not be distinguished from its character before indentation. These findings imply that the easily flowing metallic state anneals out very quickly at the temperatures considered by Clarke *et al.* or becomes unstable at low enough pressures. The further study of flow in a-Si by indentation would therefore seem to require the development of *in situ* characterization techniques.

More information on the mechanisms of viscoelastic relaxation was obtained by Liu *et al.* in internal friction studies [Liu *et al.*, 1997]. They found that the internal friction of a-Si could be reduced by hydrogenating the material by an atomic fraction of hydrogen of up to 1%, i.e. well in excess of the 0.07% hydrogen atomic fraction needed to passivate dangling bonds. Despite uncertainties concerning distribution of hydrogen in the sample [Liu *et al.*, 1999], this finding suggests that the atomic configurations responsible for local inelastic structure relaxations in a-Si may have enough common structural features to possess the chemical specificity to preferentially bond hydrogen. Unfortunately, no *ab initio* simulation studies have addressed the question of the effect of hydrogenation of a-Si on its susceptibility to undergo inelastic stress relaxations.

It is clear that none of the experiments discussed above provides a definitive description of steady state plastic flow or the geometry of the bonding environments responsible for inelastic relaxation in a-Si. Because at present individual atomic environments in amorphous materials cannot be directly imaged in the laboratory, however, no single experimental finding will likely suffice. Computer modeling will therefore continue to play a key role in interpreting the experimental results, particularly by providing the basis for constructing models of homogenized behavior that take into account relevant details of the atomic configuration of amorphous materials as well as the dynamics of structural relaxations in them. Examples of such models—initially intended for metallic glasses—are the ones provided by Bulatov and Argon [Bulatov, Argon, 1994] as well as Falk, Langer, and Pechenik [Falk *et al.*, 2004].

2.4 Pressurization experiments on network glasses

The discussion presented in section 2.3 concerned investigations of shear-induced structural relaxation in a-Si. The mechanical behavior of a-Si can also be studied by compressive loading. Although such experiments involve mainly pressure-induced relaxations, it should be kept in mind that the highly variable internal stresses in amorphous solids already involve high initial shear stresses. Changes in long-range pressure distributions can provide the appropriate conditions for these internal stresses to trigger shear transformations with randomized strains that do not give rise to an overall macroscopic shear strain.

Compression investigations were carried out on the behavior of a-Si and a-Ge for pressurization in anvil cells by Shimomura *et al.* [Shimomura *et al.*, 1974]. They found that both a-Si and a-Ge undergo sharp transitions to a more highly conducting state when condensed to pressures of 10GPa and 6GPa, respectively. Unloading, however, was accompanied by a return to a state of lower conductivity and density for both a-Si and a-Ge and by crystallization in the case of a-Ge. Thus, as in the case of the indentation experiments mentioned in section 2.3, these compression studies once again bring up the issue of the rate of annealing-out of the high-pressure metallic material or its possible instability at atmospheric pressure. Moreover, they suggest the possibility that the high-pressure metallic state thought to be the easily flowing form of a-Si in indentation studies (section 2.3) is actually one of the well-known high-pressure crystalline metallic polymorphs of Si [Young, 1991] and therefore not amorphous.

To the best of the author's knowledge, the question of the rate of annealing-out of the dense conducting state of a-Si and a-Ge has not been investigated experimentally. It is furthermore difficult to investigate by atomistic simulations as well, since those are typically capable of accessing time scales on the order of only nanoseconds. Times on the order of micro- or milliseconds are completely beyond current capabilities for simulating amorphous solids, but are nonetheless short by experimental standards. One possible avenue for a future study of the kinetics of structural relaxation by atomistic simulation

would be to extract a phenomenological spectrum of activation energies by using the scaling argument applied by Deng *et al.* [Deng *et al.*, 1989]. The degree of annealing-out of high-pressure metallic material at room temperatures could then be estimated under the relatively conservative assumption that the mechanisms of relaxation and the ordering of their activation are the same regardless of the simulation time and temperature. The second question—concerning the possibility of the high-pressure state being crystalline—was addressed in experiments on a-Si by Deb *et al.* [Deb *et al.*, 2001] who characterized the compressed conducting state found by Shimomura *et al.* using *in-situ* Raman spectroscopy. They determined that high-pressure a-Si is indeed amorphous and not crystalline, but were not able to provide more detailed information on its physical properties.

Because of experimental difficulties, therefore, the intimate characteristics of the behavior of metallic high-pressure states of a-Si and a-Ge remain inaccessible. The trends they show, however, can be compared to those present in other amorphous solids that exhibit similar phenomena upon compression and whose properties have been closely studied. An example is provided by AlGe alloy, which forms two distinct amorphous structures upon compression in an anvil cell, including a dense conducting one [Yvon *et al.*, 1995]. Unlike in a-Si, however, both amorphous forms of a-AlGe remain metastable at room temperature and pressure, allowing them to be characterized in detail. Investigation by TEM and electron diffraction showed that the structure of these two forms is well described as solidlike and liquidlike, respectively, in agreement with the results obtained for a-Si presented in this study (chapters 6 and 7).

Yvon *et al.* [Yvon *et al.*, 1995] chose to study AlGe alloy as a material that may exhibit solidlike and liquidlike amorphous structures on the basis that one of the components (Ge) has an open crystalline structure and contracts upon melting. This reasoning was based on the conjecture that these properties underlie the similarities in behavior of many directionally bonded materials—such as Si, Ge, H_2O, and SiO_2 [Angell *et al.*, 1996]—including the possible existence of multiple distinct amorphous forms. In particular, experimental findings have confirmed the existence of two distinct forms of amorphous H_2O that differ markedly in density [Mishima *et al.*, 1985]. The search for an underlying thermodynamic cause for the similarities among these substances has focused

on the prospect of their exhibiting a liquid-liquid phase transition for sufficient undercooling below their melting temperatures [Stanley *et al.*, 1994; Sastry, Angell, 2003].

2.5 Plastic deformation of glassy metals and polymers

No previous atomistic simulation studies have addressed issues of fully developed plasticity in disordered covalently bonded materials. Plastic deformation in metallic glasses and glassy polymers, however, has been extensively studied. Since many generic features of inelastic relaxation in these two types of amorphous solids are the same—e.g. the fact that plasticity is due to repeated onset of localized shearing events—it is reasonable to assume that they may also be observed in a-Si. A preliminary study of the phenomenology of plastic deformation in a-Si has confirmed these similarities [Demkowicz, 2004a]. This section therefore reviews the work done to date on plasticity in glassy metals and polymers.

Even before computing capabilities became sufficiently great to allow for meaningful atomistic simulations of plastic deformation, other methods of modeling the collective behavior of systems composed of discrete particles interacting with spherical potentials were developed. Among the most notable is the bubble raft technique, which allowed for the investigation of systems composed of hundreds of constituent particles in two dimensions. As a means to visualizing complex rearrangements occurring under deformations applied externally, this method was an invaluable tool in the qualitative study of atomic scale behavior of disordered materials [Argon, Kuo, 1979]. Upon complete description of the interbubble potential function the method became quantitative as well and yielded some of the earliest insights into the mechanisms of plastic deformation in disordered materials whose constituent atoms could be thought of as interacting with pair potentials, namely metallic glasses [Argon, Shi, 1983]. Because of its value as a rapid visualization tool, the bubble raft technique is still used today [Van Vliet, Suresh, 2002].

Using the bubble raft method, Argon and Shi [Argon, Shi, 1983] constructed a two dimensional representation of a metallic glass by mixing bubbles of two different sizes and not allowing them to arrange into crystalline domains. They then deformed the bubble raft by externally applying displacements to the walls of the raft in a way that could be interpreted as applying total system-wide strain increments. In the course of the deformation process, they observed that certain regions of the bubble raft suddenly underwent large, localized bursts of displacement. These localized rearrangements usually involved about 10 atoms. Analysis of changes in bubble positions within the active regions before and after a rearrangement clearly indicated that these transformations were shearing events and led to the irreversible accumulation of shear strain, i.e. to localized plastic deformation. Using the interbubble potential developed earlier, Argon and Shi were able to use their insight into the kinematics of atom cluster rearrangements to calculate a distribution of activation energies associated with the transformations.

These findings stood in stark contrast to the Eyring hypothesis of flow in liquids [Eyring, 1936] that—until then—had been considered a likely candidate (on grounds of structural similarity [Kauzmann, 1948]) for explaining flow in glassy materials. This hypothesis stipulated that individual atoms of a liquid or glass could irreversibly change their position in a manner similar to diffusion when an opening appeared in the surrounding medium. As indicated, however, bubble raft visualizations indicated a mechanism involving the collective motion of around 10 atoms, not just 1 as Eyring had proposed. Even more seriously, the motion of a single atom moving through open channels in the surrounding medium is a mechanism that is inherently incapable of producing shear transformations since shear cannot even be meaningfully defined unless at least 4 interacting, neighboring atoms rearrange in a cooperative manner.

In a later series of molecular dynamics computer simulations on a two dimensional single component system of particles interacting with a central potential, Deng *et al.* [Deng *et al.*, 1989] verified the results found in the bubble raft studies. Defining a local strain measure, they were able to identify transforming regions as those in which high levels of deviatoric strain had rapidly accumulated. Furthermore, they addressed the question of the correlation of excess volume distribution to the localization

of shear transformations (Turnbull, Cohen, 1958; Cohen, Turnbull, 1959; Turnbull, Cohen, 1961). By using a local structure descriptor based on the Voronoi tessellation around atomic positions, Deng verified that certain regions within the model metallic glass were more prone to undergoing irreversible transformation than others and that these were sites of high free volume.

The studies of plasticity in model metallic glasses suggested the possibility of the existence of distinct mechanisms of inelastic structure transformation in amorphous materials. Building upon the work of Deng, Bulatov and Argon [Bulatov, Argon, 1994] constructed a simplified model of metallic glasses that presupposed a single plastic deformation mechanism that could be activated by both thermal motion and mechanical stresses. This assumption was meant to combine the observations that plastic deformation in glassy metals is local and occurs preferentially at certain sites. Through a series of simulations, Bulatov and Argon showed that if interactions between inelastically transforming regions and the surrounding elastically deforming matrix material are taken into account, a single deformation mechanism is able to reproduce all of the high and low temperature behaviors observed in metallic glasses.

The model of Bulatov and Argon uses several material parameters to characterize the form of thermal and mechanical activation behavior of unit plastic events, but makes no reference to their origin. In particular, these parameters could be extracted from atomistic simulations of plasticity in materials governed by any interaction law, provided that unit plastic deformation events indeed exist in these materials. The general conclusions of the Bulatov-Argon model would therefore be expected to apply to disordered covalently bonded materials as much as to metallic glasses. Later work on plastic deformation of metallic glasses [Falk, Langer, 1998; Falk *et al.*, 2004] has largely confirmed the findings discussed above.

Unlike metals, polymers are governed by two types of atomic interaction: strong covalent bonds along polymer chain backbones and weak Van der Waals-type interactions between atoms on separate polymer chains [Theodorou, Suter, 1985b]. This comparatively more complex form of bonding along with a variety of possible chain conformations and branchings leads to a large variety of possible local structure features in polymers [Theodorou, Suter, 1986; Hutnik *et al.*, 1991a]. The kinematics of plastic

transformation in these materials is similarly more convoluted: they involve significantly larger numbers of participating atoms than in metallic glasses (on the order of hundreds [Mott *et al.*, 1993]) as well as a large variety of discernable structural rearrangements [Hutnik *et al.*, 1991b].

Nonetheless, despite the intricacies of bonding and transformation kinematics apparent in polymers, certain features of the fundamental mechanisms of plasticity in these materials are entirely analogous to those occurring in the far simpler metallic glasses. Deformation in polymers also occurs in discrete, localized bursts. It can be activated thermally as well as mechanically and the atomic rearrangements that accompany plastic deformation can be characterized as shear transformations [Mott *et al.*, 1993]. Finally, the relaxation strain spectra found in computer simulations—according to Bulatov—are not inconsistent with operation of a finite number of activated processes.

2.6 No dislocation-mediated plasticity in amorphous solids

The success of dislocation mechanics in explaining crystal plasticity prompted some investigators [Gilman, 1968] to suggest that the notion of "dislocation" can be sufficiently generalized so that a dislocation-based structure analysis could be performed on disordered materials. The difficulty with constructing such a generalization lies in the inherent reference to the crystal lattice in the traditional definition of edge and screw dislocations: both are characterized by their respective Burgers vectors [McClintock, Argon, 1966]. Such a characterization is impossible in materials that by definition do not contain a crystalline component. A number of generalizations were nevertheless made [Gilman, 1968], but only one resulted in a distinguishing criterion sufficiently unambiguous to be applied in the context of atomistic simulation. This criterion made no reference to the underlying core configuration of "generalized dislocations" and focused instead on the effect that a dislocation produces in the surrounding material. Namely, it claimed that a generalized dislocation is the kind of structure difference between two configurations that produces a difference in long-range stress fields between these two

configurations that can be characterized by the well-known stress fields produced in a crystal lattice by the introduction of screw and edge dislocations [Chaudhari *et al.*, 1979].

Using this definition as a starting point, Chaudhari *et al.* conducted computer simulations to investigate whether it would be possible to observe generalized dislocations in a metallic glass. They started by creating large samples of disordered material and characterizing the stress distributions within them. They then followed a procedure borrowed from elementary mechanics of materials textbooks for introducing dislocations into these samples: the removal of a half-plane of atoms to create an edge and the shear-like shifting of a half-plane of atoms to create a screw [McClintock, Argon, 1966]. Analysis of the resulting stress fields revealed that the difference in the distribution of stresses between the new and initial sample configurations were indeed in good agreement with those observed in crystal lattices.

Upon equilibration by potential energy minimization of the new configurations, however, the stress field associated with the edge dislocation construction vanished: no coherent difference between the initial and equilibrated edge configuration could be found. In the case of the screw construction, equilibration did not destroy the characteristic stress fields of screw dislocations in crystal lattices. Neverthelesss, the elastic energy stored in the stress fields associated with this construction was so high compared to the typical activation energy of localized shearing transformations of the kind investigated by Argon and Shi [Argon, Shi, 1983] as well as Deng *et al.* [Deng, 1989] that under normal loading conditions these shearing transformations would quickly dissipate the generalized screw dislocation. Experimental studies of dissipation of dislocation structures in crystals under irradiation confirm the relative instability of highly stressed regions in amorphous media [Cherns *et al.*, 1980].

The conclusion that can therefore be drawn from the work of Chaudhari *et al.* is that generalized edge dislocations are not stable within a disordered medium. Generalized screw dislocations, on the other hand, though stable and therefore conceivably observable, cannot be responsible for plastic flow in disordered materials because their operation is not energetically favorable compared to other deformation mechanisms (localized shear transformations) known to operate in these same materials [Argon, 1981].

2.7 Grain boundary structure in nanocrystalline network solids

The argument—mentioned in section 1.1—for the increasing difficulty of dislocation motion with decreasing grain sizes in metals holds all the more true for covalently bonded materials such as the nc-TiN/a-Si_3N_4 ceramic composites or nc-Si. The reason for this conclusion is that the lattice resistance to dislocation motion is vastly higher in covalently bonded materials than in metals. FCC metals typically have a negligible lattice resistance (about 20 MPa [Olmsted *et al.*, 2001]) and BCC metals have lattice resistances in the range of 600-900 MPa [Conrad, 1963] while the lattice resistance in Si is around 13 GPa [Ren *et al.*, 1995]. In Cu, dislocation motion ceases to play an important role in plastic flow behavior at grain sizes on the order of 10-20nm. Thus, in nc-TiN/a-Si_3N_4, where the size of crystalline grains is thought to be in the range of 4-6nm (section 1.1), the contribution of dislocation-mediated plasticity to the overall plastic response of the material can be safely ignored. As a result, the structure and mechanical behavior of intergranular material in nanocrystalline covalently bonded materials is of prime importance to understanding the plastic flow behavior of such materials.

While there have been no investigations of the mechanisms of plastic deformation by computer simulation in the case of nanocrystalline covalently bonded materials such as nc-Si, a number of studies of grain boundary structure have been undertaken [Keblinski *et al.*, 1996; Keblinski *et al.*, 1997]. These investigations have shown that for high angle boundaries between neighboring grains there forms a disordered intergranular layer of 1-3 atomic dimensions in thickness. Using computer simulations of intergranular structure in silicon bicrystals, Keblinski *et al.* [Keblinski *et al.*, 1996] have demonstrated on a number of crystal orientations that structurally indistinguishable disordered layers form both when an initially unrelaxed grain boundary is annealed as well as when two neighboring crystal slabs are allowed to grow out from the melt until they impinge upon each other. Furthermore, they show that the disordered intergranular structure is thermodynamically stable in the sense that its overall energy is smaller than that of the corresponding unrelaxed grain boundaries.

Keblinski *et al.* [Keblinski *et al.*, 1997] have also carried out computer simulations to study the structure of grain boundaries in nanocrystalline silicon. Starting with a configuration of grains that avoided all high symmetry grain boundaries, they annealed the sample and found that—much as in the case of the bicrystal—there formed a disordered intergranular layer of 1-3 atomic diameters thickness. Structurally indistinguishable grain boundaries formed when the same configuration of crystalline grains was grown from the melt, starting with a set of properly oriented crystalline seeds. Radial and angular distribution functions constructed at grain boundaries, triple junctions, and 4- and 6-fold points demonstrated that intergranular material in each of these regions could be considered disordered.

Experimental evidence in support of the existence of disordered intergranular material between highly misoriented crystalline slabs has also been found. When developing the technology of joining perfectly crystalline silicon wafers for semiconductor purposes, Furukawa *et al.* [Furukawa *et al.*, 1986] observed that the nature of the bond between wafers depended sensitively on the crystalline misorientation of the silicon wafers. In particular, when the surfaces being joined had little or no misorentation, a nearly perfect crystalline structure was formed. When two (100) surfaces were misoriented by 45 degrees, a thin grain boundary whose structure was difficult to discern resulted. If (100) and (111) surfaces misoriented by 45 degrees were joined, however, the resulting annealed intergranular structure was a disordered layer of thickness around 10 atomic diameters.

Careful study of the structure and distribution of components in the nc-TiN/a-Si_3N_4 ceramic composites suggests that the TiN phase forms crystalline grains 4-6nm in size while Si_3N_4 forms a 1-3 atomic diameter-thick disordered layer that wets the nc-TiN grains. This conclusion was reached after studies of stoichiometry [Veprek, Argon, 2002] revealed that the proportions of TiN to Si_3N_4 were just right to allow such wetting to take place. Therefore, the expected intergranular structure of Si_3N_4 in nc-TiN/a-Si_3N_4 coincides with the structure of intergranular layers in nc-Si as simulated by Keblinski *et al.*, lending support to the choice of investigating the mechanical behavior of the chemically complex nc-TiN/a-Si_3N_4 using elemental silicon as a model system.

3. Simulation methods

This chapter describes the system size and boundary condition as well as the applied mode of deformation chosen for this study. It then discusses the choice of the Stillinger-Weber potential as a model for Si as well as the molecular dynamics (MD) and potential energy minimization (PEM) algorithms used to conduct the simulations presented in subsequent chapters.

3.1 System configuration

The simulations presented in this study were conducted on systems consisting of 4096 atoms under periodic boundary conditions. These systems were deformed by successive application of volume conserving strain increments. This section details the rationale behind the choice of system size as well as the mode of applied mechanical deformation.

3.1.1 Boundary conditions and size

Boundary value problems in continuum mechanics are typically formulated using some combination of conditions that specify forces (stresses) or displacements (strains) at the boundaries of the system under consideration. Such conditions can also be applied in the discrete setting of atomistic simulation and are often of great utility in the study of free surfaces or of soft materials confined by relatively rigid surroundings. A more common approach in the study of bulk properties such as plastic deformation behavior, however, is to specify periodic boundary conditions. Under these conditions, the atomic configuration is thought to occupy a simulation cell in the shape of a general parallelepiped. The atoms at one of the surfaces of this parallelepiped undergo direct energetic interactions with atoms at the opposite surface. The application of periodic boundary conditions, therefore, is effectively a means to simulating the behavior of an

infinite body with a periodic structure. The lattice of this structure is specified by the shape of the simulation cell. The basis that decorates this lattice is just the atomic configuration contained in the simulation cell itself.

Periodic boundary conditions were adopted for the entirety of this study. Since bonded atoms undergo direct energetic interaction, it is possible under such conditions for an atom to interact with its nearest image atoms if the size of the simulation cell is small enough. Such interaction is clearly unphysical and therefore undesirable. Most empirical potentials for modeling direct bonding between atoms, however, incorporate a cutoff distance beyond which any two atoms no longer undergo any direct energetic interaction. Atomistic simulations under periodic boundary conditions that use such potentials must therefore have simulation cells whose dimensions in every direction exceed twice the cutoff distance for direct atomic interaction. In the case of the potential used in this study (see section 3.2.1) the cutoff distance is about 1.6 times the nearest neighbor distance in the diamond cubic crystalline configuration. Since the edge of the cubic unit cell for this crystalline configuration is about 2.3 times the nearest neighbor distance (see section 5.2), a system consisting of 2x2x2 diamond cubic unit cells (64 atoms) is large enough to prevent direct energetic interactions between atoms and their nearest images under periodic boundary conditions.

In addition to direct energetic interactions, atoms and their environments can undergo interactions with their images under periodic boundary conditions due to long-range elastic stress fields mediated by the intervening atoms. This limitation is inherent to atomistic simulations under periodic boundary conditions. Its effects decrease with increasing system size, however, and can serve as a basis for selecting the appropriate number of atoms to incorporate in a given simulation. The size of the atomic system considered in this study was chosen based on an analysis that assumed that—as in the case of metallic glasses [Deng *et al.*, 1989] and amorphous polymers [Mott *et al.*, 1993]—low temperature plastic flow in a-Si occurs through a series of unit deformation events. These assumptions were verified in the course of the study (chapters 8 and 9). The size of the a-Si system was made large enough to ensure that the character of these unit plastic relaxation events was not unduly affected by elastic interactions with their periodic images. This determination was accomplished on the basis of an argument used

previously by Hutnik [Hutnik *et al.*, 1991b] in the case of phenylene ring rotations in polycarbonate of bisphenol A.

Consider a small, spherical, isotropically elastic body of radius a contained within a larger surrounding body with the same elastic properties. If the small body occupies a volume fraction c of the total assemblage and there is a spherically symmetric radial misfit ε_r between the two bodies in their relaxed state, then the total elastic energy of the assemblage can be expressed as

$$U = \left(\frac{4\pi a^3}{3}\right)\left(\frac{9B\varepsilon_r^2}{2}\right)\left[\frac{2(1-2\nu)+(1+\nu)c}{2(1-2\nu)+(1+\nu)}\right]. \tag{3.1}$$

Here B is the bulk modulus and ν Poisson's ratio. Taking the limit $c \to 0$ gives the elastic energy of the assemblage when the size of the larger surrounding elastic body is allowed to become unbounded. The relative difference between this limiting value of the elastic stored energy and the value at finite c is

$$\frac{\Delta U}{U} = \frac{(1+\nu)c}{2(1-2\nu)+(1+\nu)c}. \tag{3.2}$$

The quantity $\Delta U/U$ provides an order of magnitude measure of the excess elastic energy stored in finite system with a misfitting inclusion versus and "infinite" one with a misfitting inclusion of the same size.

Section 5.5.1 exhibits typical isotropic elastic constants for the a-Si systems created in this study. Using the relation [McClintock, Argon, 1966]

$$\nu = \frac{1-2\mu/3B}{2+2\mu/3B} \tag{3.3}$$

it can be found that the Poisson ratio for a-Si is in the range of 0.35-0.4. Meanwhile, unit plastic events for a-Si occur within clusters consisting of about 10 atoms (chapters 8 and 9). Therefore, the size N of the atomic system under consideration (in terms of the

number of constituent atoms) can be related to the volume fraction c in equation 3.2 through the relation $c = 10/N$. The excess elastic energy due to the finite size of the system $\Delta U/U$ can then be made arbitrarily small by choosing a sufficiently large number of atoms N in the simulated system. The system should not be chosen so large, however, that the individual discrete stress relaxations responsible for inelastic deformation become difficult to discern from reversible elastic behavior.

According to equation 3.2, the excess elastic energy stored in a 4096-atom system (8x8x8 diamond cubic unit cells) due to its confinement within the simulation cell is on the order of 0.7%. Such a small confinement effect was deemed acceptable. Furthermore, deformation of an a-Si system consisting of 4096 atoms gives rise to clearly distinguishable stress relaxations (section 8.2), as required. Thus, all simulations presented in this study were carried out on systems containing 4096-atoms.

3.1.2 Mode of deformation

Plastic deformation simulations were carried out under volume conserving plane strain [McClintock, Argon, 1966]. Each initially equilibrated structure was deformed by applying a system-wide extension increment in the x-direction ($d\varepsilon_x$) and a contraction increment in the y-direction ($d\varepsilon_y$) while holding the z-direction length fixed. The constant volume requirement in this loading mode requires $d\varepsilon_y = -d\varepsilon_x/(1+d\varepsilon_x)$, i.e. the amount of contraction applied in the y-direction was actually slightly less than extension in the x-direction. No off-diagonal strain components were applied.

After an atomic configuration is strained, it must be re-equilibrated using relaxation by molecular dynamics (MD, section 3.3) or potential energy minimization (PEM, section 3.4). In the case of MD, volume conserving plane-strain increments with $d\varepsilon_x = 10^{-3}$ were applied. To accurately resolve all mechanical instabilities arising during a mechanical deformation simulation using PEM relaxation, however, volume-conserving plane-strain increments with $d\varepsilon_x = 3.2 \cdot 10^{-5}$ had to be applied.

Equilibrium was considered to have been attained in MD relaxation when macroscopic system characterizers such as the pressure and internal energy reached

values that were steady to within the level of internal thermal fluctuations. When deformation was conducted at a temperature of T = 300K, this state is observed to have been attained after 1000 MD time increments. Extending the time of relaxation to 10000 time increments did not result in any significant changes in the trends of behavior obtained from the simulations. The equilibrium condition used in PEM relaxation is described in section 3.4.

Section 7.3 describes MD deformation simulations conducted under constant externally applied pressure. This condition requires that the constraint of volume-conserving deformation be relaxed. This refinement was achieved by rescaling the system size to the desired pressure after application of each strain increment and using a constant pressure MD algorithm (section 3.3).

3.2 Empirical potentials

In simulations that use the empirical potential approximation, atomic nuclei are considered to be classical point masses interacting with a pre-specified, classical force laws derived from potential functions that depends on the nuclear positions. The precision obtained from conducting an *ab initio* simulation that directly solves Schrodinger's equation under some approximation is thereby lost. Atomistic simulations based on empirical potentials, however, incur significantly fewer computational costs than those based on *ab initio* methods. They are therefore preferable when applied to studies that are not concerned with a specific substance, but rather with the generic behavior of a class of materials that can be characterized by common bonding features. In particular, empirical potential simulations can be conducted on much larger atomic configurations and over longer simulated time spans than *ab initio* simulations. Since the aim of this study is to understand the plastic flow behavior of silicon as a model covalently bonded system, the empirical potential approximation has been adopted for all simulations presented here.

The assumed form of most empirical potentials is a sum of terms arising from interactions of pairs, triples, quadruplets, etc. of atoms:

$$V(r_1, r_2, \ldots r_N) = \sum_{i<j} V_2(r_i, r_j) + \sum_{i<j<k} V_3(r_i, r_j, r_k) + \ldots \tag{3.4}$$

Generic physical insights are used to choose a functional form for the potential energies V_2, V_3, etc. These functional forms generally include undetermined parameters that can be chosen to make the behavior of a collection of atoms governed by the empirical potential conform as closely as possible to the behavior of the substance being modeled. All functional forms entering into the empirical potential must satisfy the requirements of objectivity and frame indifference.

3.2.1 Stillinger-Weber potential

The Stillinger-Weber (SW) potential for silicon [Stillinger, Weber, 1985] was chosen for this study from among the other most popular options [Tersoff, 1986; Balamane *et al.*, 1992; Bazant *et al.*, 1997] for four main reasons. First, the SW potential is extremely well tested: its properties and behaviors have been studied by a number of independent investigators [Luedtke, Landman, 1989; Kluge, Ray, 1988; Keblinski *et al.*, 1996; Keblinski *et al.*, 1997; Sastry, Angell, 2003] whose work serves as a solid benchmark for further research. Second, SW Si has proved itself capable of producing amorphous configurations [Stillinger, Weber, 1985; Luedtke, Landman, 1989], disordered intergranular layers for certain grain boundaries [Keblinski *et al.*, 1996], as well as fully nanocrystalline configurations that reproduce the essential structural features of nc-TiN/a-Si_3N_4 [Keblinski *et al.*, 1997].

Third, the SW potential was chosen because it accounts for directional bonding in a particularly transparent manner: it involves only two-body and three-body interactions between atoms. An immediate question that arises about such a simple construction is whether it results in a completely accurate and precise description of the behavior of real silicon. The answer to this question cannot be unequivocal, for neither the SW potential nor any alternatives to it—being, after all, only *empirical* potentials—can do so perfectly.

This shortcoming does not in any way invalidate their use, however, since many of them—including SW—do reproduce the behavior of silicon in broad brushstrokes.

The SW potential, in particular, does better than most in reproducing the molten form of Si (an advantage that will be of importance in this study), coming closest to the experimentally observed nearest neighbor coordination of about 6.4 [Waseda, Suzuki, 1975] with a predicted coordination of around 5 [Sastry, Angell, 2003]. The Environment-Dependent Interatomic Potential (EDIP) [Bazant *et al.*, 1997] is further off the mark with a prediction of about 4.5 [Keblinski *et al.*, 2002]. The EDIP, however, predicts a coordination of 4.04 in amorphous Si (a-Si), which comes closer to the experimentally observed coordination of about 3.9 in a-Si produced by self-ion implantation [Laaziri *et al.*, 1999] than that predicted by SW (4.14 [Luedtke, Landman, 1989]). Such variations are acceptable, however, since both the SW potential and EDIP avoid stark deviations from the properties of real silicon and neither predicts manifestly unphysical behaviors. Results obtained from simulations that use these potentials can therefore be viewed as semi-quantitative.

This lack of gross errors and agreement with trends in behavior of real Si is the fourth reason for the choice of SW Si as a model material for this study. It must be kept in mind, however, that since only the *trends* in behavior of real Si are reliably reproduced, only the *trends* in the results presented in this study are expected to hold for the behavior of real a-Si. Indeed, it has been known for both SW and EDIP to give results that disagree numerically with experiments, but nevertheless perfectly reproduce the correct trends in behavior [Cai *et al.*, 2000].

The value of the SW potential for any atomic configuration, V, is a sum of interactions among pairs and triplets of atoms expressed as

$$V = \sum_{i<j} V_2(r_{ij}) + \sum_{i<j<k} V_3(r_{ij}, r_{ik}, r_{jk}) \tag{3.5}$$

where r_{ij} is the distance between atoms i and j. The potential contains characteristic length and energy parameters σ and ε. These parameters are used to nondimensionalize the component terms V_2 and V_3 as follows:

$$V_2(r_{ij}) = \varepsilon f_2(r_{ij}/\sigma)$$
$$V_3(r_{ij}, r_{jk}, r_{ik}) = \varepsilon f_3(r_{ij}/\sigma, r_{jk}/\sigma, r_{ik}/\sigma) \tag{3.6}$$

The SW potential also contains a characteristic atomic mass parameter m that corresponds to the atomic mass of Si and enters into the scaling of nuclear trajectories when they are found by integrating the dynamical equations of motion dictated by Newton's second law, e.g. using an MD algorithm (section 3.3).

The functional form of the two-body terms f_2 was chosen to be

$$f_2(r) = \begin{cases} A\left(Br^{-p} - r^{-q}\right)e^{\frac{1}{r-a}}, r < a \\ 0, r > a \end{cases} \tag{3.7}$$

This functional form exhibits the intuitive characteristics of the Lennard-Jones potential [Allen, Tildesley, 2000], i.e. hard-core repulsion at small distances followed by a potential minimum at some specified greater distance and subsequent convergence to zero at large distances. Unlike the Lennard-Jones potential, however, the two-body terms of the SW potential incorporate a weighting function that assures that the potential interaction along with all its derivatives become zero at some finite pre-specified cutoff radius a. The quantities A, B, p, and q denote tunable parameters and can be chosen to fit the form of the potential to experimental results for silicon.

The two-body terms f_2 do not account for any directional bonding among atoms. That effect is entirely included in f_3, the potential of interaction of triplets of atoms. Its form is

$$f_3 = h(r_{ij}, r_{ik}, \theta_{jik}) + h(r_{ij}, r_{jk}, \theta_{ijk}) + h(r_{jk}, r_{ik}, \theta_{ikj}) \tag{3.8}$$

where

$$h(r_{ij}, r_{ik}, \theta_{jik}) = \begin{cases} \lambda(\cos\theta_{jik} + \frac{1}{3})^2 e^{\left(\frac{\gamma}{r_{ij}-a}\right)} e^{\left(\frac{\gamma}{r_{ik}-a}\right)}, (r_{ij} < a) \text{and} (r_{ik} < a). \\ 0, (r_{ij} \geq a) \text{or} (r_{ik} \geq a) \end{cases} \tag{3.9}$$

The quantity θ_{jik} denotes the bond angle centered on atom i and bordered by the individual bonds $\mathbf{r}_{ij}$ and $\mathbf{r}_{ik}$. The essential feature of the functional form in equation 3.9 is the $(\cos\theta_{jik} + \frac{1}{3})^2$ term. When the bond angle θ_{jik} is precisely the tetrahedral angle found in the diamond cubic lattice configuration ($\theta = \cos^{-1}(-1/3) \approx 109.5^\circ$), the value of this term vanishes. All other values of the bond angle result in the last term being non-zero. Therefore, the three-body interactions so constructed favor the four-fold coordinated configuration exhibited by silicon in its diamond cubic form. The exponential terms $e^{\left(\frac{\gamma}{r_{ij}-a}\right)}$ and $e^{\left(\frac{\gamma}{r_{ik}-a}\right)}$ fulfill the same purpose as in the case of two-body interactions, namely they enforces a cutoff radius for the value of the potential interaction along with all of its derivatives. The quantities λ and γ are tunable parameters of the potential.

From the description above, it is clear that the SW potential can be thought of as essentially a Lennard-Jones potential that penalizes—through three-body interactions—bond angles deviating from those found in the diamond cubic crystal configuration. It is therefore a natural extension of the well-known Keating potential [Keating, 1966] to situations where atoms need not simply oscillate about some specified equilibrium position but can also arbitrarily rearrange.

The parameters appearing in the functional forms in equations 3.6, 3.7, and 3.9 were chosen to ensure the best agreement with the experimentally observed behavior of silicon. The criteria guiding the selection were [Stillinger, Weber, 1985]:

- Stability of the diamond cubic lattice structure at room temperature and pressure
- Temperature of the melting point
- Contraction of the diamond cubic crystalline structure upon melting
- Formation of a highly coordinated liquid form
- Lattice spacing and atomization energy of crystalline silicon

These criteria led to the following choice of parameters presented in Table 3-1.

Parameter	Numerical value
σ	0.20951 nm
ε	50 kcal/mol ≈ 2.1676 eV
m	28.0855 m_u ≈ 4.6457e-26 kg
A	7.049556277
B	0.6022245584
p	4
q	0
a	1.80
λ	21.0
γ	1.20

Table 3-1: The values of the tunable SW potential parameters in equations 3.6, 3.7, and 3.9 chosen by the potential's designers [Stillinger, Weber, 1985].

Applying dimensional analysis [Allen, Tildesley, 2000], the characteristic length σ, energy ε, and mass m of the SW potential given in table 3-1 can be used to derive an associated characteristic time t^*, pressure p^*, force f^*, and temperature T^*. The values of these derived quantities are given in Table 3-2 below.

Quantity	Formula	Numerical value
t^*	$\sqrt{m\sigma^2/\varepsilon}$	76.6 fs
p^*	ε/σ^3	37.76 GPa
f^*	ε/σ	1.658 nN
T^*	ε/k_B	25,153 K

Table 3-2: The characteristic time t^*, pressure p^*, force f^*, and temperature T^* derived from the characteristic length σ, energy ε, and mass m of the SW potential given in table 3-1. The quantity k_B denotes the Boltzmann constant.

Figure 3-1 plots the shape of the two-body SW potential term f_2 (equation 3.7) with the numerical values of tunable parameters presented in Table 3-1. Figures 3-2 and 3-3 do the same of the exponential and angle-dependent portions $e^{\left(\frac{\gamma}{r_{ij}-a}\right)}$ and $\left(\cos\theta_{ijk}+\frac{1}{3}\right)^2$ of the three-body term f_3 (equation 3.9).

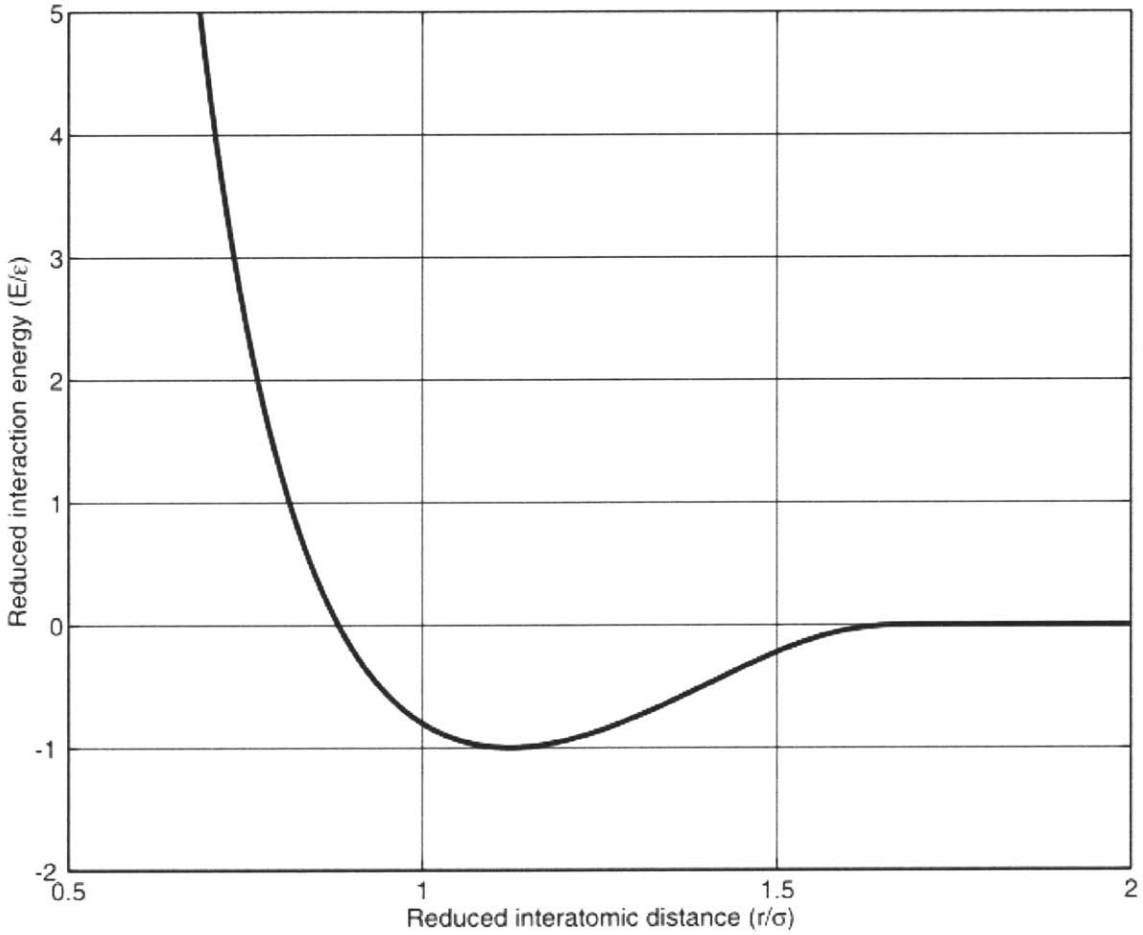

Figure 3-1: The shape of the SW two-body interaction term f_2 (equation 3.7).

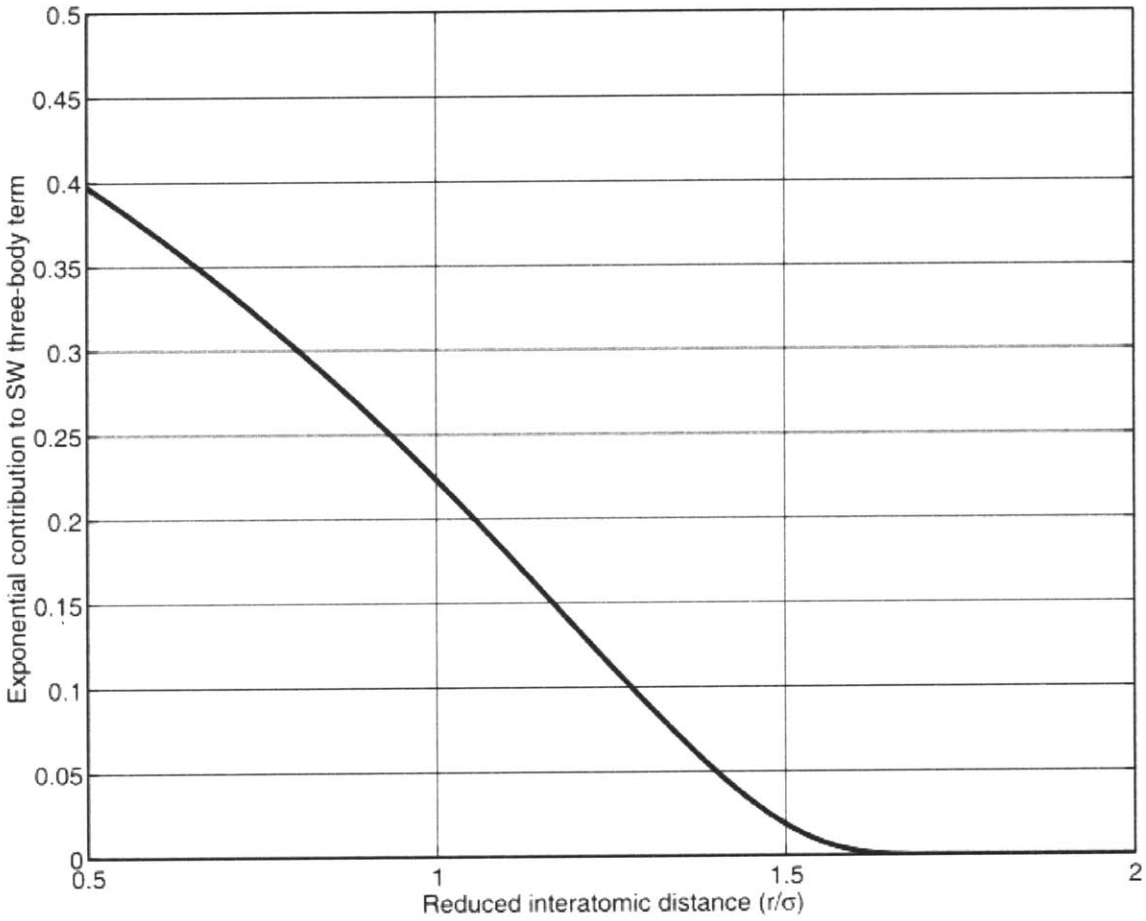

Figure 3-2: The shape of the exponential contribution $e^{\left(\frac{\gamma}{r_{ij}-a}\right)}$ to the SW three-body interaction term f_3 (equation 3.9).

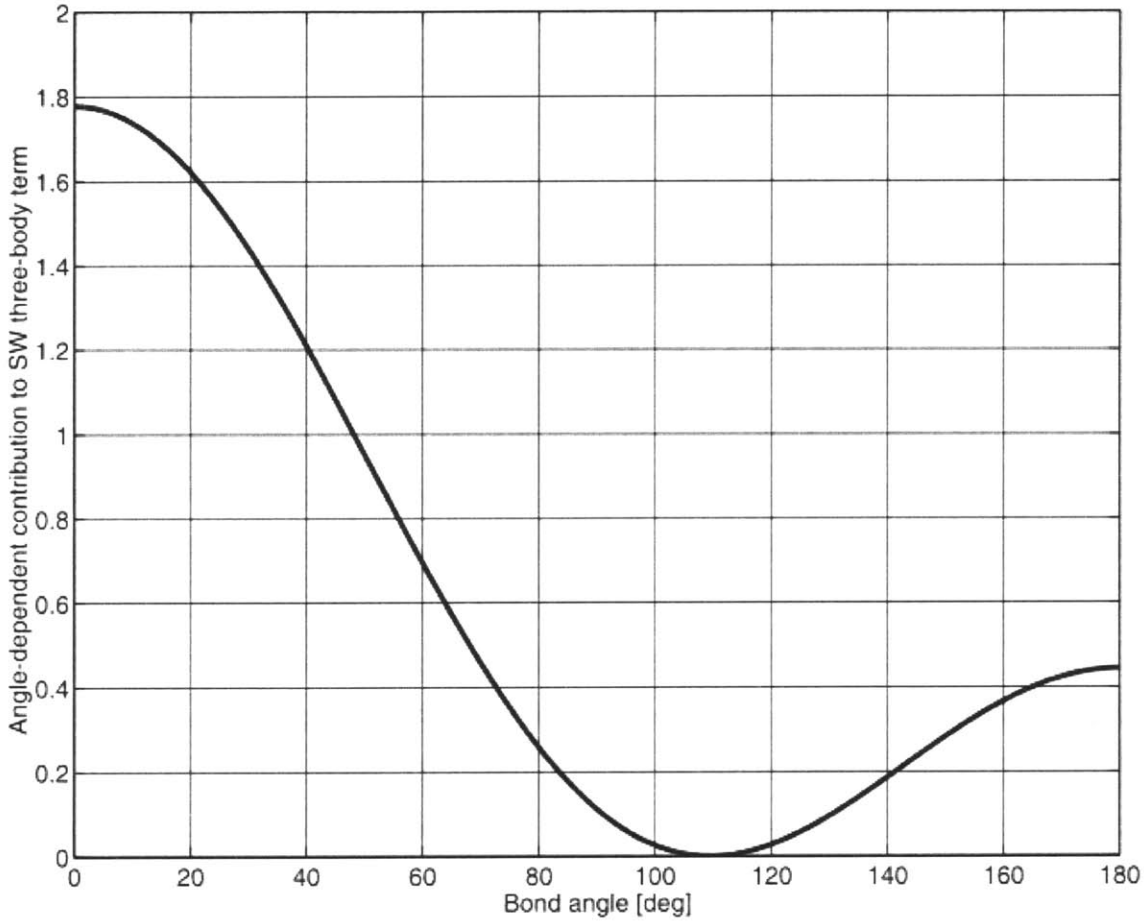

Figure 3-3: The shape of the angle-dependent contribution $\left(\cos\theta_{jik}+\frac{1}{3}\right)^2$ to the SW three-body interaction term f_3 (equation 3.9).

3.2.2 Other potentials for Si

An exhaustive comparative review of empirical potentials for Si has been prepared by Balamane *et al.* [Balamane *et al.*, 1992]. The two most popular alternatives to the Stillinger-Weber potential, however, are the Tersoff potential [Tersoff, 1986] and the Environment-Dependent Interatomic Potential (EDIP) [Bazant *et al.*, 1997].

Unlike the SW potential, the Tersoff potential [Tersoff, 1986] includes only two-body terms:

$$V = \frac{1}{2}\sum_{i,j\neq i} f_c(r_{ij})\left[Ae^{-\lambda_1 r_{ij}} - B_{ij}e^{-\lambda_2 r_{ij}}\right] \tag{3.10}$$

This choice of functional form is motivated by the realization that binding-energy curves for solid cohesion and chemisorption can be described by a single dimensionless curve and three scaling parameters [Rose *et al.*, 1983] and that this behavior can be achieved by the assumption of an interatomic potential of the form given in equation 3.10 above [Abell, 1985]. The first exponential term in brackets describes repulsion while the second describes bonding. In order to ensure that silicon have the required tendency to form the four-fold coordinated diamond cubic structure, the value of B_{ij} could not be taken to be a constant. Instead, it was given a complex functional form that reflected the weakening of bonds in a highly coordinated atomic environment. A potential cutoff radius is imposed by the weighting function f_c.

The parameters in the final functional forms of the Tersoff potential were fitted to give maximum agreement for the lattice constant and bulk modulus of diamond crystalline Si as well as for the cohesive energies of the Si_2 dimer, the diamond cubic structure, and of hypothetical Si simple cubic and FCC structures. The behavior of the potential so parameterized was tested by comparing it to results from a number of *ab initio* simulations, mainly of lattice defect structures [Tersoff, 1986]. This potential was not chosen for the present study because its relatively complex functional form does not lend itself to easy algebraic manipulation nor to immediate intuitive understanding.

Furthermore, the Tersoff potential reproduces the behavior of molten Si poorly, casting doubt upon whether it accurately reproduces the trends in behavior exhibited by real Si.

The EDIP [Bazant *et al.*, 1997] combines the approaches used in the SW and Tersoff potentials: it includes two-body and three-body interactions, both of which depend on the form of the environment of individual atoms. The highly involved parameterization of this potential results in good transferability to certain types of silicon lattice defect structures [Justo *et al.*, 1998]. As mentioned in section 3.2.1, EDIP is capable of modeling the well-equilibrated amorphous silicon structure better than the SW potential, but its performance is worse in reproducing certain properties of silicon in its liquid form. Its ability to accurately model quickly quenched (suboptimally relaxed) disordered structures is therefore in question. This drawback together with the high complexity of EDIP made its use unattractive for the purposes of this study.

3.3 Molecular dynamics (MD)

The collective behaviors of systems composed of many atoms and governed by empirical potentials are most commonly investigated by Monte Carlo (MC) and molecular dynamics (MD) simulations [Allen, Tildesley, 2000]. The former are especially convenient in studies of long-time thermodynamic behavior, particularly if the salient unit processes are already well understood. The latter are more useful when detailed investigations of atomic level motion are called for. Therefore, in cases when little is known about the physical processes governing long time collective behavior—as in the formation of a-Si from the melt and the deformation behavior of the resulting material—MD is preferred despite the greater computational resources it requires.

Given an interaction potential (section 3.2), MD simulations can be carried out by specifying an initial atomic configuration along with boundary conditions (section 3.1.1) and integrating the Newtonian equations of motion

$$\begin{aligned} \dot{r}_i &= p_i / m_i \\ \dot{p}_i &= -\nabla_{r_i} V = f_i \end{aligned} \tag{3.11}$$

Here, the value of the assumed interatomic potential is denoted by V and i indicates one of the $3N$ degrees of freedom of the system, each associated with a component of a single atom's position. The quantities r_i, p_i, m_i, and f_i denote the position, momentum, mass, and force on the i^{th} degree of freedom, respectively. Equations 3.11 are integrated using a finite difference scheme such as the commonly used Gear predictor-corrector [Allen, Tildesley, 2000]. In this method, time derivatives of atomic positions up to fifth order are stored in memory. They are used to predict the future positions and their time derivatives after a suitably chosen time increment Δt. These predicted quantities are then corrected to account for information obtained from computing atomic accelerations using the interatomic potential. The computation of potential-related quantities like atomic accelerations is by far the most time-consuming step in an MD simulation. Thus, numerical integration techniques such as the Gear predictor-corrector are preferable to Runge-Kutta-type schemes in MD simulations since they only require a single acceleration computation per time step.

Given a judicious choice of simulation parameters (such as the integration time step Δt) a simulation of the type described above results in an energy-conserving system trajectory, as predicted by equations 3.11. Additionally, a variety of specialized techniques exist to conduct simulations at constant temperature, pressure, enthalpy, Gibbs free energy, etc. [Allen, Tildesley, 2000]. Some of these techniques require a modification of the equations of motion according to Gauss' principle of least constraint [Evans, Morriss, 1984]. A well known example is the Hoover temperature-conserving algorithm [Hoover, 1983] which requires that instead of solving the classical Newtonian equations of motion 3.11 the MD algorithm be used to integrate

$$\begin{aligned} \dot{r}_i &= p_i / m_i \\ \dot{p}_i &= f_i - \xi\left(\{r_j, p_j : j = 1...3N\}\right) p_i \end{aligned} \tag{3.12}$$

$$\xi\left(\{r_j, p_j : j = 1...3N\}\right) = \frac{\sum_{j=1}^{3N} p_j f_j}{\sum_{j=1}^{3N} |p_j|^2}$$

This altered set of equations of motion can be shown to generate trajectories that sample the canonical ensemble [Evans, Morriss, 1983] just as the trajectories of 3.11 sample the microcanonical.

As mentioned before, the most time-consuming step of an MD simulation is the evaluation of an interatomic potential-related quantity such as the system potential energy or atomic accelerations. The root cause of this limitation is the need to loop over all pairs of atoms in the case of a two-body potential or all triplets of atoms in the case of a three-body potential. The number of computations required therefore scales as the second and third power of the total number of atoms, respectively, and can easily exceed one billion computations per evaluation for systems containing thousands of particles. The evaluation process, however, can be made significantly faster if the form of the interatomic potential incorporates a cutoff radius, as most do (including the SW potential; section 3.2.1). In that case each atom only interacts with other atoms within a certain a distance away from it. It can therefore be arranged through the use of linked-cell and Verlet neighbor lists [Allen, Tildesley, 2000] that the number of computations required scale linearly with the number of atoms, making large-scale MD simulation feasible.

The molecular dynamics (MD) code used in this study was made available by the Interfacial Materials Group at Argonne National Laboratory, with the kind help of D. Wolf, V. Yamakov, and P. Keblinski. This code implements system stress-control using the Parinello-Rahman method [Parinello, Rahman, 1980], which reduces to the method of Andersen in the special case of constant pressure [Andersen, 1980]. During constant pressure deformation simulations the system volume had to be rescaled occasionally to prevent pressure drift away from the intended value. Temperature control is implemented using atomic velocity rescaling. A Gear predictor-corrector integration scheme is used with time increments of 3.87 fs, i.e. about 0.05 times the characteristic time unit of the SW potential (section 3.2.1).

3.4 Potential energy minimization (PEM)

While MD is a useful method for investigating the behavior of collections of atoms obeying full Newtonian or Gauss-constrained dynamics, there are circumstances when motions of individual atoms do not have much effect on the physical phenomenon of interest and may even obscure it. Such a situation arises in the investigation of plastic deformation mechanisms at low temperature, i.e. when diffusion does not play a major role in relaxing internal stress fields [Argon, 1996a; Argon, 1996b]. It is then convenient to remove atomic motion entirely and simply ensure that the potential energy of the system is at a local minimum for each value of the externally applied load. A simulation of the type described is called a potential energy minimization (PEM) [Leach, 2001] or potential landscape [Stillinger, Weber, 1983] simulation. Since it is generally used on systems that are thermodynamically metastable—as is a-Si with respect to c-Si—it does not require the attainment of global potential energy minima. The core algorithms that lie at the heart of typical PEM simulations are therefore the classical local minimization schemes, such as the Newton-Raphson, quasi-Newton, conjugate gradient, or steepest descent methods [Bertsekas, 1999].

Newton-Raphson and quasi-Newton techniques guarantee the fastest convergence to equilibrium in the vicinity of a local minimum. Nevertheless, they require the largest computational resources and suffer from a number of inadequacies if minimization is attempted for a nonlinear potential energy function starting from an atomic configuration initially far from equilibrium. Steepest descent is the simplest and most robust of the four schemes mentioned above, but it offers the slowest rate of convergence. The conjugate gradient technique is a robust method that performs well for nonlinear potential energy functions and requires comparatively small computational resources per minimization step. Because it exhibits superlinear convergence in the vicinity of a minimum it is preferable to the steepest descent method, but cannot match the quadratic convergence rate of the Newton-Raphson algorithm near local equilibria.

Because the methods mentioned above offer different advantages depending on the proximity of a local potential energy minimum, the algorithm used in this study

implemented different techniques depending on the stage of minimization. Since an initially strained structure can be considered far from local equilibrium, the conjugate-gradient approach was always applied first. This method of minimization was terminated when the total force on each atom decreased below 10^{-8} times the characteristic force of the SW potential (section 3.2.1).

The conjugate gradient method—as all techniques for minimization of nonlinear functions—is an iterative method. Given a starting configuration, it produces a new one with a lower value of the function to be minimized. This cycle is then repeated using the configuration just obtained as the new starting configuration. Assume that at the beginning of the k^{th} cycle the system is in some configuration $\mathbf{x}^k$ where $\mathbf{x}$ is a $3N$-dimensional vector containing all the atomic positions. The system configuration is varied by displacing atoms linearly along a given direction $\mathbf{d}^k$ by some amount α^k, where $\mathbf{d}$ is a $3N$-dimensional vector and α is a scalar. The new, perturbed configuration $\mathbf{x}^{k+1}$ is

$$\mathbf{x}^{k+1} = \mathbf{x}^k + \alpha^k \mathbf{d}^k \tag{3.13}$$

Given some direction $\mathbf{d}^k$, α can be chosen by conducting a one-variable unconstrained minimization of the potential energy $V(\mathbf{x}^{k+1}) = V(\mathbf{x}^k + \alpha^k \mathbf{d}^k) = V(\alpha)$ along $\mathbf{d}^k$ using a line-minimization scheme such as the Brent method [Brent, 1973] or cubic interpolation [Bertsekas, 1999]. Once a minimizing α is found, this procedure is repeated starting from $\mathbf{x}^{k+1}$ and along a new direction $\mathbf{d}^{k+1}$ until the specified convergence criterion is met.

The heart of the conjugate gradient method lies in the selection of the line-minimization direction $\mathbf{d}$. The approach used in this study is due to Polak and Ribiere [Polak, Ribiere, 1969] and can be stated briefly as

$$\begin{aligned} \mathbf{d}^k &= -\mathbf{g}^k + \beta^k \mathbf{d}^{k-1} \\ \beta^k &= \frac{\mathbf{g}^k \cdot \left(\mathbf{g}^k - \mathbf{g}^{k-1}\right)}{\mathbf{g}^{k-1} \cdot \mathbf{g}^{k-1}} \\ \mathbf{g}^k &= \nabla_{\mathbf{x}} V\left(\mathbf{x}^k\right) \end{aligned} \tag{3.14}$$

As indicated in the last line, $\mathbf{g}^k$ is the gradient of the potential energy function V at configuration $\mathbf{x}^k$ with respect to the atomic positions $\mathbf{x}$.

If β^k were set to zero for all k in equation 3.14, the Polak-Ribiere conjugate gradient algorithm would reduce to the steepest descent method: for any initial configuration the line minimization with respect to α would be carried out along the negative gradient of the potential energy $-\nabla_{\mathbf{x}} V(\mathbf{x}^k)$, i.e. the direction where $V(\mathbf{x})$ decreases the fastest. Though it appears reasonable at first, such an approach usually yields slow (nearly linear) convergence if the minimum lies in a narrow "potential valley" [Bertsekas, 1999]. The value of selecting β as indicated in equation 3.14 is that every new minimization direction $\mathbf{d}^k$ is linearly independent of the $(k-1)$ previous directions. The frequent retracing along previous minimization directions in the approach to a local minimum characteristic of the steepest descent method is therefore avoided. As a result, the conjugate gradient method yields superlinear convergence rates, sometimes even approaching the quadratic convergence of the more complex and computation-intensive quasi-Newton methods.

When minimization is conducted far from a local minimum, the conjugate gradient scheme should be periodically "restarted" by resetting the minimization direction $\mathbf{d}^k$ to the negative gradient of the system potential energy $-\nabla_{\mathbf{x}} V(\mathbf{x}^k)$ at some suitably chosen value of k. The approach adopted in this study was to restart conjugate gradient minimization when the following "loss of conjugacy" condition was met [Bertsekas, 1999]:

$$\frac{\left(\nabla_{\mathbf{x}} V(\mathbf{x}^k)\right) \cdot \left(\nabla_{\mathbf{x}} V(\mathbf{x}^{k-1})\right)}{\left|\nabla_{\mathbf{x}} V(\mathbf{x}^{k-1})\right|^2} > 0.2 . \tag{3.15}$$

After minimization by the conjugate gradient method had proceeded to completion according to the convergence criterion mentioned above, trust region Newton-Raphson minimization steps [Bertsekas, 1999] were applied until the total force on each atom decreased below 10^{-14} times the characteristic force of the SW potential,

yielding very finely equilibrated atomic structures. In the Newton-Raphson approach, the shape of the potential surface near local equilibrium is assumed to be approximately quadratic. The location of the equilibrium position with respect to the current configuration $\mathbf{x}^k$ is therefore found by solving the matrix-vector linear system

$$\mathbf{H}^k \cdot \ddot{\mathbf{A}}\mathbf{x}^k = -\mathbf{f}^k \tag{3.16}$$

where $\mathbf{H}$ is the $3N \times 3N$ -component matrix of second derivatives of the system potential energy with respect to atomic positions (i.e. the Hessian matrix) and $\mathbf{f}$ the $3N$ -component matrix of forces on atoms. The approximated relative position of the nearest local equilibrium $\ddot{\mathbf{A}}\mathbf{x}$ can be used to find the next reference configuration $\mathbf{x}^{k+1} = \mathbf{x}^k + \ddot{\mathbf{A}}\mathbf{x}^k$. The Newton-Raphson minimization scheme then proceeds iteratively until the specified convergence criterion is met.

Note that the Newton-Raphson scheme only works if minimization is initiated sufficiently close to a local minimum. Whenever this condition had been sufficiently ensured by the preceding conjugate-gradient minimization, only about two or three Newton-Raphson steps were needed before the convergence criterion was met. Therefore, in this study, a total of only five Newton-Raphson minimization steps were allowed before it was assumed that no sufficiently near local minimum was present. In such cases, conjugate-gradient minimization was resumed and continued until a suitably tighter conjugate-gradient convergence criterion had been met.

Finally, whenever the energy minimum of the atomic system was too ill-conditioned for either the conjugate gradient or Newton-Raphson techniques to work—as is sometimes the case near the mechanical threshold of plastic relaxations (section 4.3.2, chapter 8)—a line minimization was carried out using the robust algorithm due to Brent [Brent, 1973] along the direction of the lowest stiffness non-translational eigenmode of the system Hessian matrix.

4. Analysis methods

This chapter defines the quantities and describes the methods that were used to understand the results of MD and PEM simulations presented in chapters 5 through 10.

4.1 System characterizers

This section discusses three standard quantities of interest to mechanical behavior: excess enthalpy, system-wide and atomic site stresses, and elastic constants.

4.1.1 Excess enthalpy

The potential energy V for any atomic configuration—including all metastable ones, like a-Si—can be found using the assumed form of interatomic potential (section 3.2.1). The value of this potential energy can then be compared to its value V_0 for a system consisting of the same number of atoms and at the same level of externally applied stress, but in a stable crystalline configuration. The excess enthalpy ΔH is then defined as the difference between V and V_0 normalized by the total number N of atoms in the system:

$$\Delta H = \frac{V_0 - V}{N}. \tag{4.1}$$

For a-Si close to room temperature and pressure, the reference crystalline configuration is the diamond cubic structure (section 5.2).

4.1.2 Stresses

The stress tensor of the sample being deformed is of fundamental interest in the study of its mechanical behavior. At zero temperature, it is simply the derivative of the system potential energy with respect to linearized strains of the simulation cell[3]. The full system-wide stress tensor at zero temperature for the simulated a-Si systems was therefore calculated directly from the form of the assumed interatomic potential (section 3.2.1) as [Brown, Neyertz, 1995]:

$$\tau_{ab} \cdot \not{V} = \frac{\partial V}{\partial \varepsilon_{ab}} = \sum_{i=1}^{N} \sum_{j=i+1}^{N} \left(\frac{\partial V_2}{\partial r_{ij}} \cdot \frac{\partial r_{ij}}{\partial \varepsilon_{ab}} \right) + \sum_{i=1}^{N} \sum_{j=i+1}^{N} \sum_{k=j+1}^{N} \left(\frac{\partial V_3}{\partial r_{ij}} \cdot \frac{\partial r_{ij}}{\partial \varepsilon_{ab}} + \frac{\partial V_3}{\partial r_{ik}} \cdot \frac{\partial r_{ik}}{\partial \varepsilon_{ab}} + \frac{\partial V_3}{\partial r_{jk}} \cdot \frac{\partial r_{jk}}{\partial \varepsilon_{ab}} \right) \quad (4.2)$$

where $\partial r_{ij} / \partial \varepsilon_{ab}$ denotes the change of the distance between atoms i and j under variation in applied strain increment component ε_{ab}, $\not{V}$ is the total system volume, and N the total number of atoms in the simulation cell. The effect of non-zero temperature T on the stress state is accounted for by adding the term $mNk_B T\delta_{ab}$ to equation 4.2 [Allen, Tildesley, 2000], where m is the atomic mass, N the total number of atoms in the system, and k_B the Boltzmann constant. This term affects only the hydrostatic portion of the stress tensor (section 4.2).

It is useful to decompose the system stress elements τ_{ab} in expression 4.2 into $i = 1...N$ components $(\tau_{ab})_i$ associated with atomic sites such that

$$\tau_{ab} = \frac{1}{N} \sum_{i=1}^{N} (\tau_{ab})_i \,. \quad (4.3)$$

This can be accomplished by defining

[3] Evaluation of stresses as derivatives of potential energy with respect to the deformation gradients of the simulation cell gives the same numerical results.

$$\left(\tau_{ab}\right)_i \cdot \frac{V}{N} = \frac{1}{2}\sum_{j=1}^{N}\left(\frac{\partial V_2}{\partial r_{ij}} \cdot \frac{\partial r_{ij}}{\partial \varepsilon_{ab}}\right) + \frac{1}{3}\sum_{j=1}^{N}\sum_{k=j+1}^{N}\left(\frac{\partial V_3}{\partial r_{ij}} \cdot \frac{\partial r_{ij}}{\partial \varepsilon_{ab}} + \frac{\partial V_3}{\partial r_{ik}} \cdot \frac{\partial r_{ik}}{\partial \varepsilon_{ab}} + \frac{\partial V_3}{\partial r_{jk}} \cdot \frac{\partial r_{jk}}{\partial \varepsilon_{ab}}\right) \tag{4.4}$$

The quantities $\left(\tau_{ab}\right)_i$ are called the atomic site stress tensors and serve as efficient characterizers of local internal stresses resulting from the disordered state of amorphous solids [Maeda, Takeuchi, 1981; Maeda, Takeuchi, 1982; Srolovitz *et al.*, 1983].

Note that while the summations in expression 4.2 are over all pairs and triplets of atoms occurring in the entire system, the summations in expression 4.4 are only over those pairs and triplets that contain atom i, which denotes the atomic site for which the local stress tensor $\left(\tau_{ab}\right)_i$ is evaluated. The stresses at an atomic site therefore only involve contributions from direct energetic interactions with atomic sites within a radius dictated by the interaction cutoff distance of the SW potential (section 3.2.1) and can therefore be interpreted as measures of local structural distortion of atomic environments.

4.1.3 Elastic constants

When scaled by the system volume, the second total derivatives (including the mixed derivatives) of the potential energy with respect to deformation gradients u_{ab} of the simulation cell give the zero-temperature analogs of the acoustic constants

$$A_{abcd} \cdot V = \frac{d^2V}{du_{ab}du_{cd}}, \tag{4.5}$$

which are related to the zero-temperature elastic constants C_{abcd} by [Wallace, 1972]

$$A_{abcd} = C_{abcd} + \delta_{ac}\tau_{bd}. \tag{4.6}$$

When externally strained at zero temperature, the constituents of a mechanically stable solid will in general undergo not only affine displacements, but also some small amount of non-affine relaxation, termed "sublattice displacements" in the case of

crystalline solids that lack inversion symmetry [Wallace, 1972]. The relative atomic displacements therefore deviate from the prediction of pure affine dependence on external straining and the extent of this deviation is a function of the applied strain increment. For this reason, the total second derivatives of energy with respect to straining in equation 4.5 are in general not equal to the corresponding partial derivatives. Direct calculation of the zero-temperature acoustic constants A_{abcd} from the system potential energy V must take account of these "sublattice displacements." The approach used to achieve this calculation is demonstrated in section 4.3.1.

The discussion above and in section 4.3.1 concerns characterization of elastic properties at zero-temperature. Since elastic properties are temperature-dependent, however, determining these properties at finite temperatures requires an approach involving evaluation of fluctuations of thermodynamic averages [Kluge *et al.*, 1986]. This method has proven indispensable in MD studies of homogeneous nucleation of dislocations under indentation [Li, Van Vliet, *et al.*, 2002]. Since the present study is concerned primarily with deformation behavior in the absence of thermal fluctuations, however, the determination of temperature dependence of elastic properties was not undertaken.

4.1.4 Anisotropy measures

Macroscopic samples of well-annealed single-element amorphous solids can be expected to be isotropic. Small enough samples, however, may exhibit some statistical deviation from isotropy. For any given sample, it would be convenient to gauge quantitatively that these departures from isotropy are indeed statistical in nature. This goal can be achieved on the basis of investigation of the elastic properties as expressed by the elastic constants C_{ijkl} (equation 4.6). Two different anisotropy measures are defined in this section.

Since each of the indices a, b, c, and d can take on three values, there would at first seem to be 81 independent elastic constants. The equality of mixed derivatives and the symmetry of the stress tensor, however, reduce that number to at most 21 [Wallace, 1972]. Further reduction in the number of independent elastic constants is possible for

solids that exhibit certain symmetry properties. In particular, isotropic solids are characterizable by just two independent constants, such as the bulk and shear moduli B and μ [McClintock, Argon, 1966]. These constants can be related to the 21 independent C_{abcd} by noting that under conditions of isotropy

$$\begin{aligned} C_{1111} &= C_{2222} = C_{3333} = C_{11} \\ C_{1122} &= C_{1133} = C_{2233} = C_{12} \\ B &= \tfrac{1}{3}\left(C_{11} + 2C_{12}\right) \end{aligned} \tag{4.7}$$

and

$$C_{1212} = C_{1313} = C_{2323} = \mu\,. \tag{4.8}$$

All other independent values of C_{abcd} are zero. For convenience, call the set of all elastic constants C_{abcd} whose values are predicted to be zero in elastic solids $\{C_0\}$:

$$\{C_0\} = \{C_{abcd} : (C_{abcd} = 0 \text{ for isotropic solids})\}. \tag{4.9}$$

One isotropy measure—named C_0—can therefore be defined as the average of the elements of $\{C_0\}$:

$$C_0 = \langle\{C_0\}\rangle\,. \tag{4.10}$$

The standard deviation for C_0 can be computed from the elements of $\{C_0\}$ in the usual way. For perfectly isotropic solids, $C_0 = 0$ with zero standard deviation.

Next, define

$$\mu_P = \tfrac{1}{2}\left(C_{11} - C_{12}\right). \tag{4.11}$$

Under conditions of isotropy, the relation $\mu = \mu_P$ is satisfied. For small systems, however, these two values may differ slightly. Their difference can be computed in 27 different ways from the independent values of C_{ijkl} listed in equations 4.7 and 4.8. The second isotropy measure—named $(\mu - \mu_P)$—is defined as the average of these 27 difference values. Its standard deviation is determined analogously. As with C_0, in a perfect isotropic solid $(\mu - \mu_P) = 0$ with zero standard deviation.

For the small a-Si samples considered in this study, if the two quantities C_0 and $(\mu - \mu_P)$ are zero to within statistical error as quantified by their standard deviations, then those samples are considered isotropic to within statistical fluctuations.

4.2 Hydrostatic and deviatoric tensor components

Because a-Si is an isotropic material (section 5.5.1), the results of mechanical deformation simulations are conveniently stated in terms of the pressure (p) and deviatoric ($\bar{\sigma}$) components of the complete continuum Cauchy stress tensor $\hat{\mathbf{o}}$ [McClintock, Argon, 1966]. These components are defined as

$$p(\hat{\mathbf{o}}) = -\tfrac{1}{3} tr(\hat{\mathbf{o}}) \qquad (4.12)$$
$$\bar{\sigma}(\hat{\mathbf{o}}) = \left| \hat{\mathbf{o}} - \tfrac{1}{3} tr(\hat{\mathbf{o}}) \mathbf{I} \right|$$

where tr stands for the tensor trace and $\mathbf{I}$ for the identity tensor. Deviatoric stress accounts for all shearing stresses and excludes all dilatational stress components. Both pressure and deviatoric stress can be computed for the system-wide stress tensor as well as for all atomic site stress tensors (section 4.1.2). While system-wide pressure p and stress tensor components τ_{ab} are averages over the volume of corresponding atomic site quantities, however, the system-wide deviatoric stress is not the average over the volume of atomic site deviatoric stresses. Rather, it is the deviatoric component of the volume

average atomic site stress tensors. Deviatoric strain $\bar{\varepsilon}$ is computed from the strain tensor $\mathbf{å}$ analogously to deviatoric stress.

4.3 Equilibrium paths

Potential energy minimization (PEM)—one of the two simulation methods used in this study (section 3.4)—yields sequences of equilibrated atomic configurations for ever-increasing values of externally applied loading. The system behavior when simulated by PEM is conveniently conceptualized by relating these series of atomic configurations to "equilibrium paths" in a $(3N+1)$-dimensional space [Guckenheimer, Holmes, 1983]. This approach is also often taken in the analysis of elastic structures, especially in the study of elastic stability [Thompson, Hunt, 1973].

The potential energy V of an atomic configuration containing N atoms inside a simulation cell depends explicitly on the atomic coordinates x_i where $i = 1 \ldots 3N$:

$$V = V(x_1, x_2, \ldots, x_{3N}) \tag{4.13}$$

Additionally, the potential energy depends on the shape of the simulation cell itself. Assuming as in section 3.1.1 that the simulation cell shape is describable as a general parallelepiped and choosing any convenient reference state[4], this shape dependence can be specified in terms of the total strain of the simulation cell with respect to its reference configuration

$$V = V(x_1, x_2, \ldots, x_{3N}; \mathbf{å}) \tag{4.14}$$

where $\mathbf{å}$ is the total strain of the simulation cell from its reference configuration.

In the case of plastic deformation simulations, a convenient reference configuration is the shape of the simulation cell prior to external loading. Furthermore,

[4] Examples of common reference configurations for the simulation cell are the cube of unit edge length or the shape of the initial crystalline configuration.

since deformation studies are typically undertaken with a well-defined loading mode in mind—such as the one described in section 3.1.2—the total strain of the sample can be parameterized in terms of just one loading parameter λ:

$$\mathbf{å} = \mathbf{å}(\lambda) \tag{4.15}$$

At any particular value of the external loading parameter λ for a deformation simulation, an atomic system at static equilibrium satisfies the $3N$ conditions

$$-\frac{\partial V}{\partial x_i} = f_i(x_1, x_2, \ldots x_{3N}; \lambda) = 0_i . \tag{4.16}$$

Here as before, $i = 1 \ldots 3N$.

Expression 4.16 merely states that in local equilibrium all resultant forces on atoms vanish. If the state of equilibrium is reached by applying a PEM algorithm (section 3.4) then it can also be said that this equilibrium state is stable. If it were not, then any small perturbation (arising even from numerical roundoff errors) in an unstable direction would result in a potential energy decrease and cause the system to converge to some other, preferred, stable equilibrium configuration corresponding to a local potential energy minimum.

4.3.1 Normal behavior: acoustic moduli

Suppose an initial atomic configuration that satisfies relations 4.15 is obtained, e.g. through PEM simulation. According to the inverse function theorem [Marsden, Tromba, 1996], these relations implicitly define relative atomic equilibrium positions x_i as smooth functions of λ in some neighborhood of the initial configuration if the Jacobian matrix

$$\mathbf{J} = \begin{bmatrix} \frac{\partial f_1}{\partial x_1} & \cdots & \frac{\partial f_1}{\partial x_{3N}} \\ \vdots & \ddots & \vdots \\ \frac{\partial f_{3N}}{\partial x_1} & \cdots & \frac{\partial f_{3N}}{\partial x_{3N}} \end{bmatrix} \tag{4.17}$$

is not singular. Note that since

$$\frac{\partial f_i}{\partial x_j} = -\frac{\partial^2 V}{\partial x_i \partial x_j} \tag{4.18}$$

the Jacobian matrix is simply the negative of the Hessian matrix (the matrix of second derivatives of the potential with respect to atomic positions), i.e. $\mathbf{J} = -\mathbf{H}$. The set of $3N$ functions $x_i = x_i(\lambda)$ along with the loading parameter λ are often thought of as defining a smooth "equilibrium path" in $(3N+1)$-dimensional space. Using the nomenclature of the analysis of elastic stability [Thompson, Hunt, 1973], in the regime where the Jacobian is not singular, the system is said to exhibit "normal" behavior.

In the normal behavior regime of an atomic configuration in equilibrium, the acoustic constants can be calculated explicitly. As was noted in section 4.1.3, these constants are the mixed total derivatives—scaled by system volume—of the system potential with respect to deformation gradients of the simulation cell. Taking into account the implicit dependence of atomic equilibrium positions x_i on loading parameter defined by equations 4.16 and recognizing the deformation gradient components u_{ab} of the simulation cell as legitimate choices of the loading parameter λ, the general first total derivative of system potential energy with respect to a deformation gradient component is

$$\frac{dV}{du_{cd}} = \frac{\partial V}{\partial u_{cd}} + \frac{\partial V}{\partial x_i} \cdot \frac{\partial x_i}{\partial u_{cd}} \tag{4.19}$$

and the general second total derivative is

$$\frac{d^2V}{du_{ab}du_{cd}} = \frac{\partial^2 V}{\partial u_{ab}\partial u_{cd}} + \frac{\partial^2 V}{\partial x_i \partial u_{cd}} \cdot \frac{\partial x_i}{\partial u_{ab}} + \frac{\partial^2 V}{\partial x_i \partial u_{ab}} \cdot \frac{\partial x_i}{\partial u_{cd}} + \\ + \frac{\partial^2 V}{\partial x_i \partial x_j} \cdot \frac{\partial x_i}{\partial u_{cd}} \cdot \frac{\partial x_j}{\partial u_{ab}} + \frac{\partial V}{\partial x_i} \cdot \frac{\partial^2 x_i}{\partial u_{ab}\partial u_{cd}} \tag{4.20}$$

Summation over repeated indices is implied.

Applying the equilibrium condition in 4.16 to equation 4.18 gives

$$\frac{dV}{du_{cd}} = \frac{\partial V}{\partial u_{cd}} \tag{4.21}$$

in agreement with the definition of the zero-temperature stress components in section 4.1.2. Applying 4.16 to 4.20, however, gives

$$\frac{d^2V}{du_{ab}du_{cd}} = \frac{\partial^2 V}{\partial u_{ab}\partial u_{cd}} + \frac{\partial^2 V}{\partial x_i \partial u_{cd}} \cdot \frac{\partial x_i}{\partial u_{ab}} + \frac{\partial^2 V}{\partial x_i \partial u_{ab}} \cdot \frac{\partial x_i}{\partial u_{cd}} + \frac{\partial^2 V}{\partial x_i \partial x_j} \cdot \frac{\partial x_i}{\partial u_{cd}} \cdot \frac{\partial x_j}{\partial u_{ab}}. \tag{4.22}$$

As pointed out in section 4.1.3, this total derivative is not equal to the corresponding partial derivative due to the presence of the "sublattice displacement" terms $\partial x_i / \partial u_{ab}$ arising from the implicit dependence of atomic positions on the loading parameter. In the regime of normal behavior, however, the implicit function theorem guarantees the existence of these terms. They can be calculated using a perturbation approach [Thompson, Hunt, 1973].

Since the condition 4.16 is satisfied at every point of an equilibrium path, every order of total derivative of atomic forces with respect to loading parameter vanishes, i.e.

$$\frac{d^m f_i}{d^m \lambda} = \frac{d^m}{d^m \lambda}\left(-\frac{\partial V(x_1, x_2, \ldots x_{3N}; \lambda)}{\partial x_i}\right) = 0 \tag{4.23}$$

for all m and all i. Taking this derivative for $m = 1$ gives

$$\frac{\partial^2 V}{\partial x_i \partial x_j} \cdot \frac{\partial x_j}{\partial \lambda} + \frac{\partial^2 V}{\partial x_i \partial \lambda} = 0 . \tag{4.24}$$

Equation 4.24 defines a system of $3N$ linear equations in the $3N$ unknowns $\partial x_j / \partial \lambda$. Taking a deformation gradient component u_{ab} as the loading parameter and adopting matrix-vector notation gives

$$\frac{\partial \mathbf{x}}{\partial u_{ab}} = \mathbf{H}^{-1} \cdot \frac{\partial \mathbf{f}}{\partial u_{ab}} \tag{4.25}$$

where $\mathbf{x}$ is the vector of atomic positions x_i and $\mathbf{f}$ is the vector of atomic forces f_i. Applying this formula to equation 4.22 gives the final expression for direct calculation of the acoustic constants:

$$\frac{d^2 V}{du_{ab} du_{cd}} = \frac{\partial^2 V}{\partial u_{ab} \partial u_{cd}} - \frac{\partial \mathbf{f}^{\mathrm{T}}}{\partial u_{ab}} \cdot \mathbf{H}^{-1} \cdot \frac{\partial \mathbf{f}}{\partial u_{cd}} . \tag{4.26}$$

In conjunction with equations 4.5 and 4.6, this formula can be used to determine all 21 independent elastic constants C_{abcd}.

4.3.2 Singular behavior: saddle-node bifurcations

As explained in the previous section, equilibrium paths are only defined when the Hessian matrix $\mathbf{H}$ is nonsingular. In particular, only then are the acoustic constants in equation 4.26 well defined. When $\mathbf{H}$ is singular, expression 4.25 has no meaning and the variations of atomic positions with respect to loading parameter $\partial x_j / \partial \lambda$ cannot be found. In agreement with the nomenclature of elastic stability analysis [Thompson, Hunt, 1973], the behavior of an atomic system in equilibrium with singular Hessian matrix is termed "singular."

Suppose an atomic system initially in a normal stable equilibrium state is deformed by PEM. One way for it to approach a singular equilibrium state is for one of

the eigenvalues of its Hessian matrix to approach zero from above as the loading parameter varies. This phenomenon has been confirmed in deformation studies of model metallic glasses [Malandro, Lacks, 1997; Malandro, Lacks, 1998], where the onset of discrete relaxations was accompanied by the vanishing of the stiffness of one of the normal modes. This "soft mode" phenomenon is characteristic of steady-state bifurcations of equilibrium paths [Guckenheimer, Holmes, 1983; Crawford, 1991] and plays an important role in the study of ferroelectric and antiferroelectric phase transitions [Blinc, Zeks, 1974] as well as martensitic transformations [Elliot *et al.*, 2002].

The nature of the steady-state bifurcations accompanying onset of discrete stress relaxations in deformed atomic configurations can be ascertained by evaluating two derivatives of the potential energy of the complete system at the mechanical threshold stress where the behavior of the system becomes singular. The first is V_1' : the mixed derivative of the potential energy with respect to displacements along the normal mode of vanishing stiffness or "critical eigenmode" (CE; subscript "1") and externally applied increment of loading (e.g. section 3.1.2; superscript "prime"). The second is V_{111} : the third derivative of the system potential energy with respect to displacements along the CE. In particular, if both V_1' and V_{111} are nonzero, the bifurcation is of the saddle-node type and describes the vanishing of a stable equilibrium path as it merges with an unstable equilibrium path. Figure 4-1 shows a schematic of the potential energy surface close to a saddle-node bifurcation.

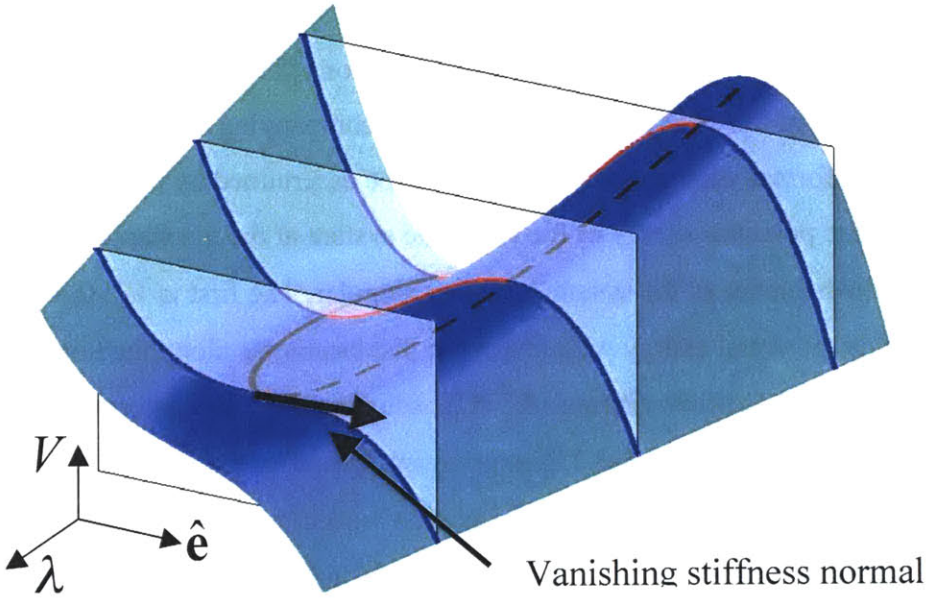

Figure 4-1: Schematic of the surface of system potential energy V in the vicinity of a saddle-node bifurcation. At a critical value of the externally applied loading λ the stable equilibrium path (solid like) merges with the unstable one (dashed line). The normal mode with vanishing stiffness—whose direction is denoted as $\hat{\mathbf{e}}$—is tangent to these two paths at their point of merger. If the externally applied strain exceeds the critical value the system exhibits "snapping" behavior as it converges to some distant equilibrium configuration.

The sudden and irreversible relaxation of stress in a system that has been strained infinitesimally beyond its mechanical threshold is a direct consequence of the finite atomic displacements necessary for the system to attain some distant stable equilibrium configuration following the vanishing of the original stable equilibrium path at the point of bifurcation. This type of behavior is often called "snapping" in the study of elastic stability [Thompson, Hunt, 1973].

All stress relaxations observed in the PEM deformation simulations described in this study (chapter 8) satisfied the conditions $V_1' \neq 0$ and $V_{111} \neq 0$ at their onset, confirming that they were all triggered by a process describable as a saddle-node bifurcation. This result is to be expected since saddle-node bifurcations typically occur in systems lacking in any intrinsic symmetry or equilibrium configurations [Guckenheimer, Holmes, 1983; Crawford, 1991]. Unlike crystal lattices, whose intrinsic symmetries induce bifurcations more complex than those of the saddle-node type [Thompson, Shorrock, 1975], a-Si—much as other atomically disordered solids—does not have any structural symmetry properties. Interestingly, this lack of intrinsic ordering has a simplifying effect on the analysis of the onset of stress relaxations in a-Si insofar as it explains the exclusive occurrence of saddle-node bifurcations during deformation.

4.4 Matrix-inclusion analysis

The following sections describe how deviations from linear-elastic deformation behavior of atomic environments can be used to gain insight into structure changes that accompany the discrete stress relaxations observed in PEM simulations [Mott *et al.*, 1993]. The author wishes to acknowledge stimulating discussions with D. M. Parks in the clarification of these methods of analysis.

4.4.1 Finite atomic displacements

Every discrete stress relaxation event in PEM deformation simulations (section 8.1) is accompanied by an internal structure rearrangement accomplished through the relative displacements of atoms. Some of these relative position changes are large and indicate a local inelastic transformation of atomic structure. Other ones, however, are small and can be considered elastic. Consequently, the overall behavior of an a-Si system undergoing stress relaxation can be viewed as the composite response of an inelastically transforming inclusion and an elastically deforming matrix that surrounds the inclusion. To identify the part of an a-Si system that undergoes an inelastic atomic structure transformation during a stress relaxation means simply to distinguish between the part whose deformation can be described as approximately elastic and the part whose deformation cannot be described that way. The elastically deforming part of the system is identified as matrix material. The complement to the elastically deforming part is called the inelastically transforming inclusion. This description of the composite response of a system to a localized inelastic structure transformation is the same as the basic setting of Eshelby's inclusion problem [Eshelby, 1957].

Previous studies have observed that structure rearrangements accompanying stress relaxations are clustered into well-localized regions and can involve relatively few [Argon, Kuo, 1979; Argon, Shi, 1983; Malandro, Lacks, 1998] or many [Mott *et al.*, 1993; Maloney, Lemaitre, 2004] participating atoms, depending on the bonding and size of the system under consideration as well as the loading conditions. Many of these studies identified the regions undergoing structure transformations by making use of strain measures appropriately generalized to individual atomic environments [Mott *et al.*, 1992; Falk, Langer, 1998; Horstemeyer, Baskes, 2000] to locate centers of high intensity non-affine atomic displacements. In this study, however, a new method for recognizing inelastically transforming inclusions that makes no recourse to strain measures is used.

Intuitively, a material is understood to behave elastically if increments in its state of deformation produce increments of the corresponding forces in linear (or nearly linear)

proportion to the deformation increments themselves. In a continuum setting, this intuition can be stated as the linear dependence of stresses on strain increments:

$$\hat{\mathbf{o}}_f = \hat{\mathbf{o}}_i + \mathbf{C}(\ddot{\mathbf{A}}\mathbf{å}). \tag{4.27}$$

Here $\hat{\mathbf{o}}_f$ and $\hat{\mathbf{o}}_i$ are the final and initial stress states, $\ddot{\mathbf{A}}\mathbf{å}$ is a strain increment tensor, and $\mathbf{C}$ is the tensor of linear elastic constants. In an atomistic setting, however, all degrees of freedom are discrete, making the determination of physically meaningful atomic site strain increments and elastic constants inconvenient. It is far more expedient to restate the intuitive relation in equation 4.27 using quantities that are more natural in the discrete, atomic setting. Consider two configurations—initial and final—of an atomic system under periodic boundary conditions. If the atomic positions in these configurations differ, but the shapes of their simulation cells are identical, then equation 4.27 can be restated as

$$\mathbf{f}_f = \mathbf{f}_i + (-\mathbf{H})\cdot(\ddot{\mathbf{A}}\mathbf{d}). \tag{4.28}$$

In expression 4.28 the force vectors $\mathbf{f}_f$ and $\mathbf{f}_i$ take the place of final and initial stress states, relative displacements $\ddot{\mathbf{A}}\mathbf{d}$ play the role of the strain increment tensor, and the negative of the Hessian matrix $\mathbf{H}$ (i.e. the matrix of second derivatives of the system potential with respect to atomic positions) plays the role of the elastic constants. More generally, if in addition to having different atomic positions, the two atomic configurations also have simulation cells whose shapes differ by a strain increment tensor $\ddot{\mathbf{A}}\mathbf{å}$, then equation 4.28 can be restated as

$$\mathbf{f}_f = \mathbf{f}_i + (-\mathbf{H})\cdot(\ddot{\mathbf{A}}\mathbf{d}) + \frac{\partial \mathbf{f}_i}{\partial \varepsilon_{ab}}\cdot\Delta\varepsilon_{ab}. \tag{4.29}$$

The quantities $\frac{\partial \mathbf{f}_i}{\partial \varepsilon_{ab}}$ are the direct variations of forces on atoms $\mathbf{f}_i$ with variations in the strain components ε_{ab}. These force variations are calculable analytically as derivatives of the total system potential, much as the components of $\mathbf{H}$. The quantities $\Delta\varepsilon_{ab}$ are the

components of the strain increment tensor **Äå**. Summation over repeated indices is implied. For a system in three dimensions consisting of N atoms, the force, displacement, and force variation vectors ($\mathbf{f}_f$, $\mathbf{f}_i$, **Äd**, $\frac{\partial \mathbf{f}_i}{\partial \varepsilon_{ab}}$) in equation 4.29 have $3N$ components while the Hessian matrix **H** has $3N \times 3N$ components.

If a system undergoes a deformation that is not purely linear elastic, the total forces on individual atoms in its final configuration can be decomposed into a linear elastic contribution—calculable by equation 4.29—and some excess force increment **Äf**:

$$\mathbf{f}_f^{total} = \mathbf{f}_f^{elastic} + \ddot{\mathbf{A}}\mathbf{f}. \tag{4.30}$$

Identifying $\mathbf{f}_f^{elastic}$ with $\mathbf{f}_f$ in expression 4.29, the force deviation **Äf** can be expressed as

$$\ddot{\mathbf{A}}\mathbf{f} = \mathbf{f}_f^{total} - \mathbf{f}_f^{elastic} = \left(\mathbf{f}_f^{total} - \mathbf{f}_i\right) + \mathbf{H} \cdot (\ddot{\mathbf{A}}\mathbf{d}) - \frac{\partial \mathbf{f}_i}{\partial \varepsilon_{ab}} \cdot \Delta\varepsilon_{ab} \tag{4.31}$$

The final forces on atoms in a discrete system that has undergone purely linear elastic deformation would be exactly predicted by equation 4.29. By construction the force deviation **Äf** computed for such a case using expression 4.31 would therefore be zero. It would be nonzero for a system that underwent deformation that was not purely linear elastic.

So far the force deviation **Äf** for a deforming system was considered as a complete $3N$-component vector. If the components of the force deviation vector are considered separately, however, they can be used to distinguish between a linear-elastically deforming matrix and inelastically transforming inclusion. If the environment of some atom undergoes an essentially linear elastic deformation, the 3 components (x, y, and z) of the force deviation **Äf** corresponding to that atom will be nearly zero. Meanwhile, if the atomic environment in question deforms in a way that departs strongly from linear elasticity, these force deviation components will be large. For the environment of any atom k, therefore, a measure of deviation from linear elastic deformation can be defined as

$$\delta_k = \frac{\sqrt{(\ddot{\mathbf{A}}\mathbf{f})_{k,x}^2 + (\ddot{\mathbf{A}}\mathbf{f})_{k,y}^2 + (\ddot{\mathbf{A}}\mathbf{f})_{k,z}^2}}{|\ddot{\mathbf{A}}\mathbf{f}|} \tag{4.32}$$

where $(\ddot{\mathbf{A}}\mathbf{f})_{k,x}$ is the x-component on atom k of the complete force deviation vector $\ddot{\mathbf{A}}\mathbf{f}$ and $|\ddot{\mathbf{A}}\mathbf{f}| = \sqrt{\sum_{\alpha=1}^{3N} (\ddot{\mathbf{A}}\mathbf{f})_\alpha^2}$ is simply the norm of $\ddot{\mathbf{A}}\mathbf{f}$. Once calculated, the atomic measures of deviation from linear elasticity δ_k are sorted in descending order. Then the number n of atoms in an inelastically transforming inclusion is defined by

$$\sqrt{\sum_{j=1}^{n} \delta_{k(j)}^2} > 0.95 \tag{4.33}$$

where $k(j)$ denotes the atom k corresponding to the j^{th} position in the sorted queue of deviation measures δ_k.

In words, the procedure above identifies the environments of atoms with $\delta_k \approx 0$ as undergoing linear elastic deformation and therefore considers them part of the elastically deforming matrix. The inelastically transforming inclusion is the complement of the elastically deforming matrix. It is composed of the smallest number of atoms necessary to account for at least 95% of the norm of the force deviation vector $\ddot{\mathbf{A}}\mathbf{f}$. The fact that n is indeed the smallest number of atoms necessary to do so is ensured by counting the atoms with the largest contribution to the norm of the force deviation first in the summation in equation 4.33. The specific atoms forming the inclusion are simply the first n atoms from the sorted queue $k(j)$. The atoms comprising the elastically deforming matrix are then the remaining $(N - n)$ atoms in the queue. It should be emphasized that the distinction between matrix and inclusion based on the above analysis is inherently approximate. In particular, the cutoff in equation 4.33 can be chosen larger or smaller, yielding more or less conservative estimates of the extent of inelastically transforming inclusions, respectively. It has been found, however, that the conclusions

from the analyses to be presented in this study are unaffected by varying this cutoff between 0.90 and 0.99, indicating that they are robust with respect the chosen level of approximation.

4.4.2 Infinitesimal atomic displacements

In the previous section it was shown that knowledge of the finite atomic displacements accompanying stress relaxations can be used to distinguish between elastically deforming matrix material and an inelastically transforming inclusion in the case of each relaxation. A similar analysis can be carried out at the mechanical threshold preceding a stress relaxation to find a "triggering inclusion" where local yielding of strained material initiates. Unlike the transformation process associated with stress relaxations, however, triggering is described not by finite displacements of atoms but rather by the infinitesimal variations in their positions included in the CE (section 4.3.2). The framework for distinguishing between matrix and inclusion material described in section 4.3.1 can still be applied if the total forces in the "final" configuration (equation 4.29) are expressed as a Taylor expansion around the initial configuration:

$$\mathbf{f}_f^{total} = \mathbf{f}_i + (-\mathbf{H})\cdot\mathbf{d} + \tfrac{1}{2}(-\mathbf{t}) + \ldots \tag{4.34}$$

Here $\mathbf{d}$ is the $3N$-component vector of displacement increments and $\mathbf{H}$ the Hessian (matrix of second derivates of the system potential energy with respect to these displacements), as before. The term named $\mathbf{t}$ is the quadratic contribution to the expansion in equation 4.34. It is a vector quantity that depends on the third derivatives of the system potential energy with respect to displacement as

$$t_k = \frac{\partial^3 V}{\partial x_a \partial x_b \partial x_k} d_a d_b . \tag{4.35}$$

where t_k is the k^{th} component of the vector $\mathbf{t}$ and d_a is the a^{th} component of the displacement increment vector $\mathbf{d}$. There is no contribution in equation 4.34 from terms of

the type $\frac{\partial \mathbf{f}_i}{\partial \varepsilon_{ab}}$ (unlike in equation 4.29) because triggering is assumed to occur at a fixed shape of the simulation cell. Summation over repeated indices is implied in both equation 4.34 and 4.35.

Applying the definition in equation 4.31 to the description of force variations during triggering in equation 4.34 gives

$$\ddot{\mathbf{A}}\mathbf{f} \approx -\tfrac{1}{2}\mathbf{t} \tag{4.36}$$

if the expansion for forces in equation 4.34 is truncated after the quadratic term. In the case of the CE—which describes the kinematics of triggering (section 4.3.2)—the vector of infinitesimal displacement increments can be written

$$\mathbf{d} = s\hat{\mathbf{e}} \tag{4.37}$$

where $\hat{\mathbf{e}}$ is the unit CE vector and s is a scalar displacement parameter. Equations 4.36 and 4.37 therefore give

$$\left(\ddot{\mathbf{A}}\mathbf{f}\right)_k \approx -s^2 \frac{\partial^3 V}{\partial x_a \partial x_b \partial x_k} e_a e_b = -s^2 V_{11k} \tag{4.38}$$

where $-V_{11k}$ are the components of the vector of second derivatives with respect to displacements along the CE (denoted by subscript 1, section 4.3.2) of forces on individual atoms. Knowing the shape of the CE, V_{11k} can be determined analytically from the form of the empirical potential governing the system. Alternatively, they can also be found by evaluating numerically the second derivatives of forces on atoms along the CE. The latter method was used in this study.

The force deviations in equation 4.38 describe the departure from the predictions of linear elasticity in the case of the infinitesimal displacements associated with triggering. They can be used in conjunction with equations 4.32 and 4.33 to define a triggering inclusion for the onset of every stress relaxation event. These inclusions are

always localized in the vicinity of atomic sites that undergo the largest relative displacements, as quantified by the components of the unit CE vector $\hat{\mathbf{e}}$. The degree of localization exhibited by V_{11k}, however, is always significantly greater than that exhibited by $\hat{\mathbf{e}}$ because the latter—in addition to containing information about the atomic cluster undergoing localized yielding—also characterizes the compatibility-induced elastic flexing of the surrounding matrix material.

In light of the above development a clear distinction must be made between these triggering inclusions and the inelastically transforming inclusions defined in section 4.4.1. While the latter characterize finite and irreversible atomic rearrangements, the former merely probe nonlinear departures from linear elastic behavior under infinitesimal displacement, in particular their spatial localization. These departures, however, carry a specific meaning in the case of triggering of stress relaxations. At the mechanical threshold, the component of the return force against displacements along the CE that is linear in those displacements vanishes and the system can undergo a finite atomic rearrangement given even an infinitesimal increment in loading. The largest of the deviations from linear elasticity V_{111} in this situation specify the fastest growing force components that initiate this finite atomic rearrangement. The atomic sites with the highest measure of deviation from linear elasticity δ_k (equation 4.32) indicate the location where it nucleates.

4.5 Numerical methods

The efficient implementation of atomistic simulations as well as analysis of the obtained results normally requires use of specially constructed algorithms. Such algorithms are generally the subject of intense research in the fields of applied mathematics and computer science, but are often made available along with documentation and diagnostic tools on freely accessible sites such as Netlib [Netlib]. This section describes the application of certain such algorithms for the purposes of the research presented here.

4.5.1 Sparse matrix numerical linear algebra methods

Many of the methods described in chapters 3 and 4—for example the Netwon-Raphson stage of PEM simulations (section 3.4) or the matrix-inclusion analysis for finite atomic displacements (section 4.4.1)—make use of the matrix $\mathbf{H}$ of second derivatives of the system potential with respect to atomic positions (i.e. the stiffness or Hessian matrix). This matrix can be calculated directly from the form of the assumed interatomic potential (section 3.2.1) and stored in the traditional $3N \times 3N$ array of elements, where N is the number of constituent atoms in the system. Such an approach, however, is extremely memory intensive for atomic systems of the size considered in this study (section 3.1.1).

Storing the Hessian matrix $\mathbf{H}$ as a $3N \times 3N$ array of elements overlooks a significant simplification that is possible in the case of nearly homogeneous systems of atoms governed by potentials that have built-in cutoff distances for direction atomic interaction, as in the case of the SW potential. The off-diagonal elements of the Hessian matrix that correspond to pairs atoms separated by a distance greater than the cutoff are therefore identically zero. Since the vast majority of atoms in homogeneous systems satisfy this condition, most of the elements comprising the full Hessian matrix are indeed zero and the matrix is termed "sparse." If each atom has on average N_c neighbors within the cutoff distance of the governing interatomic potential, then a vector of size $3N \cdot 3N_c$ is sufficient to store all elements of the Hessian matrix. Such a storage scheme is called "sparse vector form" [Duff *et al.*, 1986] and was adopted for the purposes of this study.

The benefits of storing the Hessian matrix in sparse vector form are not limited to savings in computer memory: they also hold out the opportunity of performing efficient numerical linear algebra calculations using iterative methods. Indeed, application of direct numerical linear algebra methods to problems involving systems of the size considered in this study is often infeasible without access to vast computational resources [Trefethen, Bau, 1997; Demmel, 1997]. Most iterative numerical linear algebra algorithms require the user to provide an external function that carries out a fundamental operation, such as the multiplication of some matrix by a given vector. In the case of the applications considered in this study, an algorithm was constructed for multiplying the Hessian matrix by an arbitrary vector. Because this matrix is stored in sparse vector form

as discussed above, a single multiplication by a vector involves only $3N \cdot 3N_c$ operations (rather than the $(3N)^2$ that would be required if the Hessian were stored as a $3N \times 3N$ array).

The matrix-vector multiplication algorithm constructed for the purposes of this study was sufficient to efficiently obtain solutions to linear systems of equations involving the Hessian matrix as well as to conduct partial diagonalization of the Hessian matrix. Solutions of linear systems involving the Hessian matrix were found using the SYMMLQ iterative scheme [Paige, Saunders, 1975] (available online at Netlib [Netlib]). Selected eigenvalues and eigenvectors of the Hessian matrix were determined as needed using the ARPACK implementation of the Implicitly Restarted Arnoldi Method (IRAM) [Lehoucq *et al.*, 1998], available online at Netlib [Netlib].

4.5.2 Sorting

The matrix-inclusion analyses presented in section 4.4 call for sorting of the atomic site measures of deviation from linear elasticity δ_k (equation 4.32). In this study, sorting was performed using the SLATEC implementation of DPSORT [Singleton, 1969] (available on Netlib [Netlib]).

4.5.3 MATLAB

An indispensable tool in conducting research on numerical models is an analysis software package like MATLAB [MathWorks]. The standard routines included in MATLAB were used in this study to perform a variety recurring tasks such as to compile histograms, find isocontours of two-dimensional distributions, and plot data.

5. Creating a-Si by melting and quenching

This section describes the creation of a-Si systems of differing densities by quenching molten silicon at different quench rates. The physical properties of variously quenched a-Si systems are then determined.

5.1 Methods of creating model a-Si structures

The available methods that attempt to create computer models of a-Si can be broadly classified into two categories: direct construction by bond switching [Wooten *et al.*, 1985] and melting and quenching [Luedtke, Landman, 1989]. The former starts with a diamond cubic crystalline sample and progressively disorders it by rearranging individual bonds according to pre-specified rules. These rules are chosen with the aim of achieving the best possible structural agreement with the continuous random network (CRN) model [Zachariasen, 1932]. Although effective for small system sizes, this method becomes cumbersome when thousands of atoms are involved. The bond-switching process is furthermore inherently unphysical, as no instance of such "self-amorphization" at low temperatures has been observed in silicon.

Due to the fast crystallization kinetics of molten silicon, quenching is normally not a viable way of creating a-Si experimentally [Tanaka *et al.*, 1999]. Furthermore, melting and quenching as a means to creating computer models of a-Si has been known at times to produce final structures whose character was further from the anticipated CRN model than when bond switching was used [Luedtke, Landman, 1989]. To address this perceived problem, some investigators have proposed new bond-switching algorithms [Barkema, Mousseau, 1996; Valiquette, Mousseau, 2003]. Others have gone as far as to reparameterize the Stillinger-Weber potential altogether [Vink *et al.*, 2001]. In this study, however, melting and quenching is viewed as the single method that makes the least number of extraneous assumptions about the dynamics of the system and the final a-Si structure. Therefore, it was adopted as the method of choice for creating a-Si systems.

5.2 Initial condition: diamond cubic crystalline Si

The initial conditions provided for the simulation were the positions of atoms in a perfect diamond cubic silicon crystal. This configuration corresponds to the structure of Si-I: the stable phase of silicon at room temperature and pressure [Young, 1991]. The diamond cubic structure can be described in terms of cubic unit cells—each containing eight atoms—repeating in the x, y, and z directions. Although this cubic cell is not the primitive cell (the primitive unit cell is similar to the one for the FCC configuration, but contains two atoms [Ziman, 1995]), it is convenient for the purposes of both constructing and visualizing a crystalline silicon (c-Si) configuration. Table 5-1 provides the relative coordinates of the 8 atoms in the diamond cubit unit cell when arranged in such a way that all atoms are stationary and in equilibrium (corresponding to zero temperature).

Atom no.	x-coordinate	y-coordinate	z-coordinate
1	0.00	0.00	0.00
2	0.00	0.50	0.50
3	0.50	0.00	0.50
4	0.50	0.50	0.00
5	0.25	0.25	0.25
6	0.75	0.75	0.25
7	0.25	0.75	0.75
8	0.75	0.25	0.75

Table 5-1: The relative (unscaled) coordinates of the 8 atoms comprising the diamond cubic unit cell.

Figure 5-1 illustrates the arrangement of atoms in the diamond cubic crystal structure. It is easy to see that in this configuration each atom has four nearest neighbors, i.e. diamond cubic c-Si is four-fold coordinated. Furthermore, the angle between any two nearest neighbor bonds of any central atom is equal to $\theta = \cos^{-1}(-1/3) \approx 109.5^{\circ}$. The size and shape of the simulation cell was chosen in such a way as to minimize the overall system potential energy (corresponding to zero stress). In the case of the SW potential, this amounts to scaling the relative atomic coordinates in Table 5-1 by a factor of about

2.5909, giving a nearest neighbor distance of ~1.12 in scaled units for the Stillinger-Weber potential or 0.235 nm.

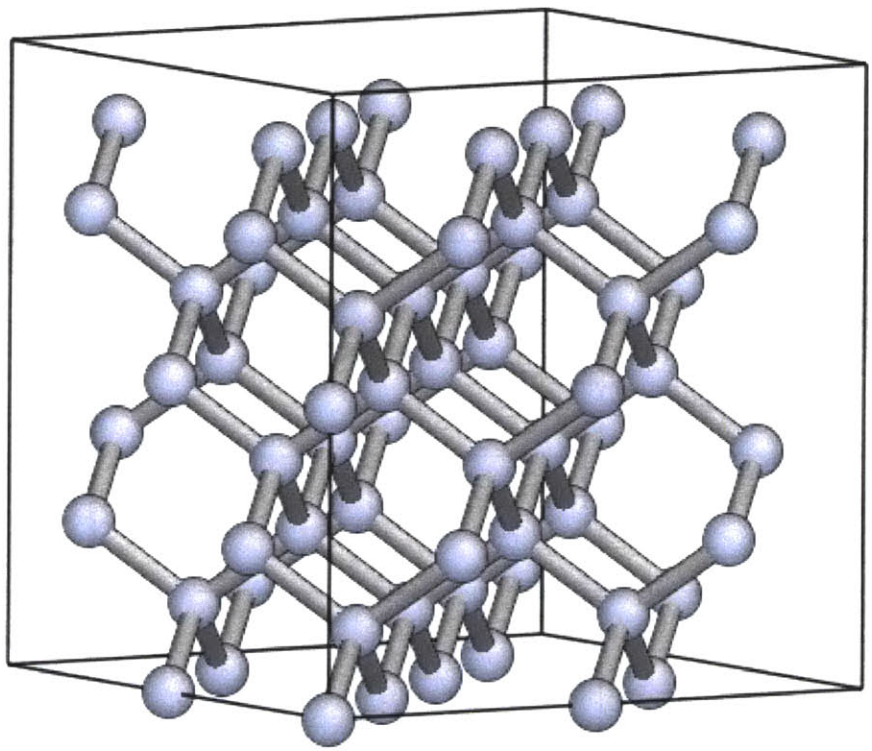

Figure 5-1: The configuration of atoms in the diamond cubic crystal structure. In the Stillinger-Weber potential for silicon, the equilibrium distance between nearest neighbor atoms (i.e. the bond length) in this configuration is about 1.12.

5.3 Melting

The initial c-Si structure was melted by conducting constant zero pressure MD simulations at increasing temperatures. Starting at T=25K, the temperature was increased by increments of 25K up to T=4000K. After each temperature increment, the structure

was equilibrated for 2000 MD time increments: a total of about 7.74 ps. The rate of temperature increase was therefore about $3.23 \cdot 10^{12}$ K/s, i.e. much higher than can normally be achieved experimentally (with the possible exception of pulsed laser melting [Thompson *et al.*, 1984]). Conducting the melting process at lower rates of temperature increase did not, however, yield any changes in the observed melting profile. This insensitivity to heating rate can be explained by lack of temperature-activated relaxation processes in the crystalline state and the very fast thermodynamic equilibration of atomic positions in the liquid state.

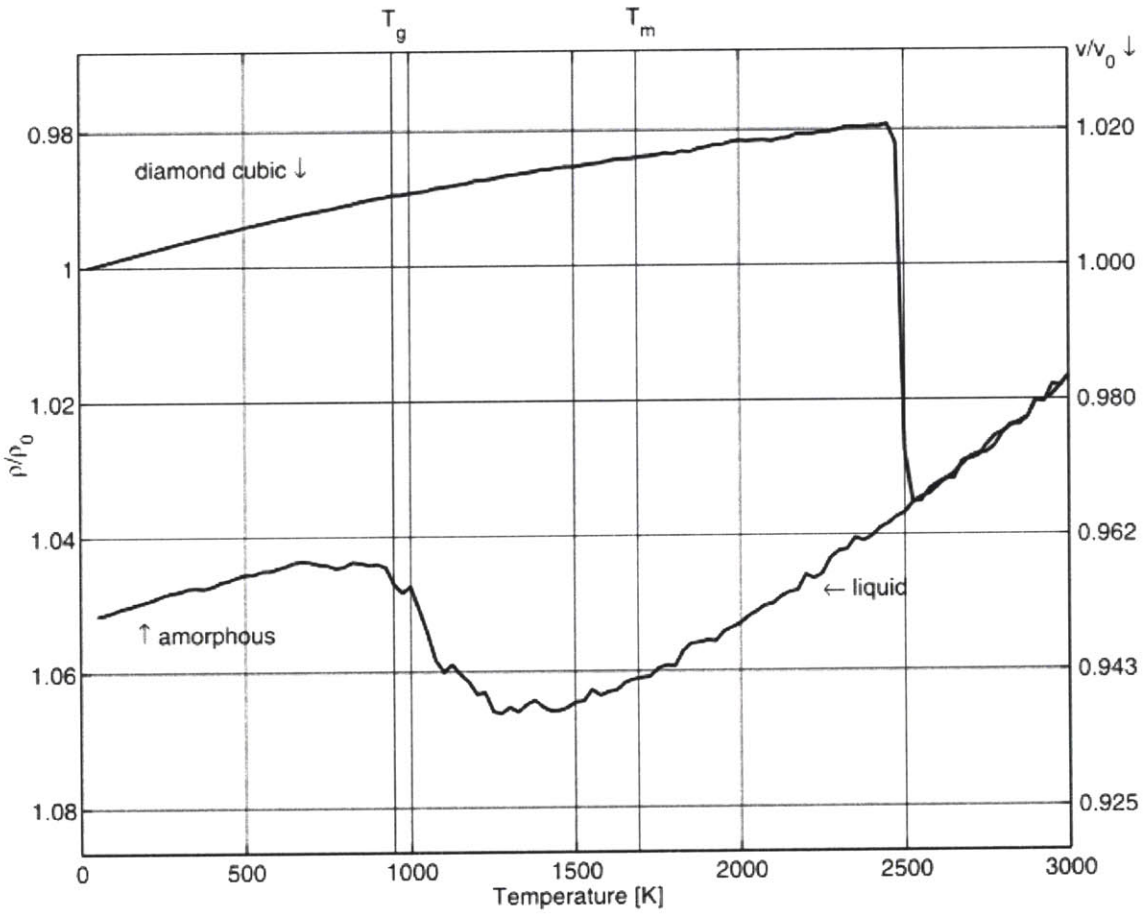

Figure 5-2: The simulated silicon system contracts upon melting at a temperature of about 2500K, i.e. at over 800K above the accepted melting temperature for the SW potential of ~1690K.

The dependence of system density and specific volume during melting is shown in figure 5-2. The most prominent feature of this profile is the sudden system contraction

by about 5.4% at a temperature of about 2500K. This contraction coincides with the melting of the crystalline configuration and is a well-verified characteristic of Si [Glazov *et al.*, 1969]. It is characteristic not only of silicon, but also of many substances that exhibit open crystalline structures [Angell *et al.*, 1996], the best known of these being water. Indeed, obtaining a drop in volume upon melting was one of the central motivations behind the choice of parameters for the SW potential [Stillinger, Weber, 1985].

Although melting of c-Si in a MD simulation such as the one described here occurs at about T=2500K, this is not the phase transition temperature between the crystalline and molten state, i.e. it is not the thermodynamic melting temperature T_m. Broughton and Li showed that T_m for the Stillinger-Weber potential is 1691 ± 20K [Broughton, Li, 1987]. Because, however, the initial crystalline arrangement in the simulation described here was flaw-free, the system could undergo a high degree of overheating due to the large barrier to nucleating an initial molten region. Defects such as grain boundaries can serve as preferred sites for easy nucleation of the melt. If such defects are introduced into the initial configuration, the temperature at which the system undergoes melting is drastically decreased and approaches T_m [Phillpot *et al.*, 1989]. The rigorous evaluation of the thermodynamic melting temperature by MD simulation requires allowing for free temperature adjustments until a state of equilibrium is attained in a mixture of coexisting solid and liquid phases of the material.

Figure 5-3 demonstrates that the radial distribution function (RDF) for molten silicon shows the disappearance of long-range order, as expected. By integrating the RDF up to the first "trough" after the nearest neighbor peak it can be concluded that the average coordination of molten Si as modeled by the Stillinger-Weber potential is around 5, which is in good agreement with the experimentally determined value of about 6.4 [Waseda, Suzuki, 1975]. The nearest neighbor angular distribution function (ADF) for molten silicon is shown in figure 5-4. It demonstrates a loss of definition in the bond angles between nearest neighbors.

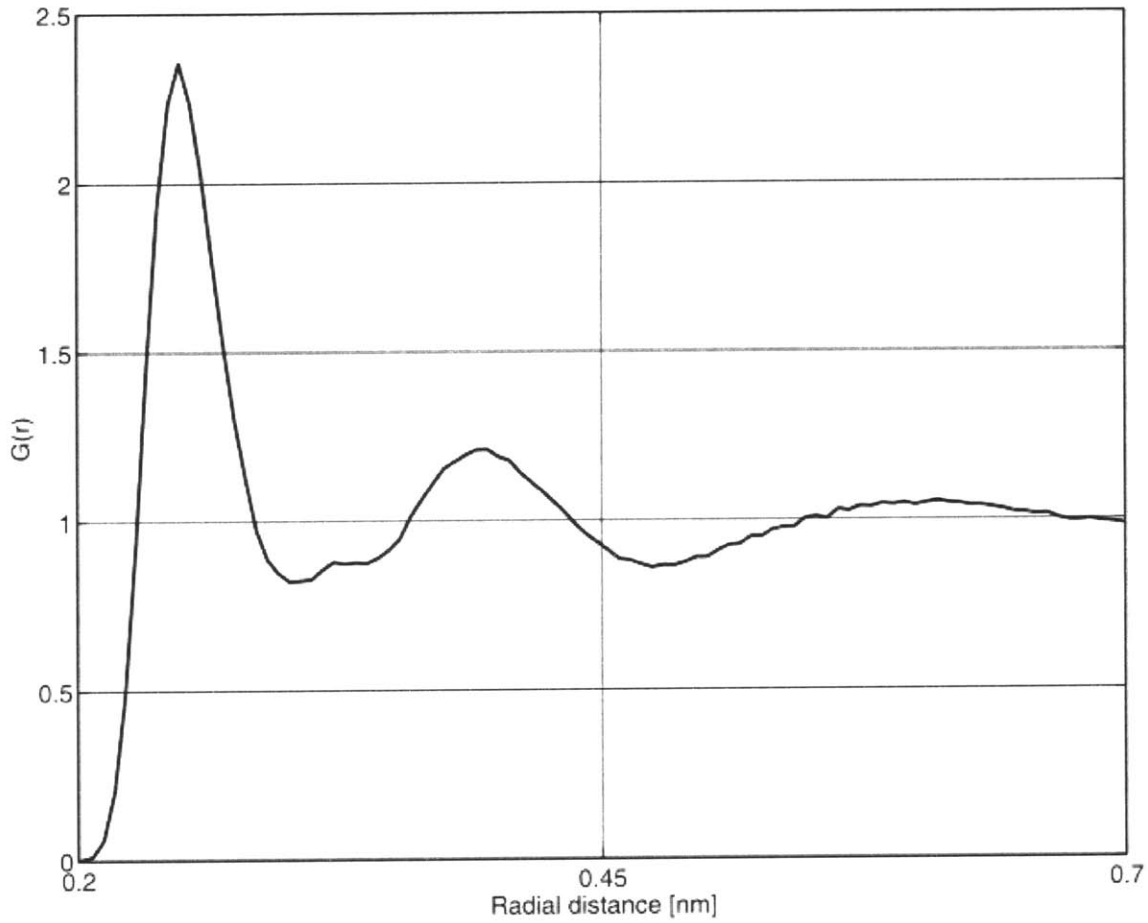

Figure 5-3: Radial distribution function (RDF) of molten silicon.

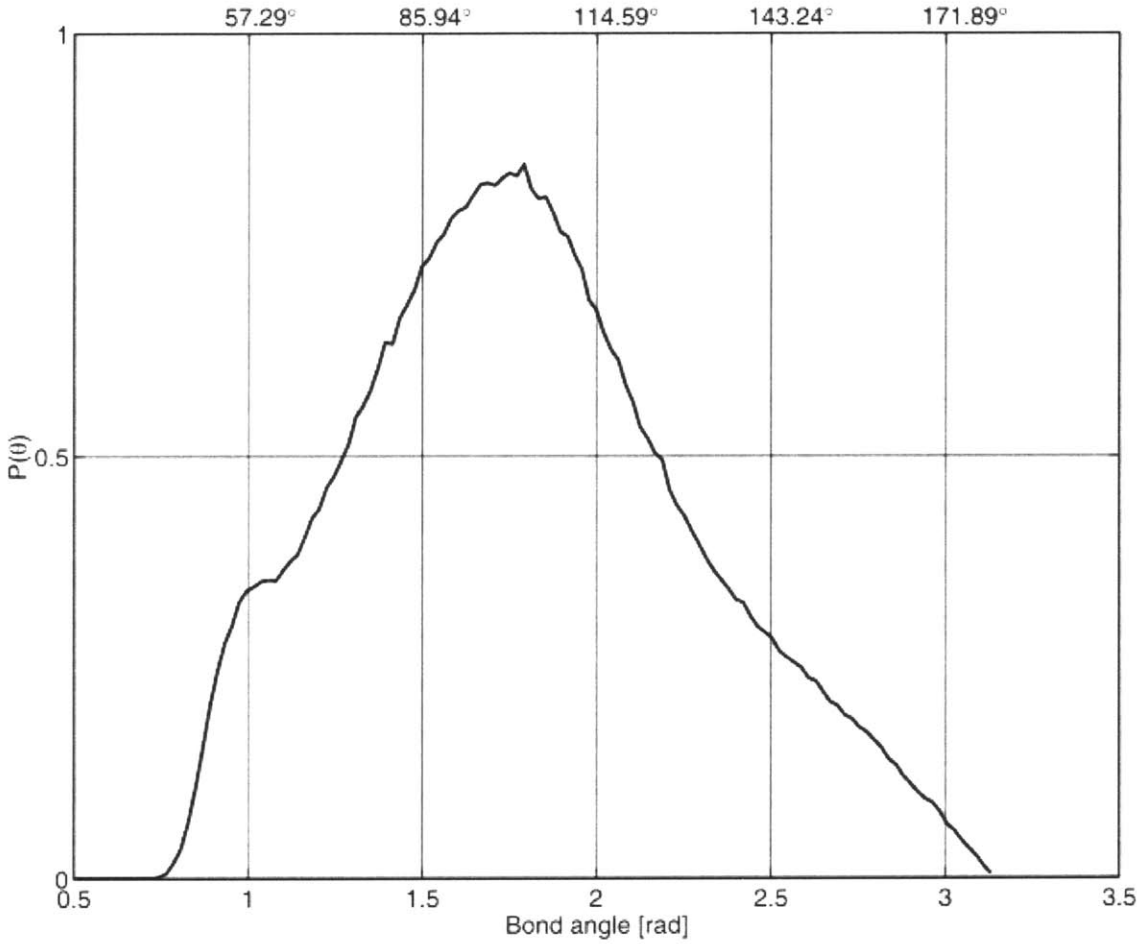

Figure 5-4: Angular distribution function (ADF) of molten silicon.

5.4 Quenching

Liquid silicon was quenched by decreasing the temperature in increments of 2K and equilibrating for times ranging between 10 and 25000 MD time steps, corresponding to quench rate ranging between $1.49 \cdot 10^{10}$ K/s and $3.73 \cdot 10^{13}$ K/s. The resulting variation of densities and relative volumes is depicted in figure 5-5. The system persists in the molten state for temperatures far below the melting temperature and eventually vitrifies at T_g: the glass transition temperature. This undercooling phenomenon is analogous to the overheating described in section 5.3 in that a transition to the thermodynamically stable state (the crystalline state, in this case) is impeded by a nucleation barrier. Much as this nucleation barrier can be reduced in the case of melting by the insertion of defects into the crystal structure, it can be eliminated in the case of crystallization if a small crystalline nucleus is added at a temperature slightly below T_m. The molten material surrounding it then crystallizes on time scales accessible to MD simulation [Keblinski *et al.*, 1996; Keblinski *et al.*, 1997]. The time scale for the spontaneous creation of such a nucleus, however, is prohibitive given current computational capabilities unless specially modified empirical potentials are used [Nakhmanson, Mousseau, 2002].

While increasing degrees of overheating lead crystalline structures to become increasingly unstable under thermal motion resulting in an eventual spontaneous transition to the molten state, increasing degrees of undercooling are accompanied by ever decreasing atomic mobilities making it more difficult for crystalline nuclei to form and grow. Eventually, mobilities become so low that the underlying liquid configuration becomes "kinetically frozen" and no longer undergoes significant thermally induced structural relaxation. The temperature at which this phenomenon occurs is called the glass transition temperature T_g and is easily identified to be about 950 K by the rapid change in thermal expansion coefficient of the material. The vitrified material below T_g is called amorphous silicon (a-Si). Note from figures 5-2 and 5-5 that the thermal expansions of c-Si and a-Si are nearly identical at $\alpha_{c-Si} = 1.26 \cdot 10^{-5} K^{-1}$ and

$\alpha_{a-Si} = 1.14 \cdot 10^{-5} K^{-1}$, respectively. The thermal expansion coefficient of the liquid, however, is nearly four times higher: $\alpha_{l-Si} = 4.18 \cdot 10^{-5} K^{-1}$.

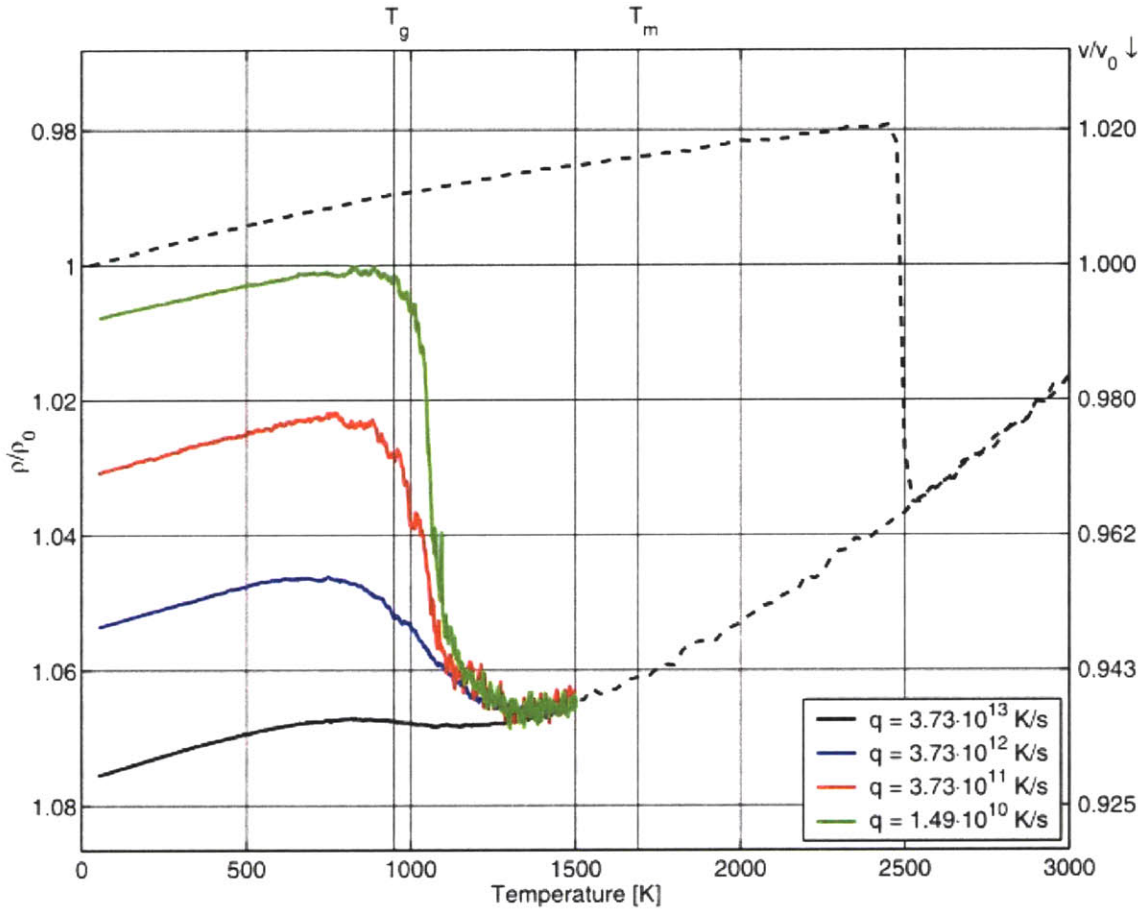

Figure 5-5: When quenched, molten Si vitrifies at a glass transition temperature of about 950K. The final density of the resulting a-Si depends sensitively on the applied rate of quenching. All quench rates are in K/s. Densities and volumes are shown scaled by the density and specific volume of SW c-Si at zero temperature and pressure: $\rho_0 = 2323.8\, kg/m^3$ and $v_0 = 4.3033 \cdot 10^{-4}\, m^3/kg$.

5.5 Characterization

Unlike the melting phase transition from crystal to liquid structures [Huang, 1987], the exact physical nature of the glass transition is not yet well understood. The phenomenology of vitrification, however, is directly accessible to atomistic study. This

subsection characterizes the phenomenological dependence of physical properties of a-Si systems on the quench rates used to produce them as well as the correlations among those properties.

5.5.1 Density, average coordination, and elastic constants

It is clear from figure 5-5 that the densities of the final a-Si structures obtained by quenching are highly sensitive to the quench rate used in creating them. The lowest density a-Si structures approach a density slightly higher than that of c-Si as shown in figure 5-6 and are obtained using the slowest quench rates. Faster quench rates yield higher density structures. This quench rate dependence of a-Si densities is paralleled by the quench rate dependence of average atomic coordinations of a-Si, shown in figure 5-7. Fast quenching gives rise to higher atomic coordination values while slow quenching results in lower coordinations, approaching a coordination slightly higher than that of c-Si. Both the densities and coordination numbers approach asymptotic values when extrapolated to infinitely slow quenching.

Figures 5-6 and 5-7 indicate that the rate of approach to the asymptote is the same for both system densities and average coordinations. This observation is confirmed by their linear dependence on each other, as figure 5-8 shows. Similar quench rate dependencies are observed for the excess enthalpies and isotropic elastic constants (bulk and shear moduli) of a-Si. As demonstrated in figures 5-9 through 5-11, all of these quantities are therefore conveniently parameterized in terms of the densities of the quenched a-Si structures.

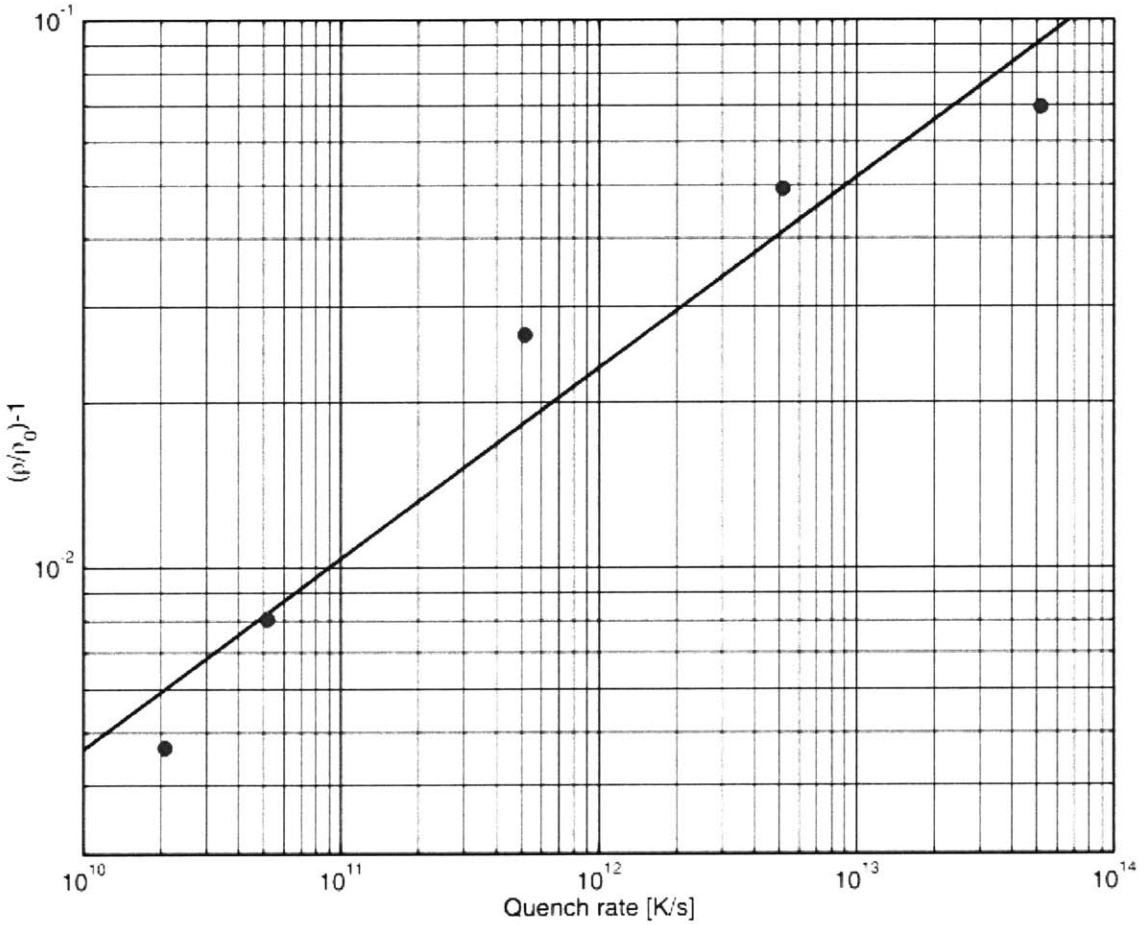

Figure 5-6: The quench rate dependence of a-Si densities. Densities approach an asymptotic value just below the diamond cubic crystal density for ever-slower quenching.

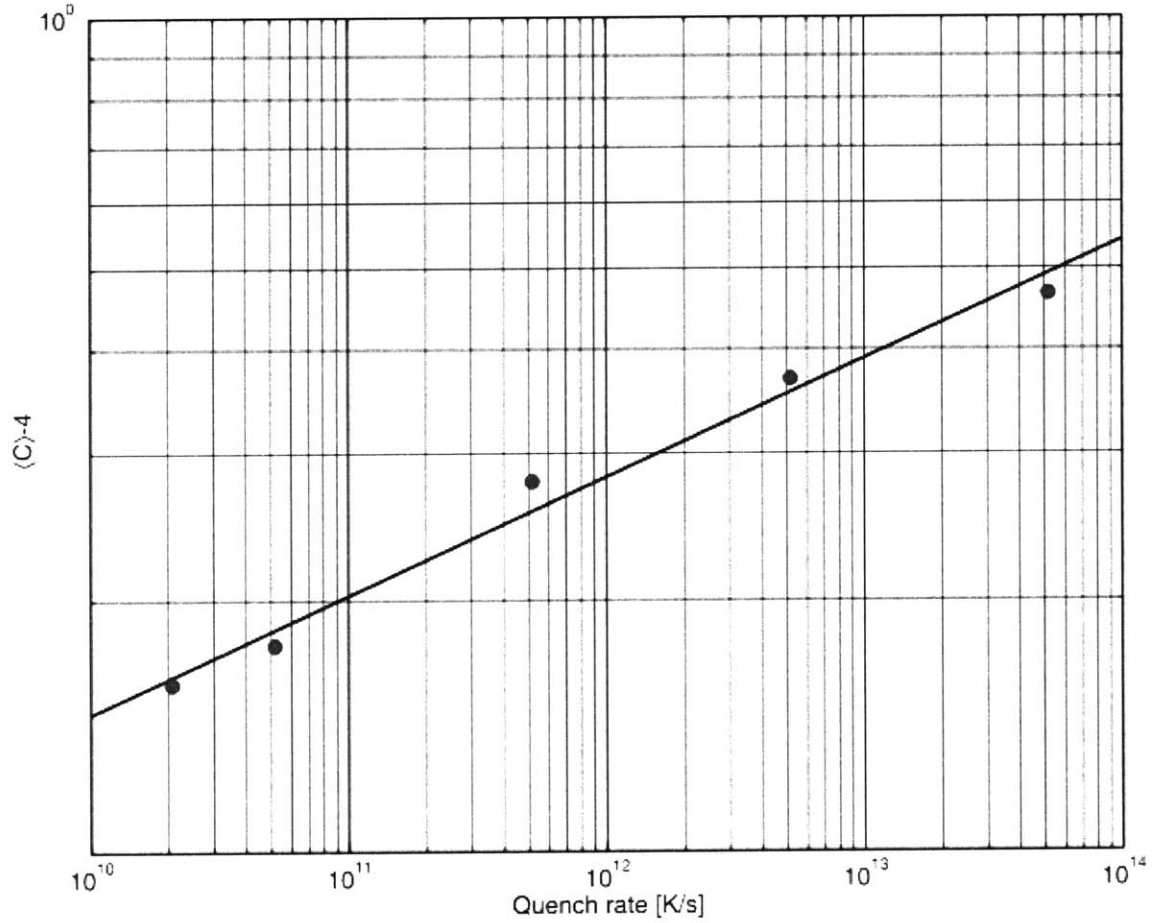

Figure 5-7: The quench rate dependence of a-Si average coordinations. Average coordinations approach an asymptotic value just above the diamond cubic crystal coordination of 4 for ever-slower quenching.

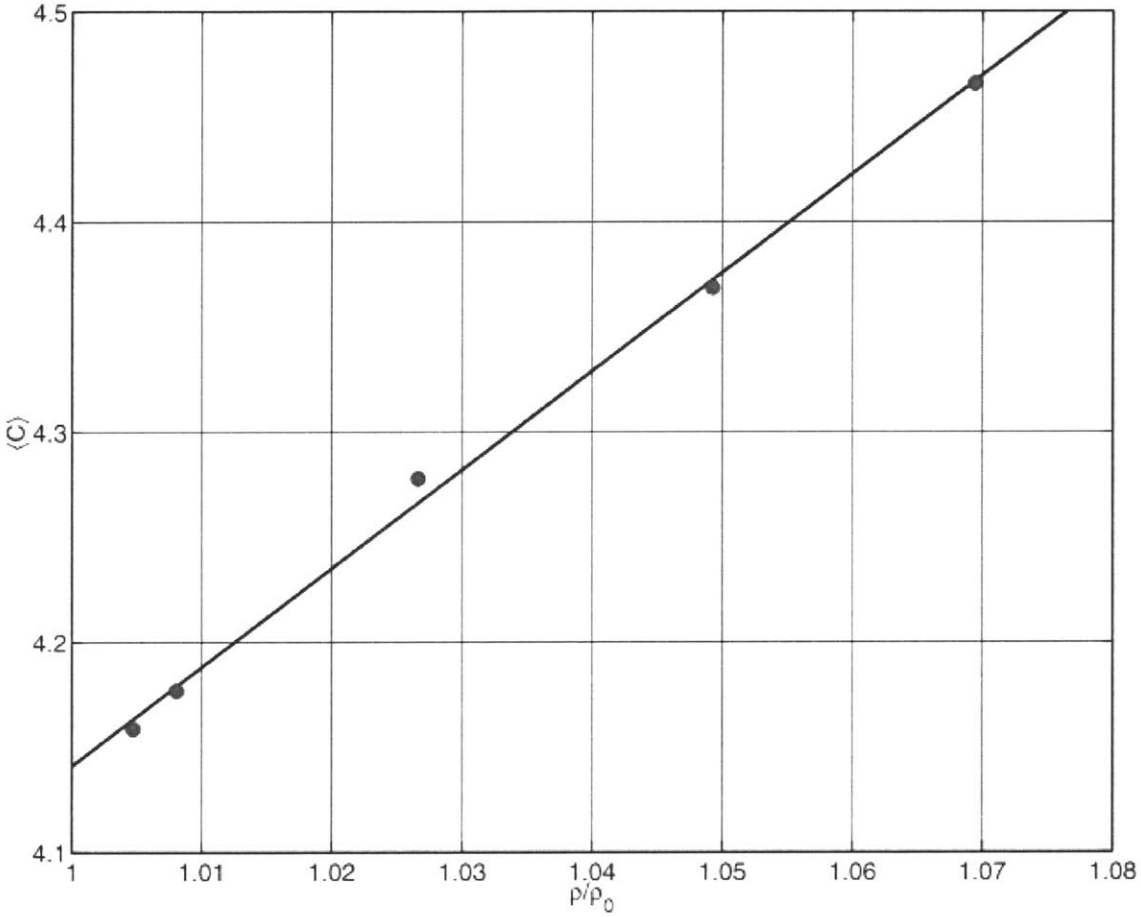

Figure 5-8: Average coordinations of as-quenched a-Si systems vary approximately linearly with their densities: $\langle C \rangle \approx 4.69 \cdot (\rho/\rho_0) - 0.55$.

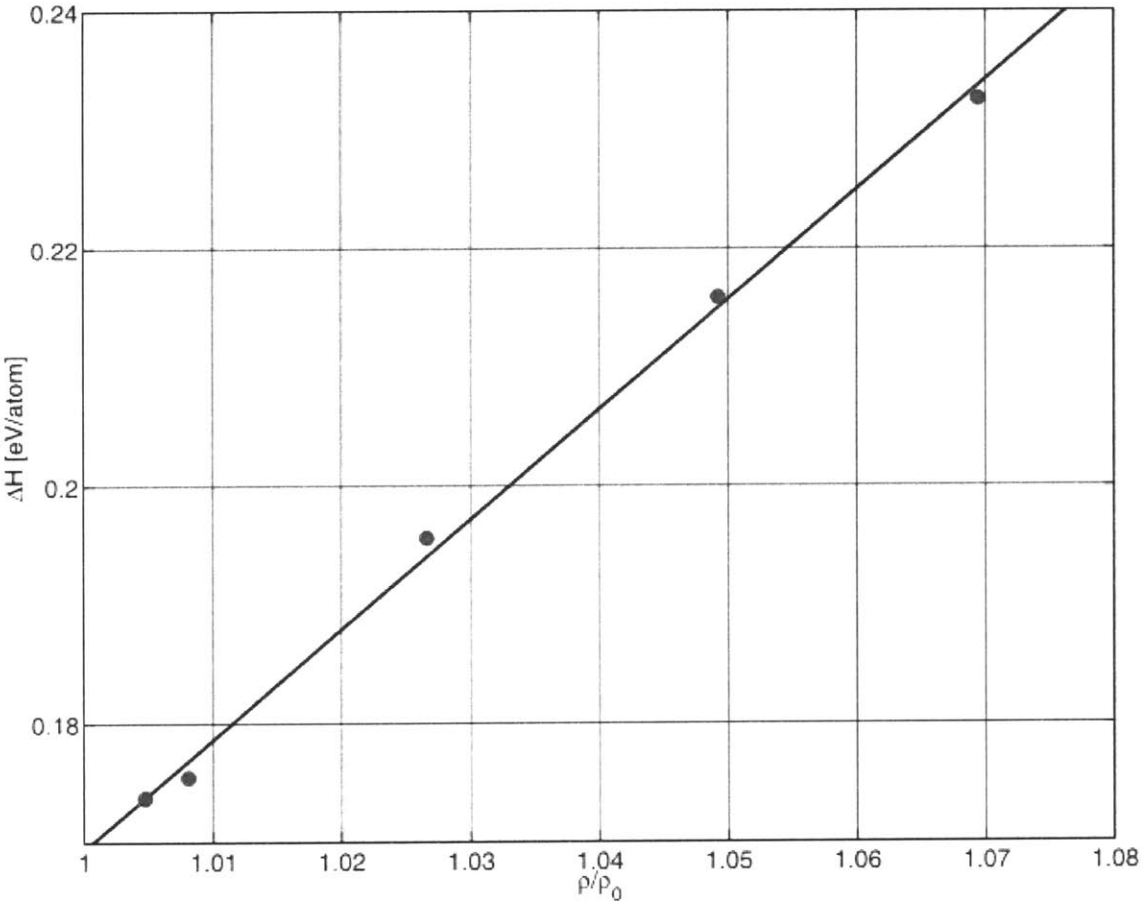

Figure 5-9: Excess enthalpies of as-quenched a-Si systems vary approximately linearly with their densities: $\Delta H \approx 0.93 \cdot (\rho/\rho_0) - 0.76$ eV/atom.

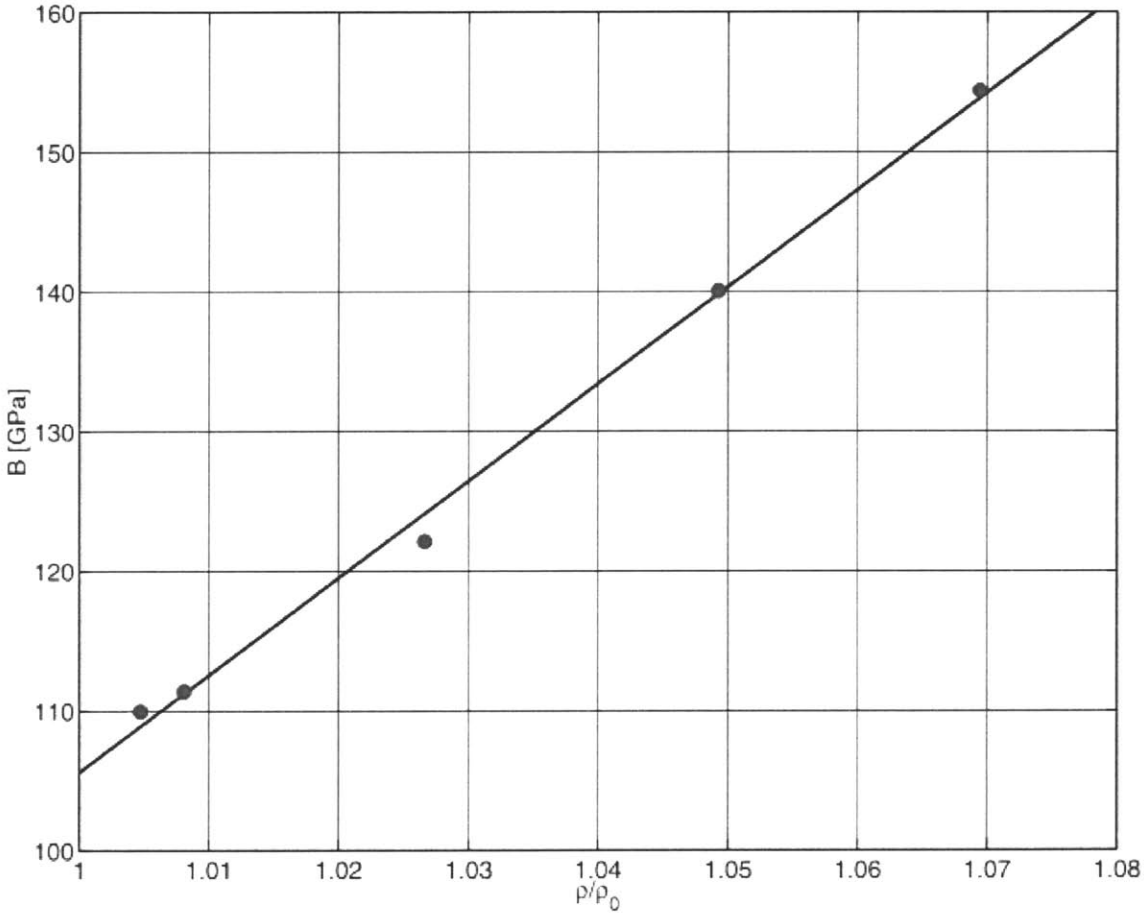

Figure 5-10: Bulk moduli of as-quenched a-Si systems vary approximately linearly with their densities: $B \approx 695 \cdot (\rho/\rho_0) - 589$ GPa.

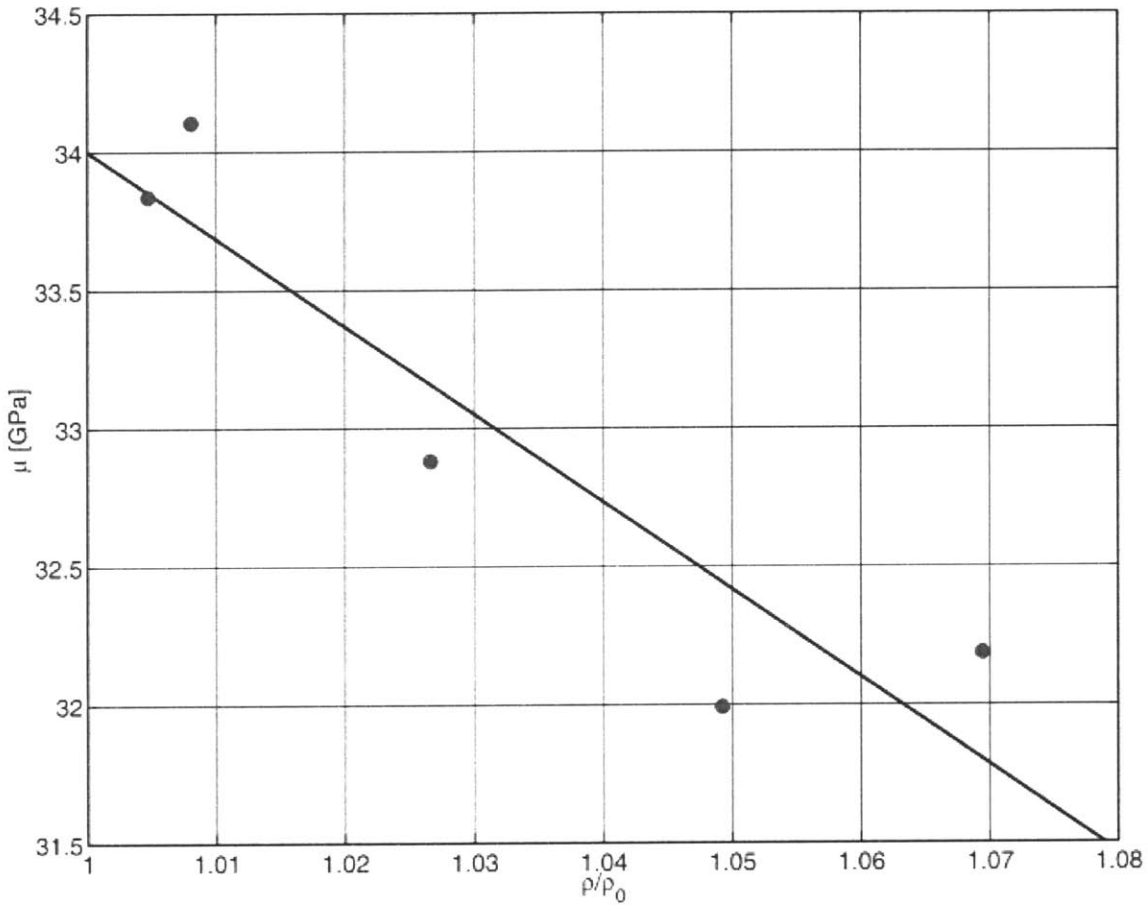

Figure 5-11: Shear moduli of as-quenched a-Si systems vary approximately linearly with their densities: $\mu \approx -31.7 \cdot (\rho/\rho_0) - 65.7$ GPa.

Determination of the full set of 21 independent elastic constants for as-quenched a-Si systems of varying densities allows for the determination of the anisotropy measures described in section 4.1.4. These measures are shown in Table 5-2 and confirm that the a-Si systems created by quenching are isotropic to within statistical error.

ρ/ρ_0	$(\mu - \mu_P)$, [GPa]	C_0, [GPa]
1.0694	0.1015 ± 1.2513	-0.0832 ± 0.7686
1.0492	0.9566 ± 2.0887	0.5108 ± 0.7933
1.0266	0.3784 ± 1.4821	-0.2142 ± 0.5079
1.0080	-0.5189 ± 0.8797	-0.1719 ± 0.6245
1.0047	-0.2833 ± 0.6296	-0.0345 ± 0.4777

Table 5-2: The anisotropy measures defined in section 4.1.4 confirm that the a-Si systems created by melting and quenching are isotropic to within statistical error.

5.5.2 Radial and angular distribution functions

Characterization of the atomic structures of the variously quenched a-Si configurations is accomplished by using radial and angular distribution functions (RDFs and ADFs). Figures 5-12 and 5-13 plot these functions for as-quenched a-Si structures of four different densities, i.e. produced using four different rates of quenching. The RDFs—shown in figure 5-12—all exhibit distinct nearest neighbor peaks and a split second nearest neighbor peak. The nearest neighbor distance for low-density systems is sharper and smaller than in the case of high density ones. Furthermore, the lower-length section of the split second nearest neighbor peak is attenuated for low-density systems while the higher-length section is intensified. The opposite is true for high-density systems. The ADFs—given in figure 5-13—show an intensification of the peak at $\sim 109.5^{\circ}$ (the characteristic bond angle of the diamond cubic crystal configuration) with decreasing density. These changes in structure are consistent with a tendency of a-Si to gradually become more like c-Si when allowed to relax for increasing periods of time, while still retaining its amorphous structure.

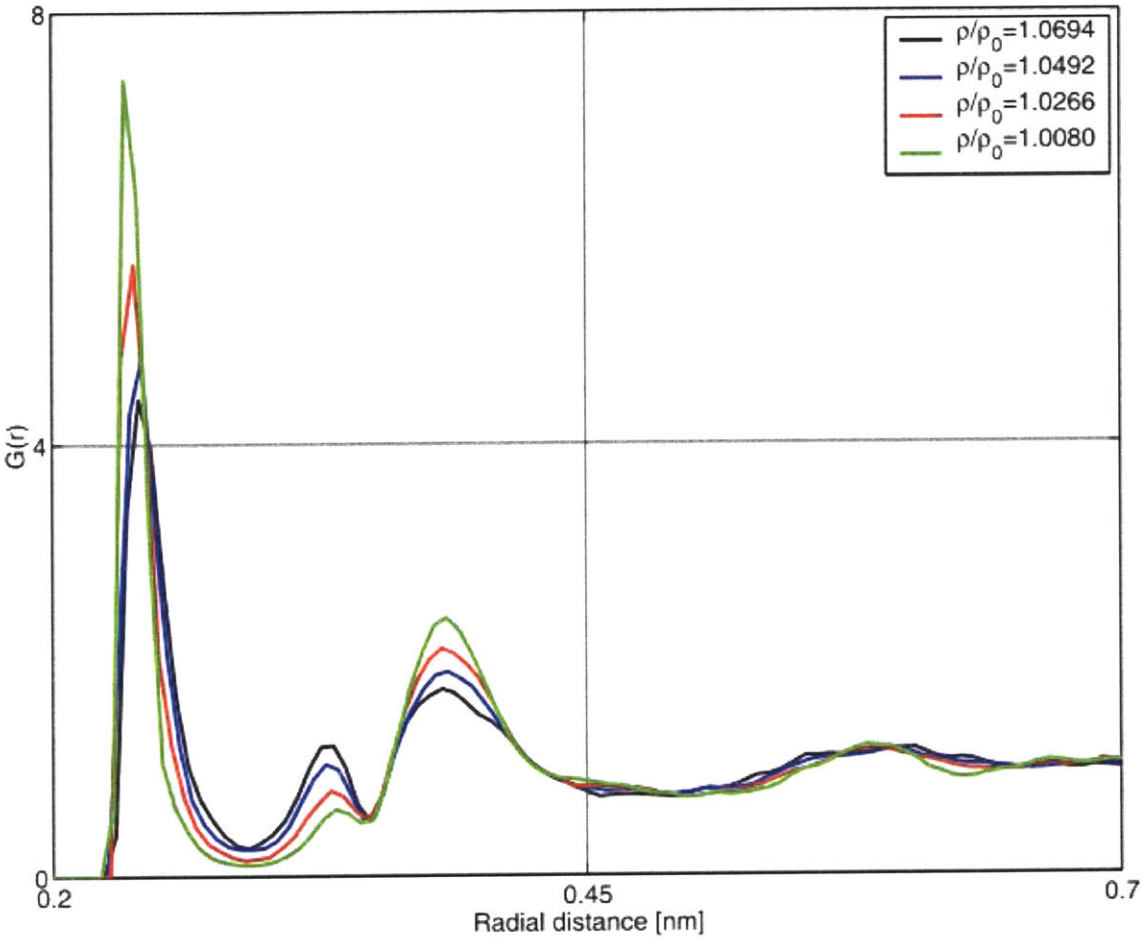

Figure 5-12: The radial distribution functions (RDFs) for as-quenched a-Si systems of four different densities.

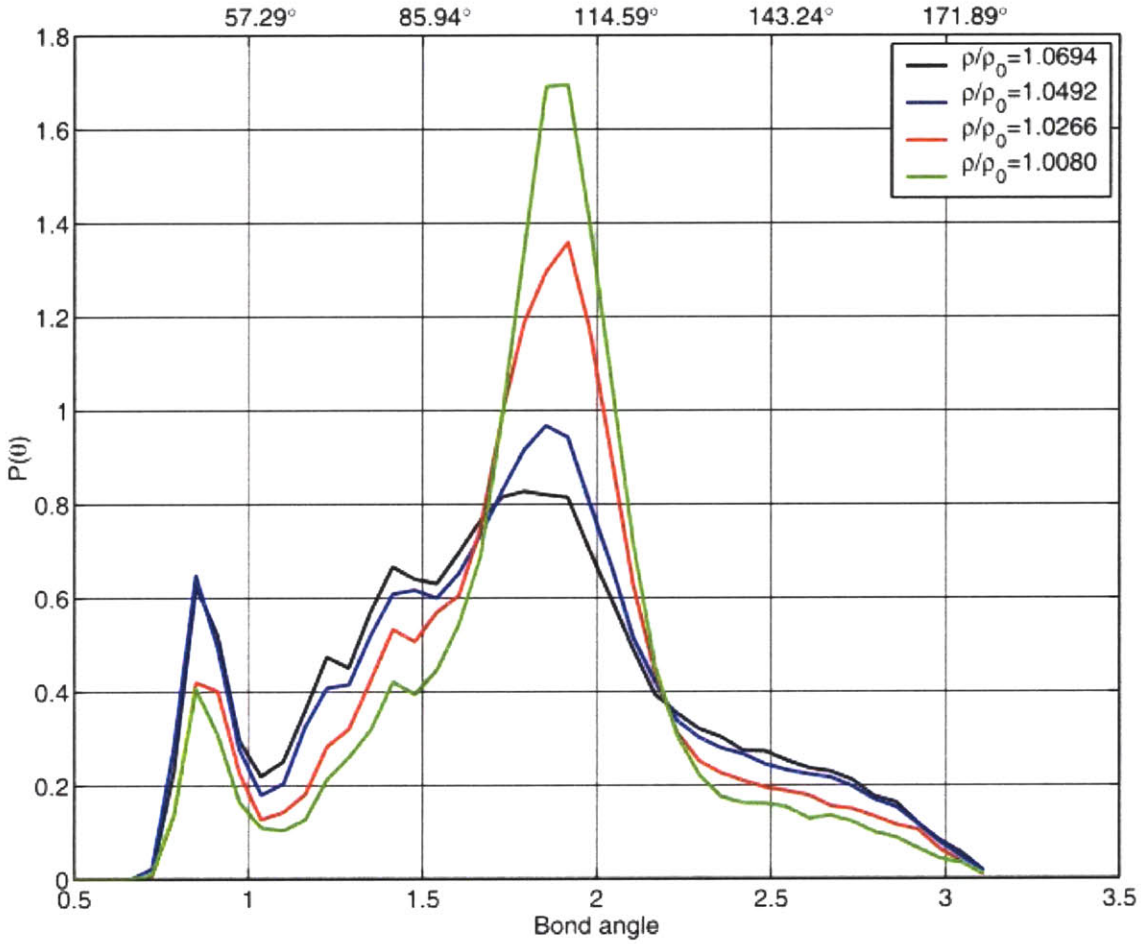

Figure 5-13: The nearest-neighbor angular distribution functions (ADFs) for as-quenched a-Si systems of four different densities.

5.5.3 Atomic stress distributions

Further insight into the nature of atomic environments in a-Si structures of different densities can be obtained by investigation of the atomic level stresses introduced in section 4.1.2. Figures 5-14 and 5-15 show histograms of atomic level pressures and deviatoric stress components for a typical a-Si system. These quantities exhibit a large spread of values, indicating that—much as in the case of metallic glasses [Srolovitz *et al.*,

1983]—individual atomic environments in a-Si are far more distorted than the level of overall system stress (i.e. the average of atomic stresses, section 4.1.2) would indicate. Using dimensional analysis, the characteristic length and energy scales of the Stillinger-Weber potential can be used to calculate the characteristic stress scale [Allen, Tildesley, 2000] of ~37.76GPa (section 3.2.1), which is approximately the same as the decohesion stress of SW Si. Figures 5-14 and 5-15 demonstrate that the stress level of certain atomic environments approaches that of decohesion.

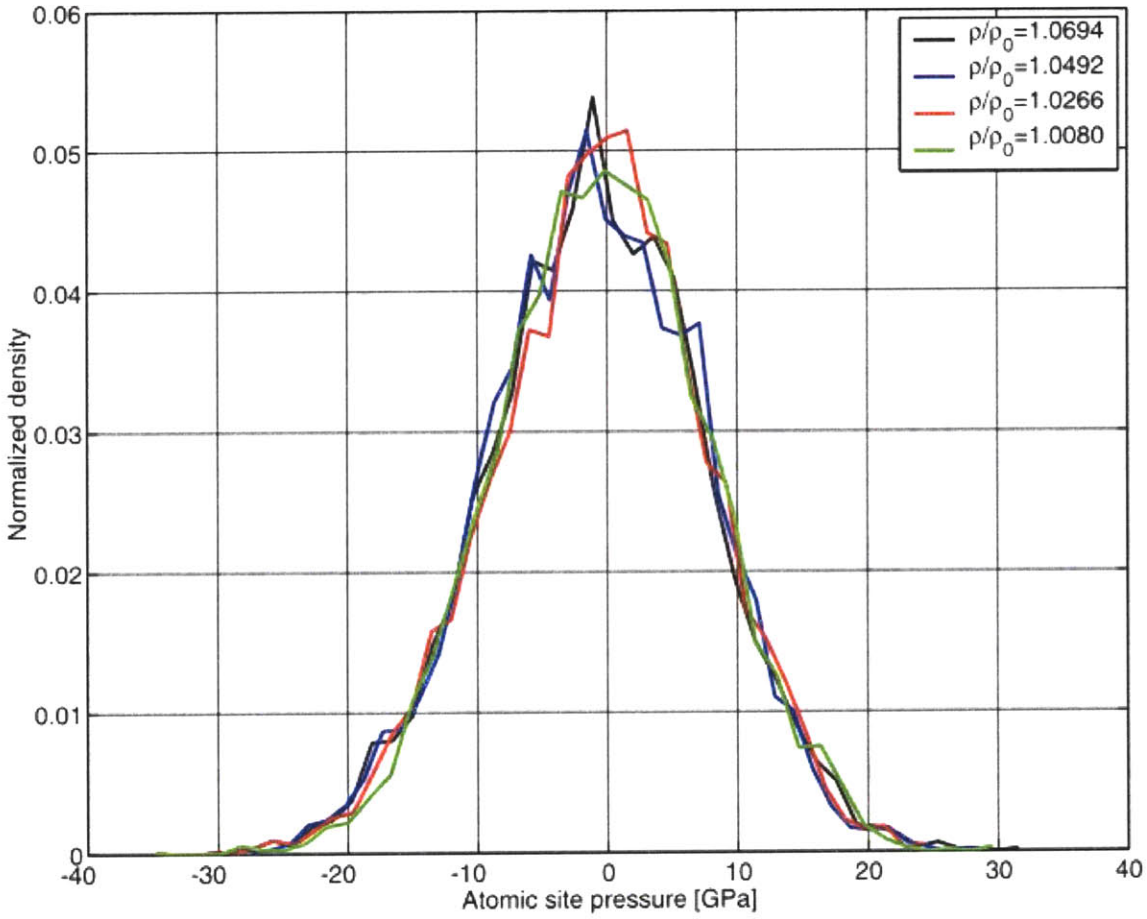

Figure 5-14: Distributions of atomic level pressures for four different density as-quenched a-Si structures demonstrate that local atomic environments exhibit a broad range of stress states, even though the average system stress may be close to zero. The largest atomic level pressures approach the approximate decohesion-level stress for SW Si of about 37.8 GPa.

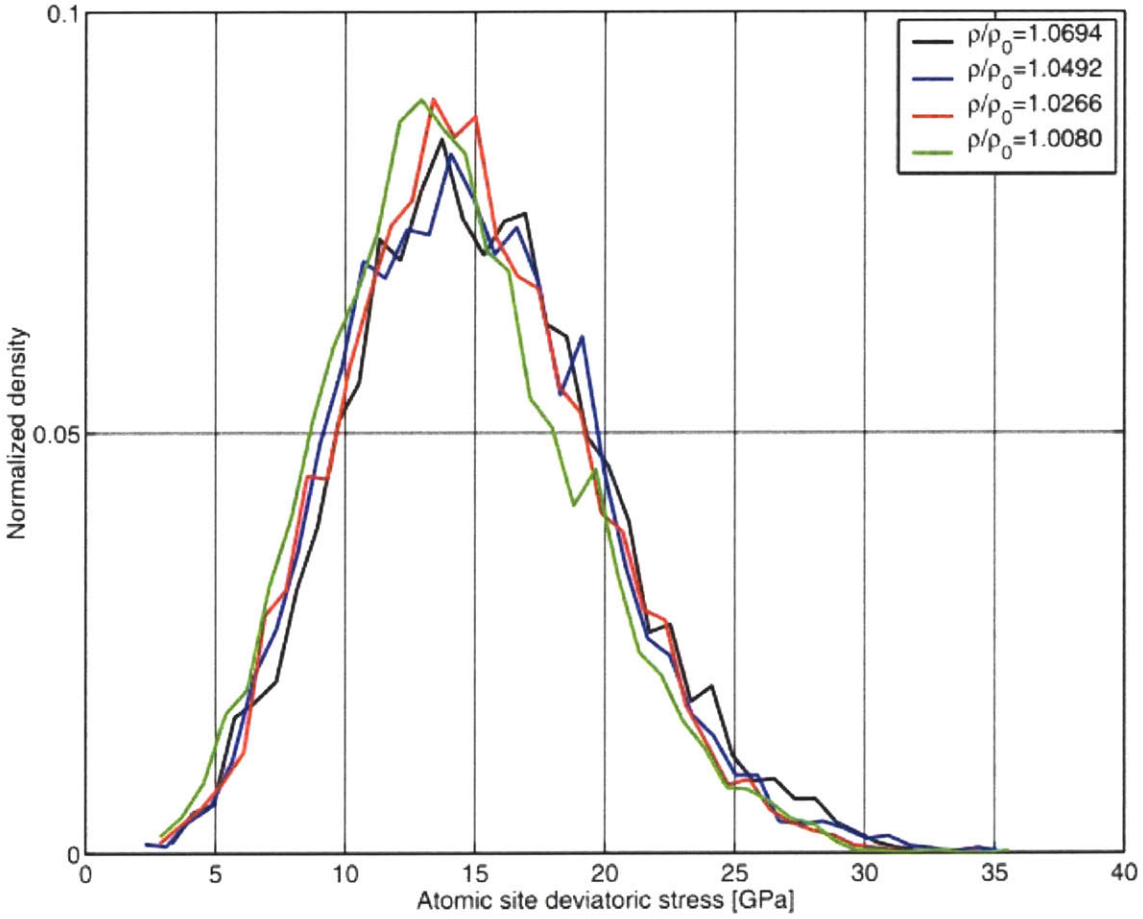

Figure 5-15: Distributions of atomic level deviatoric stresses for four different density as-quenched a-Si structures demonstrate that local atomic environments exhibit a broad range of stress states, even though the average system stress may be close to zero.

Figures 5-16 and 5-17 show that the standard deviation of atomic pressures and the average of atomic deviatoric stresses demonstrate a distinct dependence of the average level of distortion in atomic environments on quench rate. Recall that the average of atomic pressures simply gives the overall system pressure (section 4.1.2). The higher atomic site stresses in quickly quenched structures can be viewed as the principal cause for the larger excess enthalpies of such structures (figure 5-9), the latter being related to the elastic strain energies associated with the atomic site stresses.

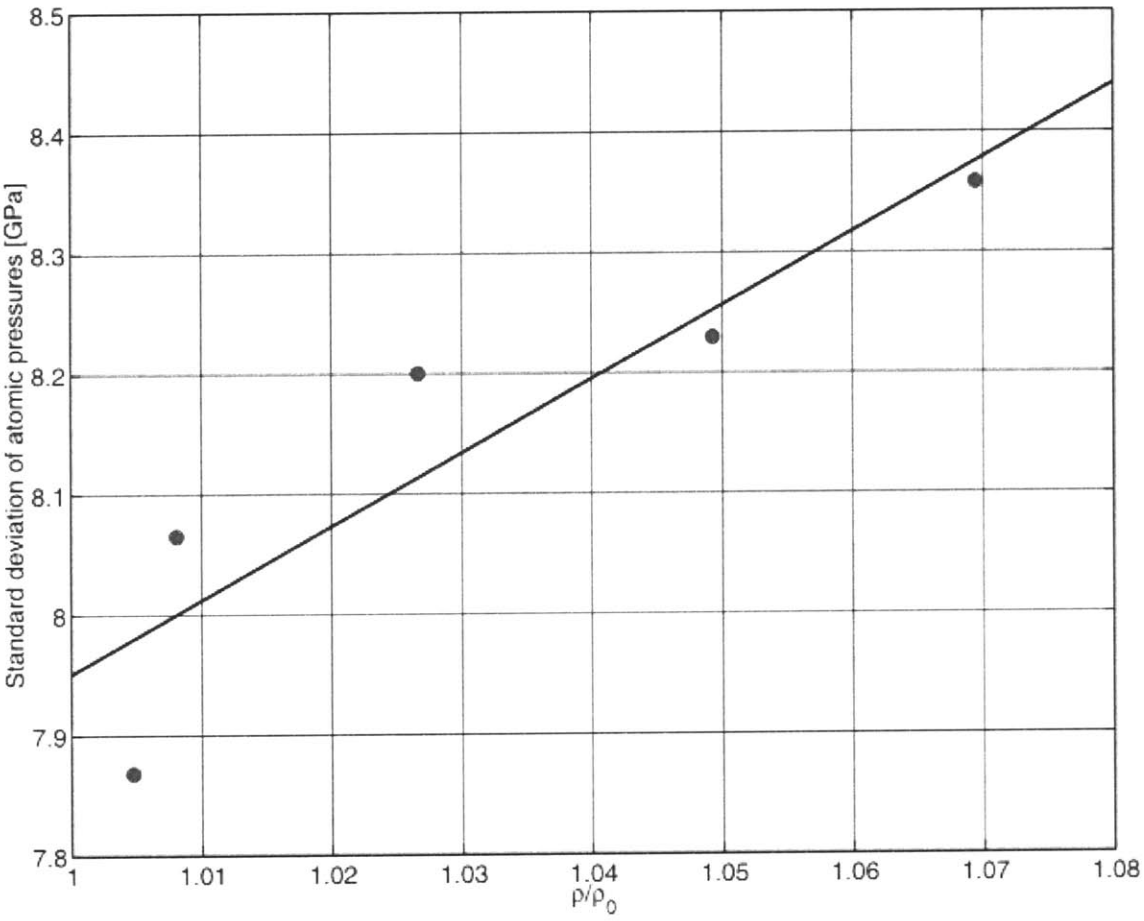

Figure 5-16: The standard deviation of atomic level pressures in a-Si structures are directly correlated to the quench rates used to create them, as evidenced by the linear dependence of these quantities upon density. Recall that the average of atomic pressures simply gives the overall system pressure (section 4.1.2).

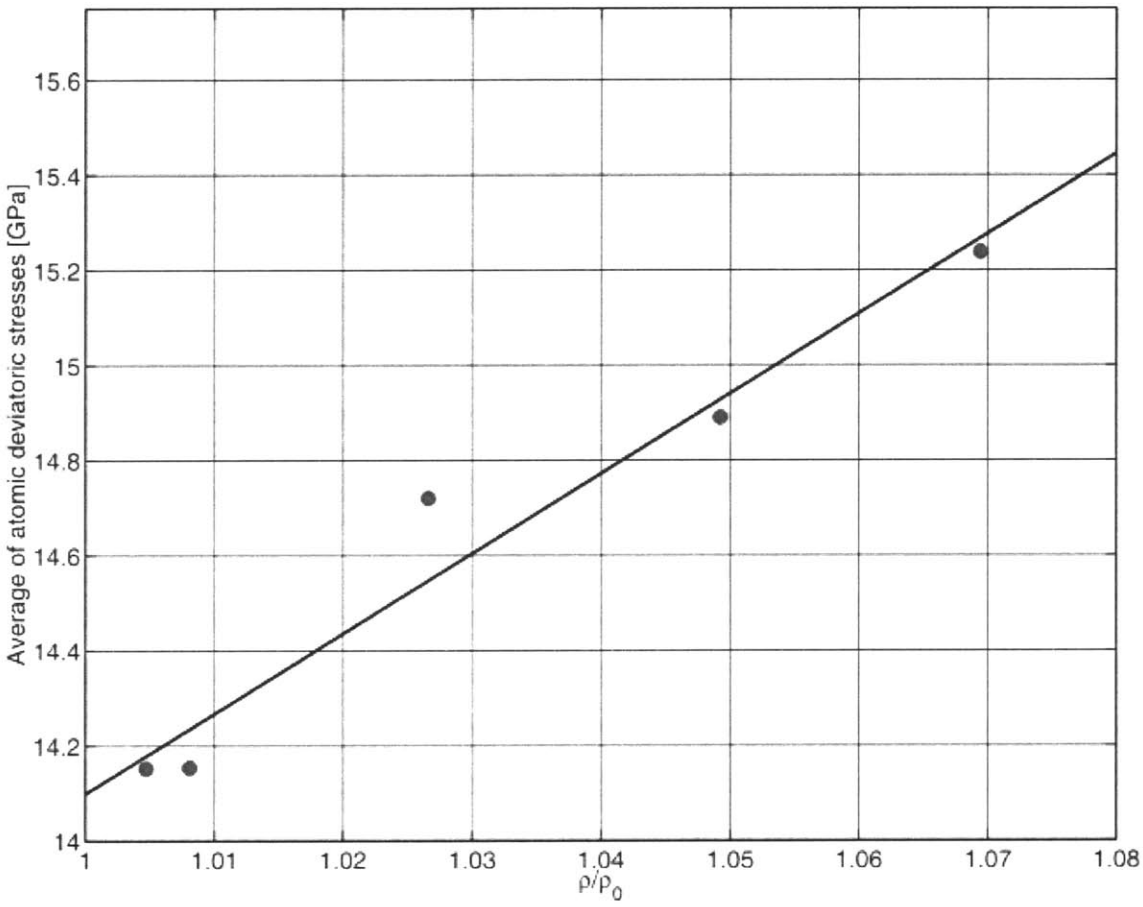

Figure 5-17: The average atomic deviatoric stress levels in a-Si structures are directly correlated to the quench rates used to create them, as evidenced by the linear dependence of these quantities upon density.

5.6 Comparison with experiments and previous simulations

To compare the results of the melting and quenching simulations presented here with experimental findings, it is necessary to observe that the quench rates used in MD simulations are several orders of magnitude higher than the highest ones typically attainable in practice. Therefore, the a-Si samples studied in experiments should be thought of as extremely well relaxed and only the best-relaxed a-Si systems prepared by

MD should be compared to them. Table 5-3 lists several parameters evaluated for the slowest-quenched system created as part of this study. It demonstrates acceptable agreement with experimental results as well as with previous simulations. It should be noted that the best-relaxed system obtained in this study reached a lower value of potential energy than all previous simulations known to the authors, including ones that resorted to highly intricate or unphysical methods [Barkema, Mousseau, 1996].

	Best-quenched a-Si	Previous simulations	Experiment
Coordination	4.15	4.14[a]	3.8-4.1[d]
Bulk modulus	110 GPa	106 GPa[b]	~100 GPa[e]
Shear modulus	34 GPa	33 GPa[b]	~38 GPa[e]
Potential energy	-4.16 eV/atom	-4.12 eV/atom[c]	N/A

Table 5-2: The characteristics of the best-quenched a-Si samples described in this study are in good agreement with experiment and previous simulations. References: a) [Luedtke, Landman, 1989]; b) [Kluge, Ray, 1988]; c) [Barkema, Mousseau, 1996]; d) [Laaziri *et al.*, 1999]; e) [Jiang *et al.*, 1990].

At first glance, the melting and quenching behavior of Si stands in stark contrast to that of metals, which expand upon melting and yield glasses of increasing density at slower quench rates [Turnbull, Cohen, 1961]. Nevertheless, it is clear that both a-Si and metallic glasses exhibit a fundamental similarity in their quench rate dependence: in both cases slower quenching leads to the creation of disordered solids whose character, as determined by densities, coordinations, etc., approaches that of the parent crystalline phase while fast quenching produces structures similar to the liquid phase.

6. Structure of atomic environments in a-Si

This section shows that all atomic environments of every a-Si structure can be unambiguously characterized as "solidlike" or "liquidlike" based on the means and standard deviations of their nearest neighbor bond angles. The relative proportion of each type of atomic environment in any a-Si system can be characterized by the mass fraction of liquidlike atomic environments ϕ. They physical properties of an a-Si system with any value of ϕ can be determined from the properties of liquidlike and solidlike atomic environments using the rule of mixtures.

6.1 Moments of nearest neighbor bond angle distributions

The mutual interrelationship of a-Si densities, coordinations, and excess enthalpies as well as structural features as described by RDFs, ADFs, and atomic level stress distributions discussed in section 5.5 strongly suggests that variations in these quantities can be explained using a single, well-defined atomic-level structure descriptor. To find this descriptor, a characterization of the local structure of atomic environments in a-Si was proposed based on the nearest-neighbor bond angles at each atomic site [Demkowicz, Argon, 2004]. Every atom i in the a-Si systems studied here forms bonds with its m_i nearest neighbor atoms. These bonds define $n_i = \frac{1}{2} m_i (m_i - 1)$ nearest neighbor bond angles for atom i. Call these bond angles θ_{ij}, $j = 1 \ldots n_i$ and define their mean and standard deviation as

$$\mathrm{M}_i = \frac{1}{n_i} \sum_{j=1}^{n_i} \theta_{ij} \tag{6.1a}$$

$$\Sigma_i^2 = \left(\frac{1}{n_i} \sum_{j=1}^{n_i} \theta_{ij}^2 \right) - \mathrm{M}_i^2 \tag{6.2a}$$

The quantities M_i and Σ_i can be computed for the atomic environment of each individual atom i. They can therefore act as effective characterizers of the local structure of atomic bonding environments. The motivation for choosing means and standard deviations of nearest neighbor bond angles as such characterizers stems from the quench rate dependence of radial and nearest-neighbor angular distribution functions (RDFs and ADFs) of a-Si systems, as described in section 5.5.2. This dependence clearly indicates differences in atomic level structure and suggests finding "local" RDFs and ADFs for individual atomic environments. Naturally, the smooth RDFs and ADFs presented in figures 5-12 and 5-13 are composite functions that incorporate information from numerous atomic environments and cannot be determined for individual sites. By conducting averages over the nearest neighbor bond angles, however, it is possible to find effective moments of "local" ADFs. The means and standard deviations of bond angles described in equations 6.1a and 6.1b are just such moments and can therefore be viewed as quantities describing the local atomic site ADFs. Higher moments of nearest neighbor bond distributions—such as skewness and curtosis—did not yield any more insight into the structure of atomic environments in a-Si than did their means and standard deviations alone.

6.2 Two distinct types of atomic environment

The distributions of the values of M_i and Σ_i for all 4096 atoms in a-Si systems of differing densities are shown in figures 6-1 and 6-2. It is immediately apparent that these distributions are bimodal. Moreover, the distributions for a-Si systems of differing densities exhibit different peak heights, but no change in peak positions or abatement of bimodality.

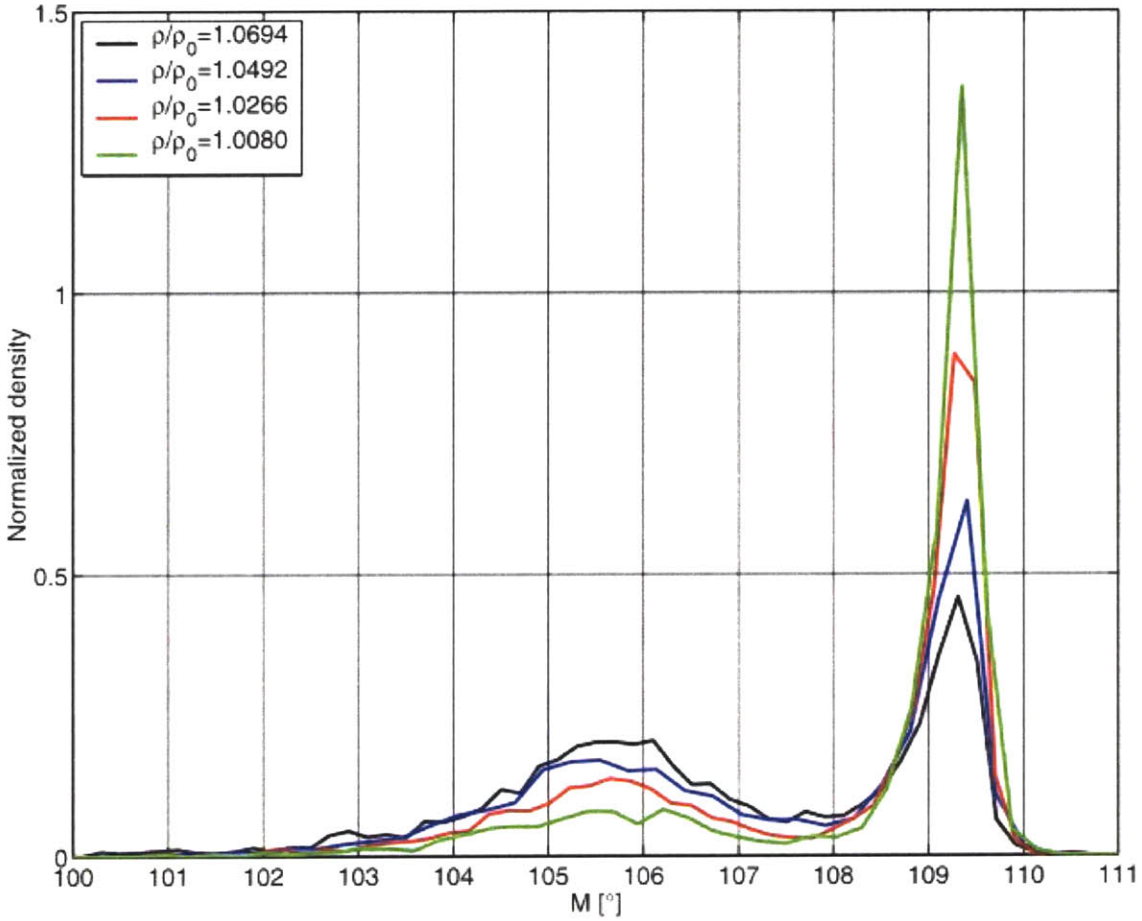

Figure 6-1: The distributions of means M_i (equation 6.1a) of nearest-neighbor bond angles for the atomic environments in a-Si systems of differing densities are bimodal. Systems of differing densities exhibit different relative peak heights, but no shift in the peak positions or abatement of bimodality.

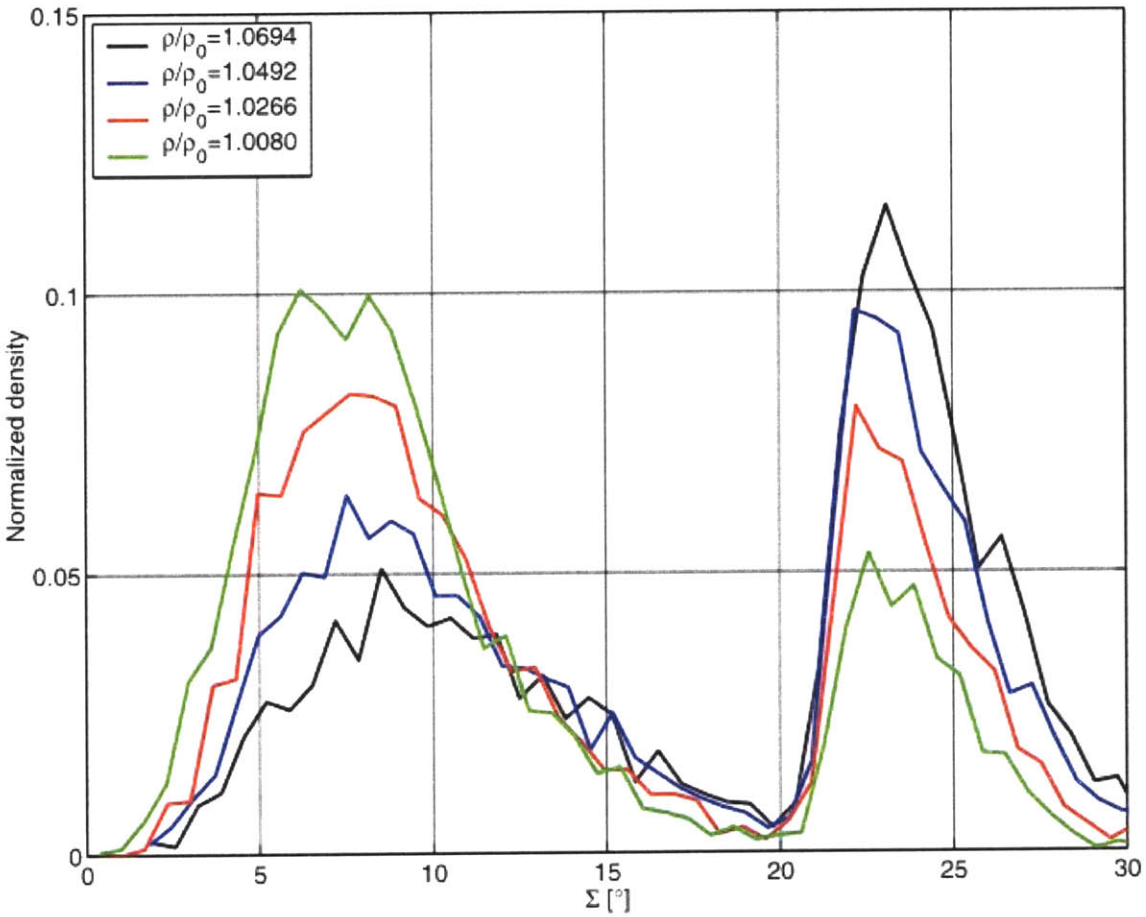

Figure 6-2: The distributions of standard deviations Σ_i (equation 6.2a) of nearest-neighbor bond angles for the atomic environments in a-Si systems of differing densities are bimodal. Systems of differing densities exhibit different relative peak heights, but no shift in the peak positions or abatement of bimodality.

Plotting M_i and Σ_i against each other for all 4096 atoms in a typical a-Si system shows in figure 6-3 that the two quantities are correlated. In particular, the distribution peaks in figures 6-1 and 6-2 are made up of contributions from the same atomic environments. The characterization of local structure of atomic environments based on the values of M_i and Σ_i therefore allows for their separation into two distinct types, which—for reasons explained below—were named "solidlike" and "liquidlike," following the terminology introduced by Cohen and Grest [Cohen, Grest, 1979].

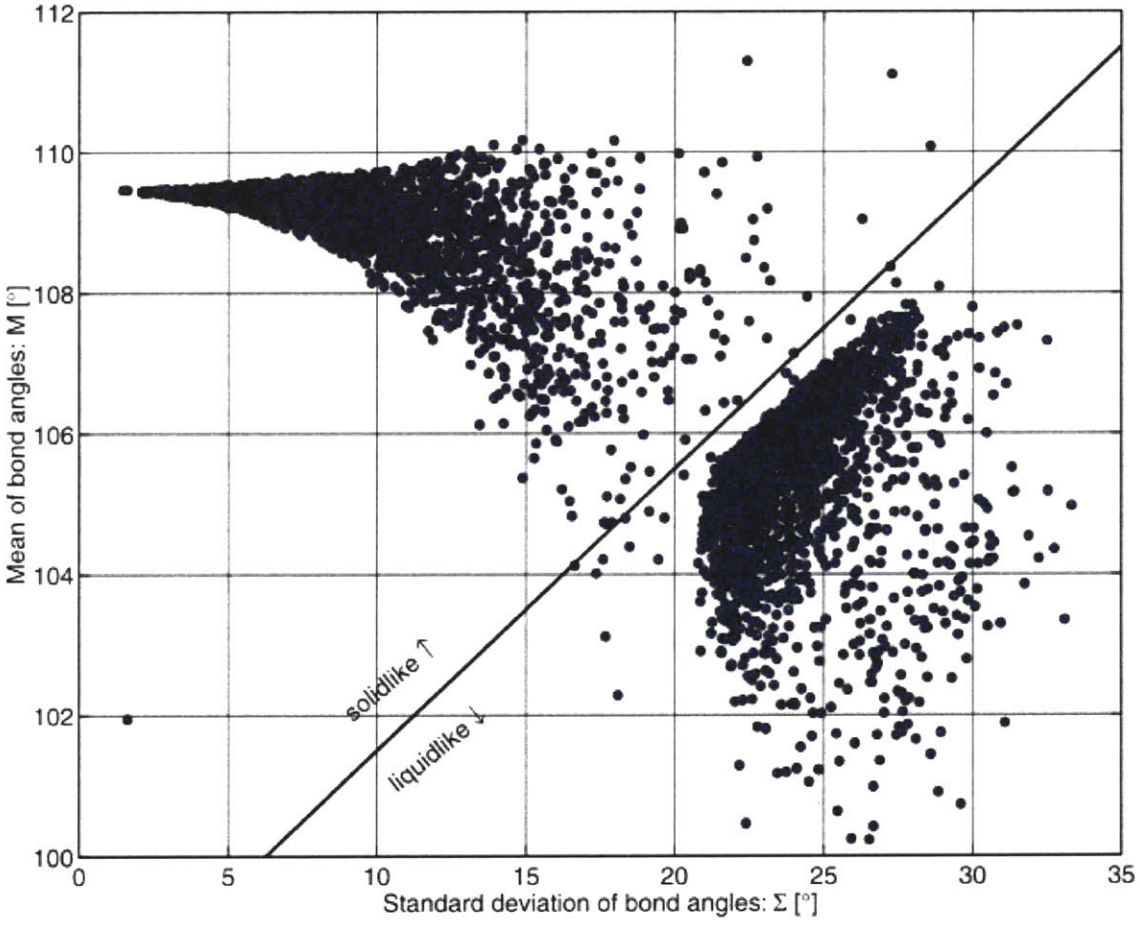

Figure 6-3: Atomic environments in a-Si are naturally separated into two distinct types based on clustering in the means M_i (equation 6.1a) and standard deviations Σ_i (equation 6.1b) of the nearest neighbor bond angles that surround them.

6.3 Properties of the two atomic environments

Once all atomic environments in an a-Si system have been classified by the above analysis, they could be viewed—for all practical purposes—as two separate species, each with well-defined physical properties. Furthermore, when the number of liquidlike and solidlike atomic environments in a given a-Si system is known, a unique mass fraction of each environment in that system can then be defined: it is simply the ratio of the number of atoms with that environment to the total number of atoms in the system. Moreover, since there are only two unambiguously distinguishable atomic environments in a-Si the sum of their mass fractions must equal unity. Consequently, the "composition" of each a-Si system can be summarized by the mass fraction of just one of the environments. It will be convenient—for reasons addressed in chapter 7—to choose the mass fraction of liquidlike atomic environments ϕ as such a descriptor. Figure 6-4 shows that there is an approximately linear dependence of ϕ in as-quenched a-Si systems on their densities.

Given that such properties as coordination, excess enthalpy, and isotropic elastic constants exhibit an approximately linear dependence on system density (see section 5.5) it is clear that they also exhibit a corresponding linear dependence on ϕ. The composite properties of a-Si systems with a given ϕ thus arise from the rule of mixtures applied to the properties of liquidlike and solidlike atomic environments alone. More precise determinations of composite properties are the aim of homogenization theory [Torquato, 2002].

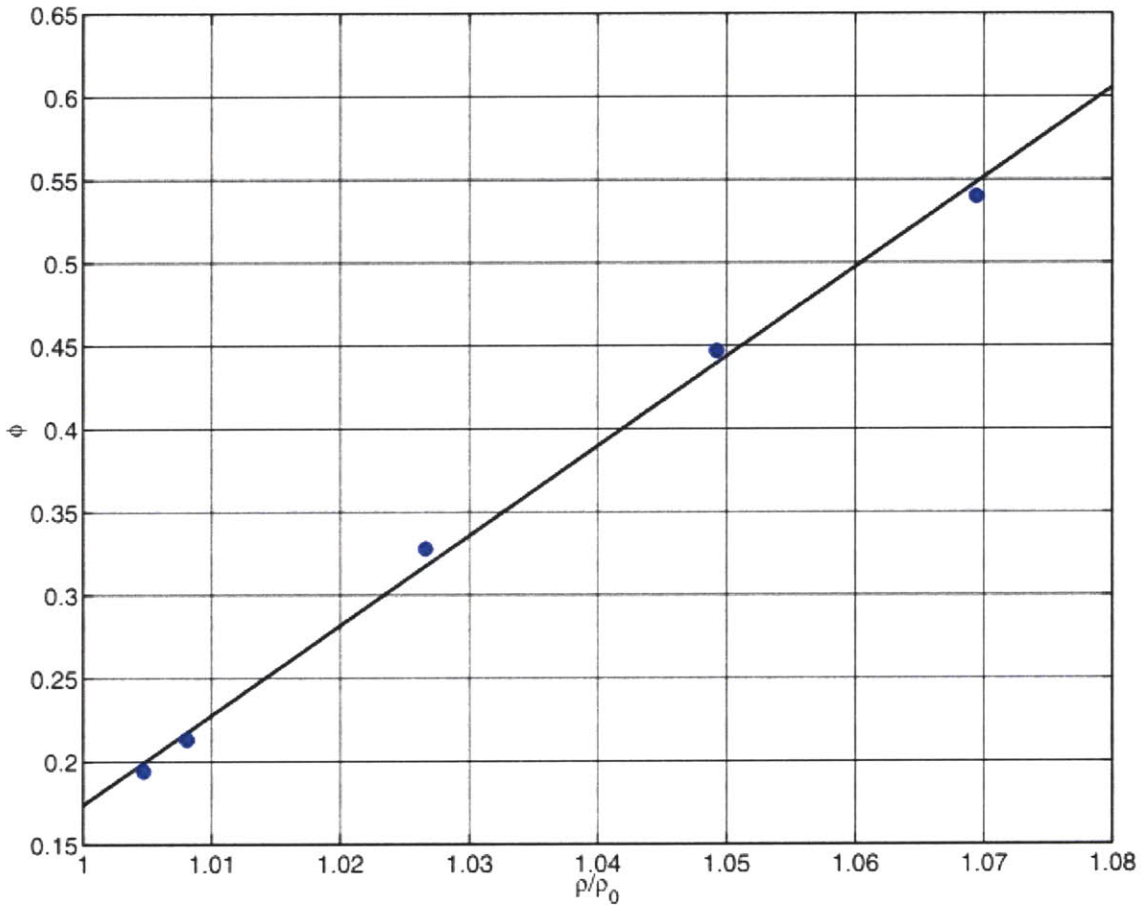

Figure 6-4: The mass fraction ϕ of liquidlike atomic environments present in variously quenched a-Si systems depends approximately linearly on their relative density ρ/ρ_0 : $\phi \approx 5.40 \cdot (\rho/\rho_0) - 5.22$. The density of SW c-Si at zero temperature and pressure is $\rho_0 = 2323.8\, kg/m^3$.

6.3.1 Radial and angular distribution functions

Both the RDFs and ADFs can be found for the two atomic environments distinguished in section 6.2. This determination was accomplished in this study by accumulating separately the contributions of solidlike and liquidlike atomic environments to the overall system RDF and ADF. To approximate the RDFs and ADFs for "pure" solidlike a-Si and liquidlike a-Si, contributions were considered only from those atomic environments whose nearest neighbor atoms had atomic environments of the same type. The results are presented in figures 6-5 through 6-8 and immediately indicate why the two types of atomic environment were termed "solidlike" and "liquidlike": inspection of their RDFs and ADFs indicates that one has a structure that resembles that of molten Si while the other more closely resembles diamond cubic silicon (especially in the ADF).

The RDFs in figure 6-5 shows that the atomic environment termed "solidlike" exhibits a sharply defined nearest neighbor distance as well as unambiguous second nearest neighbor shell. The ADF in figure 6-6 further reinforces the solidlike character of this atomic environment: it appears to be no more than a broadened version of the ADF for diamond cubic crystalline silicon. Figure 6-7 exhibits the RDF for liquidlike a-Si. Unlike the RDF in figure 6-5, its nearest neighbor distance is not very sharply defined as can be seen from the rather shallow depth of the "trough" between the nearest neighbor peak and the next peak. Furthermore, the second nearest neighbor shell in figure 6-7 exhibits a stark lack of definition: it comprises two peaks separated by a shallow trough. The ADFs for both liquid and liquidlike a-Si (figure 6-8) show a marked deviation from the unimodal distribution about the tetrahedral angle of the diamond cubic configuration apparent in figure 6-6. The RDFs and ADFs for liquidlike atomic environments in a-Si bear significantly greater similarity to the RDFs and ADFs for molten silicon than to that of crystalline silicon. Nevertheless, some important differences are apparent. The RDF for molten Si does not exhibit any troughs between the first and second nearest neighbor shells nor does it show the shorter-distance peak of the two split peaks of the second nearest neighbor shell. Similarly, the ADF for liquid silicon exhibits no troughs, but that of liquidlike a-Si does at an angle of about 60 degrees.

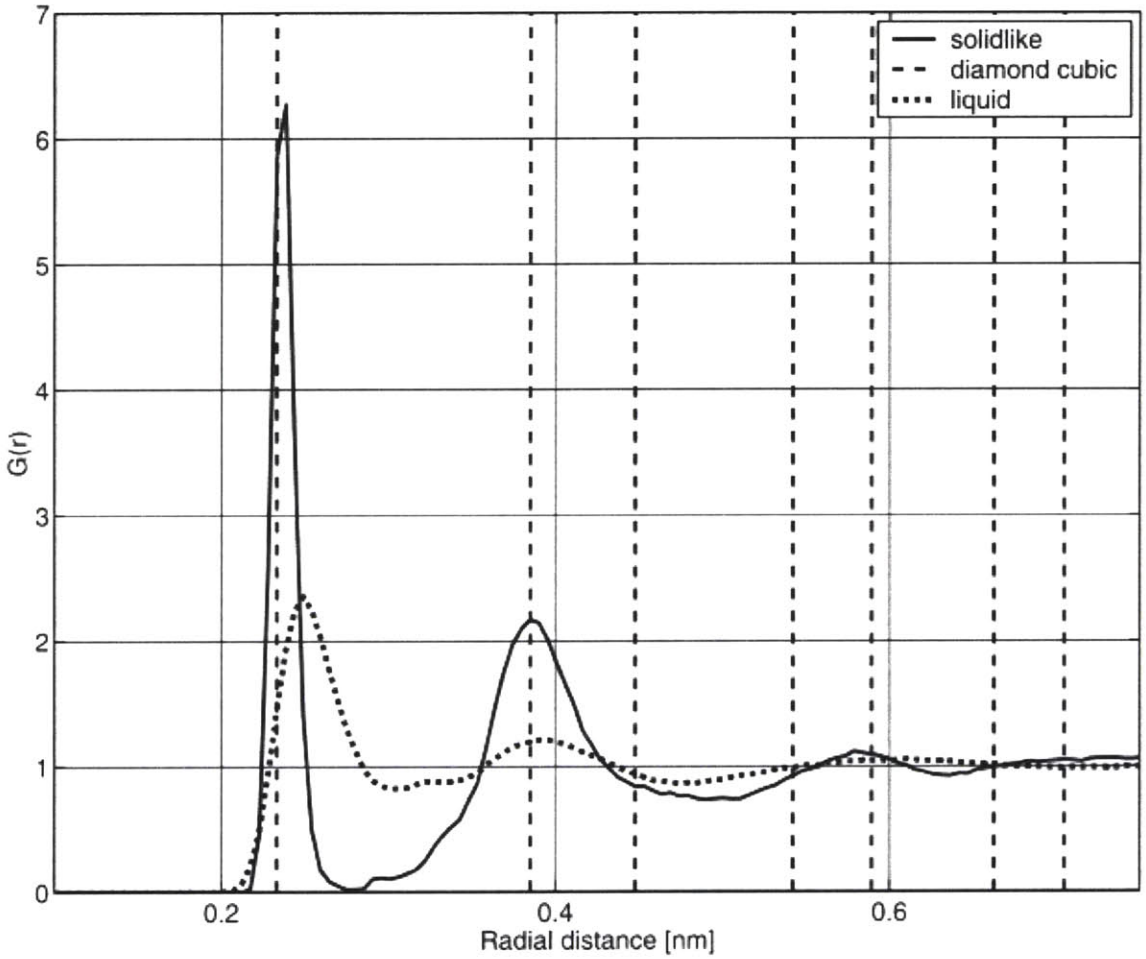

Figure 6-5: Comparison of RDFs for the solidlike atomic environment of a-Si, diamond cubic c-Si, and liquid Si.

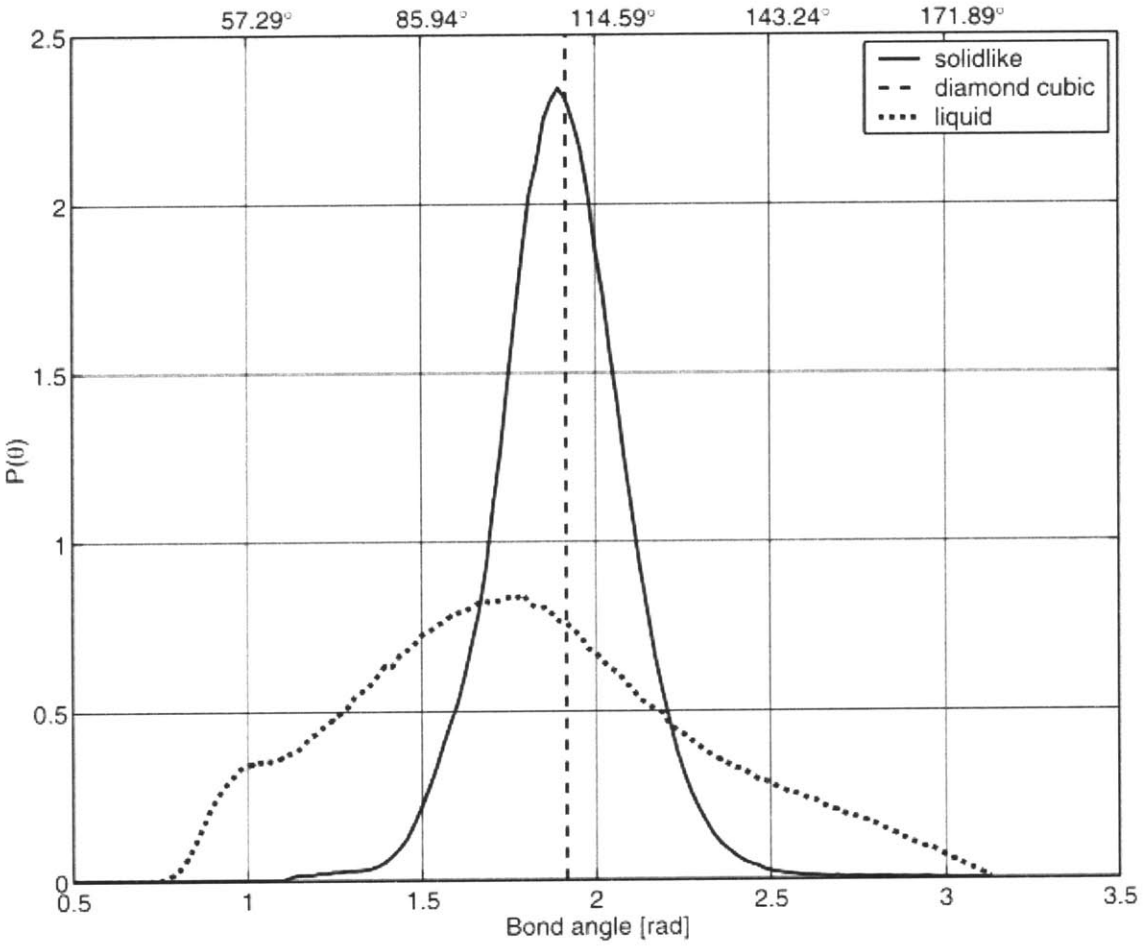

Figure 6-6: Comparison of ADFs for the solidlike atomic environment of a-Si, diamond cubic c-Si, and liquid Si.

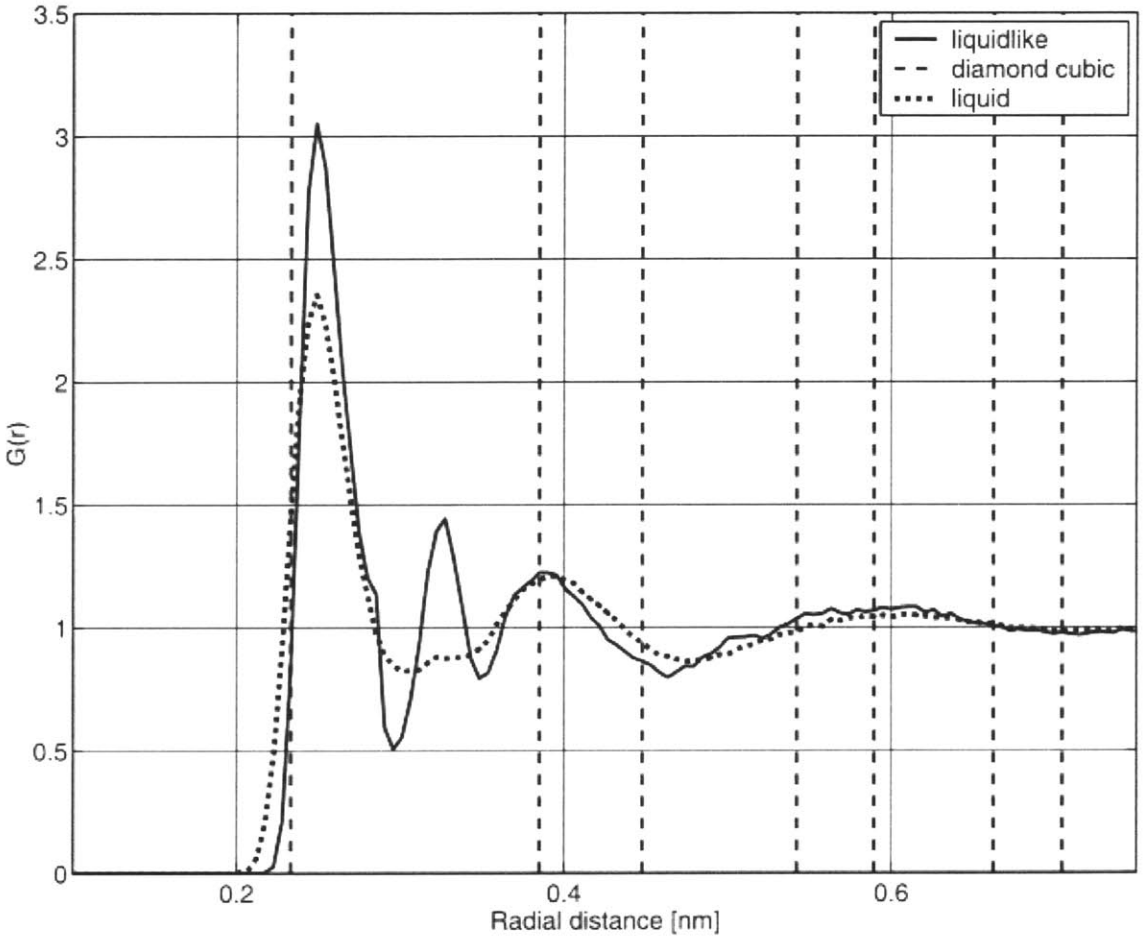

Figure 6-7: Comparison of RDFs for the liquidlike atomic environment of a-Si, diamond cubic c-Si, and liquid Si.

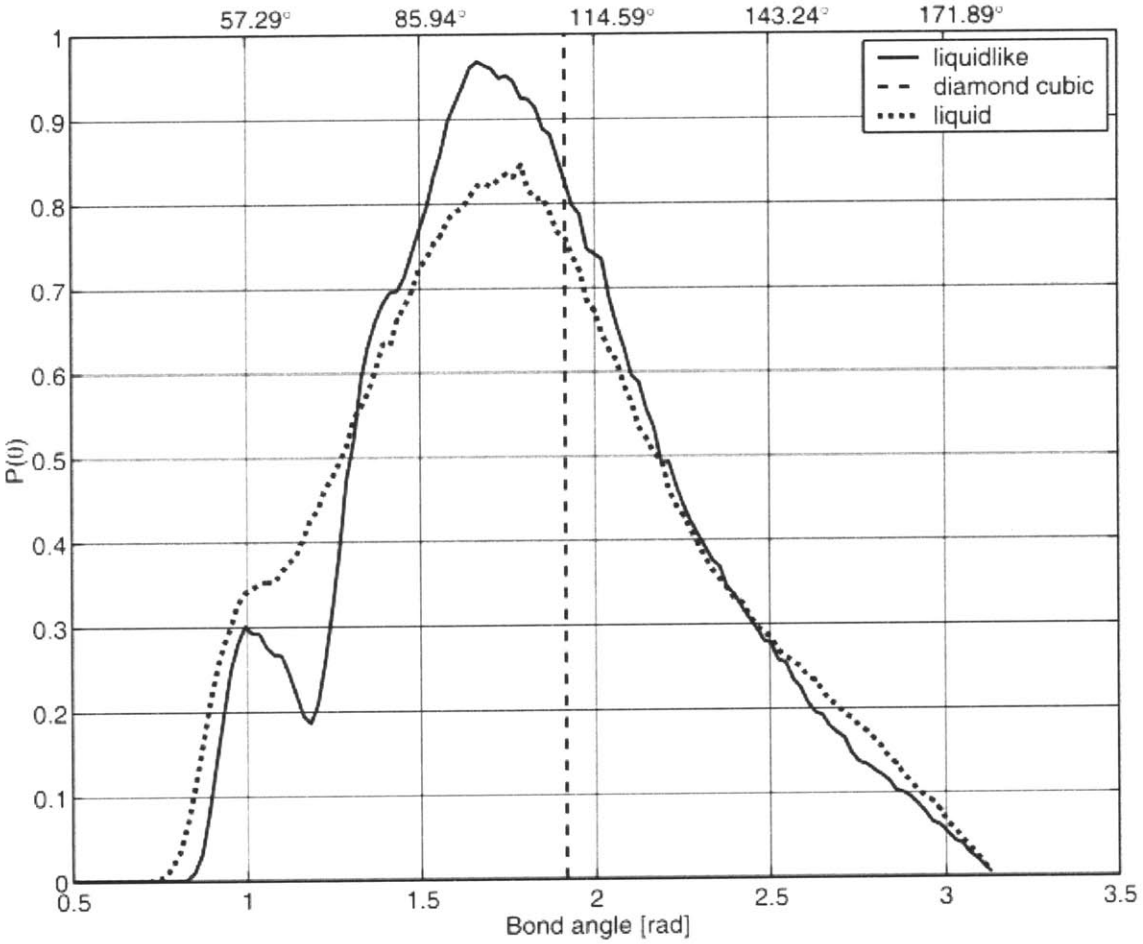

Figure 6-8: Comparison of ADFs for the liquidlike atomic environment of a-Si, diamond cubic c-Si, and liquid Si.

6.3.2 Densities, average coordinations, and binding energies

The "liquidlike" and "solidlike" character of the two distinct atomic environments found in a-Si is further reinforced by their average densities, coordinations, as well as two-body and three-body contributions (see section 3.2.1) to atomic binding energies, presented in Table 6-1. Each of these quantities is in close agreement for diamond cubic c-Si and solidlike a-Si as well as for liquid Si and liquidlike a-Si.

	Diamond cubic Si (T=0K)	Liquid Si (T=1690K≈T_m)	Solid-like a-Si (T=300K)	Liquid-like a-Si (T=300K)
Coordination	4	5.13±0.86	4.00±0.06	4.97±0.40
Density	2324 kg/m^3	2386 kg/m^3	2256 kg/m^3	2554 kg/m^3
E_b 2-body	-8.67 eV	-9.93±0.95 eV	-8.82±0.37 eV	-10.45±0.52 eV
E_b 3-body	0 eV	3.60±1.21 eV	0.91±0.54 eV	4.16±0.89 eV

Table 6-1: Comparison of diamond cubic c-Si and liquid Si with solidlike a-Si and liquidlike a-Si via their average coordinations, densities, and 2-body and 3-body contributions to atomic binding energies (E_b).

6.3.3 Distribution throughout the system

The distribution of each environment throughout the simulation cell was studied using standard two-point correlation functions [Torquato, 2002], the coarseness characterizer of Lu and Torquato [Lu, Torquato, 1990], autocorrelations like those used in the study of surface morphology [Rasigni *et al.*, 1983], and various cluster shape measures [Theodorou, Suter, 1985a]. In the course of these studies, no evidence was ever found for nonhomogeneity or anisotropy in the distribution of these two atomic environments. A coherence length for each environment spanning approximately two interatomic distances was the only form of nonuniformity that was observed. In particular, neither of the two types of atomic environments exhibited any tendency to cluster into phase domains. These conclusions are confirmed by direct visualizations of the distribution of liquidlike and solidlike atomic environments in a-Si configurations. Figure 6-9 shows two such visualizations for systems of differing ϕ.

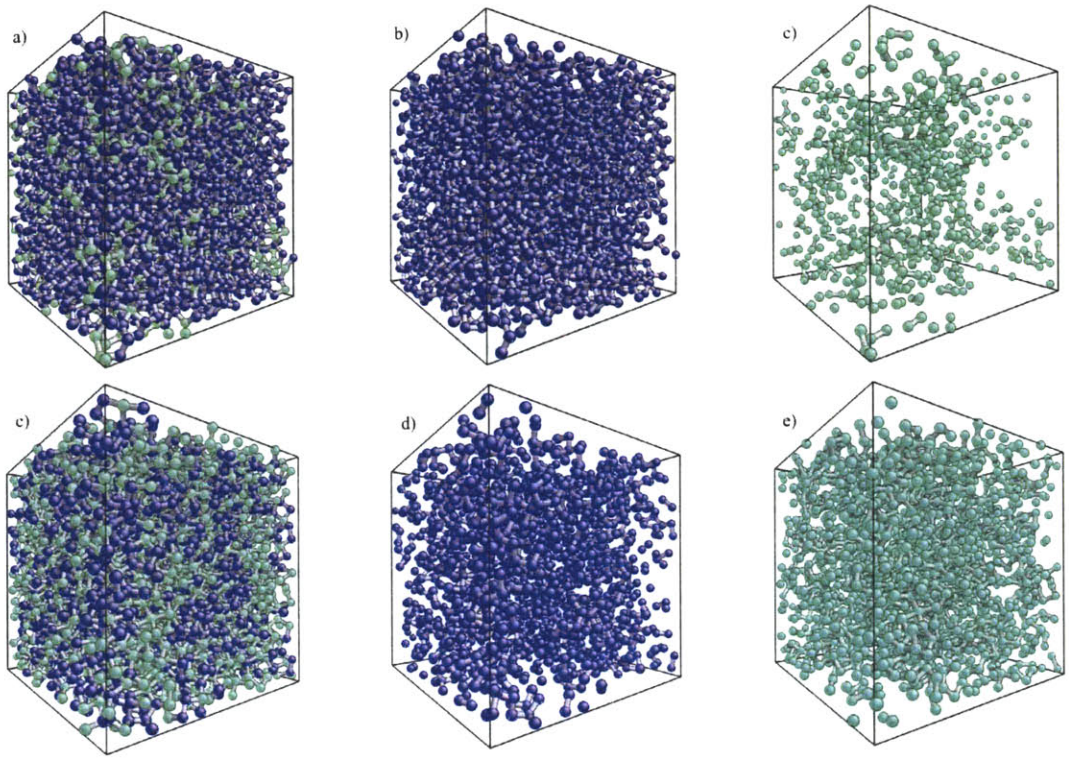

Figure 6-9: Visualizations of the composition of two a-Si systems in terms of solidlike (dark) and liquidlike (light) atomic environments are shown above. Frames (a), (b), and (c) respectively show all atomic environments, only the solidlike ones, and only the liquidlike ones for a system with specific density $\rho/\rho_0 = 1.008$. Frames (d), (e), and (f) are the corresponding depictions for a system with $\rho/\rho_0 = 1.069$. As expected, the denser system has a higher liquidlike mass fraction ϕ. These visualizations illustrate that the distribution of solidlike and liquidlike atomic environments in as-quenched a-Si systems is uniform and isotropic.

6.4 Relation to existing models of amorphous materials

It must be stressed that both the solidlike and liquidlike atomic environments are forms of solid amorphous Si. The solidlike form lacks long-range order despite a short-range resemblance to the diamond cubic structure. The liquidlike form bears a structural similarity to molten silicon, but it is nonetheless vitrified. Furthermore, precedents for glassy materials whose structures resemble either the solidlike or liquidlike atomic environments in a-Si already exist in the literature [Zallen, 1979]. Specifically, the

solidlike atomic environment is well described as a continuous random network (CRN) [Zachariasen, 1932]. This model was originally proposed for oxide glasses and claims that the nearest-neighbor environment of each atom is topologically the same as it would be in its crystalline configuration. An immediate consequence of this description is that the average coordination of atoms in a CRN must be the same as that of the crystal, as is indeed the case for solidlike a-Si (Table 6-1). Long-range order is lost in the CRN model primarily due to variations in nearest-neighbor bond angles, but not in nearest-neighbor bond lengths, which are thought to be too stiff to undergo significant changes. The RDF and ADF for the solidlike atomic environment (figures 6-5 and 6-6) agree with these assumptions.

The liquidlike atomic environment of a-Si, on the other hand, bears certain characteristic features of dense random packing (DRP) [Cargill, 1975]. Specifically, its short-range atomic ordering differs topologically from that of c-Si, as evidenced by its on-average higher and broadly distributed coordination number (Table 6-1). The broadened nearest neighbor peak in the RDF and wide distribution of nearest-neighbor bond angles in the ADF (figures 6-7 and 6-8) for liquidlike a-Si reinforce this conclusion. The DRP model, however, bears a close resemblance to the arrangement of atoms in a metallic or hard-sphere liquid [Bernal, 1964], with the notable exception that the DRP exhibits a split peak in the second nearest-neighbor shell while simple liquids have just one smooth second nearest neighbor peak [Allen, Tildesley, 2000]. These characteristics are perfectly mirrored in the relation of liquidlike a-Si to liquid Si (figure 6-7). Of course the liquidlike a-Si environment is not strictly a dense random packing: the DRP model was originally developed to describe ball bearing packings and metallic glasses, both of which generally have close-packed crystalline structures (coordination of 12) and disordered states with average coordinations around 11. It is amazing, therefore, that the other characteristics of DRP described above hold so well for liquidlike a-Si, whose average coordination is close to 5 (Table 6-1). This agreement suggests that the crucial link between DRP and liquidlike a-Si is their relation to the structure of the corresponding molten state of the material each aims to represent.

7. Deformation of a-Si at T=300K by MD

This section describes the spectrum of plastic flow behaviors exhibited by a-Si systems of differing densities under both constant volume and constant pressure deformation. It is shown that the mass fraction of liquidlike atomic environments ϕ can be viewed as a plasticity carrier in a-Si. This view is supported by cyclic loading and annealing simulations.

7.1 Constant volume deformation

The mechanical behavior of a-Si was probed by deforming four selected systems from their initial as-quenched state to large strain, i.e. to strains much larger than the initial yield strain. Each of these systems had a different density, correlated to the rate of quenching used to create it, as described in section 5.5. Deformation was carried out at constant volume as described in section 3.1.2 using MD simulation at a temperature of 300K: well below the glass transition temperature of 950K, i.e. in the regime of low-temperature plasticity [Argon, 1996b].

7.1.1 Mechanical response

The stress-strain and pressure-strain curves obtained from the deformation simulations at constant volume are shown in figures 7-1 and 7-2. They exhibited considerable jerkiness due to the discrete nature of the atomic structure rearrangements responsible for plasticity and the small size of the simulation cell. Averaging of stress-strain curves from many deformation simulations of systems with similar densities and quenching histories smoothes out this jerky response while reinforcing general deformation characteristics like the level of yield and steady-state flow stress. The smoothness of stress-strain curves obtained experimentally through the study of

macroscopic systems is a consequence of such ensemble averaging of discrete atomic-level events.

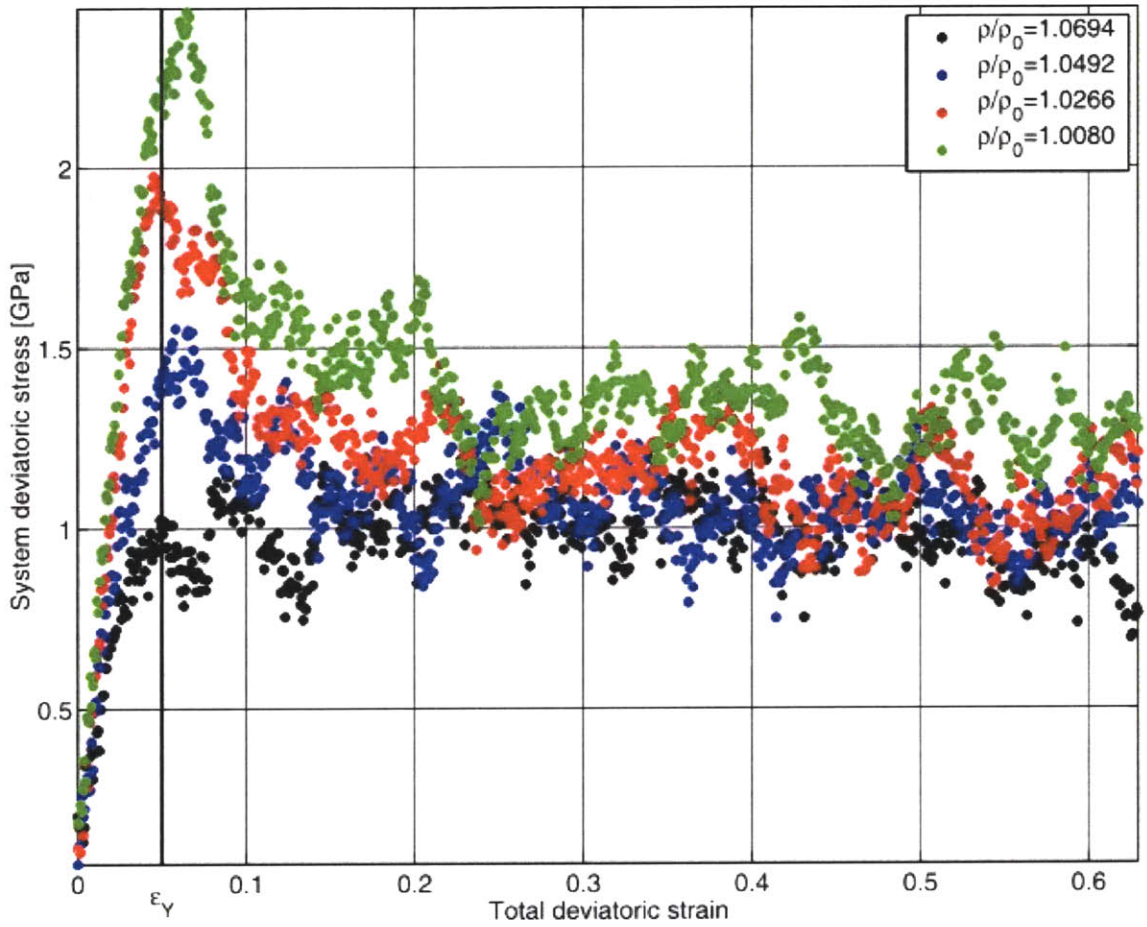

Figure 7-1: The variation of system deviatoric stress $\bar{\sigma}(\hat{\mathbf{o}})$ as a function of the deviatoric component of the total externally applied strain $\bar{\varepsilon}(\mathring{\mathbf{a}})$ for four a-Si structures of differing densities undergoing large-strain plastic flow under constant volume.

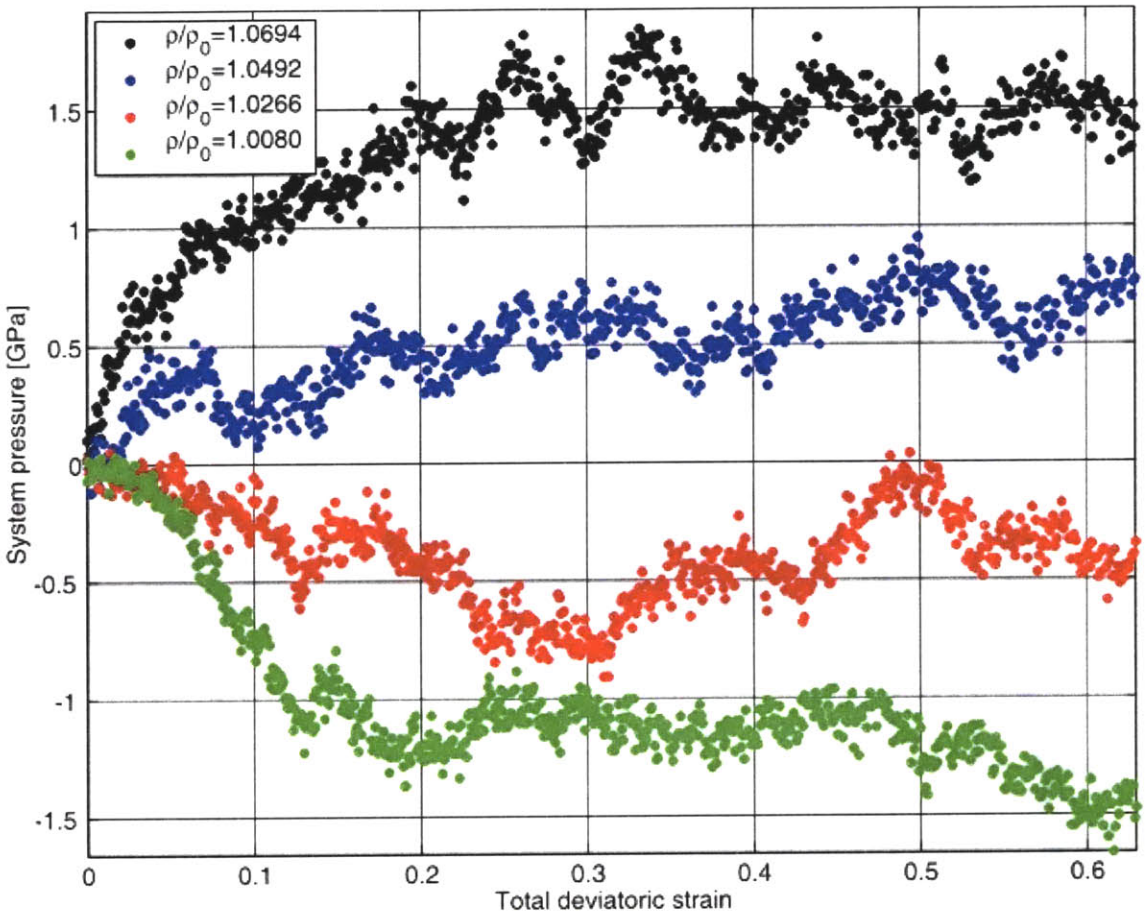

Figure 7-2: The variation of system pressure $p(\hat{\mathbf{o}})$ as a function of the deviatoric component of the total externally applied strain $\bar{\varepsilon}(\mathring{\mathbf{a}})$ for four a-Si structures of differing densities undergoing large-strain plastic flow under constant volume.

Deformation of as-quenched structures of differing densities shows that the character of plastic behavior is crucially dependent on system density. For the system of lowest density, three significant features of deformation behavior are immediately discernable. First, elastic loading (albeit nonlinear) terminates with a sharp yield phenomenon. Second, initial yield is followed by significant strain softening (figure 7-1). Third, plastic deformation is accompanied by a dramatic drop of system pressure well below zero (figure 7-2). The first two of these three phenomena have also been observed in simulations [Bulatov, Argon, 1994; Falk, Langer, 1998] and experiments [Safarik *et al.*, 2005] on aged metallic glasses but the third is entirely novel. The pressure drop

during deformation at constant volume corresponds to volume contraction in constant pressure deformation and stands in stark contrast to the behavior of metallic glasses, which expand during deformation. Figure 7-1 also shows that no well-defined yield point is observed for high enough initial densities.

Furthermore, high-density systems do not exhibit the pressure drop apparent in the deformation behavior of low-density systems. Instead, their pressure increases drastically, corresponding to a system dilatation under constant pressure. Unlike in metallic glasses where the pressure and deviatoric stress attain steady state at the same strain, the pressure in these dense structures stabilizes at higher strain than does the deviatoric stress.

7.1.2 Atomic-level structure evolution

The behavior described above suggests that a-Si systems undergo some structural evolution as they deform. First, the strain softening and pressure drop of systems with low initial density indicates a gradual transition to a denser, easily flowing state. Lack of sharp yielding for initially dense systems reinforces the view that denser structures flow more easily. Meanwhile, the prolonged change in pressure during deformation of these systems indicates that in the flow state, kinetic equilibrium is established between structural components of varying density. All of these changes are well described by the separation of a-Si into solidlike and liquidlike atomic environments (chapter 6).

Figure 7-3 shows the change in ϕ during deformation of the four a-Si systems of different densities. Each structure starts out with a different liquidlike fraction that changes during deformation and levels off when steady state flow is reached. The smallest initial fraction of liquidlike atomic environments is found in the best-annealed structures and increases in the course of strain softening, in agreement with the observed drop in pressure in those structures (the liquidlike environment is denser than the solidlike one; section 6.3.2). Increasing volume fractions of liquidlike component can therefore be associated with decreasing resistance to plastic flow of a-Si structures. Conversely, structures with low liquidlike fractions can be expected to exhibit a high initial resistance to plastic flow.

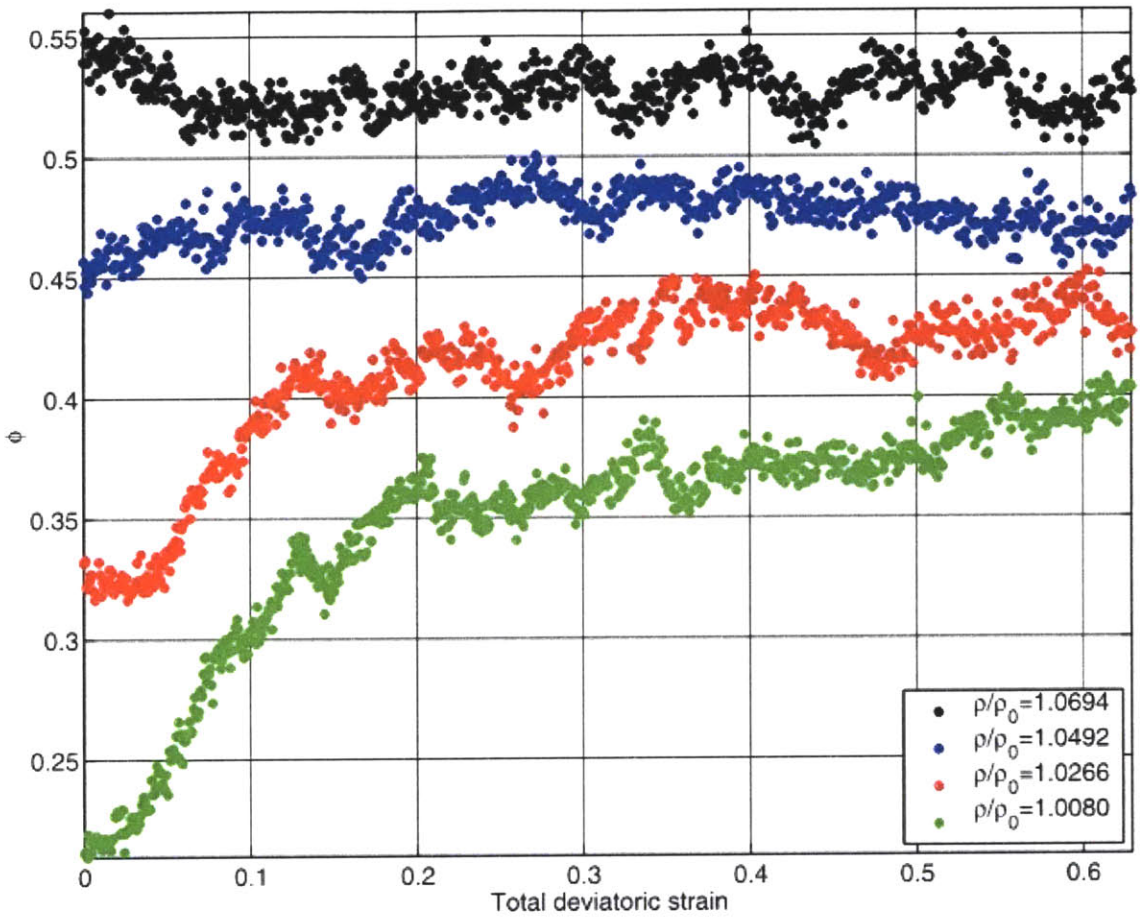

Figure 7-3: The variation of system liquidlike mass fraction ϕ as a function of the deviatoric component of the total externally applied strain $\bar{\varepsilon}(\text{å})$ for four a-Si structures of differing densities undergoing large-strain plastic flow under constant volume.

7.1.3 Localization of structure changes

Figure 7-3 demonstrates that the attainment of steady state flow requires that structure transformations take place between the solidlike and liquidlike atomic environments. Some insight into the character of these transformations can be gained by visualizing the regions within deformed a-Si systems that have undergone transformations in the type of their atomic environments (from solidlike to liquidlike or vice versa) during the course of plastic flow. Figure 7-4 shows that during plastic deformation of an a-Si system with an initially high value of ϕ there appears not to be any tendency for atomic environment structure transformations to localize exclusively

within any particular region of the simulation cell. In that system, therefore, the distribution of liquidlike and solidlike environments remains uniform. In the case of an a-Si system with an initially low ϕ, however, these transformations occur predominantly within a relatively distinct plane spanning the simulation cell and oriented along a direction of maximum resolved shear stress, as figure 7-5 demonstrates. The rising proportion of liquidlike mass fraction therefore is not uniformly distributed throughout this system. There should, however, exist a length scale sufficiently short such that the distribution of liquidlike environments across it can be considered approximately uniform on average. A unique average local flow stress as a function of ϕ would then exist for chunks of a-Si material of such characteristic length.

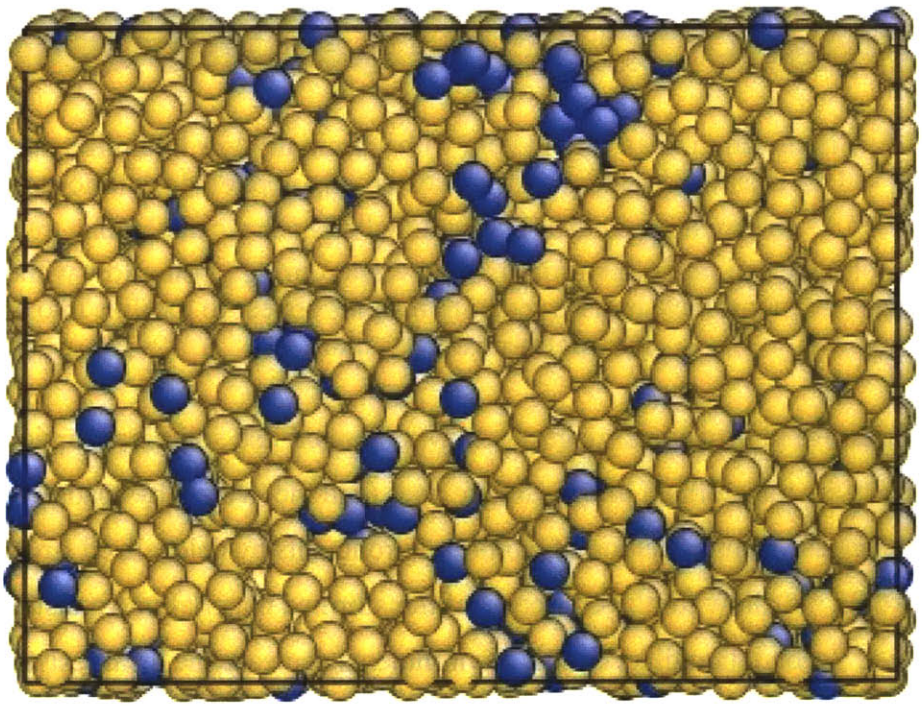

Figure 7-4: Visualization of an a-Si system with an initially high liquidlike mass fraction of ϕ = 0.55 after deformation to a total externally applied deviatoric strain of $\bar{\varepsilon}(\text{å}) = 0.12$. The environments of light-colored atoms have undergone transitions between solidlike and liquidlike form (or vice versa) during plastic flow while those of the dark-colored atoms have not. Structure transitions appear to be distributed homogenously.

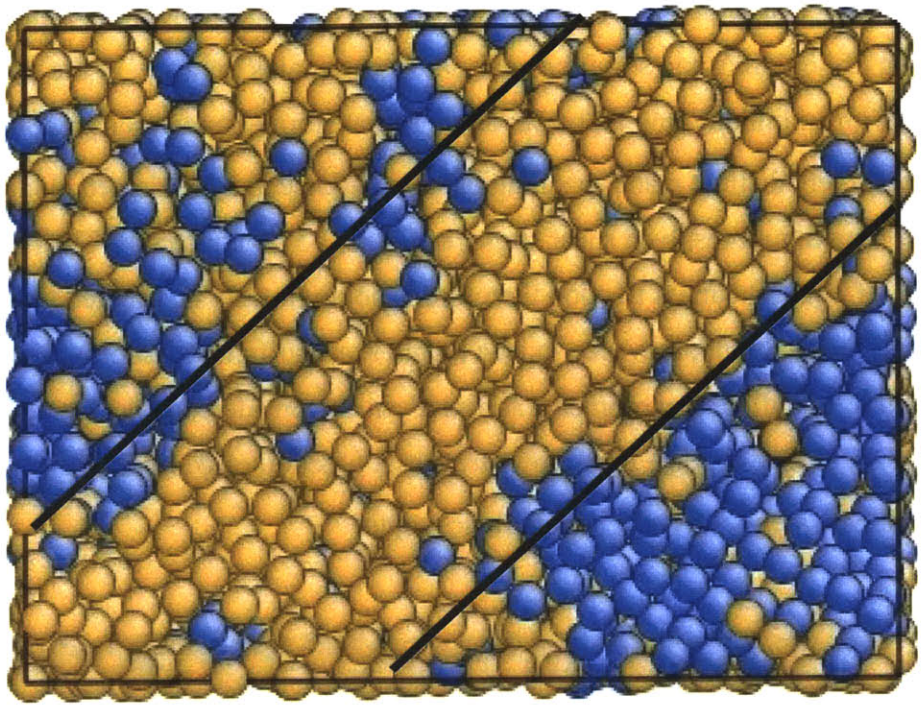

Figure 7-5: Visualization of an a-Si system with an initially low liquidlike mass fraction of $\phi = 0.22$ after deformation to a total externally applied deviatoric strain of $\bar{\varepsilon}(\text{å}) = 0.12$. The environments of light-colored atoms have undergone transitions between solidlike and liquidlike form (or vice versa) during plastic flow while those of the dark-colored atoms have not. Structure transitions appear to localize into a relatively well-defined zone, as indicated.

The above observations suggest two hypotheses. First, solidlike atomic environments are transformed into liquidlike ones (and vice versa) by spatially localized structure changes. Transformation of atomic environments by delocalized structure changes would not allow for the clustering of transformed material into a distinct zone, as in figure 7-5. Second, liquidlike atomic environments decrease the local resistance of a-Si to plastic flow. Structure transformations occur preferentially within the distinct zone of figure 7-5 because a higher ϕ has been created there as a result of previous transformations while the material outside that zone is locally more resistant to plastic flow. On the other hand, there are enough liquidlike environments initially distributed throughout the system in figure 7-4 to enable structure transformations to initiate practically anywhere. These two hypothesis are essentially concerned with the existence

and character of discrete mechanisms of plastic flow in a-Si and the local conditions of its onset. They are addressed in detail in chapter 8.

7.2 Unloading and annealing

Based on the above observations, mass fractions of liquidlike component ϕ can be viewed as "plasticity carriers" for a-Si in analogy with dislocation densities in c-Si [Alexander, Haasen, 1968]. For this comparison to hold, however, it is necessary that annealing "ages" the structure, making it more resistant to initiation of plastic flow while plastic deformation "rejuvenates" it, making it more amenable to plastic flow. To probe this issue, an initially well-relaxed a-Si structure has been plastically deformed to high strain, allowing it to develop a significant liquidlike mass fraction ϕ as shown in figure 7-6. This a-Si system was then plastically deformed back to its initial configuration by straining it in the reverse direction to that of initial loading. Figure 7-7 demonstrated that because the system contained a high liquidlike mass fraction at the beginning of reverse deformation, it did not exhibit a yield phenomenon, confirming that its internal atomic arrangement has indeed been "rejuvenated."

Upon returning to its original shape, the a-Si system was annealed for nearly 4ns at a temperature of 925 K—i.e. just below the glass transition temperature of 950 K—and slowly quenched. As illustrated in figure 7-8, most of the liquidlike mass fraction accumulated as a result of previous plastic deformation was thereby removed. Next, the system was once again plastically deformed to high strain. Figure 7-9 shows that the system then exhibited a distinct yield phenomenon along with strain softening and an increase in the liquidlike volume fraction. It may therefore be concluded that annealing does indeed age the a-Si structure, resulting in an increased resistance to plastic flow. The identification of the mass fraction of liquidlike atomic environments ϕ as the plasticity carrier for a-Si is therefore a valid mesoscopic description of the internal structure changes in a-Si during plastic deformation. It is a good candidate for an internal variable characterizing the state of the material in a possible continuum description of plasticity in a-Si [Anand, Gurtin, 2003; Anand, Su, 2005].

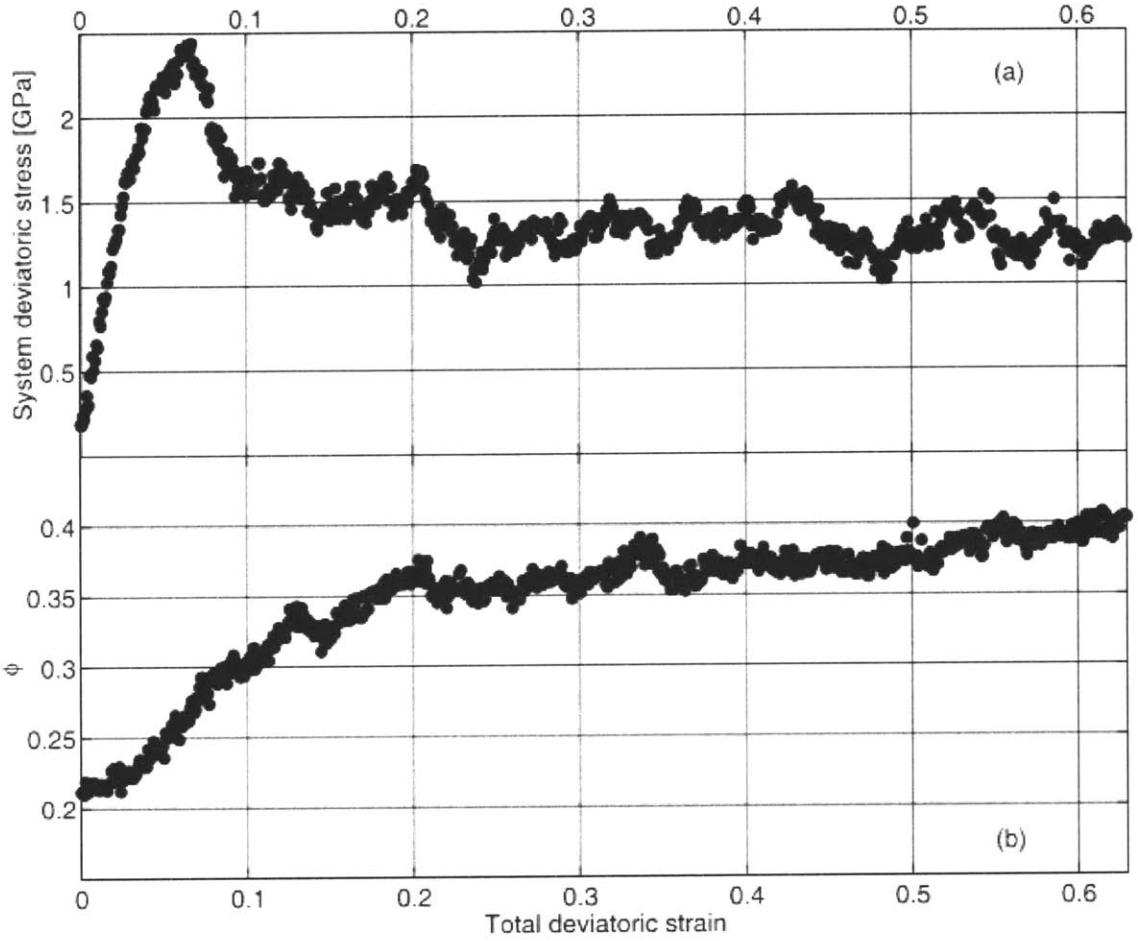

Figure 7-6: An initially well-annealed a-Si system has a low liquidlike mass fraction. It exhibits a distinct yield phenomenon and strain softens as the liquidlike mass fraction increases.

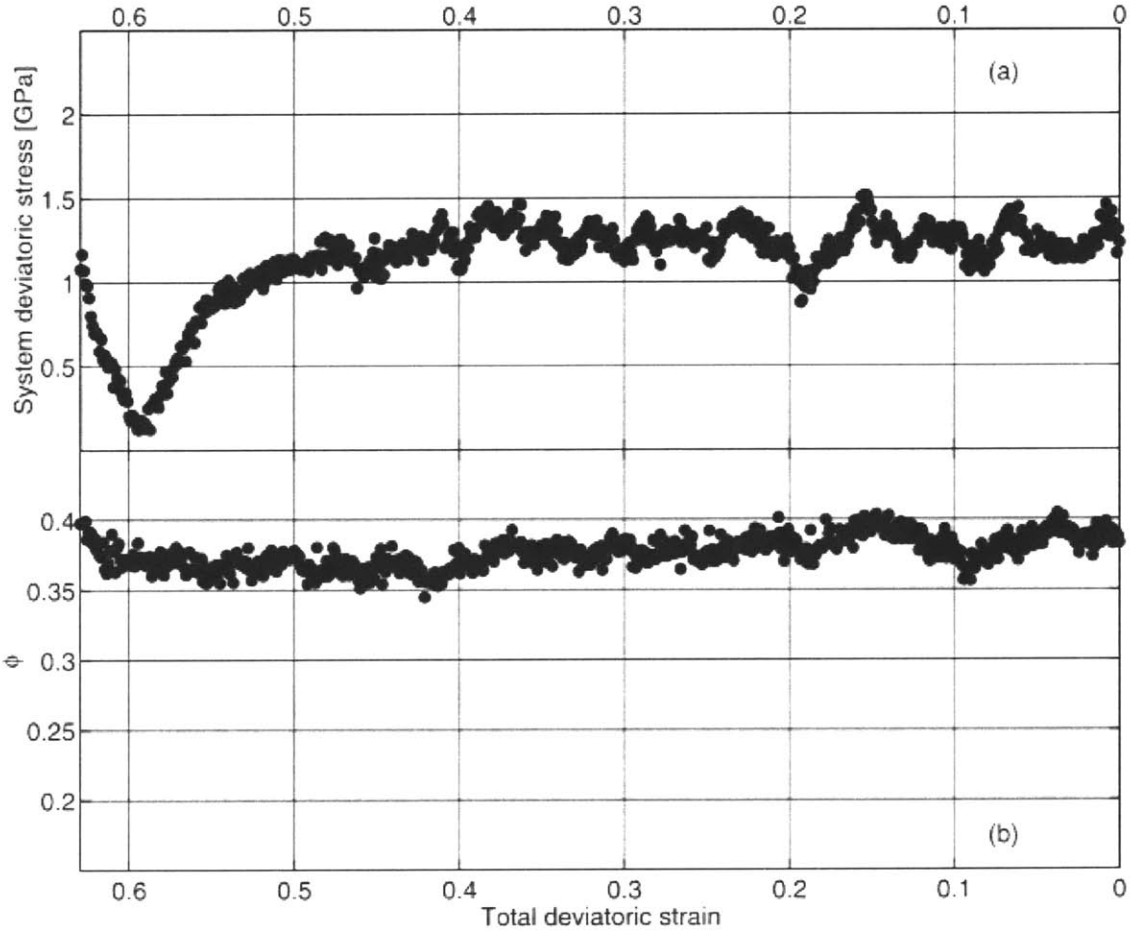

Figure 7-7: The deformed a-Si system from figure 7-6 has an initially high liquidlike mass fraction, created as a result of plastic deformation. Upon unloading, it did not exhibit a yield phenomenon or strain softening. The values of deviatoric stress in the dip observed upon deforming in the reverse direction are attributed to elastic unloading and reloading combined with a Bauschinger effect. Note that the deviatoric stress $\bar{\sigma}(\hat{\mathbf{o}})$ is an intrinsically positive quantity (section 4.1).

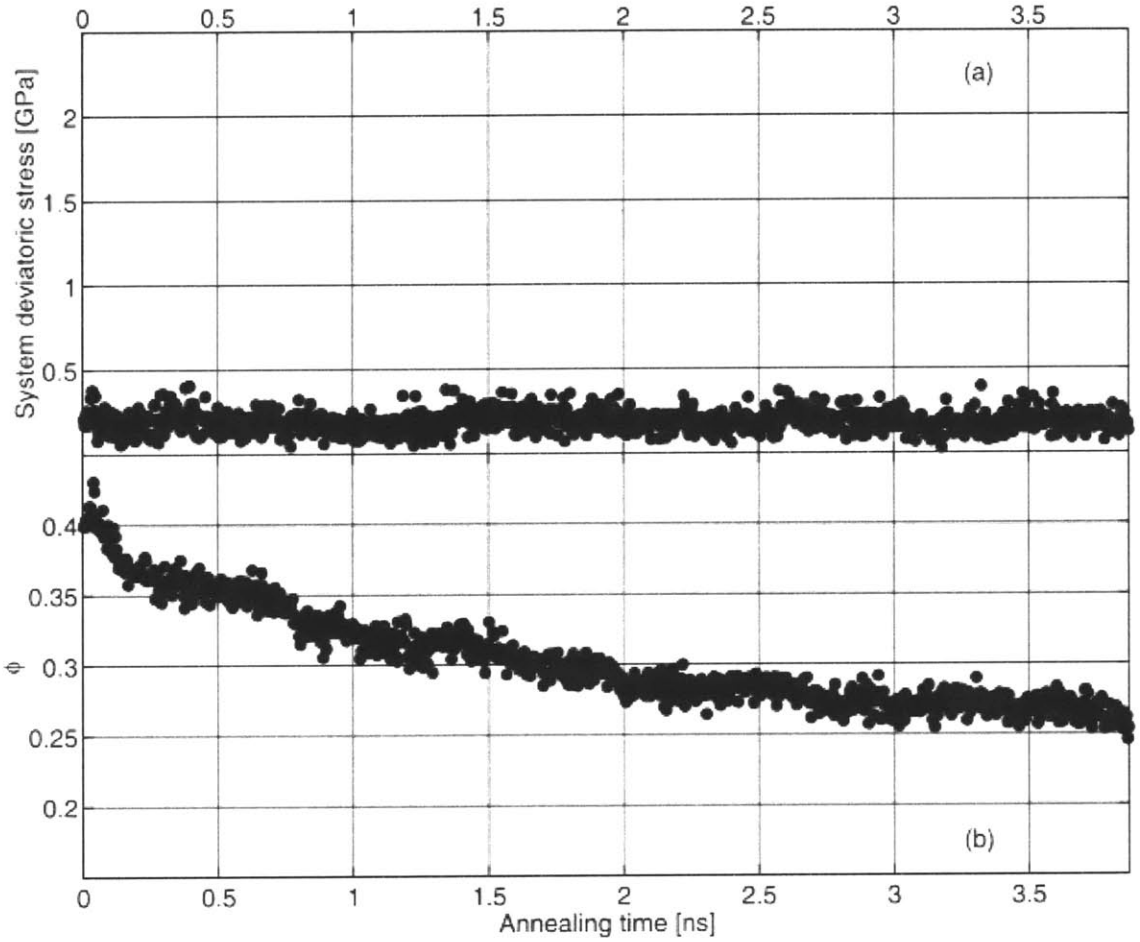

Figure 7-8: After the a-Si structure in figures 7-6 and 7-7 had been cyclically deformed it was annealed at 925K for nearly 4ns, removing much of the liquidlike mass fraction that had previously accumulated as a result of plastic deformation.

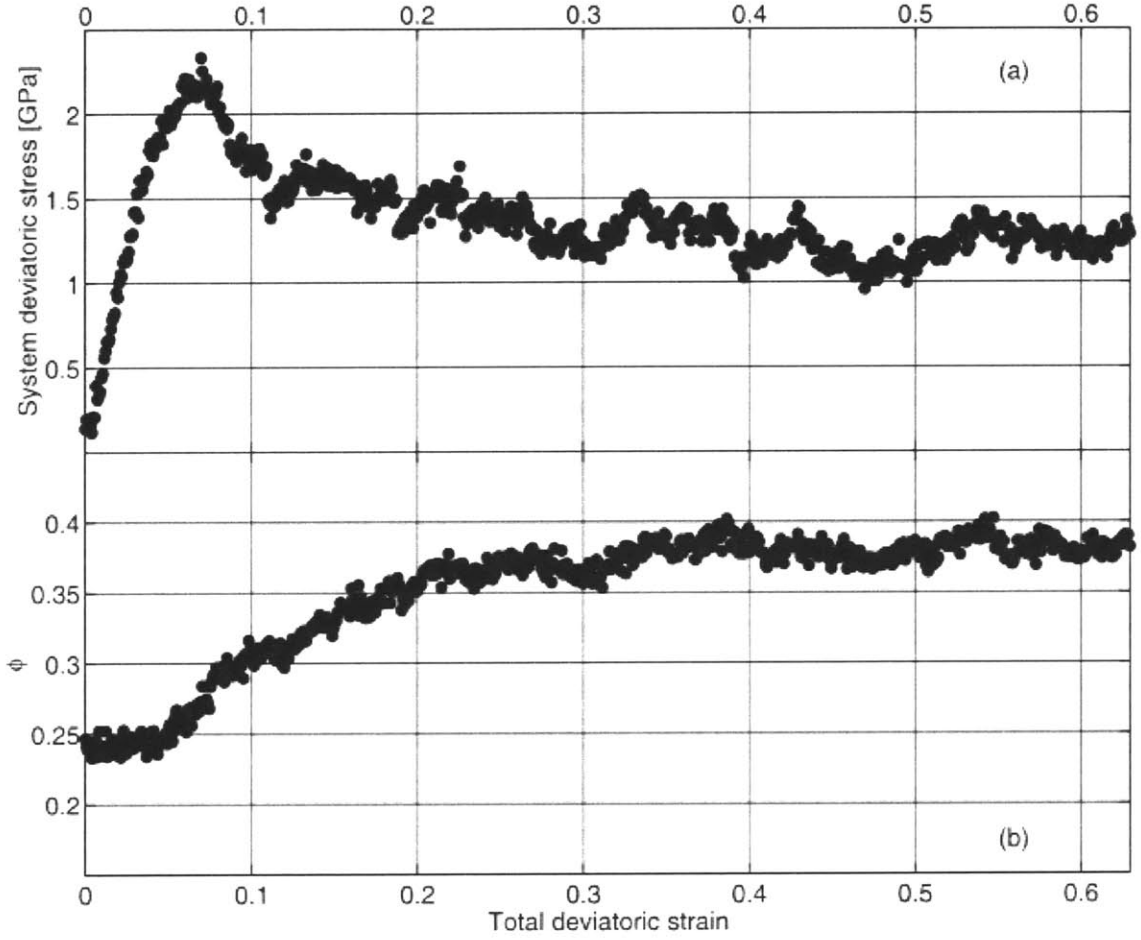

Figure 7-9: Once the liquidlike mass fraction of the a-Si system cyclically deformed in figures 7-6 and 7-7 was reduced by annealing (figure 7-8), the system once again exhibited a distinct yield phenomenon and strain softening accompanied by an increasing liquidlike mass fraction upon plastic deformation.

7.3 Constant pressure deformation

In the constant volume simulations of plastic flow presented in section 7-1, ϕ fails to converge to a unique value during steady state flow for the four density structures considered in this study (figure 7-3). This apparent discrepancy is removed when the possibility of direct dependence of mechanical properties on pressure is taken explicitly into account. In constant volume simulations, the system pressures are allowed to change. They converge to different steady-state values in the case of each of the four density structures considered (figure 7-2). Plastic deformation in these structures was therefore simulated once again, this time by MD at constant zero externally applied pressure (section 3.3), though also at a temperature of 300K. The same strain increments were applied to the a-Si structures as before (section 3.1.2), except that the total system volume was allowed to change during the subsequent relaxation so as to maintain approximately zero constant externally applied pressure. The MD algorithm used does not yield a strictly constant pressure, but rather one that oscillates about the prescribed value. The standard deviation, however, of pressure oscillations in the deformation simulations presented here was just under 60 MPa: a negligible quantity compared to the extent of flow-induced pressure variation in the constant volume deformation simulations (figure 7-2).

The results of constant pressure deformation simulations are presented in figures 7-10 through 7-12. Comparison of figures 7-10 and 7-1 shows that there is no appreciable difference in the behavior of the deviatoric stress from that in the case of constant volume deformation. As expected, the density changes under constant pressure (figure 7-11) mirror the pressure changes under constant volume (figure 7-2) and the values of ϕ undergo similar evolution in both cases (figures 7-12 and 7-3). Unlike in the constant volume simulations, however, both the system volumes and liquidlike mass fractions in the constant pressure simulations eventually converge to unique steady-state flow values. These results confirm that the differing liquidlike mass fractions ϕ at steady-state flow are indeed due to their direct pressure dependence.

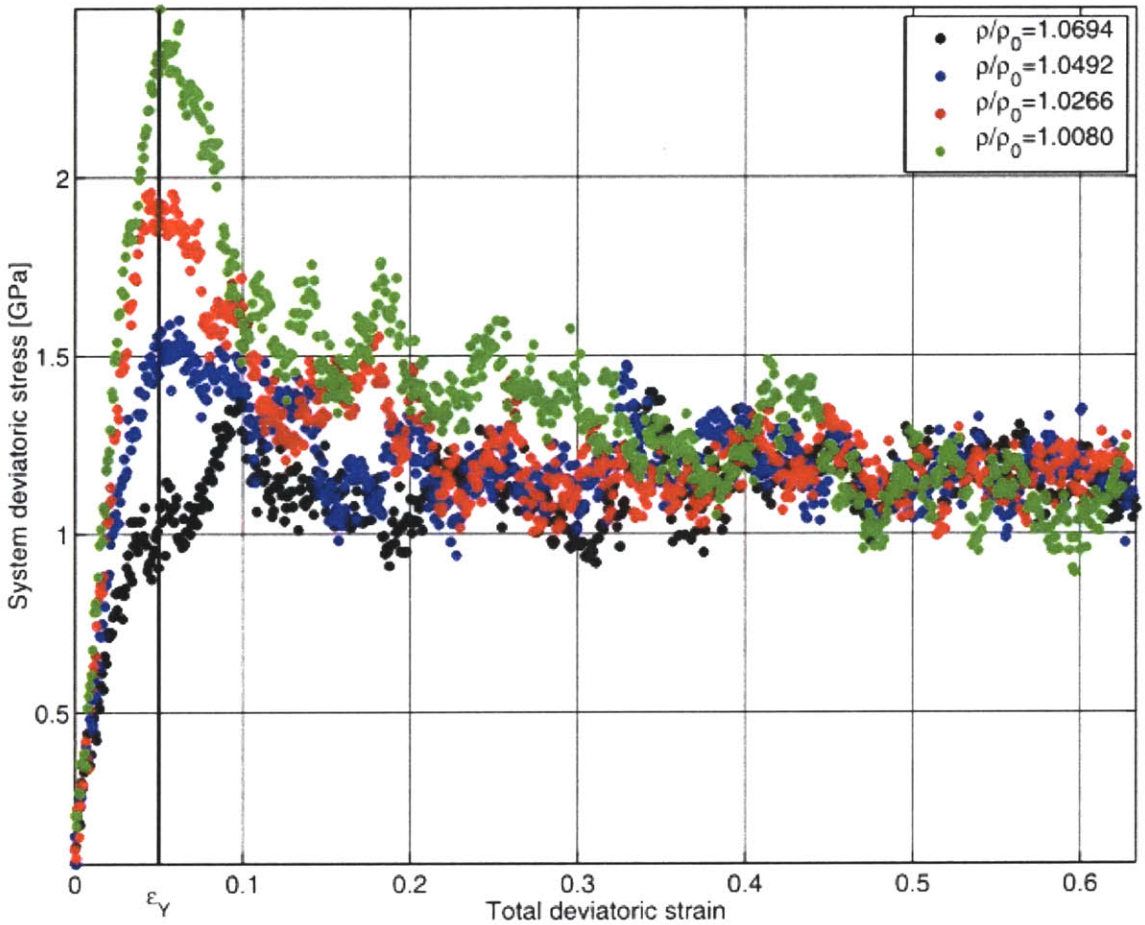

Figure 7-10: The variation of system deviatoric stress $\bar{\sigma}(\hat{\mathbf{o}})$ as a function of the deviatoric component of the total externally applied strain $\bar{\varepsilon}(\mathring{\mathbf{a}})$ for four a-Si structures of differing densities undergoing large-strain plastic flow under zero pressure.

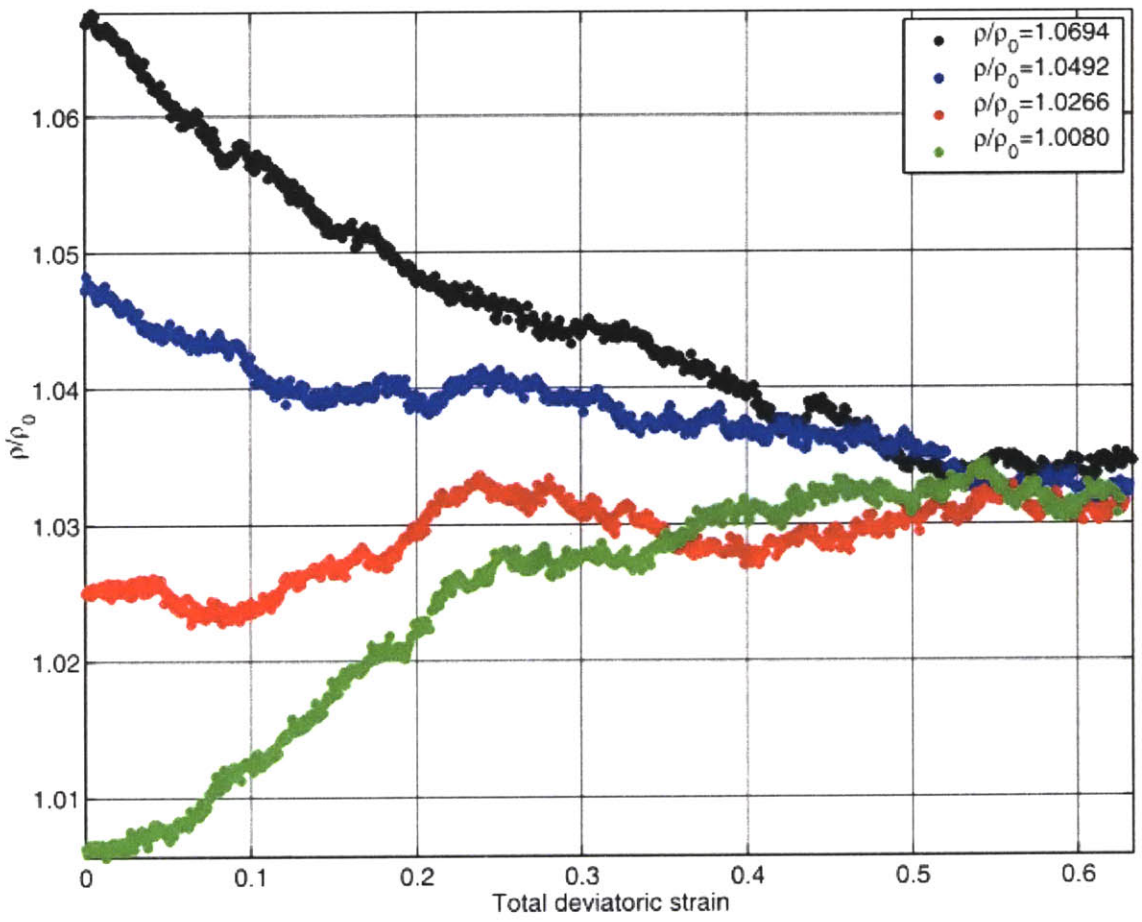

Figure 7-11: The variation of system relative density ρ/ρ_0 as a function of the deviatoric component of the total externally applied strain $\bar{\varepsilon}(\text{å})$ for four a-Si structures of differing densities undergoing large-strain plastic flow under zero pressure.

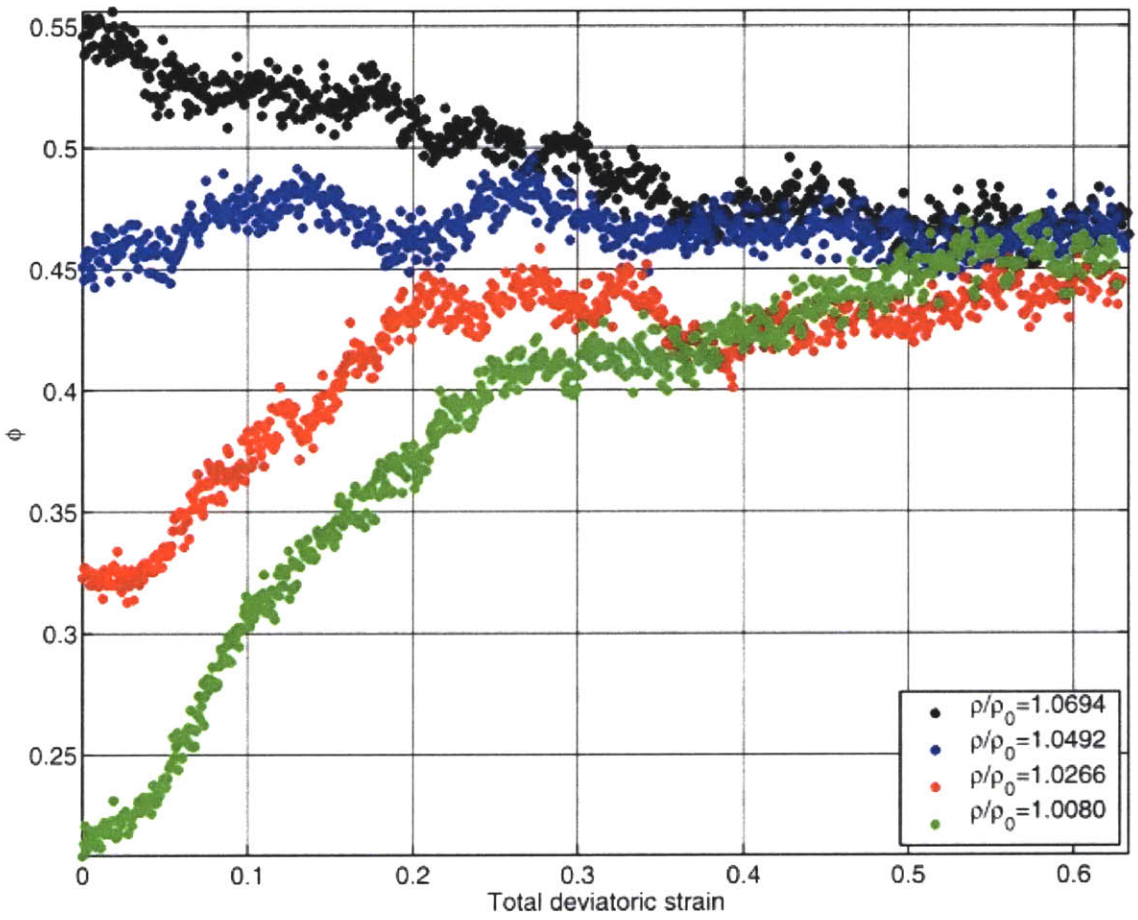

Figure 7-12: The variation of system mass fraction of liquidlike atomic environments ϕ as a function of the deviatoric component of the total externally applied strain $\bar{\varepsilon}(\text{å})$ for four a-Si structures of differing densities undergoing large-strain plastic flow under zero pressure. Note that unlike in the case of deformation under constant volume (figure 7-3) all systems converge to a single value of ϕ characteristic of steady state flow.

8. Study of mechanisms of stress relaxation by PEM

This chapter identifies discrete stress relaxations as the source of low-temperature inelastic behavior in a-Si. Each relaxation is accompanied by an atomic structure rearrangement describable as an autocatalytic avalanche of unit inelastic shearing events. The local yielding criterion satisfied at onset and necessary for the propagation of these avalanches is found.

8.1 Mechanisms of flow in MD and PEM are isoconfigurational

In the work described in chapter 7, relaxation of externally strained structures was accomplished using molecular dynamics (MD) simulation at a constant temperature of T=300K. Because the thermal motion of atoms in MD simulations obscures the intimate details of individual atomic-level structure transformations, however, the mechanisms of plasticity in a-Si are more conveniently studied using the effectively zero temperature relaxation technique of potential energy minimization (PEM) [Leach, 2001]. This approach is justified if it can be argued that the same mechanisms of structure change are responsible for plasticity at 0K and 300K. A sufficient condition for this requirement to be satisfied is for plastic deformation at 300K to be considered to occur at low-temperature.

In low-temperature plasticity, diffusion processes leading to recovery or the direct accumulation of plastic strains have negligible effect on the overall system mechanical behavior [Argon, 1996b]. Key atomic rearrangements leading to plasticity can then be described as occurring near the mechanical threshold of plastic relaxation in the absence of thermal agitation. Temperature-dependence of the elastic moduli and thermal activation of these rearrangements are together responsible for the lowering of the flow stress at low finite temepature [Argon, 1996a], but they do not alter the mechanism of stress relaxation itself. For this reason the atomic rearrangements responsible for plasticity at differing low temperatures are often referred to as "isoconfigurational." In

the case of disordered solids, isoconfigurational plastic transformations continue to occur up to temperatures approaching the glass transition temperature [Yip *et al.*, 2000].

To confirm that the mechanisms responsible for plasticity in a-Si as simulated by MD at 300K are isoconfigurational to those occurring near the mechanical threshold in the absence of thermal motion, the constant volume deformation behavior found previously by MD simulation (section 7.1) was compared to effectively zero-temperature constant volume deformation behavior as simulated by PEM. The four series of configurations generated by constant volume deformation using MD were used as points of reference for the PEM simulations carried out afterwards: every configuration in each series was brought to its closest equilibrium configuration by setting all of its atomic velocities to zero (effectively removing all thermal motion) and bringing the system potential energy to its nearest local minimum by minimizing it with respect to the atomic positions. A particular configuration was then chosen from each of the four series as a starting point for deformation using PEM simulation. Amorphous solids have no true elastic limit, but show isolated inelastic relaxations separated by regions of reversible deformation behavior even at low stress levels [Deng *et al.*, 1989; Mott *et al.*, 1993]. Thus, in order to decrease the computation costs in the relatively uninteresting regime of "elastic-like" deformation, these initial structures were chosen from among highly strained configurations in each of the four series generated by MD simulation.

Figures 8-1 through 8-3 compare the mechanical behavior of a-Si when deformed plastically at constant volume by MD at T=300K and by PEM. In agreement with what was said at the beginning of this section, finite temperature deformation as simulated by MD differs from the effectively zero temperature PEM case mainly by the decreased level of flow stress (figure 8-1) [Argon, 1996a; Lacks, 2002]. The pressure changes (figure 8-2) as well as the variation of liquidlike mass fraction ϕ (figure 8-3) on the other hand exhibit closely similar trends for the two simulation methods. The internal atomic structure of a-Si during deformation by MD and PEM can therefore be thought to undergo comparable changes, confirming that low-temperature plasticity in a-Si is indeed governed by a mechanism of internal structure transformation that is isoconfigurational to the mechanism of zero-temperature transformation.

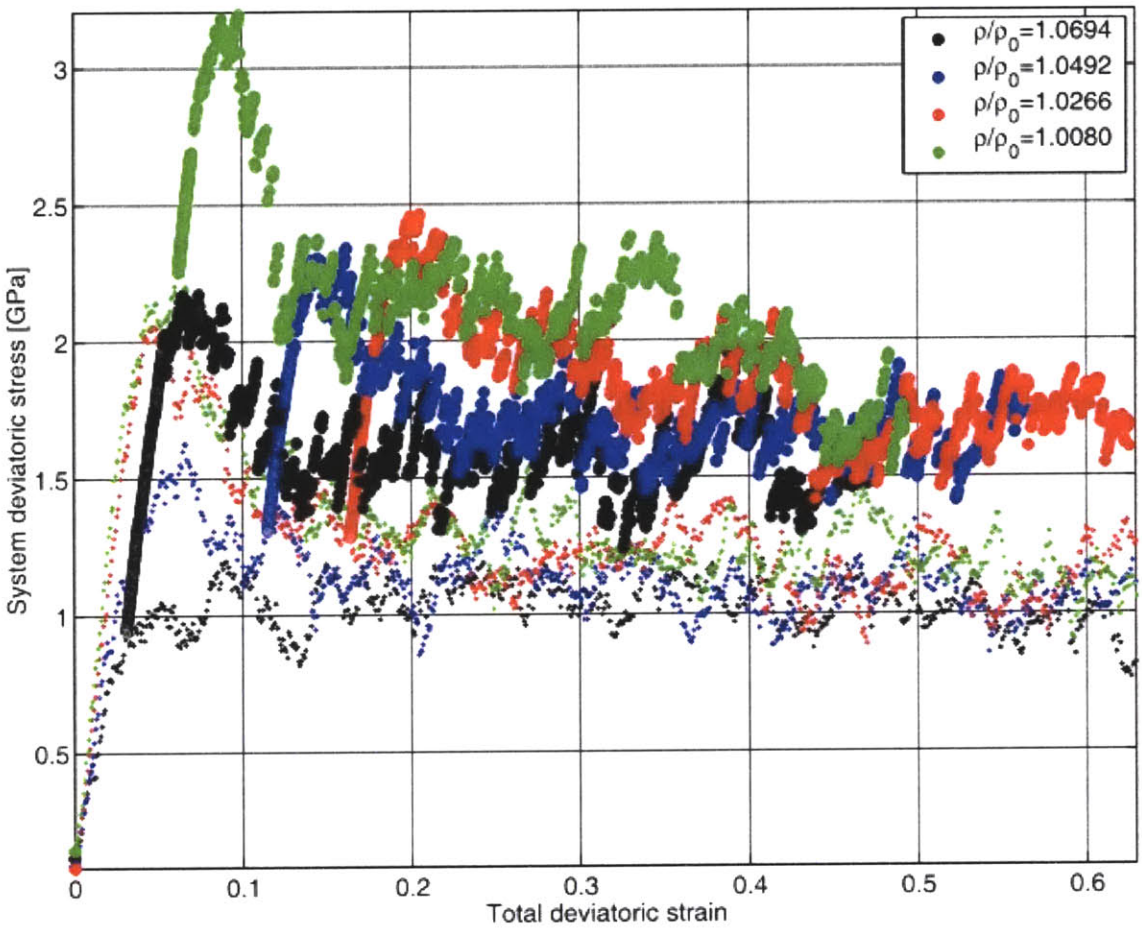

Figure 8-1: The variation of system deviatoric stress $\bar{\sigma}(\hat{\mathbf{o}})$ as a function of the total externally applied deviatoric strain $\bar{\varepsilon}(\mathring{\mathbf{a}})$ for four a-Si systems of differing densities undergoing large-strain plastic flow under constant volume. The mechanical behavior of a-Si as simulated by PEM (large markers) follows closely similar trends when compared with its behavior as simulated by MD at T=300K (small markers). The elevation of the steady-state flow stress is taken to be a result of the temperature dependence of elastic constants and the effect of thermal activation near the mechanical transformation threshold stress [Argon, 1996a].

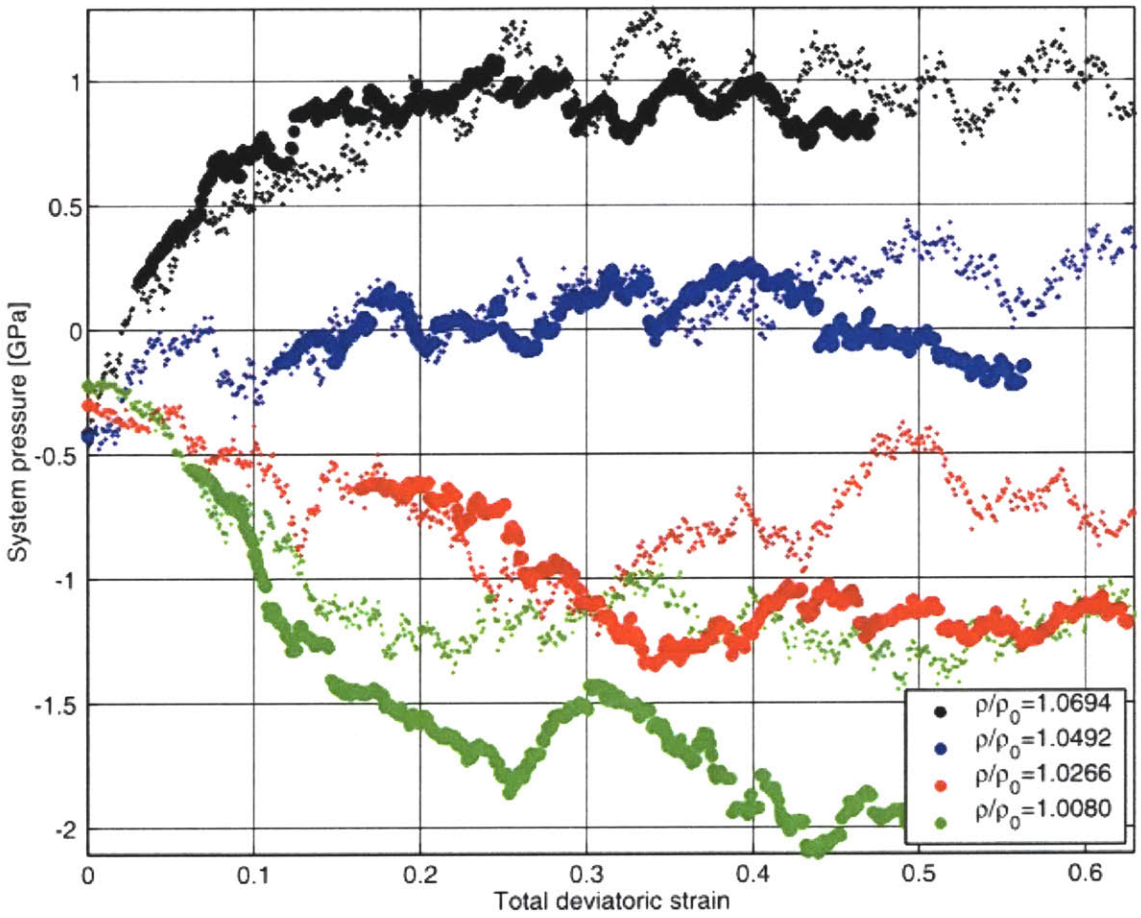

Figure 8-2: The variation of system pressure $p(\hat{\mathbf{o}})$ as a function of the total externally applied deviatoric strain $\bar{\varepsilon}(\mathring{\mathbf{a}})$ for four a-Si systems of differing densities undergoing large-strain plastic flow under constant volume. The mechanical behavior of a-Si as simulated by PEM (large markers) follows closely similar trends when compared with its behavior as simulated by MD at T=300K (small markers).

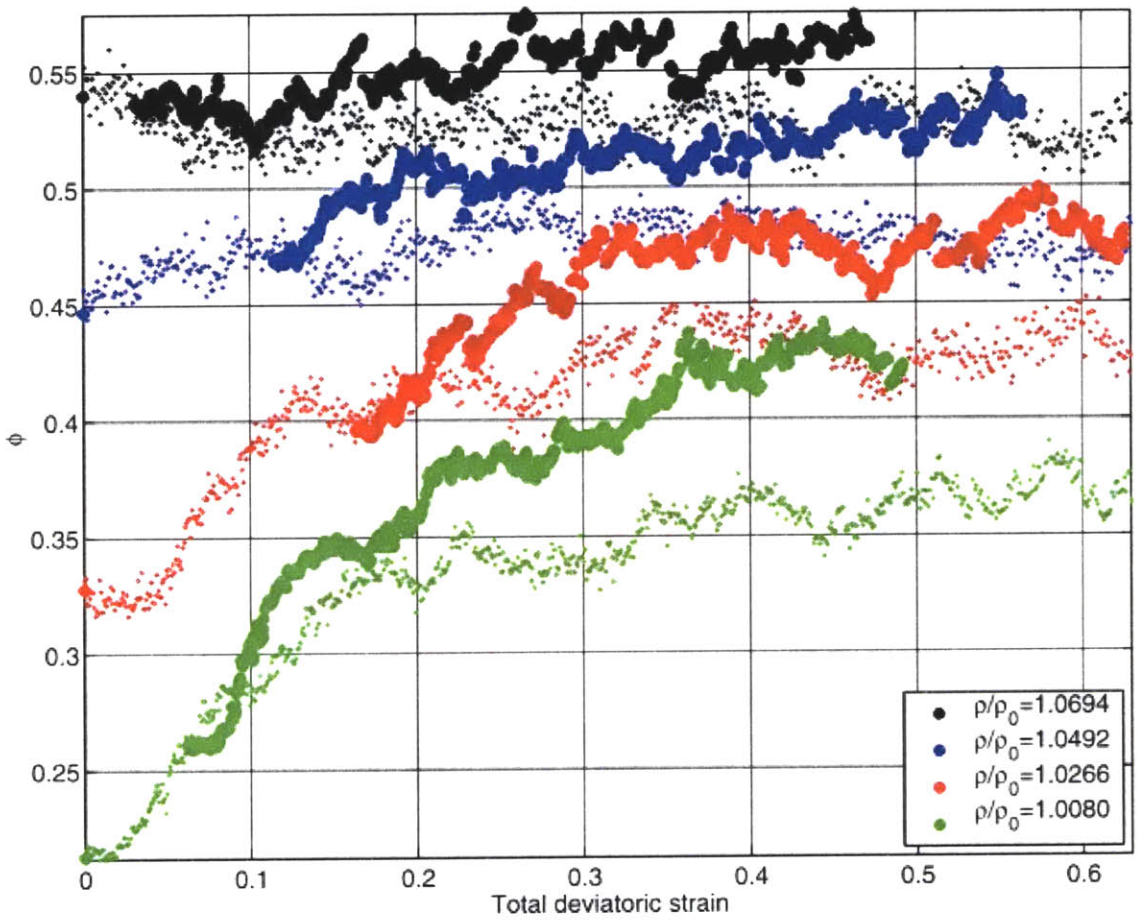

Figure 8-3: The variation of the mass fraction of liquidlike atomic environments ϕ as a function of the total externally applied deviatoric strain $\bar{\varepsilon}(\text{å})$ for four a-Si systems of differing densities undergoing large-strain plastic flow under constant volume. The mechanical behavior of a-Si as simulated by PEM (large markers) follows closely similar trends when compared with its behavior as simulated by MD at T=300K (small markers).

8.2 Discrete stress relaxations as the source of inelastic behavior in a-Si

Closer inspection of a section of a typical stress-strain curve obtained using PEM—presented in figure 8-4—reveals that it is composed of regions of smooth, reversible variation of stress separated by sudden isolated, discrete, and irreversible stress relaxations, each occurring at a well-defined mechanical threshold stress (figure 8-4a and 8-4b). As in the case of glassy polymers [Mott *et al.*, 1993] and metallic glasses [Lund, Schuh, 2004; Maloney, Lemaitre, 2004], such irreversible stress relaxations are the source of inelastic behavior in a-Si. The ensemble average of large numbers of these events is responsible for the apparently smooth overall plastic deformation behavior of large samples of a given material. Figure 8-4c) shows that the largest changes in liquidlike mass fraction ϕ coincide with the largest stress relaxations. Nevertheless, some fluctuations in ϕ do occur in regions of reversible stress variation, indicating that while changes in the nature of atomic environments are induced primarily by inelastic stress relaxations they can also result from elastic flexing of bond angles.

A total of 4201 discrete stress relaxations were observed in the course of the four series of PEM deformation simulations summarized in figures 8-1 through 8-3. The intensity of each relaxation can be described by finding its stress increment tensor, defined as

$$\ddot{A}\hat{\mathbf{o}} = \hat{\mathbf{o}}_f - \hat{\mathbf{o}}_i, \tag{8.1}$$

where $\hat{\mathbf{o}}_i$ denotes the system stress tensor at onset and $\hat{\mathbf{o}}_f$ at completion of the relaxation. The pressure and deviatoric components of $\ddot{A}\hat{\mathbf{o}}$ associated with the 4201 observed events can be computed as described in section 4.1.

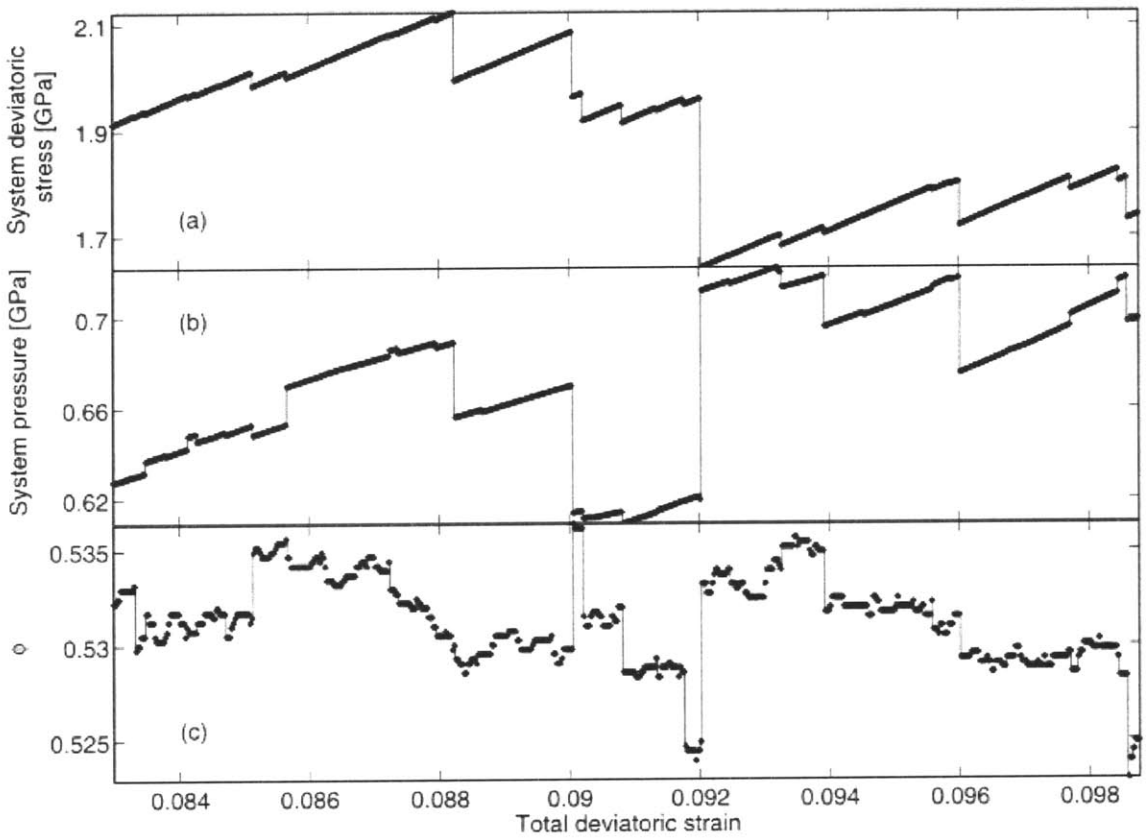

Figure 8-4: Variation of (a) deviatoric stress $\bar{\sigma}(\hat{\mathbf{o}})$, (b) pressure $p(\hat{\mathbf{o}})$, and (c) mass fraction ϕ of liquidlike atomic environments as functions of total externally applied deviatoric strain $\bar{\varepsilon}(\mathring{\mathbf{a}})$ over a typical section of a PEM plastic deformation simulation. The stress-strain plots are composed of regions of smooth reversible deformation (denoted by dots) punctuated by discrete irreversible stress relaxations (vertical lines), each occurring at a well-defined threshold stress. The largest changes in ϕ coincide with the largest stress relaxations. Nevertheless, some fluctuations in ϕ do occur in regions of reversible stress variation. Data for this figure was obtained by enlarging the plots shown in figures 8-1 through 8-3 for the a-Si system with $\rho/\rho_0 = 1.0694$ in the range of total deviatoric stress presented above.

The pressure components of the stress relaxation increment tensors were distributed symmetrically about zero. As shown in figure 8-5, the normalized distribution of their absolute values can be described as a power law with the approximate form $0.0144 \cdot \left(\frac{|p(\ddot{A}\hat{o})|}{37.76GPa} \right)^{-1.28}$. The normalized distribution of deviatoric stress relaxation increments can be described as a power law with the approximate form $0.0162 \cdot \left(\frac{\bar{\sigma}(\ddot{A}\hat{o})}{37.76GPa} \right)^{-1.29}$, as illustrated in figure 8-6. Here 37.76 GPa is the approximate decohesion stress for SW Si obtained by dimensional analysis from the characteristic energy and length of the SW potential (section 3.2.1).

The intensity of internal structure change accompanying every stress relaxation can additionally be characterized by the number of atomic environments whose character changed during the relaxation from liquidlike to solidlike or vice versa. This quantity will be called χ. Figures 8-7 and 8-8 respectively plot the pressure $p(\ddot{A}\hat{o})$ and deviatoric $\bar{\sigma}(\ddot{A}\hat{o})$ components of the stress increment tensor $\ddot{A}\hat{o}$ associated with each stress relaxation against the corresponding value of χ. While the pressure increments $p(\ddot{A}\hat{o})$ and χ show no recognizable correlation (figure 8-7), the deviatoric stress increments and χ are directly correlated (figure 8-8). This finding indicates that in amorphous Si every unit of stress relaxation is accompanied by a characteristic increment of internal structure change. Furthermore, since the number of environment changes only correlates to the deviatoric stress increment and not the pressure increment, it can be concluded that internal structure changes in a-Si during discrete stress relaxations are shear-induced.

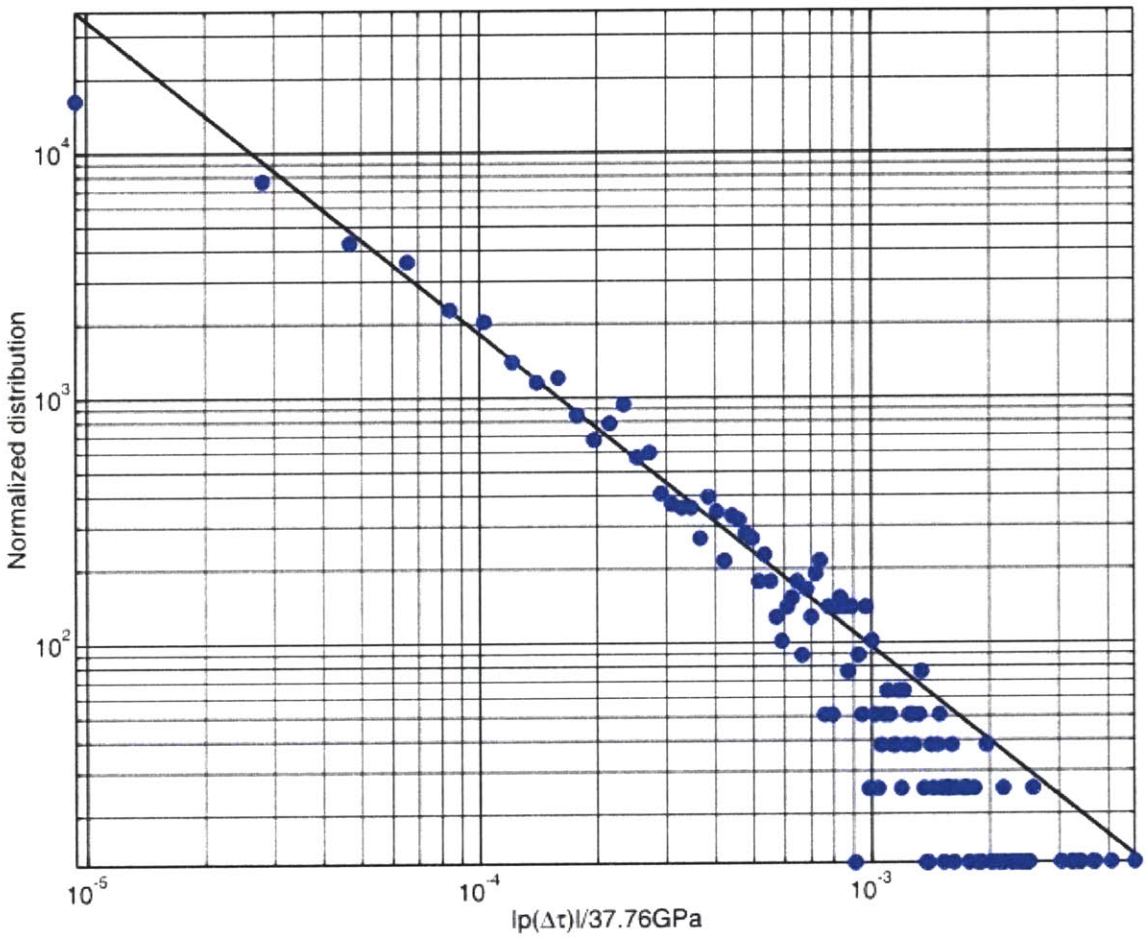

Figure 8-5: The absolute values of the pressure components $p(\ddot{A}\hat{o})$ of stress relaxation increment tensors $\ddot{A}\hat{o}$ follow a power law distribution.

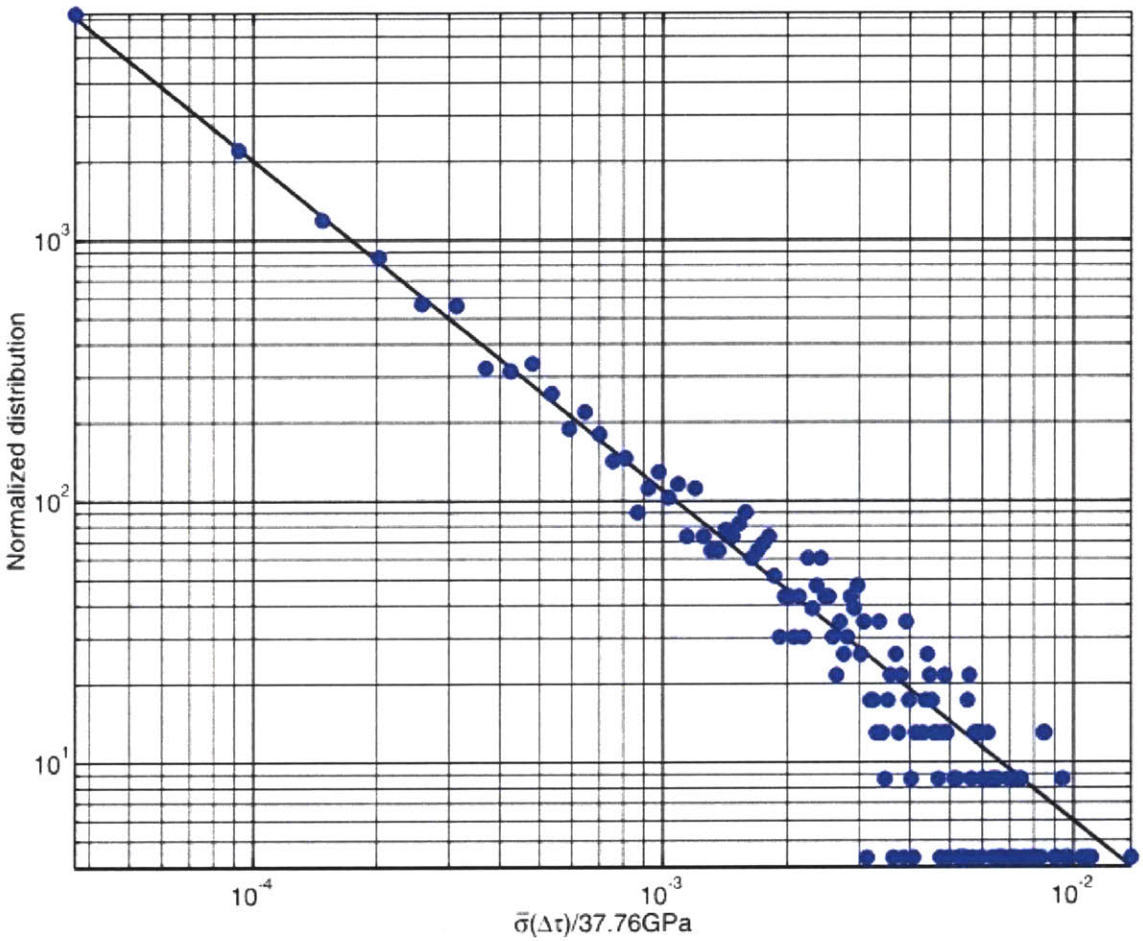

Figure 8-6: The absolute values of the deviatoric component $\bar{\sigma}(\ddot{\mathbf{A}}\hat{\mathbf{o}})$ of stress relaxation increment tensors $\ddot{\mathbf{A}}\hat{\mathbf{o}}$ follow a power law distribution.

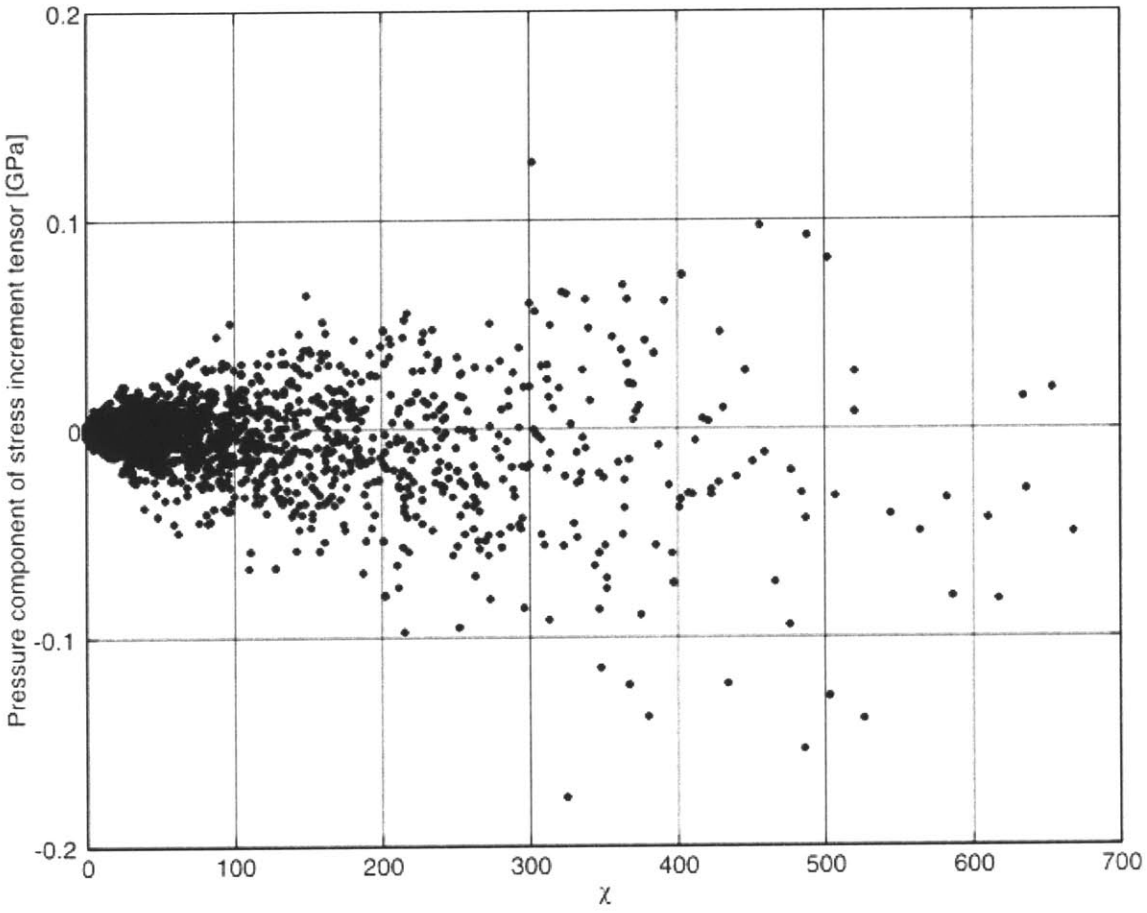

Figure 8-7: The number χ of atomic environments whose character changes during a stress relaxation (from liquidlike to solidlike or vice versa) does not correlate to the pressure component $p(\ddot{\mathbf{A}}\hat{\mathbf{o}})$ of the associated stress increment tensor $\ddot{\mathbf{A}}\hat{\mathbf{o}}$ (equation 8.1).

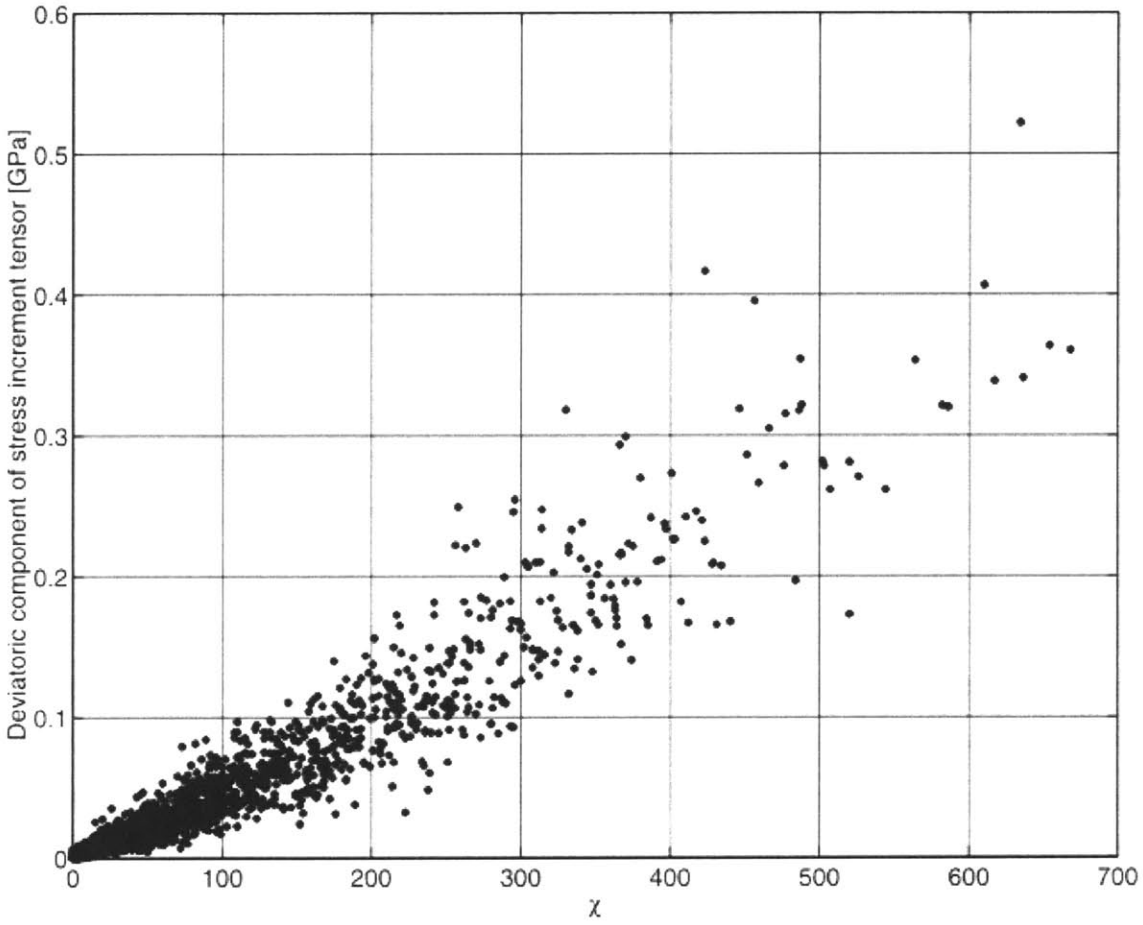

Figure 8-8: The number χ of atomic environments whose character changes during a stress relaxation (from liquidlike to solidlike or vice versa) is directly correlated to the deviatoric component $\bar{\sigma}(\ddot{\mathbf{A}}\hat{\mathbf{o}})$ of the associated stress increment tensor $\ddot{\mathbf{A}}\hat{\mathbf{o}}$ (equation 8.1).

No correlation was found between any of the components of the mechanical threshold stress $\hat{\mathbf{o}}_i$ at onset of relaxations and $p(\ddot{\mathbf{A}}\hat{\mathbf{o}})$, $\bar{\sigma}(\ddot{\mathbf{A}}\hat{\mathbf{o}})$, or χ. The intimate details of structure changes that accompany discrete stress relaxations, however, are a means to studying the mechanisms of plastic flow in a-Si while the conditions at the mechanical thresholds preceding these relaxations can elucidate the local yielding criteria at onset of atomic rearrangements. These mechanisms and onset conditions are analyzed in detail in sections 8.3 and 8.4.

8.3 Autocatalytic avalanches of unit shearing events

Each stress relaxation observed in PEM simulations is accompanied by an internal atomic rearrangement. As discussed in section 4.4.1, part of that rearrangement can be thought of as a localized inelastic transformation while the rest of it is attributed to elastic flexing. The method described in section 4.4.1 was therefore used to identify the inelastically transforming inclusions associated with the 4201 discrete stress relaxation events observed in the course of PEM deformation simulations. The atomic arrangements at the mechanical thresholds (just before relaxation) and at completion of the ensuing stress relaxations served as initial and final system configurations, respectively. Both configurations are by construction in equilibrium, so $\mathbf{f}_i = \mathbf{f}_f^{total} = 0$ in equation 4.30. Furthermore, the shapes of their simulation cells differ by $\ddot{\mathbf{A}}\mathbf{a}$ equal to one externally applied volume-conserving system strain increment, as described in section 3.1.2.

Figures 8-9 and 8-10 show visualizations of two representative transforming inclusions found by the matrix-inclusion analysis. One of them (figure 8-9) is composed of 12 atoms grouped into one cluster. The other one (figure 8-10) is larger at 154 atoms and appears to consist primarily of two separate atomic clusters (and a handful of isolated atoms). The atomic clusters observed in both inclusions are well localized, as can be concluded by observing that they are confined to relatively compact regions within the simulation cell.

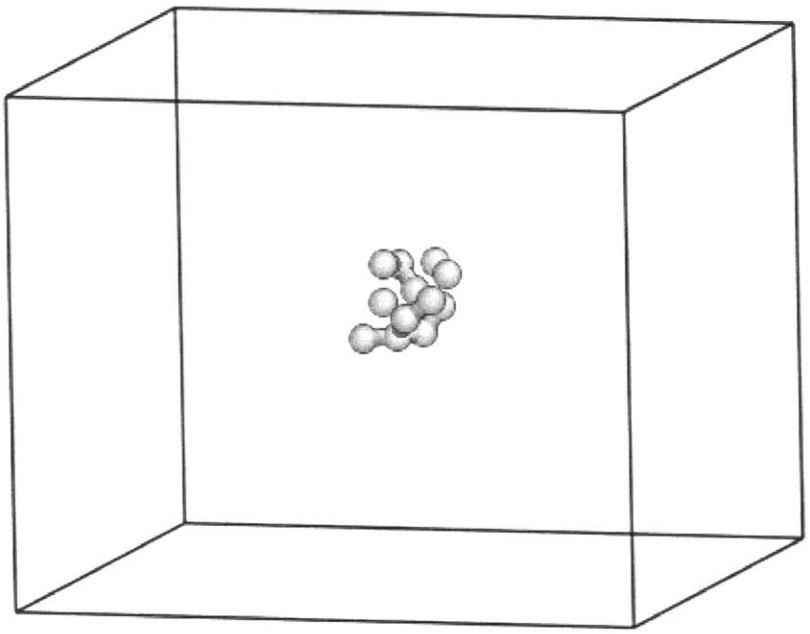

Figure 8-9: Visualization of a typical inelastically transforming inclusion. This one consists of 12 atoms in a single cluster.

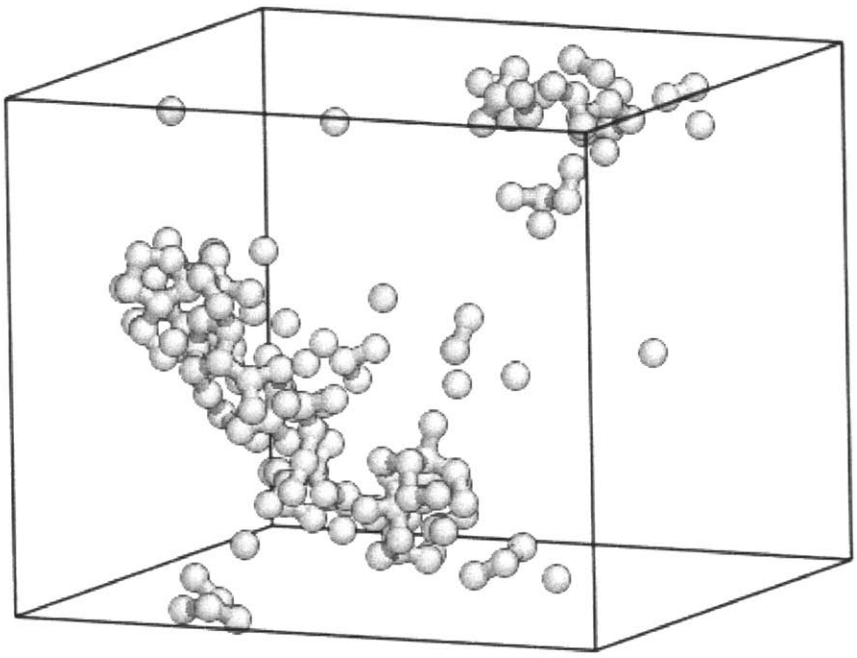

Figure 8-10: Visualization of a typical inelastically transforming inclusion. This one consists of 154 atoms grouped mainly into two separate clusters.

As illustrated in figure 8-11, the sizes of the 4201 inelastically transforming inclusions—defined as the number n of atoms composing each one— were distributed according to a power law of approximate form $7.36 \cdot n^{-1.97}$. They ranged between 3 and just over 600 atoms. Meanwhile, figures 8-7 and 8-8 show that the number χ of atomic environment changes during stress relaxations reaches a maximum of almost 700. This observation prompts an investigation of whether all transitions of atomic environments between the solidlike and liquidlike types occur as a result of inelastic rearrangement or if some of them are caused by flexing of bond angles in the elastically deforming matrix, as suggested in section 8.2.

The exact proportion of atomic environment transitions taking place elastically and inelastically can be found by plotting the number χ_{inc} of such transitions taking place within the nearest neighbor shells of atoms comprising inelastically transforming inclusions against the total number χ occurring during stress relaxations, as shown in figure 8-12. Evidently about 40% of such transitions occur due to inelastic transformation and the rest due to elastic flexing. This conclusion is not materially affected by varying the cutoff chosen in equation 4.32 for finding the atoms comprising inelastically transforming inclusions. Figures 8-13 and 8-14 visualize the location of atomic environments that undergo a change in their type and are not in the nearest neighbor shells of atoms comprising the inelastically transforming inclusion for the two inclusions shown in figures 8-9 and 8-10.

More importantly, however, the sizes of transforming inclusions n exhibited a similar correlation to the pressure and deviatoric components of the stress relaxation tensor $p(\ddot{\mathbf{A}}\hat{\mathbf{o}})$ and $\bar{\sigma}(\ddot{\mathbf{A}}\hat{\mathbf{o}})$ as did the number χ of atomic environment changes during the stress relaxations (figures 8-7 and 8-8). Specifically, figure 8-15 shows that $p(\ddot{\mathbf{A}}\hat{\mathbf{o}})$ and n show no recognizable correlation. Meanwhile, figure 8-16 demonstrates that $\bar{\sigma}(\ddot{\mathbf{A}}\hat{\mathbf{o}})$ and n are roughly linearly related, suggesting there exists for amorphous Si a characteristic increment of stress relaxation per unit volume, i.e. a "unit" inelastic deformation event. Furthermore, since inclusion sizes only correlate to the deviatoric component of stress increments and not the pressure component, such a unit event can be characterized as a shear transformation with an uncorrelated dilatational component.

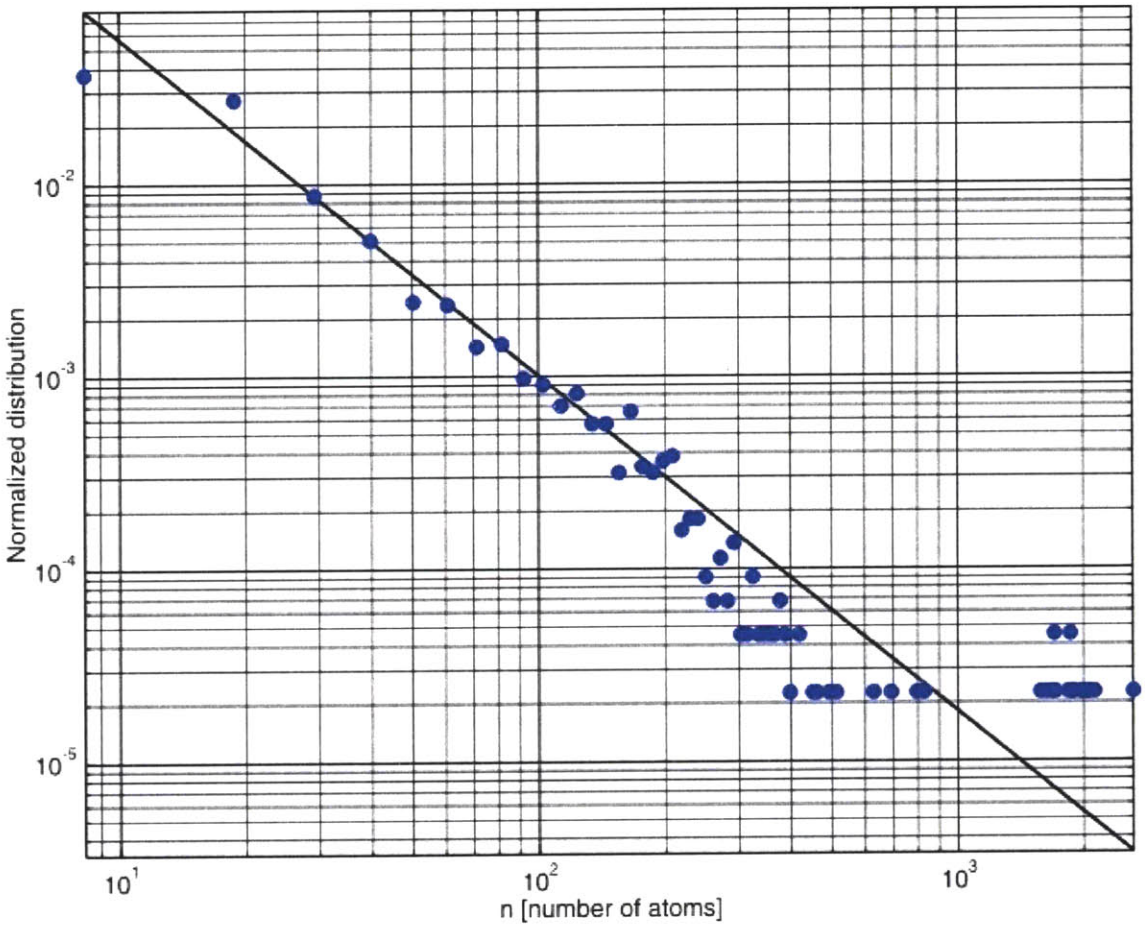

Figure 8-11: The sizes of inelasticaly transforming inclusions n follow a power law distribution.

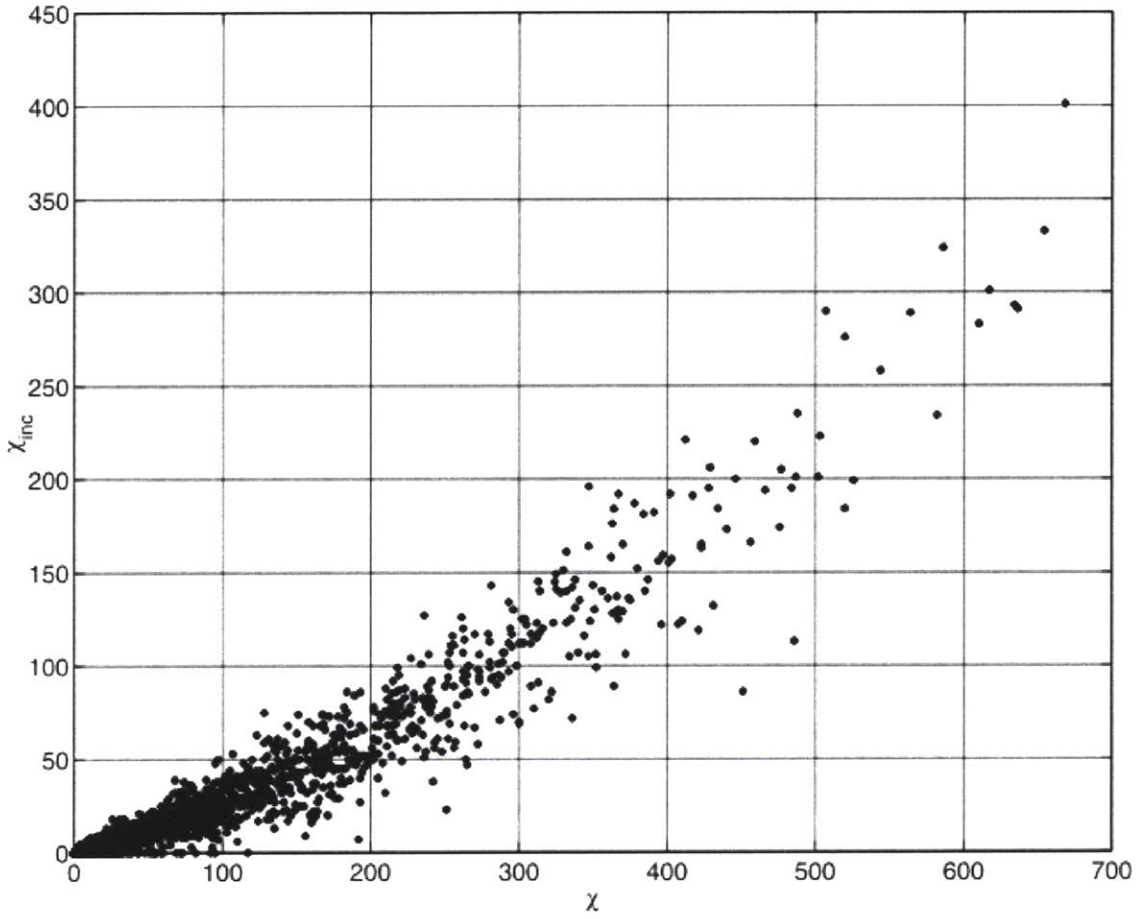

Figure 8-12: The numbers χ_{inc} of atomic environment transitions (from liquidlike to solidlike and vice versa) that take place within the nearest neighbor shells of atoms comprising inelastically transforming inclusions are plotted against the total numbers χ occurring during stress relaxations. It can be concluded that about 40% of such transitions occur due to inelastic transformation and the rest due to elastic flexing.

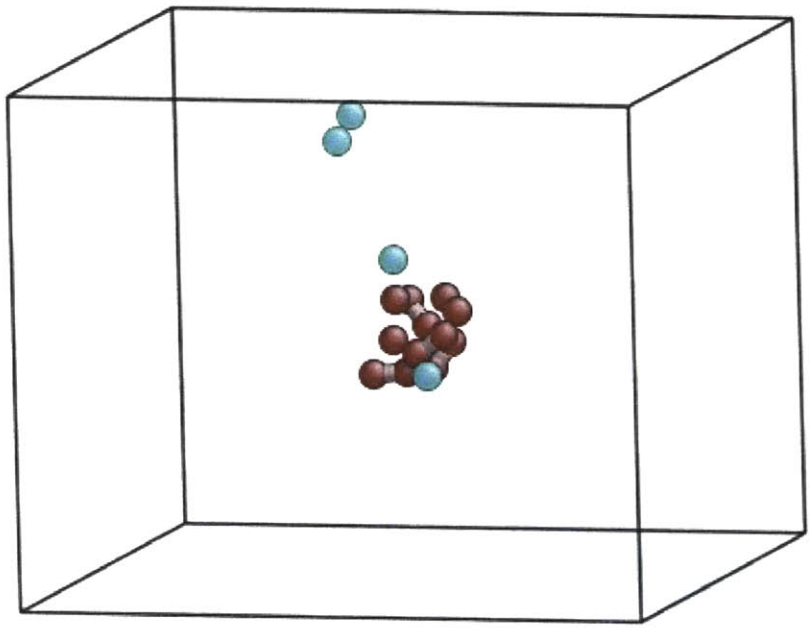

Figure 8-13: Visualization of atomic environment transitions for the inelastically transforming inclusion exhibited in figure 8-9. The dark atoms are those that constitute the inelastically transforming inclusion itself. The light atoms denote environments that changed their type (from liquidlike to solidlike or vice versa), but are not part of the nearest neighbor shells of the atoms that constitute the inclusion.

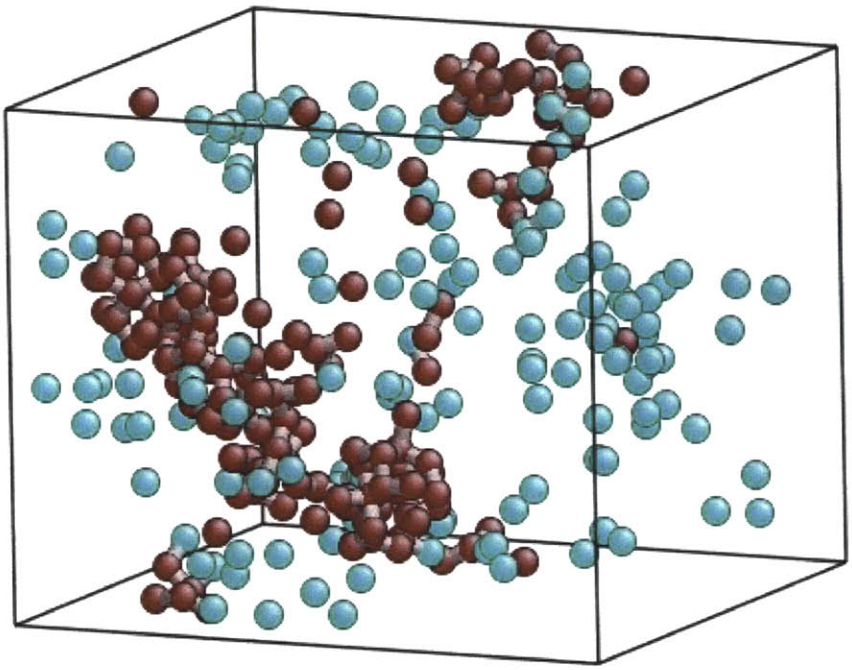

Figure 8-14: Visualization of atomic environment transitions for the inelastically transforming inclusion exhibited in figure 8-10. The dark atoms are those that constitute the inelastically transforming inclusion itself. The light atoms denote environments that changed their type (from liquidlike to solidlike or vice versa), but are not part of the nearest neighbor shells of the atoms that constitute the inclusion.

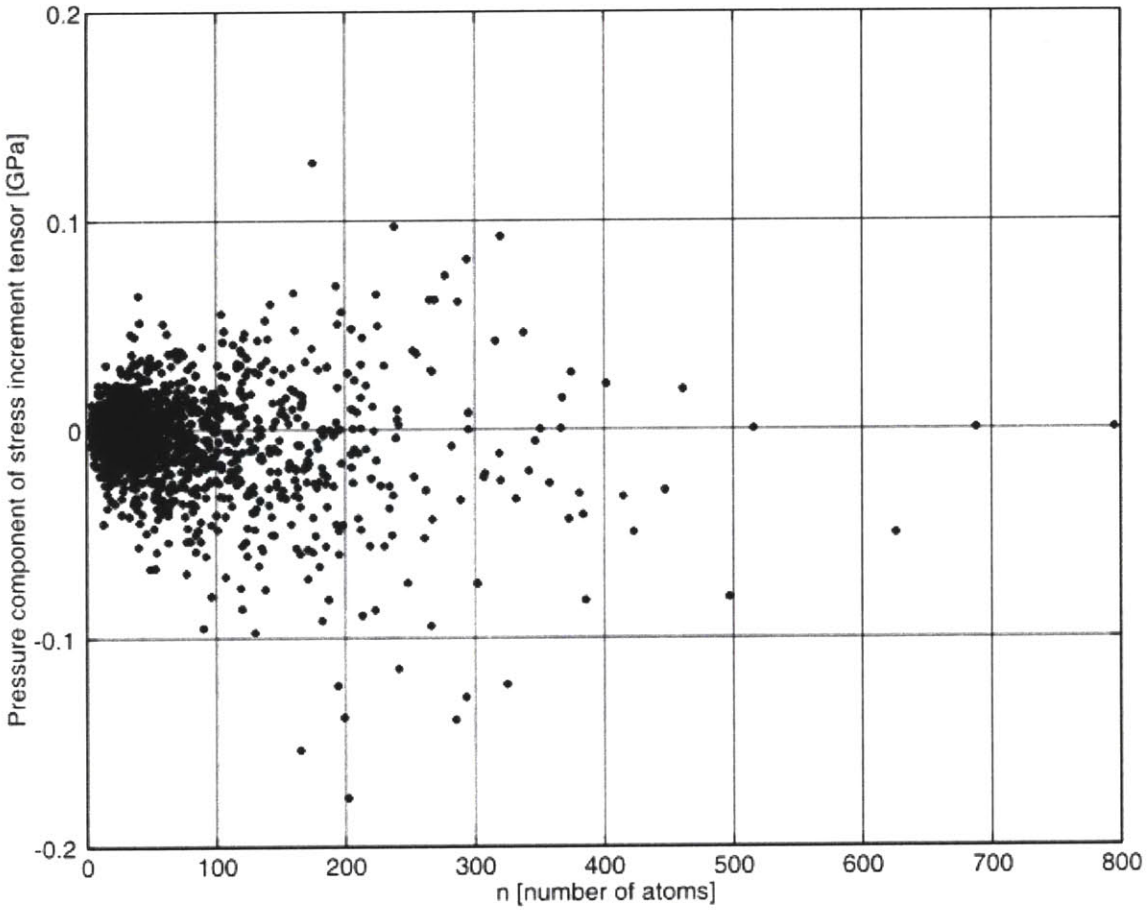

Figure 8-15: The pressure component $p(\ddot{A}\hat{o})$ of the stress relaxation increment tensor $\ddot{A}\hat{o}$ shows no distinguishable correlation to the size n of the associated transforming inclusion.

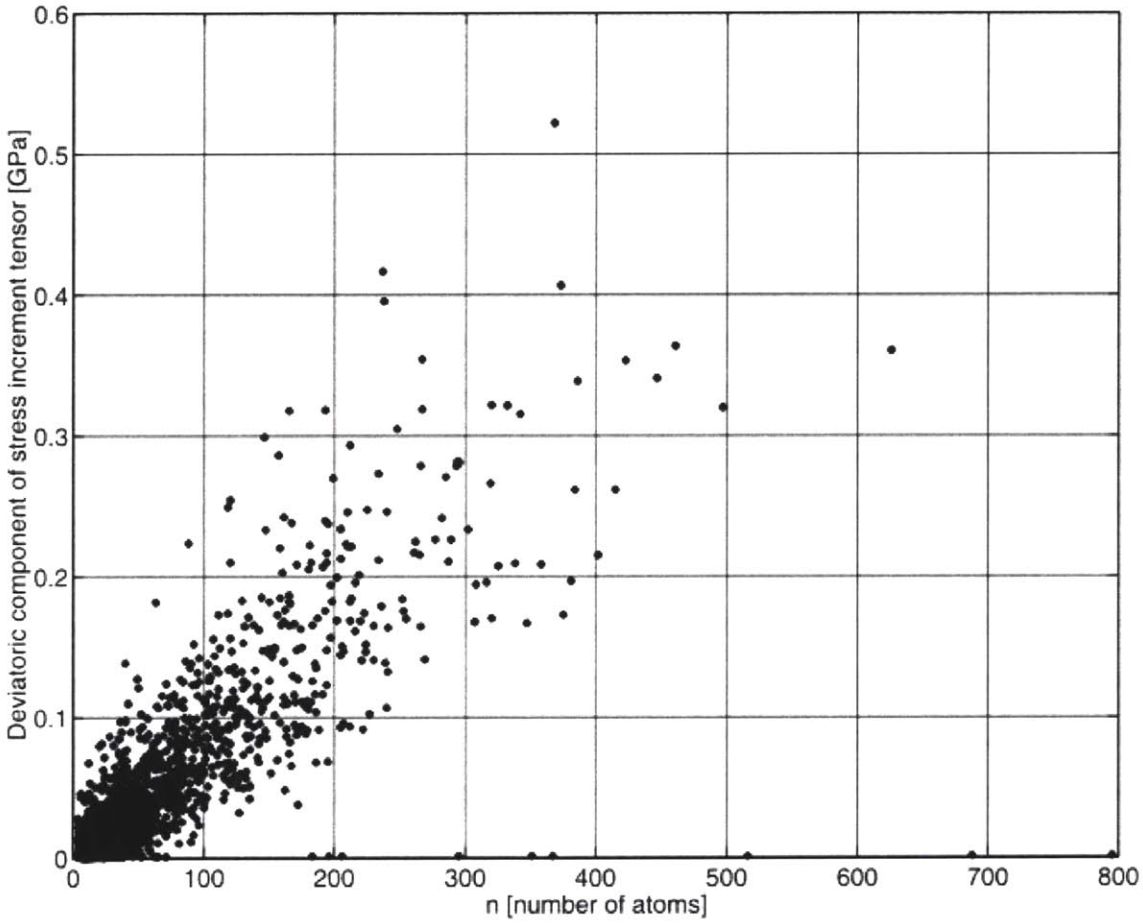

Figure 8-16: The deviatoric component $\bar{\sigma}(\ddot{A}\hat{o})$ of the stress relaxation increment tensor $\ddot{A}\hat{o}$ is roughly linearly related to the inclusion size n.

This conclusion is further reinforced by examination of the evolution of the transforming inclusions during the process of structure relaxation (carried out by potential energy minimization, as described in section 3.3) that begins just beyond their mechanical threshold and ends with the eventual system-wide equilibration of the atomic configuration. Such examination is carried out for the two representative transforming inclusions visualized in figures 8-9 and 8-10. The progress of the relaxation procedure is gauged by finding the norm of the vector of atomic displacements $\ddot{\mathbf{A}}\mathbf{d}$ from the reference configuration at the beginning of the relaxation to the current configuration at any given stage of the relaxation. The increasing size of the inelastically transforming inclusion is monitored at every step of the relaxation process using the matrix-inclusion analysis described in section 4.4.1 with the system configuration at the mechanical threshold as a reference state. Quantities such as potential energy, system pressure and deviatoric stress, as well as total number χ of atomic environment transitions are also monitored.

Figure 8-17 shows that the inelastic transformation of the small inclusion visualized in figure 8-9 proceeds in a single spurt associated with a sudden decrease in system potential energy and deviatoric stress as well as an increase in inclusion size and the total number of atomic environments that underwent structure transitions. Figure 8-18 demonstrates that similar intermittent spurts occur during the inelastic transformation of the larger inclusion visualized in figure 8-10. In both cases, the system deviatoric stress is progressively relaxed as the extent of elastically transformed material increases, confirming the hypothesis of a characteristic increment of shear stress relaxation per unit volume of transformed material.

Furthermore, visualizations—in figure 8-19—of the aggregation of inelastically transformed regions in the case of the larger of the two inclusions indicate that successive transformation generally occurs in the vicinity of previously transformed material. This observation suggests that inelastic relaxation in a-Si is an autocatalytic avalanche of unit shear relaxations that continues so long as a local yielding criterion is satisfied. Since inelastic relaxation can change the local distribution of stresses and cause elastically-induced changes in the type of atomic environments throughout the neighboring matrix material, inelastic transformations can also initiate in atomic clusters that are close to but

disconnected from the body of the cluster that originally underwent inelastic transformation. The details of the local yielding phenomenon responsible for the local onset of inelastic transformation are investigated next.

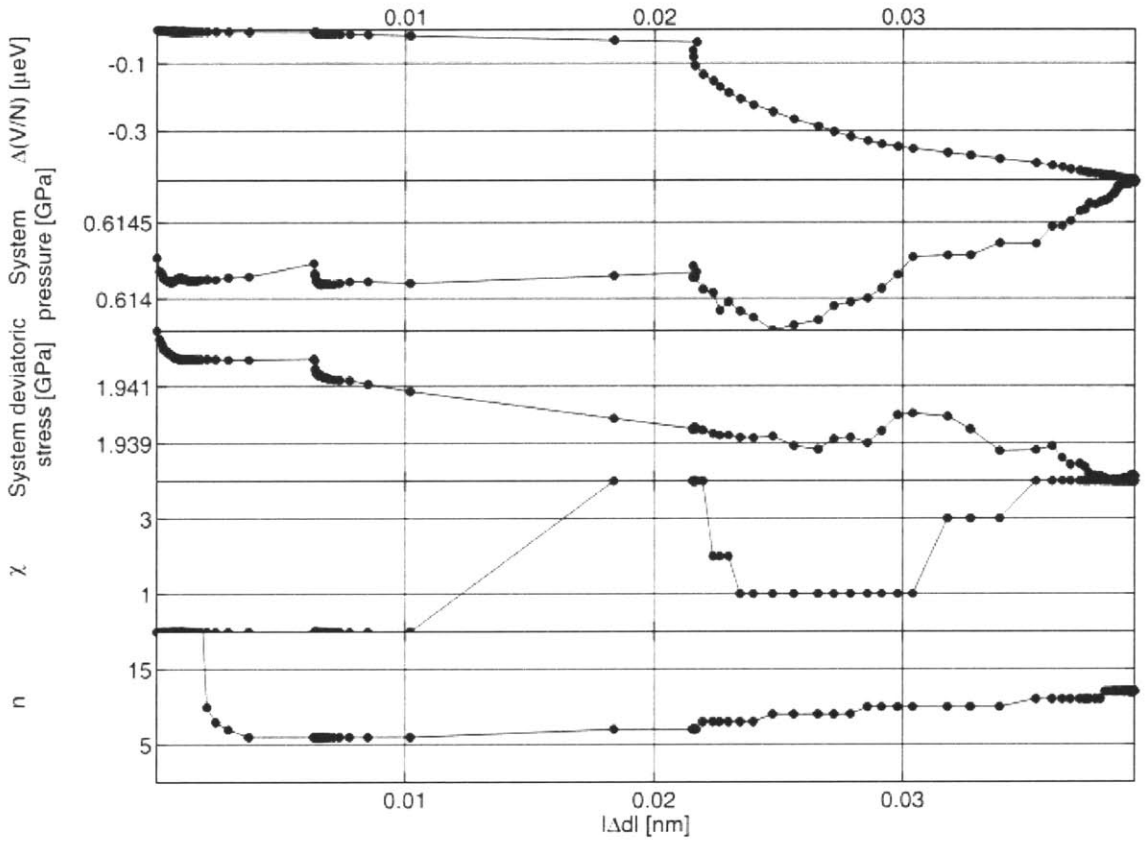

Figure 8-17: The variation of system potential energy increment per atom $\Delta(V/N)$ $[\mu eV]$, system pressure $p(\hat{\mathbf{o}})$ and deviatoric stress $\bar{\sigma}(\hat{\mathbf{o}})$ $[GPa]$, number χ of atomic environment changes, as well as size n of the inelastically transforming inclusion as functions of the norm of the atomic displacement vector $|\ddot{\mathbf{A}}\mathbf{d}|$ for the small relaxation visualized in figure 8-9.

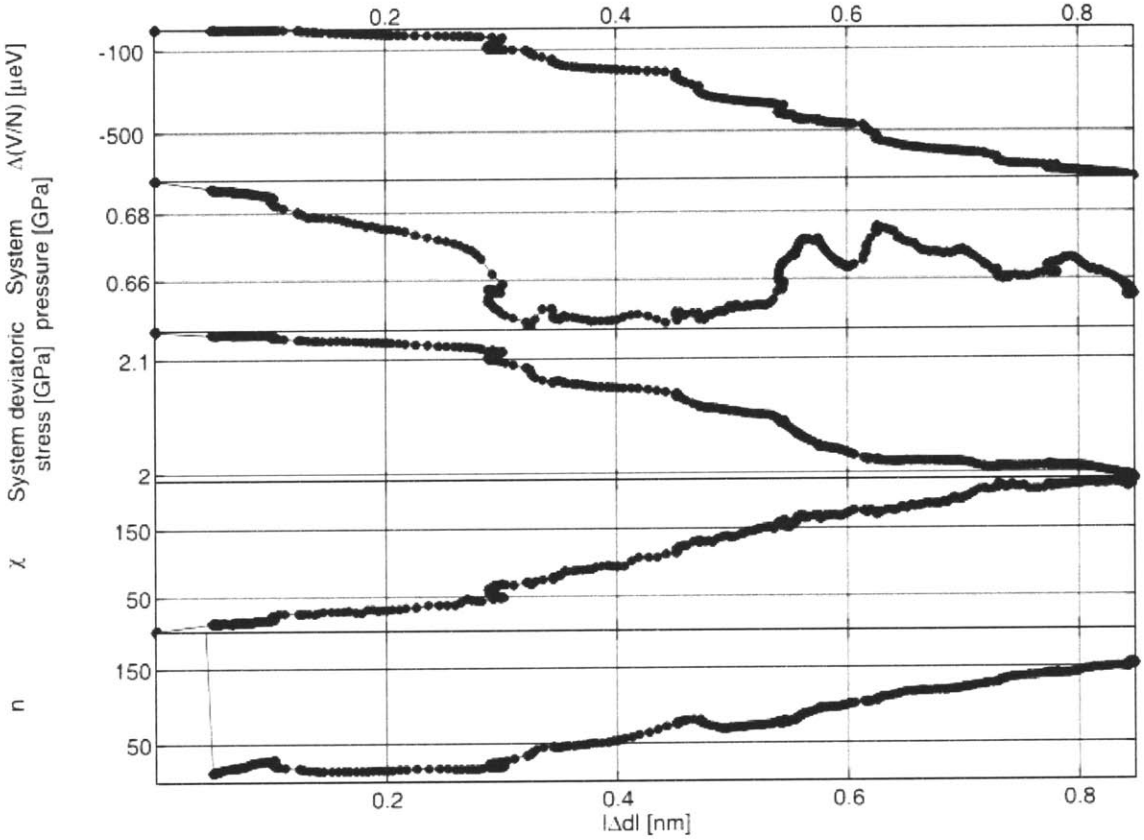

Figure 8-18: The variation of system potential energy increment per atom $\Delta(V/N)$ $[\mu eV]$, system pressure $p(\hat{\mathbf{o}})$ and deviatoric stress $\bar{\sigma}(\hat{\mathbf{o}})$ $[GPa]$, number χ of atomic environment changes, as well as size n of the inelastically transforming inclusion as functions of the norm of the atomic displacement vector $|\ddot{\mathbf{A}}\mathbf{d}|$ for the large relaxation visualized in figure 8-10.

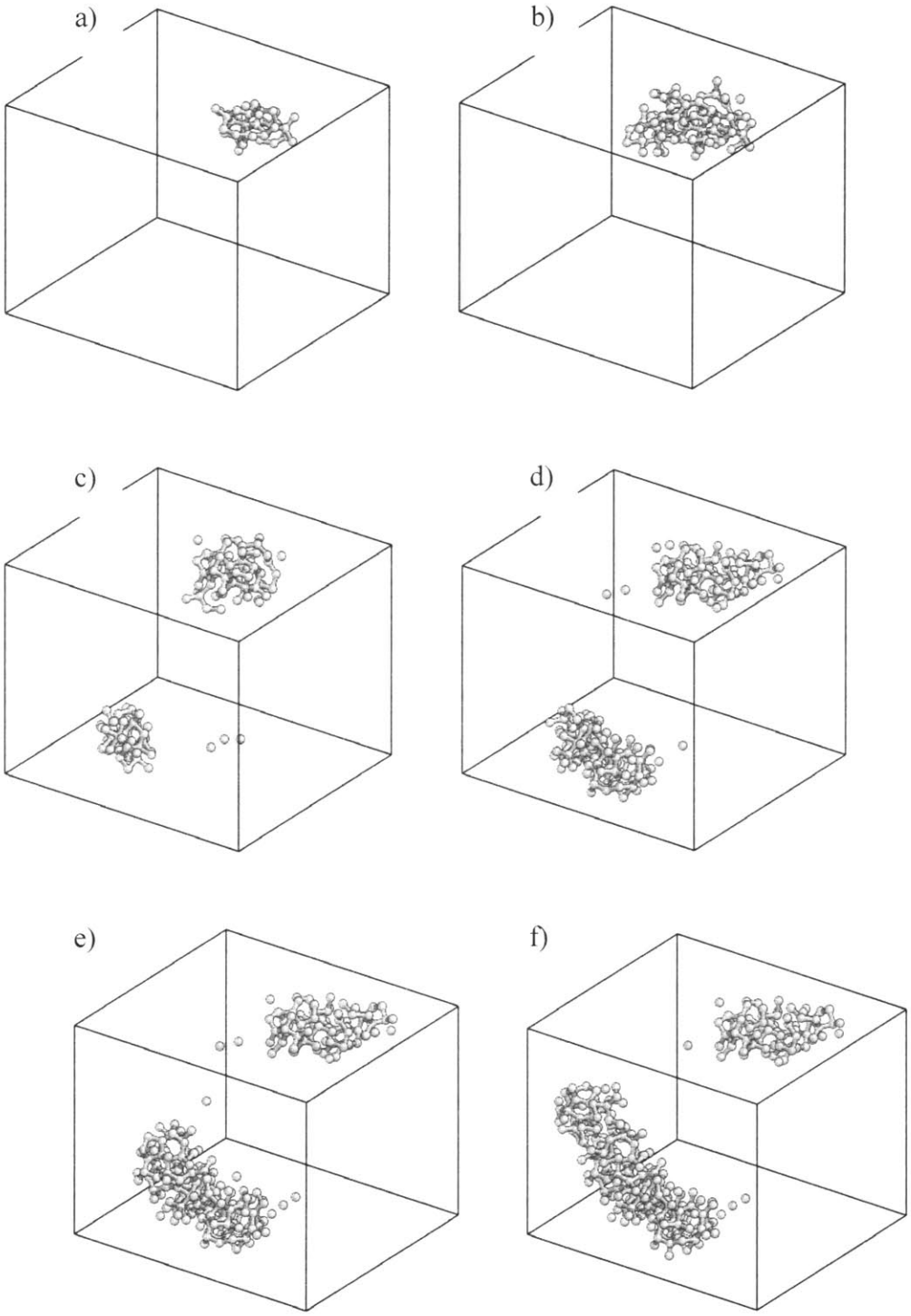

Figure 8-19: Visualization of the evolution of the inelastically transforming inclusion shown in figure 8-10 and analyzed in figure 8-18. The norms of the atomic displacement vector $|\ddot{A}\mathbf{d}|$ in each frame are: (a) 0.049 nm, (b) 0.103 nm, (c) 0.392 nm, (d) 0.593 nm, (e) 0.629 nm, and (f) 0.705 nm.

8.4 Local yielding criterion

One way to investigate the character of the local yielding condition proposed in section 8.3 above is to recognize that each of the autocatalytic avalanches of unit events that account for the observed stress relaxations must have been initiated or "triggered" when such a condition was satisfied. It should therefore be possible to find the characteristics of local yielding by investigating the onset of discrete relaxations. In agreement with the discussion in section 4.3.2, the onset of each discrete relaxation was accompanied by the vanishing of the stiffness of one of the normal modes of the complete Hessian matrix for the a-Si system, as illustrated in figure 8-20 (the method of finding these stiffnesses was described in section 4.5.1).

Figures 8-21 and 8-22 show that the decrease of successive normal mode stiffnesses below zero and their eventual increase back towards positive values also accompanies the progress of inelastic transformations themselves. The consecutive vanishing of these normal mode stiffnesses corresponds to the repetitive onset of local yielding during the autocatalytic avalanches of unit events in the a-Si systems after the initial triggering of a stress relaxation. These successive onset phenomena could also serve as a basis for the study of local yielding in a-Si, but it is easier to only consider the initial triggering of stress relaxation instead.

All 4201 stress relaxations observed in the PEM deformation simulations discussed in section 8.1 satisfied the conditions $V_1' \neq 0$ and $V_{111} \neq 0$ at their onset, confirming that they were all triggered by a process describable as a saddle-node bifurcation, as stated in section 4.3.2. The shape of the eigenmode corresponding to the eigenstiffness whose value vanishes at the mechanical threshold (i.e. the critical eigenmode or CE) can be used to find a cluster of atoms that triggers the ensuing stress relaxation according to the method developed in section 4.4.2. Figures 8-23 and 8-24 show visualizations of two such "triggering inclusions." These two inclusions were found at the mechanical thresholds associated with the transforming inclusions visualized in figures 8-9 and 8-10.

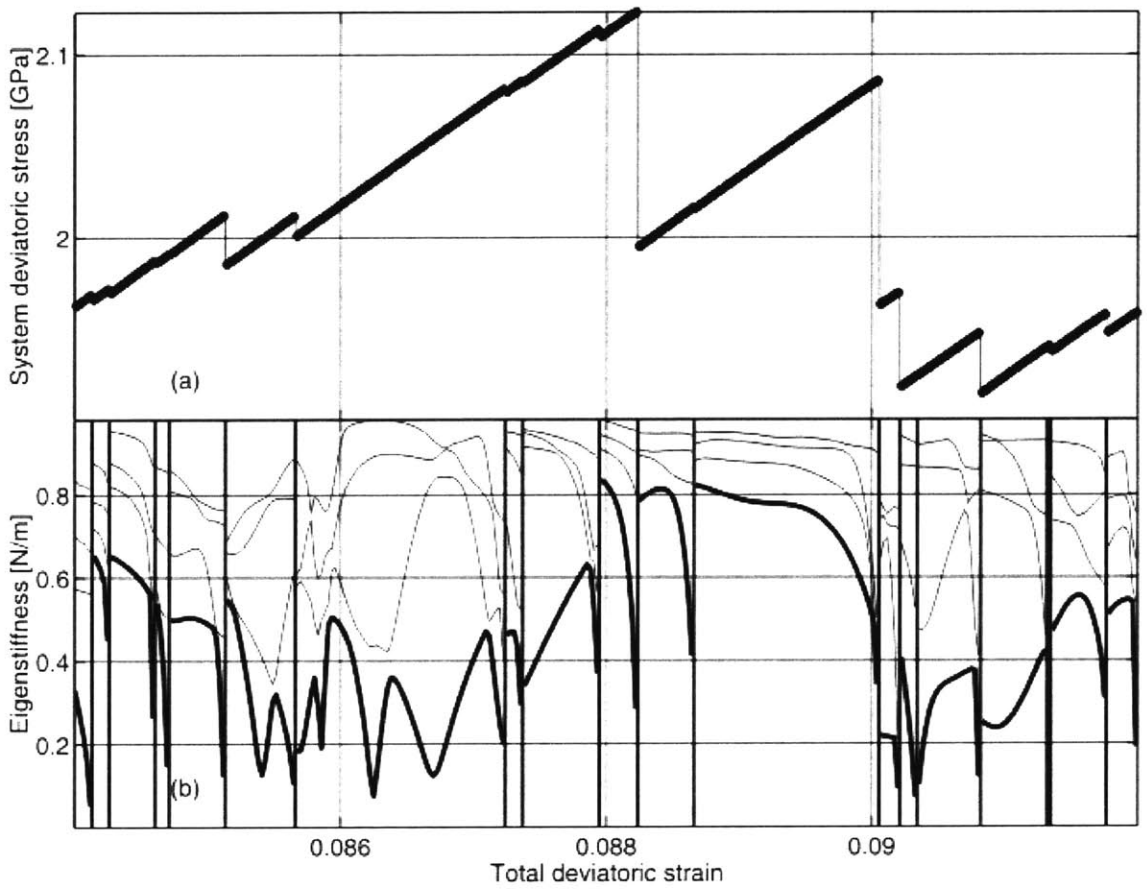

Figure 8-20: The onset of every discrete stress relaxation is accompanied by the vanishing of the stiffness of one of the normal modes of the complete Hessian matrix for the a-Si system. Data for this figure was obtained from PEM deformation of the a-Si system with $\rho/\rho_0 = 1.0694$ in the range of total deviatoric stress presented above.

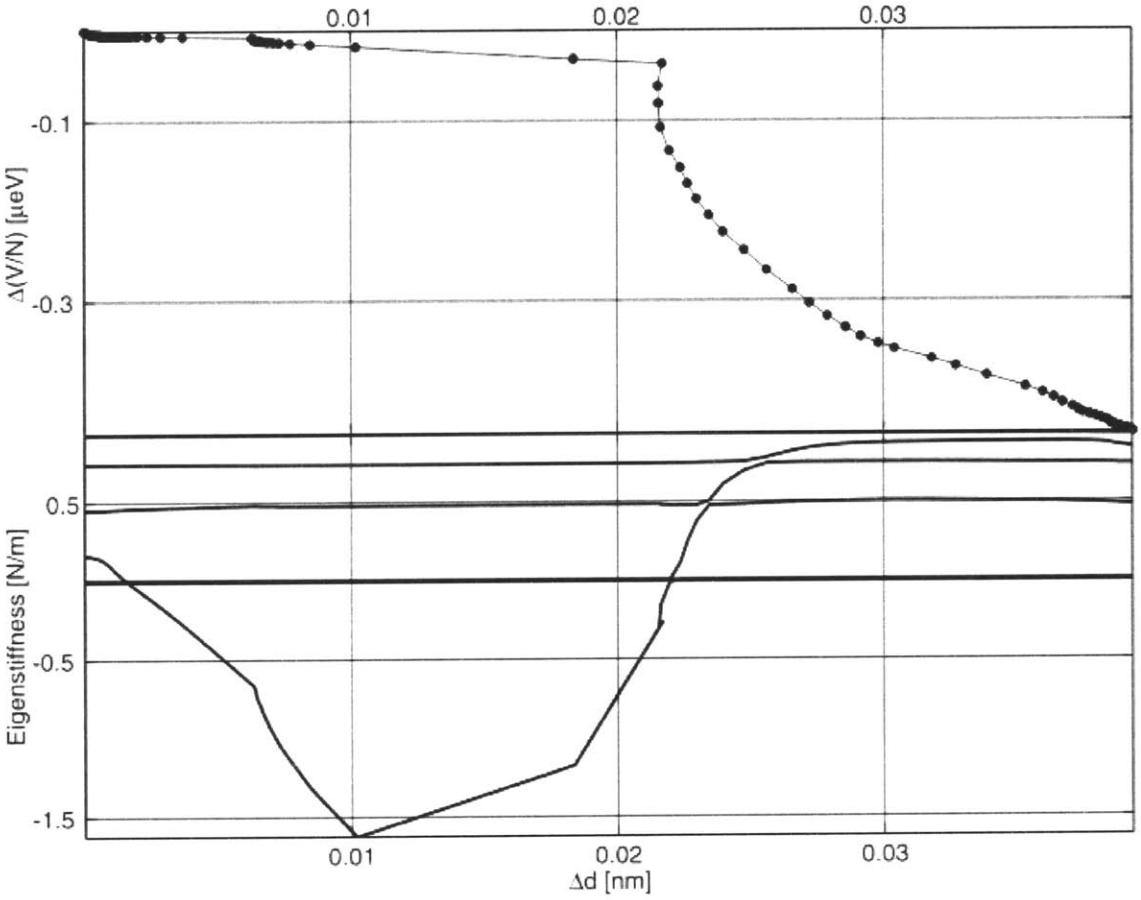

Figure 8-21: The decrease of a normal mode stiffness below zero and its eventual increase back towards positive values accompanies the progress of the small inelastic transformation analyzed in figure 8-17 and visualized in figure 8-9.

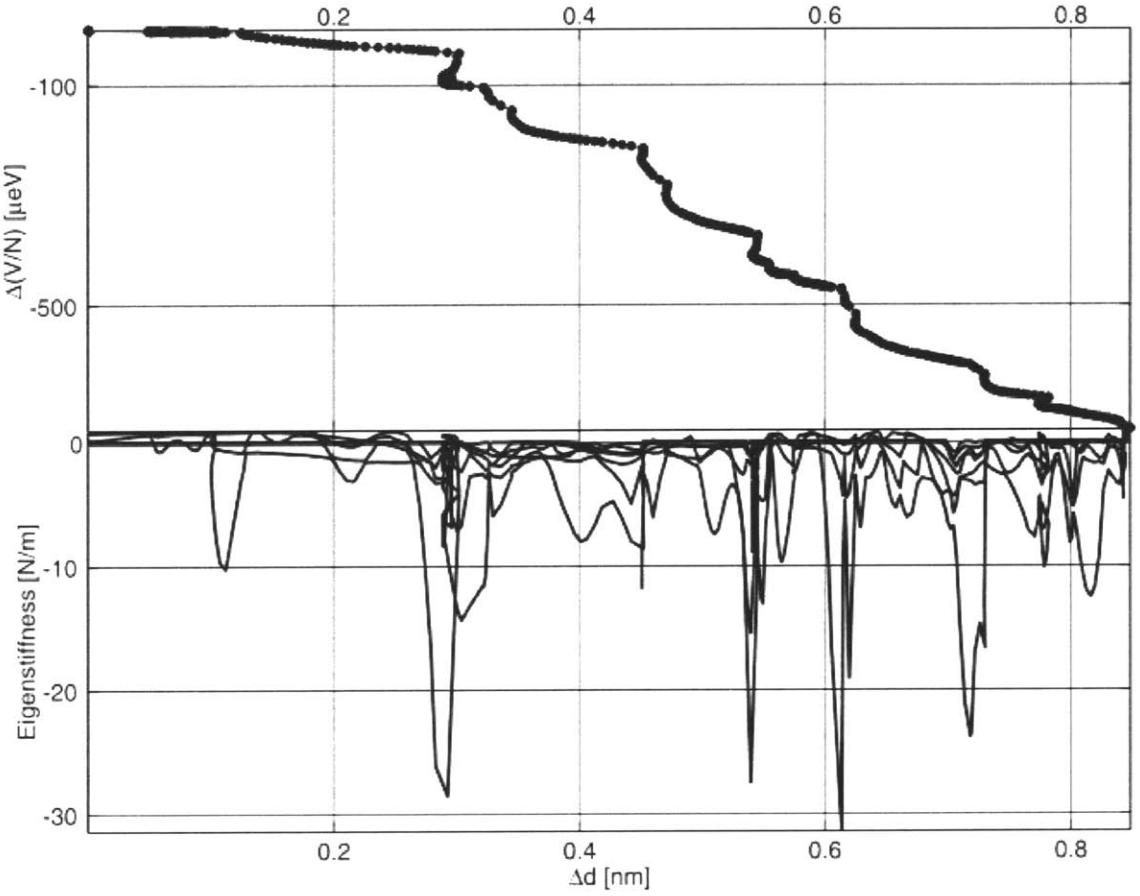

Figure 8-22: The decrease of successive normal mode stiffnesses below zero and their eventual increase back towards positive values accompanies the progress of the large inelastic transformations analyzed in figure 8-18 and visualized in figure 8-10.

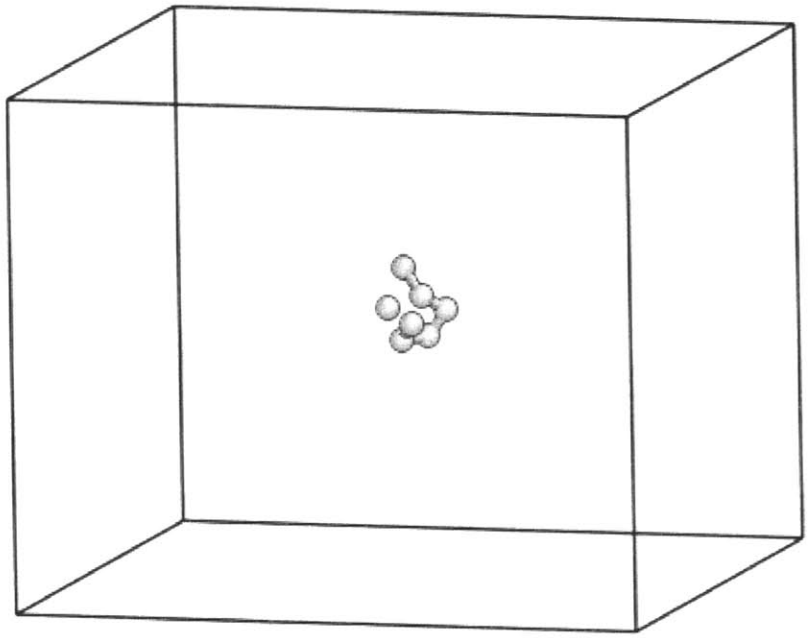

Figure 8-23: The triggering inclusion found at onset of the stress relaxation associated with the transforming inclusion visualized in figure 8-9. This inclusion consists of 7 atoms.

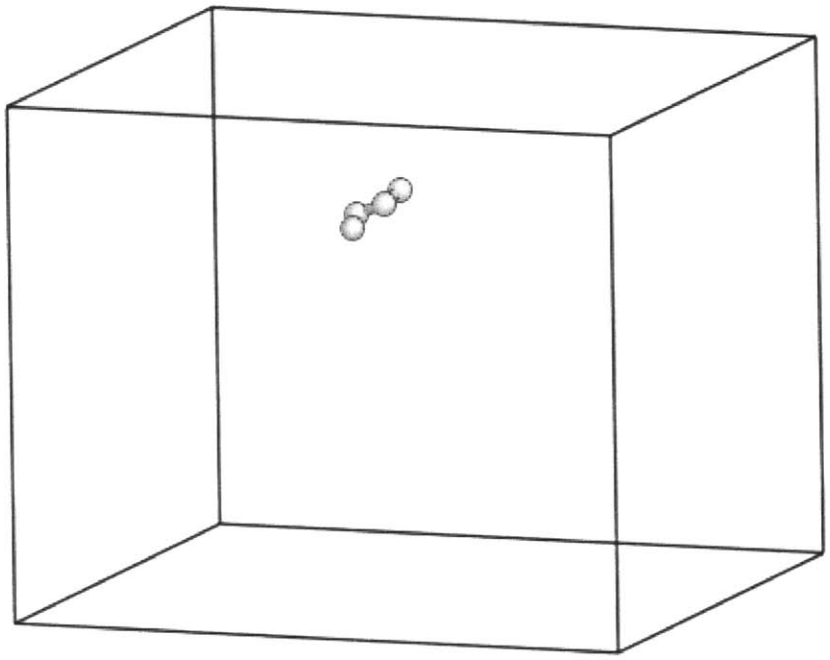

Figure 8-24: The triggering inclusion found at onset of the stress relaxation associated with the transforming inclusion visualized in figure 8-10. This inclusion consists of 4 atoms.

The triggering inclusions in figures 8-23 and 8-24 are compact and well localized. They consist of 7 and 4 atoms, while the corresponding transforming inclusions (figures 8-9 and 8-10) contain 12 and 154 constituent atoms, respectively. By investigating the onset of the 4201 stress relaxations found in this study, it was determined that triggering inclusion sizes are distributed exponentially with an average of 7.3 atoms per inclusion. The distribution of triggering inclusion sizes is plotted in figure 8-25. Furthermore, as shown in figures 8-26 through 8-28, the sizes of these inclusions are not correlated to the components of the ensuing stress relaxation increments or the sizes of the associated transforming inclusions, suggesting that all irreversible stress relaxations—regardless of their magnitude—are triggered in the same way on average.

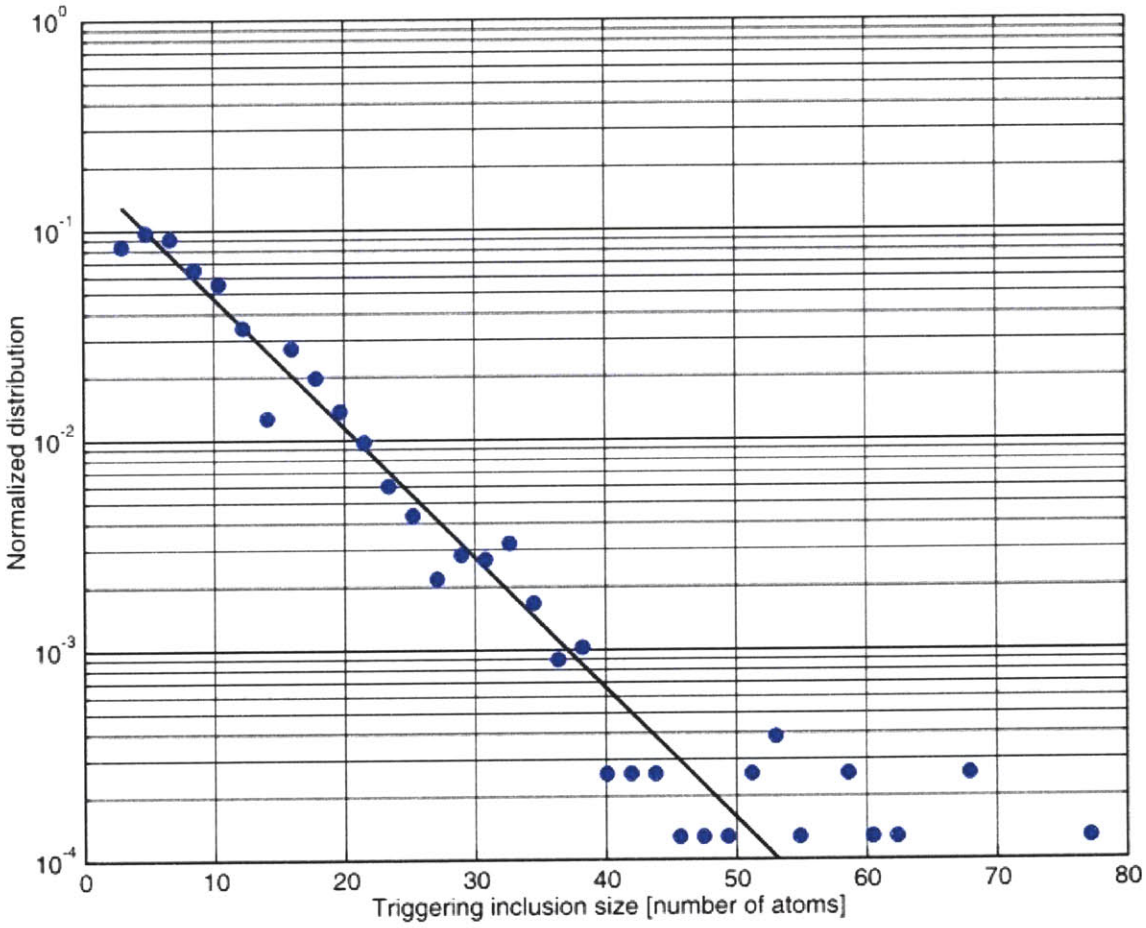

Figure 8-25: The sizes of triggering inclusions follow an exponential distribution.

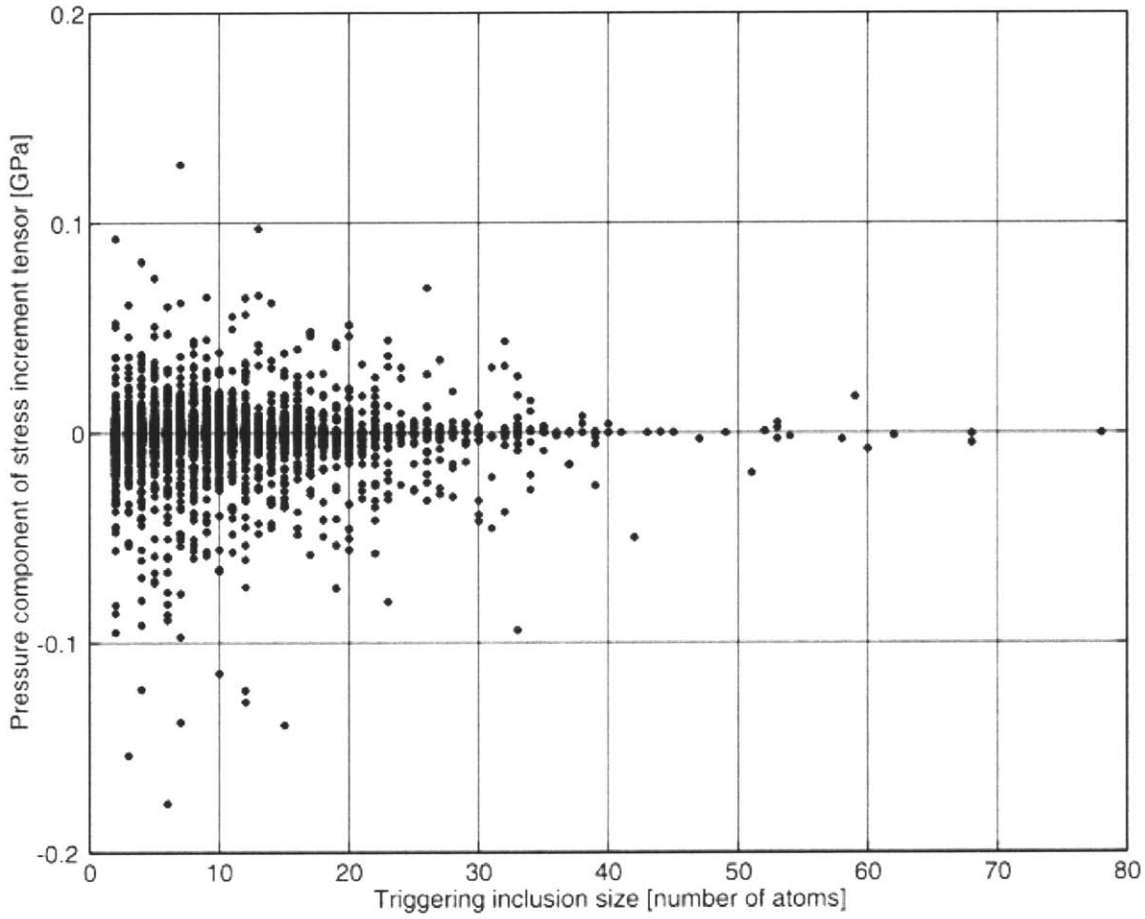

Figure 8-26: Triggering inclusion sizes are not correlated to pressure component $p(\ddot{A}\hat{o})$ of stress relaxation increment tensor $\ddot{A}\hat{o}$.

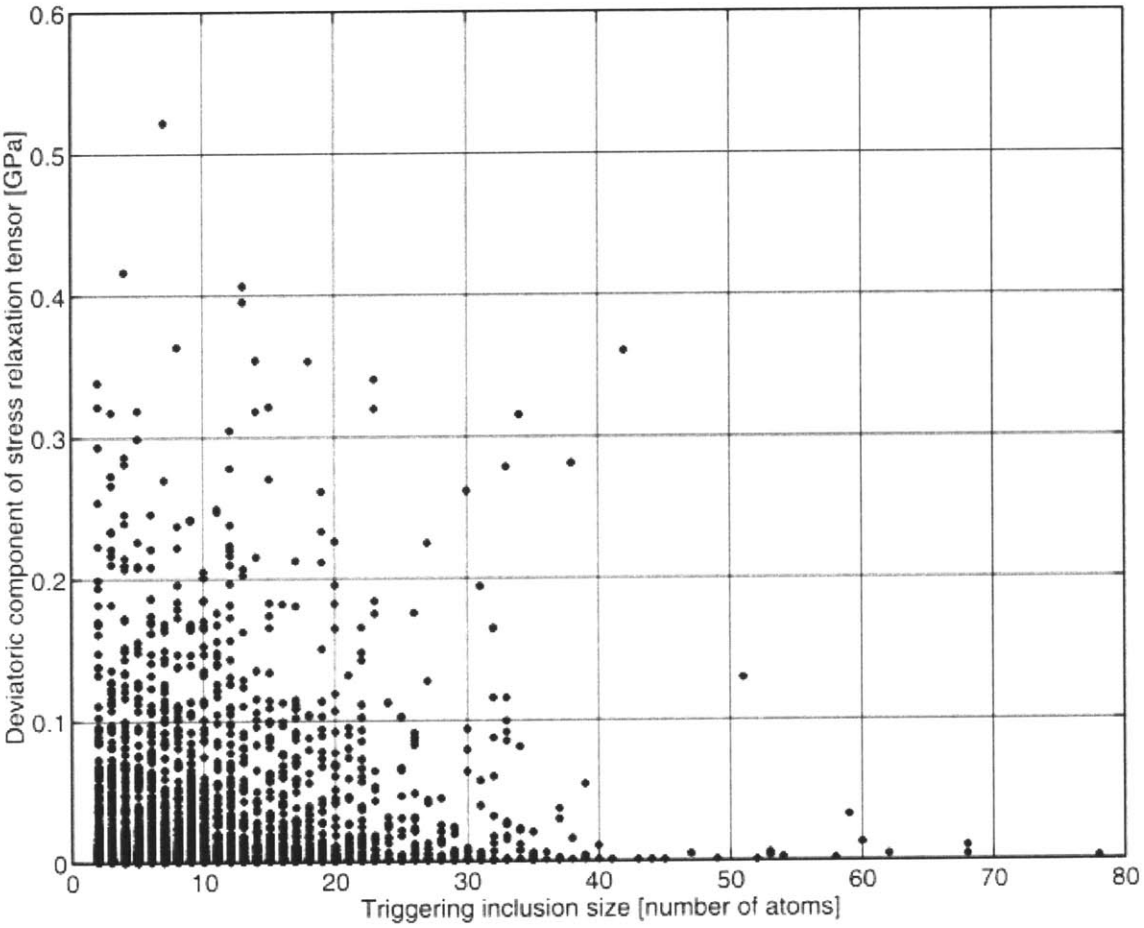

Figure 8-27: Triggering inclusion sizes are not correlated to deviatoric component $\overline{\sigma}(\ddot{A}\hat{o})$ of stress relaxation increment tensor $\ddot{A}\hat{o}$.

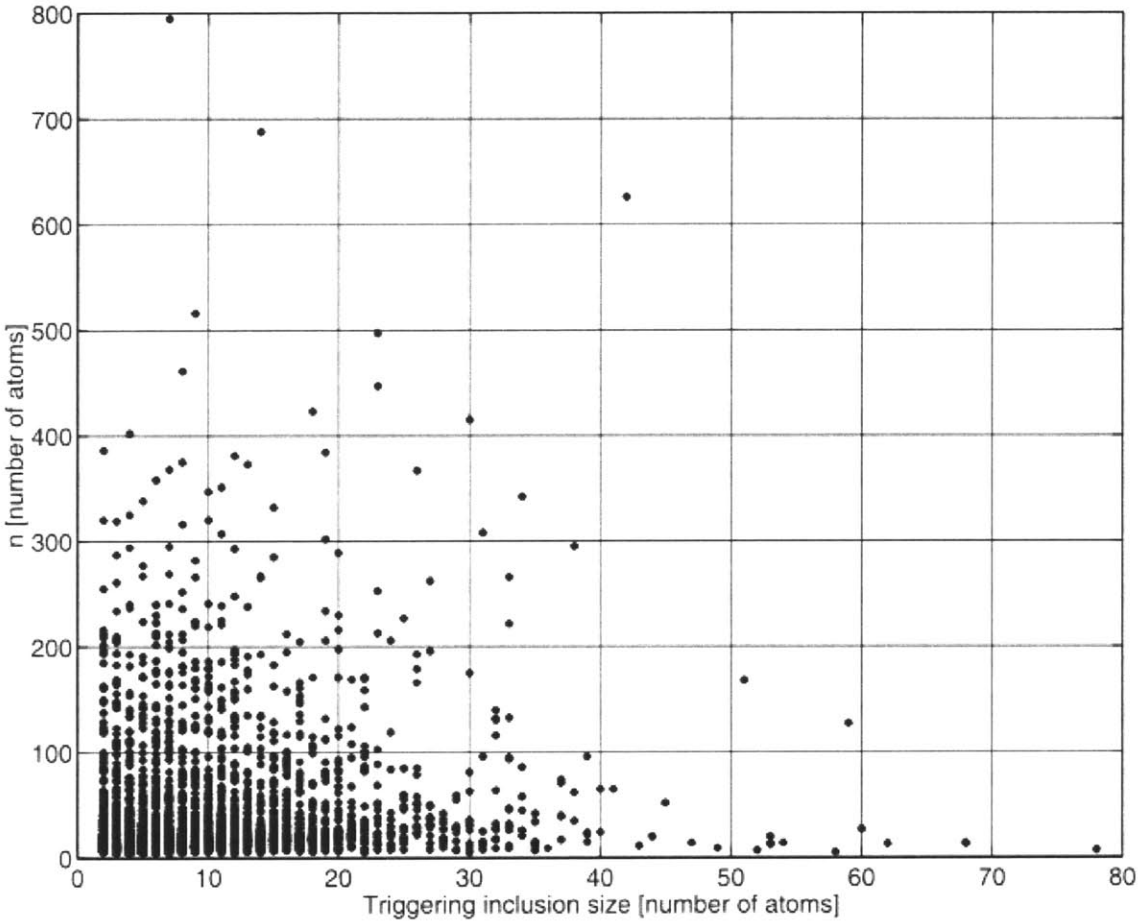

Figure 8-28: Triggering inclusion sizes are not correlated to the sizes n of inelastically transforming inclusions.

To determine the local yielding criterion leading to the onset of stress relaxations, the total stress tensor characterizing the environment of each triggering inclusion was found. This determination is accomplished by summing up the individual atomic stress tensors (section 4.2.2) of all atoms in a cluster composed of the inclusion atoms along with their nearest neighbors. The pressure and deviatoric components of this stress tensor $p(\ddot{\mathbf{A}}\hat{\mathbf{o}})$ and $\bar{\sigma}(\ddot{\mathbf{A}}\hat{\mathbf{o}})$ are obtained. The mass fraction ϕ of liquidlike material in the clusters is also calculated. In about 8.7% of all cases it is found that the triggering inclusion consists of 2 or 3 distinct atomic clusters. In such situations, both the stress state and ϕ are determined separately for each cluster.

Figures 8-29 and 8-30 plot average values of the cluster deviatoric stress as a function of the cluster pressure and ϕ. A clear quadratic dependence of the deviatoric stress on both quantities confirms the existence of a well-defined micro-yield surface. As expected based on the results in chapter 7, figure 8-29 confirms that increasing ϕ results in a declining yield stress. It also shows, however, that for high enough ϕ this trend reverses and an increasing yield stress is observed. The minimum yield stress occurs at about $\phi = 0.6$. Figure 8-30 shows that the dependence of yield stress on pressure is relatively less pronounced than the dependence on ϕ. Minimum yield stresses are achieved at about zero pressure. According to the analysis in section 8.3, inelastic transformations in a-Si proceed as autocatalytic avalanches of unit inelastic shearing events so long as the local yielding criterion presented in figures 8-29 and 8-30 is satisfied at some location in the system.

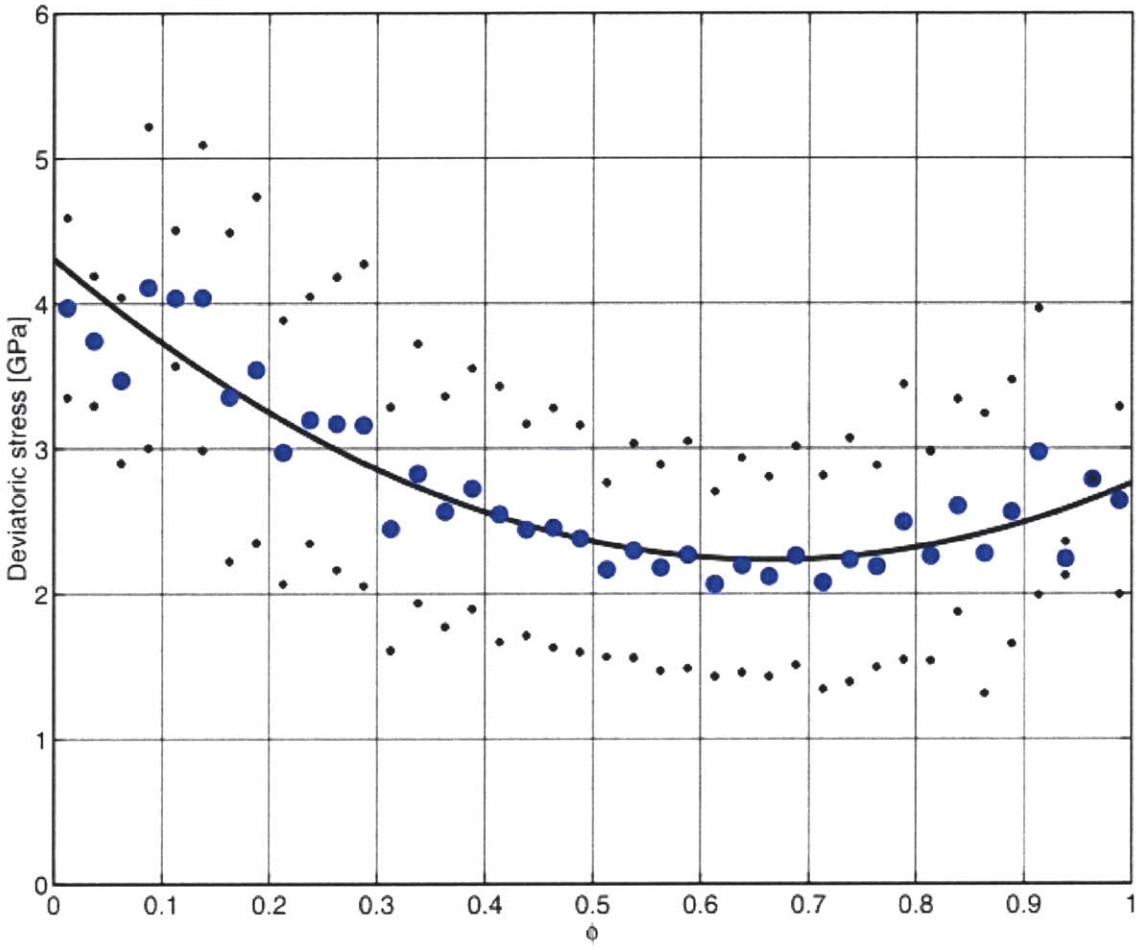

Figure 8-29: Average dependence of the local deviatoric stress $\overline{\sigma}(\hat{\mathbf{o}})$ of triggering inclusion clusters on the liquidlike mass fraction ϕ of those clusters. Small dots denote the envelope of ± one standard deviation. The dependence exhibited is described well by a quadratic fit.

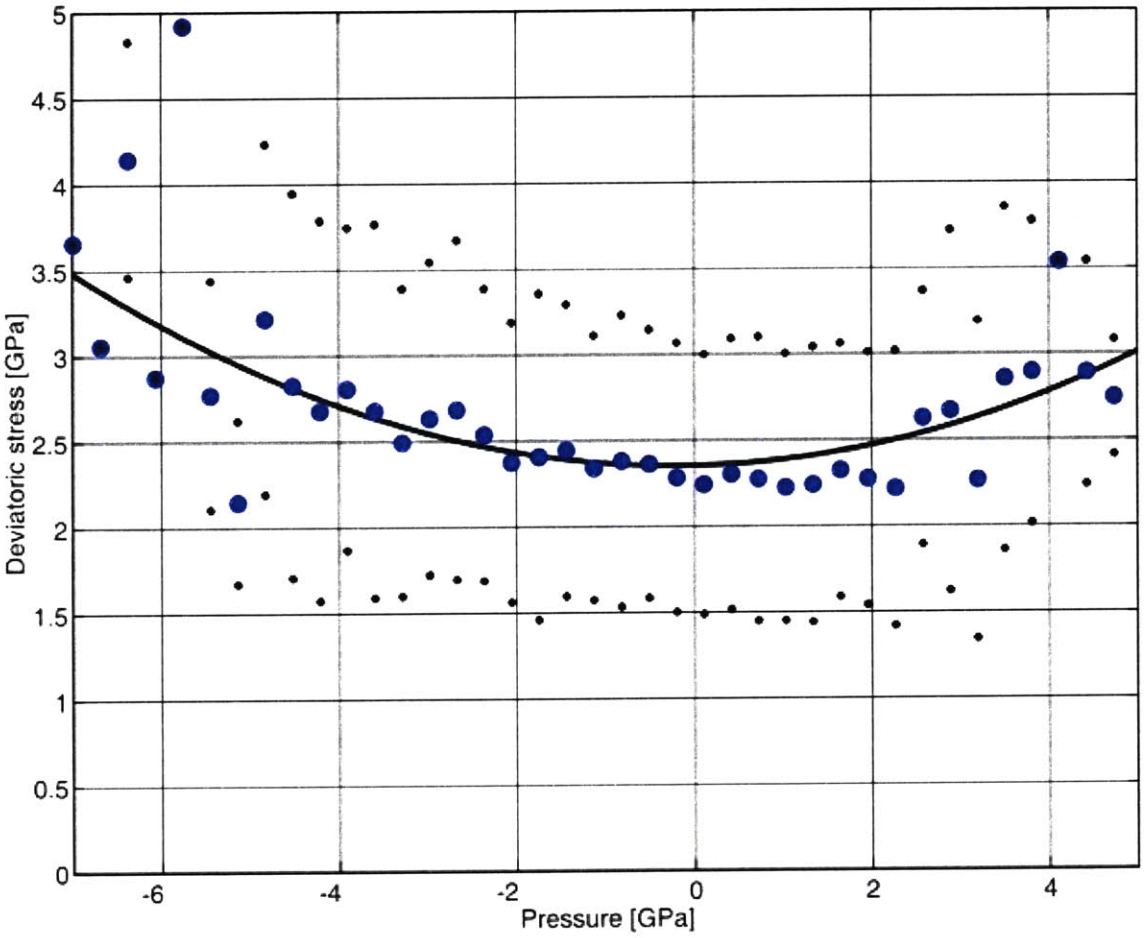

Figure 8-30: Average dependence of the local deviatoric stress $\bar{\sigma}(\hat{\mathbf{o}})$ of triggering inclusion clusters on their pressure $p(\hat{\mathbf{o}})$. Small dots denote the envelope of ± one standard deviation. The dependence exhibited is described well by a quadratic fit.

9. Structure and kinematics of unit shearing events

This chapter describes the statistical approaches used to characterize the geometry of the unit inelastic shearing events postulated in chapter 8. The characterization is accomplished by finding recurring structural and kinematical features of bonding configurations in the 4201 triggering and transforming inclusions found during PEM deformation simulations. The unit shearing event is found to consist of bond length transitions across a characteristic instability-producing bond (IPB) length between the two split peaks of the second nearest neighbor shell in the RDF for bulk a-Si in steady-state flow. The nearest neighbor environments of bonds undergoing such transitions are found to undergo bond angle changes that correlate to the underlying bond length change.

9.1 Statistical approach to characterizing unit events

It was argued in chapter 8 that there exists a unit inelastic structure transformation characteristic of a-Si that is responsible for stress relaxations as well as their initial triggering. Simple inspection of the structure of triggering inclusions (figures 8-23 and 8-24) and inelastically transforming inclusions (figures 8-9 and 8-10), however, revealed no such readily identifiable atomic rearrangement. Information concerning recurring structural and kinematical features at onset of stress relaxations can nevertheless be obtained by adopting a statistical approach to the analysis of the structure and the kinematics of transformation of triggering and transforming inclusions.

Previous studies [Bernstein *et al.*, 2000; Valiquette, Mousseau, 2003] of mechanisms of structure transformations in a-Si for phenomena other than plastic flow reveal the importance of developing appropriate methods of "pattern recognition" to extract recurring features from large sets of events. Certain such methods tailored to the needs of studies of stress-induced inelastic deformation have made their appearance in work on dry foams [Kabla, Debregeas, 2003] and silica glass [Ekunwe, Lacks, 2002]. The new approaches developed for the work presented here rely on evaluating combined

distribution functions over all 4201 triggering and transforming inclusions observed during the course of PEM deformation simulations (see chapter 8). They will be described as they arise in the following sections.

9.2 Instability-producing bonds (IPBs) in triggering inclusions

Bond lengths characteristic of triggering inclusions were found by compiling a histogram of all the collected interatomic distances present in each of the 4201 triggering inclusion found in the course of PEM deformation simulations (see chapter 8). To facilitate comparison with the bonding characteristics of bulk a-Si, this histogram was scaled in the same way as a radial distribution function (RDF) of bulk material is usually scaled [Allen, Tildesley, 2000]. Such a structure analysis process yields an "ensemble average RDF"—plotted in figure 9-1—for material comprising triggering inclusions. Since the triggering inclusions are compact, it is not surprising that they contain few atom pairs separated by distances larger than the second-nearest neighbor distance in bulk a-Si, as reflected by the vanishing of the ensemble average RDF at large distances. Their compactness also explains the common occurrence of nearest-neighbor bonds. Within the second-nearest neighbor shell, however, the ensemble average RDF reveals a striking deviation in the bonding environments of triggering inclusions from those of bulk a-Si. Specifically, the split second nearest neighbor peak of bulk a-Si is suppressed while the bond length corresponding to the trough between its two parts is highly over-represented. This bond length is within the cutoff distance for direct atomic interaction in the SW potential (1.8 in reduced units, i.e. 0.377 nm; see section 3.2.1).

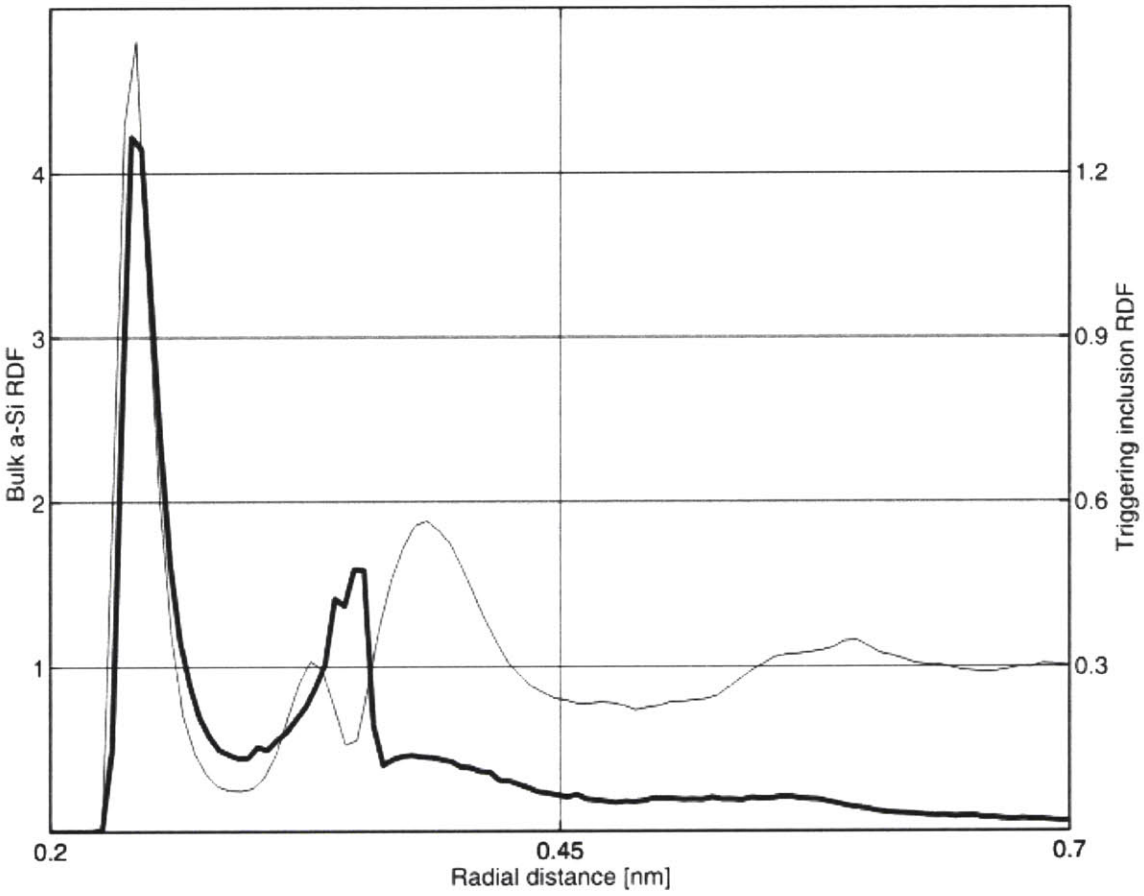

Figure 9-1: A radial distribution function (RDF) compiled from interatomic distances among atoms comprising triggering inclusions (thick line) is compared to a typical RDF for bulk a-Si in a state of steady flow (thin line). The two parts of the split second nearest neighbor peak observed in bulk a-Si are missing from the triggering inclusion RDF while bond lengths corresponding to the trough between them are over-represented.

In addition to the structural information contained in the atomic arrangement of each triggering inclusion, characteristics of the kinematics of onset of stress relaxations can be found by investigating the shape of the normal mode whose stiffness vanishes (i.e. of the "soft mode" or CE; see section 4.3). The relative atomic displacements contained in the CE at the onset of each stress relaxation can be used to find the relative changes in interatomic distances in each triggering inclusion according to the formula

$$\dot{r}_{ij} = \frac{r_{ij,x}}{r_{ij}}\left(s\cdot\hat{e}_{j,x} - s\cdot\hat{e}_{i,x}\right) + \frac{r_{ij,y}}{r_{ij}}\left(s\cdot\hat{e}_{j,y} - s\cdot\hat{e}_{i,y}\right) + \frac{r_{ij,z}}{r_{ij}}\left(s\cdot\hat{e}_{j,z} - s\cdot\hat{e}_{i,z}\right). \tag{9.1}$$

where $\hat{e}_{j,x}$ is the x-component of the displacement of atom j from the complete unit CE vector $\hat{\mathbf{e}}$, $r_{ij,x}$ is the x-component of the position vector of atom j with respect to atom i, and $\dot{r}_{ij}$ is the change of distance between the two atoms for displacements along the CE. Each CE is defined to within the arbitrary multiplicative constant s, as in section 4.4.2 (equation 4.36). For convenience, this constant is chosen in each case so that the greatest absolute value of change in interatomic distance in the triggering inclusion is unity, i.e. $\left|\dot{r}_{ij}\right|_{\max} = 1$. After all relative changes of interatomic distances in each of the 4201 triggering inclusions have been computed, the average of their absolute values is found as a function of the interatomic distance itself. An analogue of the ensemble average RDF is thereby obtained except that instead of characterizing the average *density* of triggering inclusion material at a given interatomic separation it specifies the average *absolute value of the relative change in interatomic distance* as a function of interatomic separation.

The function described above is presented in figure 9-2. It shows that the nearest-neighbor bond lengths in triggering inclusions undergo the least relative length change at onset of stress relaxations, i.e. they are the stiffest bonds. Meanwhile, the bond lengths corresponding to the trough of the split second nearest neighbor peak in bulk a-Si undergo the most pronounced length changes at the onset of stress relaxations: they dominate the kinematics of triggering of internal structural transformations. To

underscore their role in triggering local yielding, these bond lengths shall be given the suggestive name of "instability-producing bonds" or IPBs. There is a third bond length that undergoes relatively large length changes at the onset of stress relaxations. It is the length located between the first and second nearest neighbor shells of bulk a-Si, as figure 9-2 shows. This bond, however, is not commonly present in the triggering inclusions (figure 9-1) and so is not accorded a similar role to that of the IPBs.

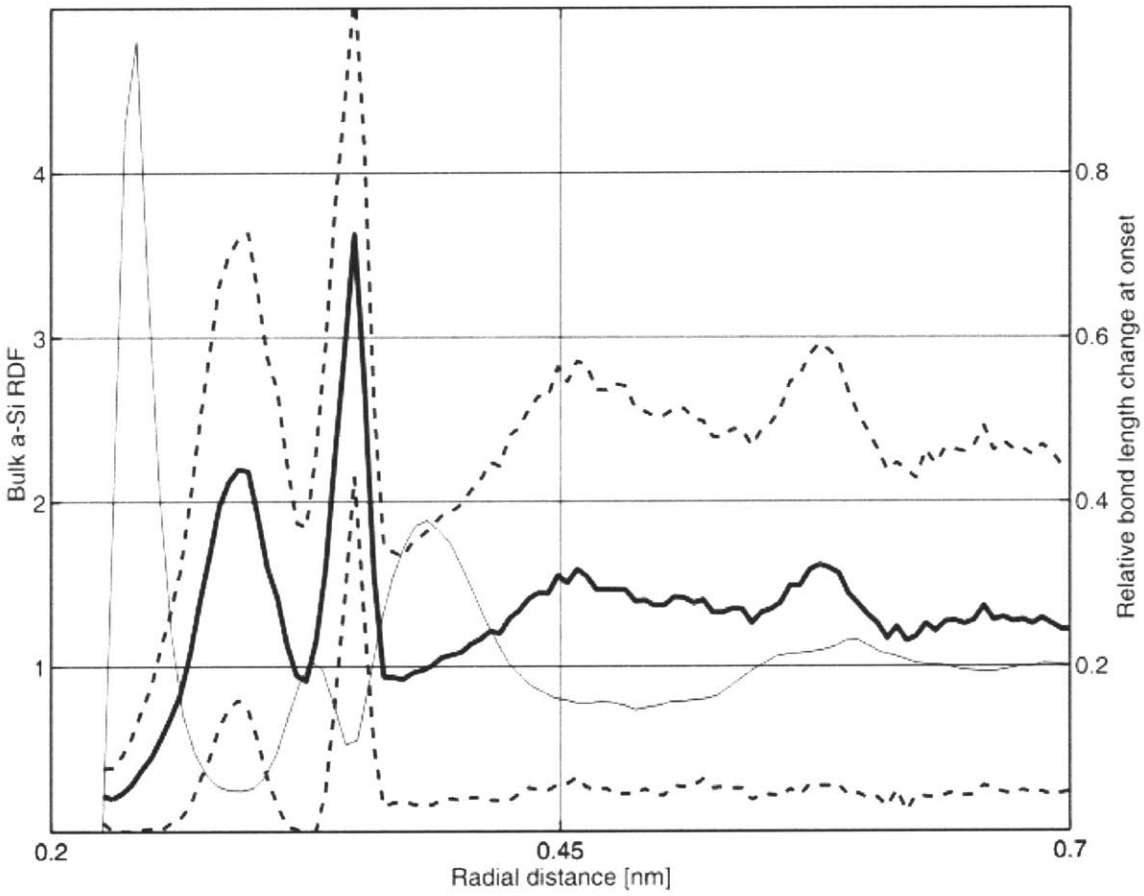

Figure 9-2: The radial distribution of average relative bond length changes in triggering inclusions at onset of stress relaxations (thick solid line) is compared to a typical RDF for bulk a-Si in steady state flow (thin line). The thick dashed lines represent the envelope of ± one standard deviation. Bond lengths corresponding to the trough between two parts of the split second nearest neighbor peak in a-Si undergo the largest relative length changes at onset of stress relaxations.

If IPBs are the fundamental structural components of the unit shearing events responsible for triggering plasticity in a-Si, then they must interact with their immediate

atomic environments to produce shear strains. In particular, IPB length changes should induce rearrangements in the nearest neighbor shells of the atoms at the IPB endpoints. These rearrangements must not involve significant displacements of nearest neighbor atoms out of their shells since—according to figure 9-2—nearest neighbor bond lengths do not change appreciably during onset of stress relaxations. The rearrangements should therefore amount to the reshuffling of atoms within the nearest neighbor shells themselves. For every nearest neighbor of atoms at IPB endpoints, such reshuffling can be described by changes in the two angles pictured in figure 9-3: one axial (α) and the other lateral (β).

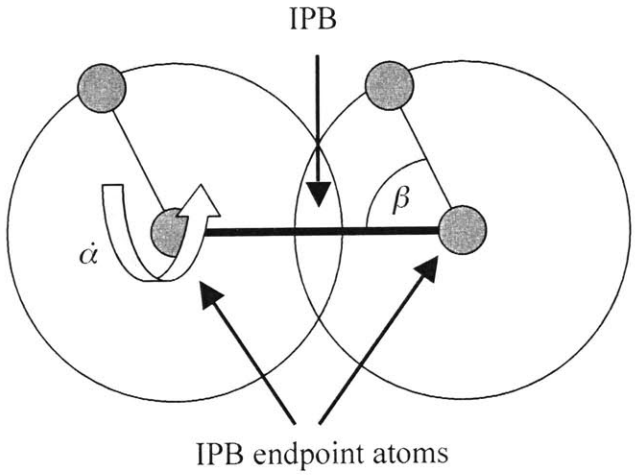

Figure 9-3: Since nearest neighbor bond lengths do not undergo significant length changes at onset of stress relaxations, the rearrangement of atoms in the nearest neighbor shells of IPB endpoints can be described by changes in the axial angle α and lateral angle β.

To characterize the nearest neighbor distribution as a function of lateral angle β, all such angles for all atoms in the 4201 triggering inclusions that are in the nearest neighbor shells of IPB endpoint atoms were found. A histogram of these lateral angles is presented in figure 9-4.a. Furthermore, the relative changes of lateral angles $\dot{\beta}$ at onset of stress relaxations can be determined directly from the shape of the CE, much as relative bond length changes can be found from the CE using equation 9.1. For ease of comparison with the relative length change of the underlying IPB, $\dot{\beta}$ for each atom was

multiplied by its (relatively unchanging) distance to the IPB endpoint upon which it neighbors and then divided by the relative length change of the underlying IPB (to avoid dividing by numbers close to zero, only IPBs with absolute values of relative length change above 0.7 were considered). The quantities thus determined characterize lateral incremental atomic displacements tangent to their nearest neighbor shells per unit length change of the underlying IPB. Plotting the averages of these relative tangential displacements against the lateral angles at which they occur yields figure 9-4.b. Note the similarity in the analysis described above to the one carried out before on triggering inclusion interatomic distances and their relative changes. Indeed, figure 9-4.b is to figure 9-4.a what figure 9-2 is to figure 9-1.

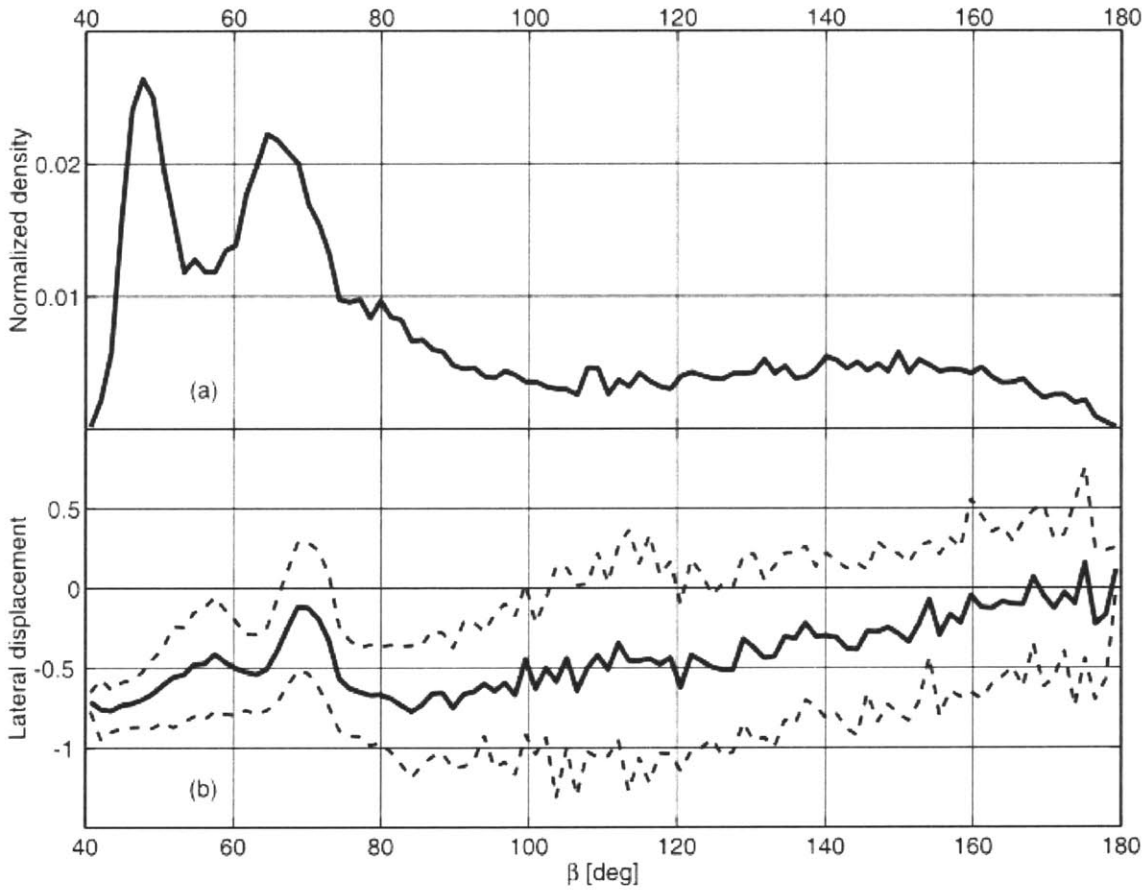

Figure 9-4: The distribution of lateral bond angles β for IPBs in triggering inclusions shows concentrations of atoms at 47 and 65 degrees (a). The corresponding average lateral displacements (see text for definition) are negatively correlated to the length change of the underlying IPB and are greatest for atoms at lateral angles of about 47 degrees (b). The dashed lines in (b) represent the envelope of $\pm$ one standard deviation.

Figure 9-4.a demonstrates that high concentrations of IPB endpoint nearest neighbor atoms occur at lateral angles of about 47 and 65 degrees. Of these two angles, the one at 47 degrees exhibits the largest relative changes at onset of stress relaxations, as indicated in figure 9-4.b. Figure 9-4.b also shows that changes in lateral angles are generally negatively correlated to the change in length of the underlying IPBs, i.e. β increases when the underlying IPB length decreases and vice versa. It would be tempting to think that the nearest neighbor atoms of IPB endpoints at lateral angles around 47 and 65 degrees occur in some characteristic numbers or mutual configurations. No clear evidence of such regularities was found, however, so the results of the above analysis must be interpreted as characterizing the structure and kinematics of IPB endpoint nearest neighbor shells *on average* with the understanding that the environments of specific individual IPBs may vary. It is not inconceivable that if a more sophisticated "pattern recognition" scheme than the one described were applied, a finite catalogue of atomic configurations surrounding IPB endpoints could be compiled. The compilation of such a catalogue, however, was not attempted in this study.

A similar analysis to the one presented above was carried out for changes in the axial angles α, but no readily recognizable characteristic kinematical behavior of the nearest neighbors of IPB endpoint atoms was found. Distributions of nearest neighbor bond angles in the triggering inclusions as well as of their relative changes were also investigated, but did not yield any unambiguous insights. Within the limits of the structure analysis schemes used in this study, therefore, it can be concluded that the IPBs and the associated regularities in the nearest neighbor shells of their endpoint atoms are the only atomic arrangements characteristic of a-Si material comprising triggering inclusions and leading to onset of local yielding. The number of IPBs per triggering inclusion appears to be proportional to the number of atoms comprising the inclusion, with an average of about 12 IPBs per inclusion.

9.3 Bond length transitions in second-nearest neighbor shell

To confirm that unit plastic events in a-Si consist of shear transformations involving IPBs and the nearest neighbor shells of their endpoints, an analysis analogous to the one presented in section 9.2 above was carried out on the transforming inclusions associated with the stress relaxations that follow each triggering event (see chapter 8). While the kinematics of triggering inclusions is described by the relative incremental atomic displacements in the CE, however, during the ensuing stress relaxations each atom displaces by some finite amount with respect to all other atoms. Therefore, instead of evaluating the relative change in interatomic distances as before, the distance between each pair of atoms in each transforming inclusion at onset was compared to the finitely different distance between the same pair after the stress relaxation had proceeded to completion. Thus, two interatomic distances are obtained for every pair of atoms in each inelastically transforming inclusion: one at the onset of the stress relaxation and one corresponding to the fully equilibrated final configuration. This calculation was performed in transforming inclusions for all 4201 stress relaxations observed in this study. All of the initial interatomic separations r_i collected this way can be plotted against the corresponding final separations r_f yielding a plot of points scattered in the plane. Points lying close to the diagonal in such a plot denote interatomic distances that do not change appreciably during a stress relaxation. Those lying below the diagonal correspond to distances that decrease while those lying above the diagonal to those that increase. For ease of visualization, a distribution density of these points can be compiled and isocontours of this distribution plotted.

Figure 9-5 shows the result of the analysis described above. Most interatomic distances do not undergo changes that commonly recur, as indicated by the fact that the isocontours are mostly centered on the diagonal. There is only one exceptional interatomic distance with nearby isolated off-diagonal isocontours: the distance corresponding to an IPB length (~0.346 nm; see figures 9-1 and 9-2). These isocontours indicate well-defined transitions of bond lengths from just below the IPB length to just above it, and vice versa. These transitions therefore correspond to bond length migration

between the two portions of the split second nearest neighbor peak in the RDF of bulk a-Si during discrete stress relaxations, as illustrated in figure 9-6.

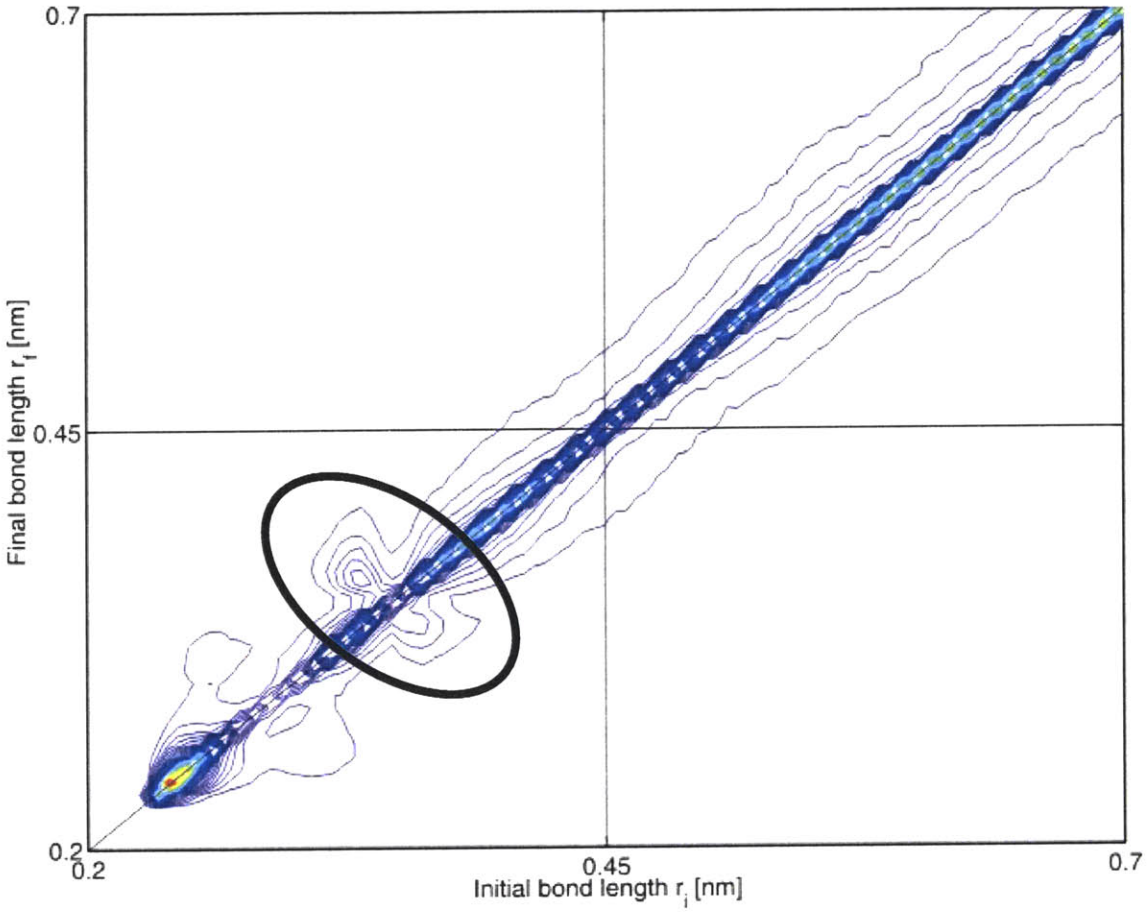

Figure 9-5: Plotting isocontours of distributions of initial vs. final interatomic distances for atoms comprising transforming inclusions of material that deforms inelastically during stress relaxations reveals recurring bond length changes. Most isocontours center on the diagonal, indicating bond lengths that do not change length on average. The clearest departure from this trend occurs in the circled region, which denotes bond length transitions across the IPB length (~0.346 nm).

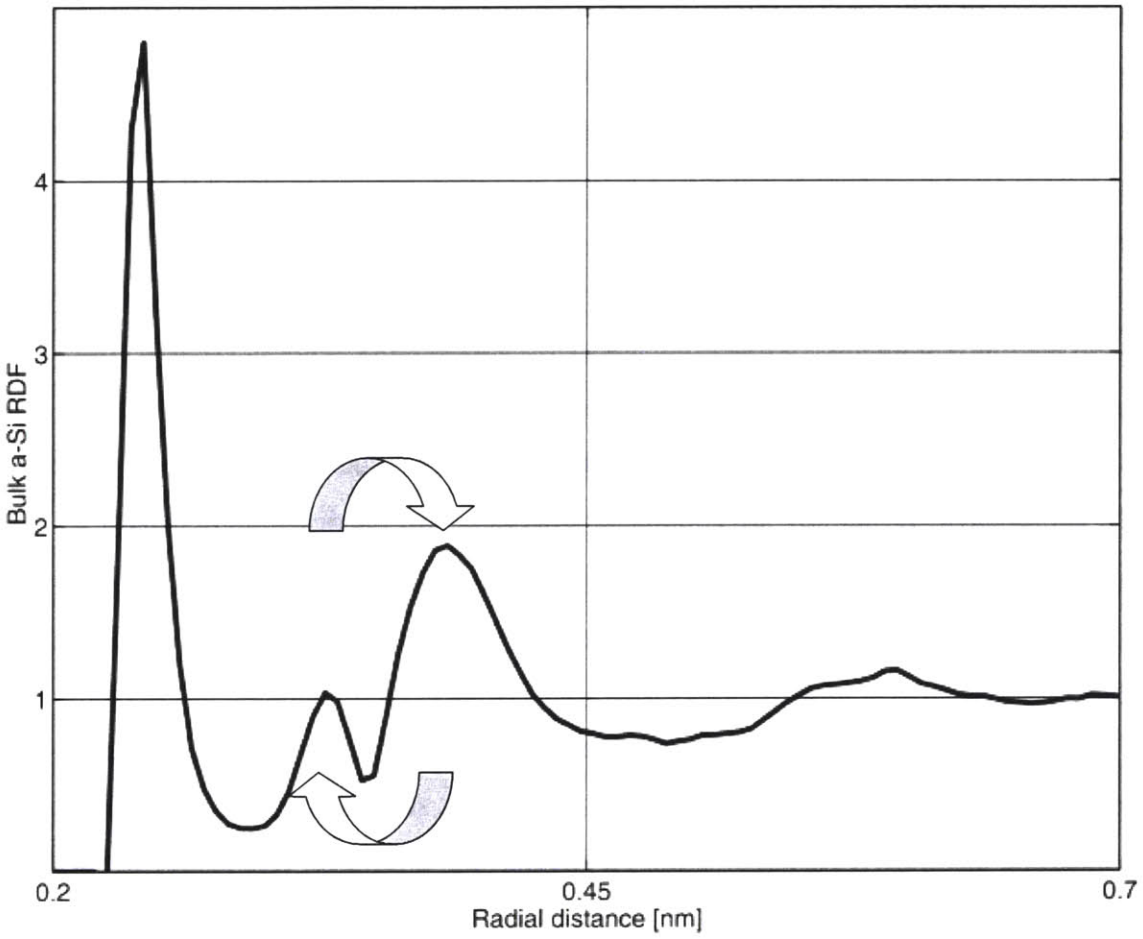

Figure 9-6: The transitions across the IPB length demonstrated in figure 9-5 indicate that inelastic relaxation is accompanied by bond length circulation between the two split peaks of the second-nearest neighbor shell of bulk a-Si undergoing steady flow.

In addition to the behavior close to the IPB length, figure 9-5 indicates some activity in the nearest neighbor shell. It is immediately clear, however, that this activity is mostly confined to the nearest neighbor shell itself, i.e. that during a stress relaxation nearest neighbor bonds are not commonly broken or formed in the inelastically transforming inclusion. This analysis does not imply that isolated bond breaking or –re-forming events do not take place, but rather that they are not characteristically recurring on average and therefore do not play a role of any prominence compared to that of transitions across the IPB length.

Changes in lateral angles of nearest neighbors of endpoint atoms (figure 9-3) of bond lengths that undergo a transition across the IPB length (figure 9-5) can be studied analogously to interatomic distance changes. For every atom in the nearest neighbor shell of an endpoint of a bond length that crosses the IPB length, the initial and final values of the lateral angle β_i and β_f are computed. Isocontours of the distribution density of initial vs. final lateral angle values are plotted in figure 9-7. It is evident that the only lateral angles that undergo transitions that recur on average are the same ones that exhibit the largest changes at onset of stress relaxations (figure 9-4.b), namely ~47 degrees. Finally, figure 9-8 plots the increments in lateral angles against the increments in the underlying bond length changes across the IPB length, showing that changes in lateral angles and the underlying bond lengths are negatively correlated, just as they are at onset of stress relaxations (figure 9-4.b).

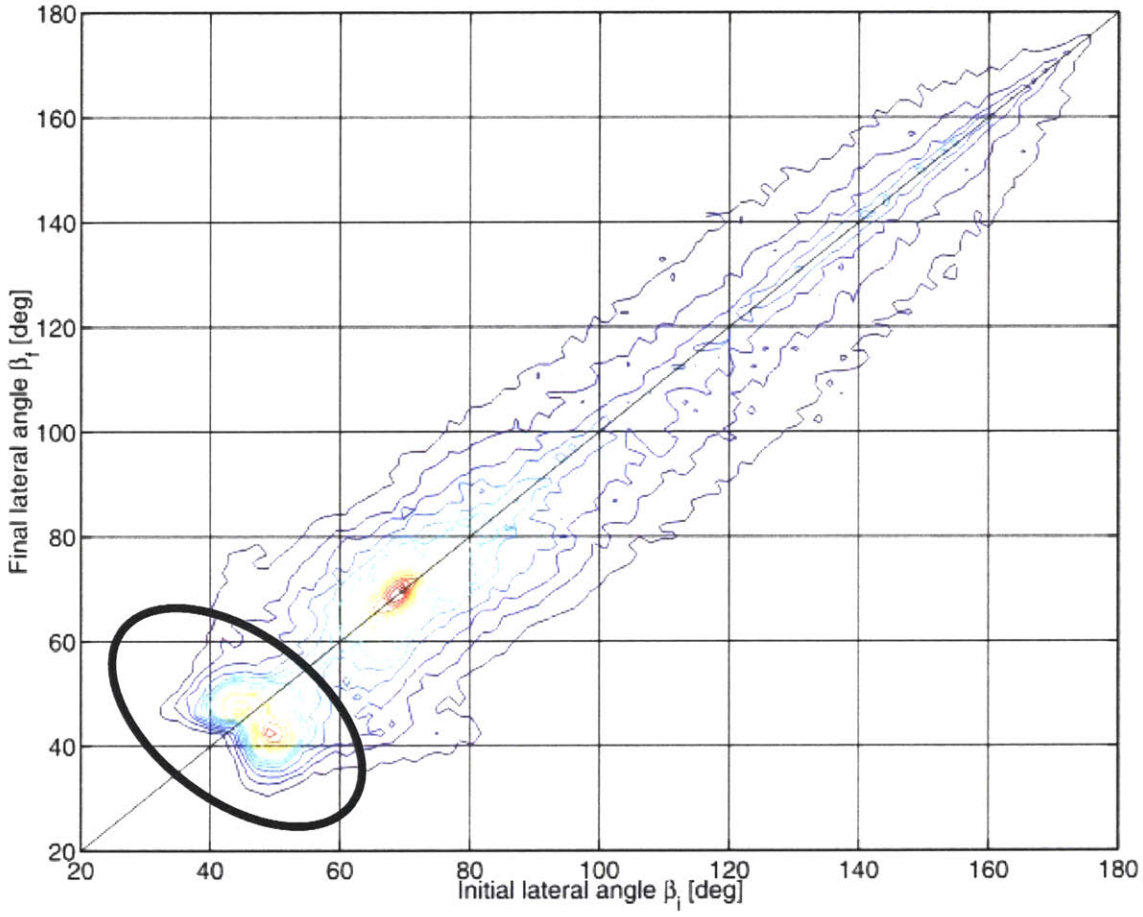

Figure 9-7: Plotting isocontours of distributions of initial vs. final values of lateral angles β (figure 9-3) for atoms in the nearest neighbor shells of endpoints of bonds that transition across the IPB length (figure 9-5) reveals recurring lateral angle changes in the inelastically transforming inclusions. Most isocontours center on the diagonal, indicating angles that do not change on average. The clearest departure from this trend occurs in the circled region, which denotes lateral angle transitions across the ~47 degrees.

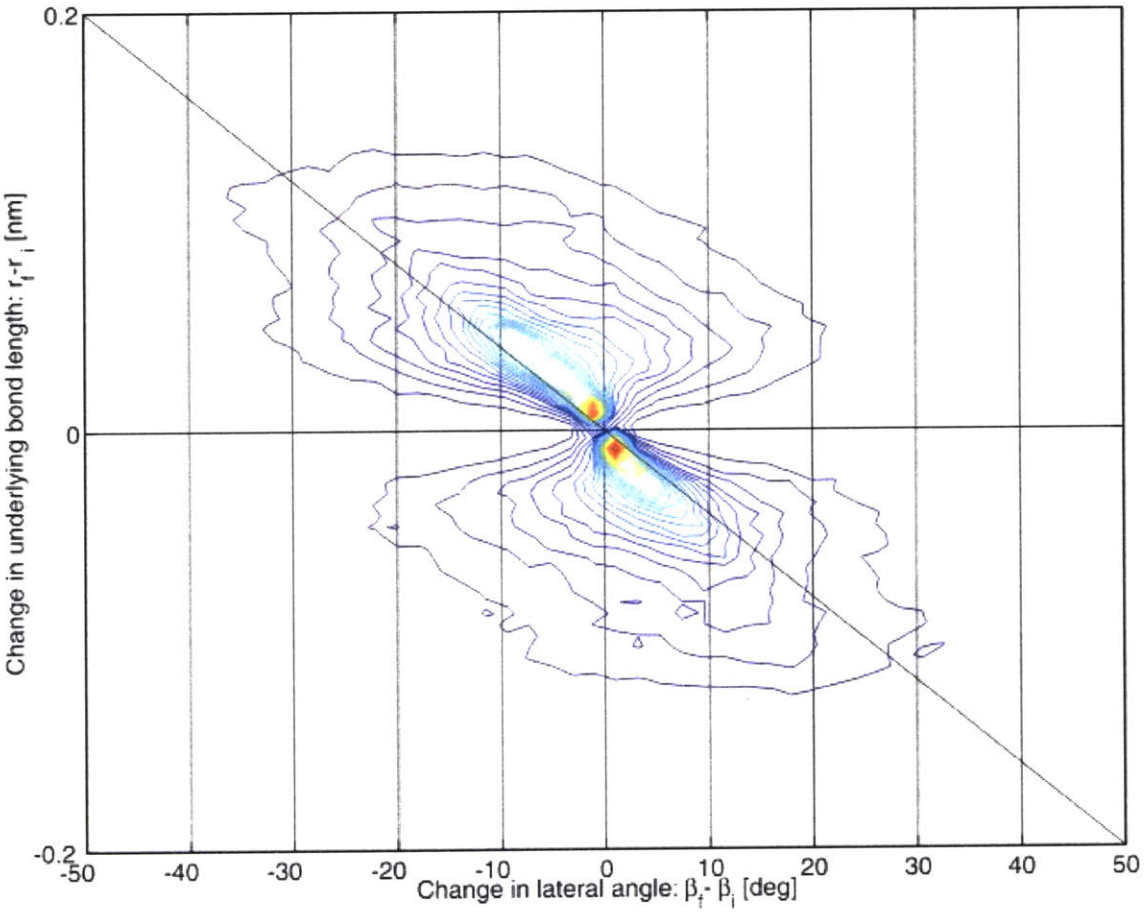

Figure 9-8: Plotting isocontours of distributions of lateral angle changes $(\beta_f - \beta_i)$ against changes in length $(r_f - r_i)$ of the underlying bond (all of which undergo a transition across the IPB length, as indicated in figure 9-5) shows that the two are negatively correlated. This result agrees with the findings for kinematics of IPB environments in triggering inclusions at onset of stress relaxations (fig. 9-4.b).

This analysis of recurring structure changes in transforming inclusions confirms that bond length transitions in the second nearest neighbor shell across the IPB length and the associated distortions in their immediate atomic environments are the dominant features of the fundamental unit plastic events responsible for irreversible stress relaxations observed in this study. Figures 9-9 and 9-10 show visualizations of two typical atomic configurations associated with these recurring unit events in the transforming inclusions. The number of such events in every stress relaxation was found to be linearly proportional to the size of the associated inelastically transforming inclusion with on average 7 events for every 10 inclusion atoms.

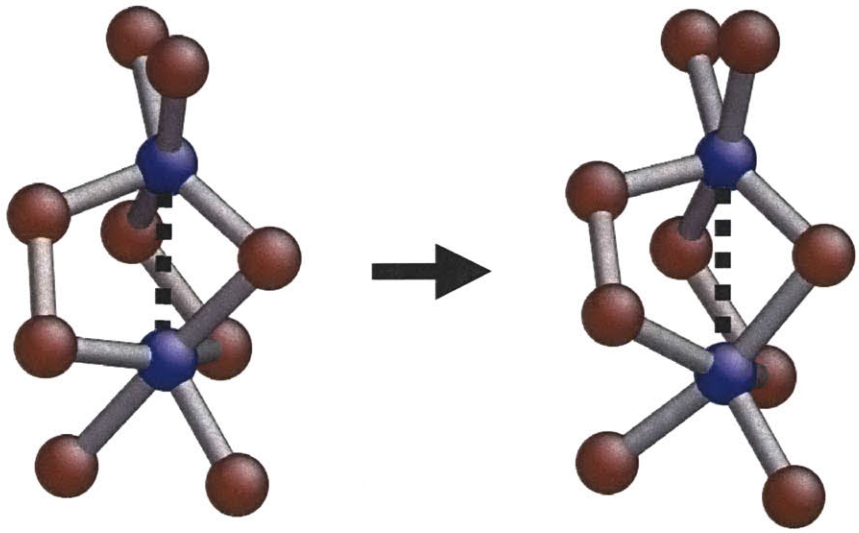

Figure 9-9: Atomic configuration changes associated with nearest neighborhoods of a bond that undergoes a transition across the IPB length. Endpoints of the bond that undergo this transition are shown in blue while their nearest neighbors are shown in red. The bond undergoing the transition elongates beyond the IPB length. The atom that neighbors on both endpoints of the transitioning bond exhibits a lateral angle that crosses the threshold of 47 degrees discussed in figure 9-7.

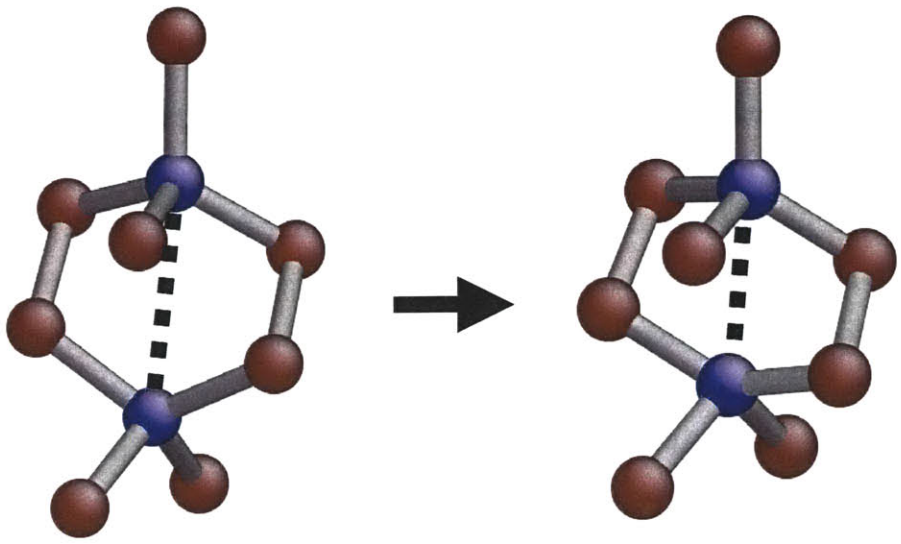

Figure 9-10: Atomic configuration changes associated with nearest neighborhoods of a bond that undergoes a transition across the IPB length. Endpoints of the bond that undergo this transition are shown in blue while their nearest neighbors are shown in red. The bond undergoing the transition contracts to below the IPB length. In this configuration there is no atom whose lateral angle crosses the threshold of 47 degrees discussed in figure 9-7, but the lateral angles of nearest neighbor atoms do show a negative correlation to the underlying bond length change, as demonstrated in figure 9-8.

10. Role of a-Si in plastic deformation of nanocrystalline Si

This chapter uses the insights gained from the study of plasticity in a-Si to elucidate the stages of plastic flow in a model quasi-columnar nc-Si structure.

10.1 Model quasi-columnar nc-Si structure

As discussed in the Introduction (chapter 1) the present study of plasticity in a-Si was motivated by a desire to explain the ultrahardness of nc-TiN/a-Si_3N_4 ceramic composite coatings using SW silicon as a model material in atomistic simulations. The review of prior work done on elucidating the structure of intergranular regions in SW nc-Si (section 2.7) mentioned in particular the work of Keblinski *et al.* [Keblinski *et al.*, 1997] who found radial and angular distribution functions for the amorphous intergranular regions of SW nc-Si. Comparison of these RDFs and ADFs to the corresponding RDFs and ADFs for solidlike and liquidlike a-Si atomic environments (section 6.3.1) shows that the a-Si grain boundary regions of nc-Si are almost entirely solidlike in structure. This finding indicates that these grain boundary regions would be resistant to plastic flow—as expected from the behavior of the analogously bonded a-Si_3N_4 in nc-TiN/a-Si_3N_4—and that the onset of plastic flow in them would require the overcoming of an energetic barrier associated with the creation of a sufficient mass fraction ϕ of liquidlike material.

To probe these questions, low temperature plasticity was studied using constant volume MD deformation simulation on a model quasi-columnar nc-Si structure constructed by D. Farkas of Virginia Technical University. A visualization of this model nc-Si structure is shown in figure 10-1.

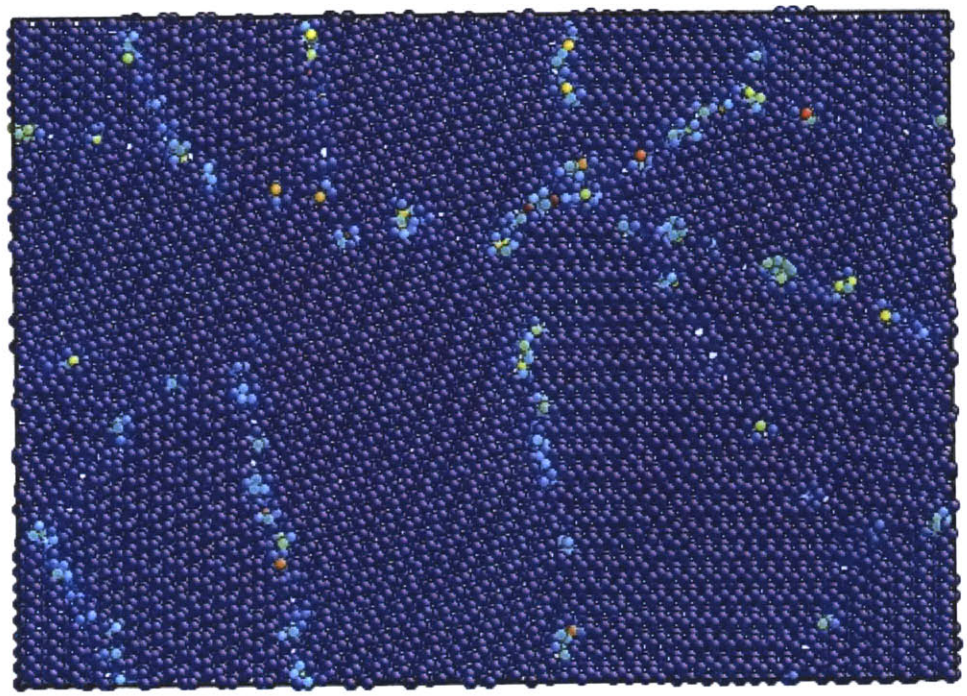

Figure 10-1: A visualization of the quasi-columnar nc-Si structure whose plastic deformation behavior was investigated in this study. Atoms are colored according to the contribution of the three-body interaction term of the SW potential (section 3.2.1) to their binding energies. This contribution serves as a good identifier of atomic sites whose neighborhoods depart strongly from crystallinity. For blue atoms it is nearly zero, indicating perfect crystallinity.

The nc-Si structure under consideration consists of 21399 atoms in a high-aspect ratio configuration approximately 20nm in length, but only 1nm (5 atoms) in thickness. Its grains are randomly oriented, but only to within the restrictions placed upon them by periodic boundary conditions. Because of this restriction, not all grain boundary orientations that are possible in a bulk columnar granular material are admissible in this model system.

In preparation for simulations of plastic deformation, the quasi-columnar nc-Si structure pictures in figure 10-1 was annealed for about 15ns at 950K, i.e. at about the glass transition temperature of a-Si (section 5.4). No noticeable change in the structure of intergranular regions was observed as a result of annealing, indicating that the configuration is not in a highly metastable configuration.

10.2 Mechanical response

The quasi-columnar nc-Si structure described in section 10.1 was quenched down to a temperature of 300K and deformed by the methods described in section 3.1.2: volume conserving plane-strain increments were successively applied (the sample thickness was held constant) followed by MD relaxation. Plastic deformation was conducted for three different initial externally applied pressures, i.e. for three different initial system-wide dilatations. Figures 10-2 and 10-3 present the dependencies of deviatoric stress and system pressure on total deviatoric strain.

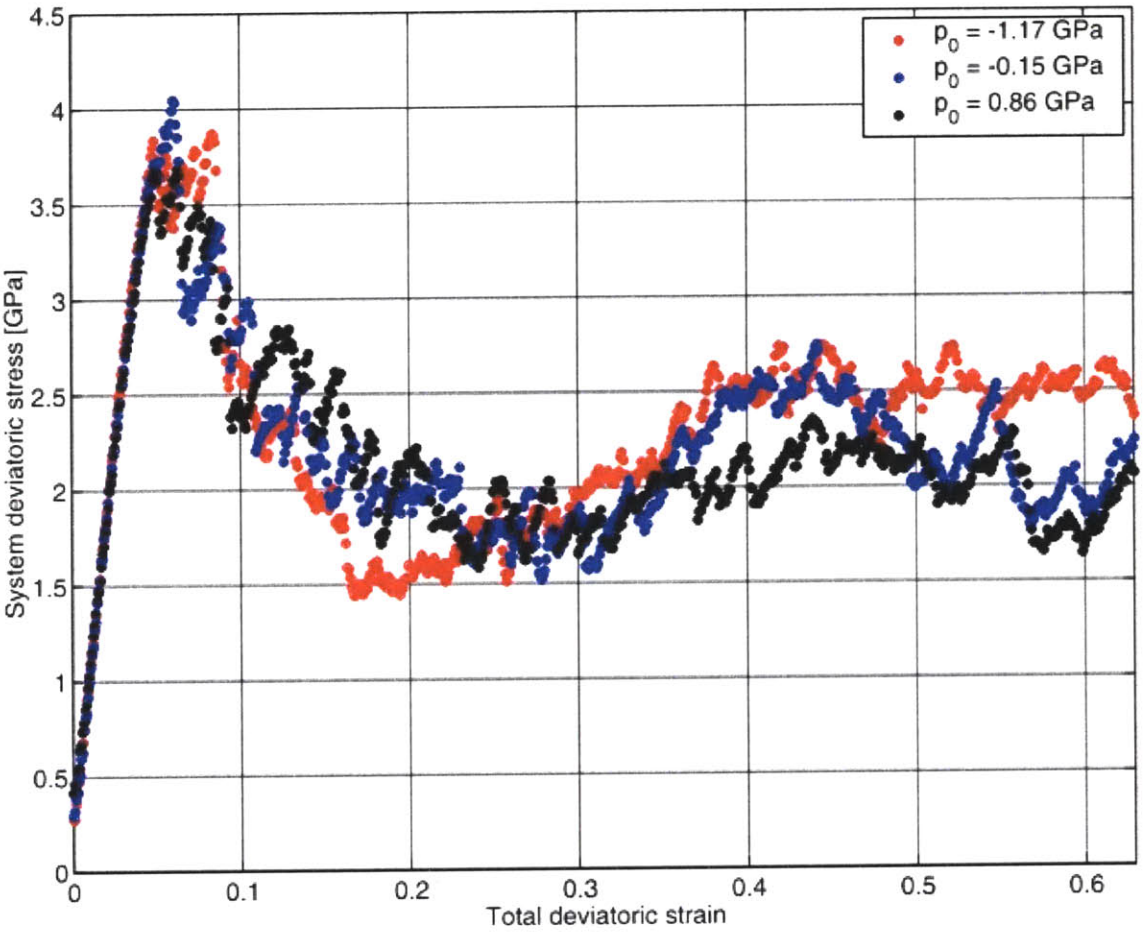

Figure 10-2: The dependence of deviatoric stress $\bar{\sigma}(\hat{\mathbf{o}})$ on the total deviatoric strain $\bar{\varepsilon}(\mathring{\mathbf{a}})$ during constant-volume plane strain plastic deformation at 300K of the quasi-columnar SW nc-Si sample described in section 10.1 at differing initial values of externally applied pressure.

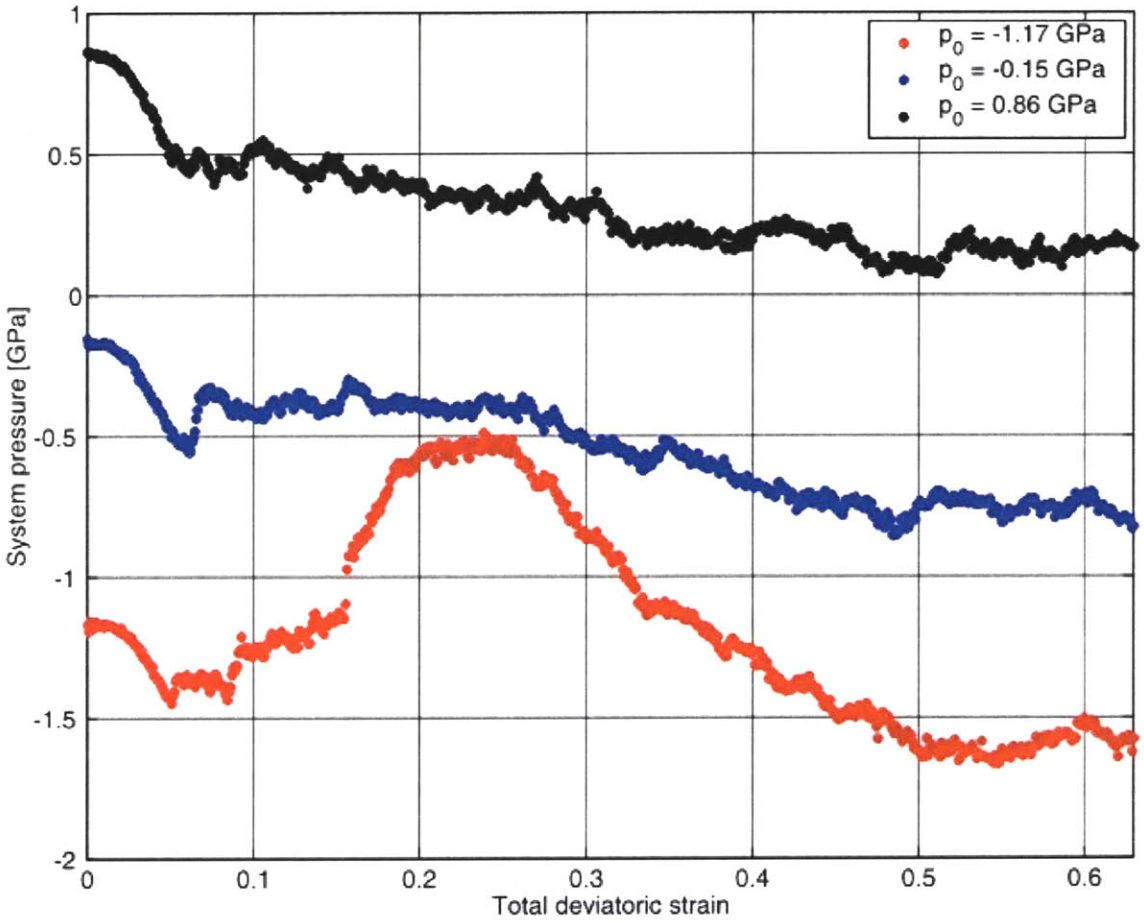

Figure 10-3: The dependence of system pressure $p(\hat{\mathbf{o}})$ on the total deviatoric strain $\bar{\varepsilon}(\mathring{\mathbf{a}})$ during constant-volume plane strain plastic deformation at 300K of the quasi-columnar SW nc-Si sample described in section 10.1 at differing initial values of externally applied pressure.

Figure 10-2 demonstrates a high deviatoric yield stress followed by strain softening. The level of yield stress normalized by the shear modulus for c-Si is about 0.1, a value which compares favorably with that deduced for the nc-TiN/a-Si_3N_4 ceramic composite coatings that motivated this study, namely 0.086 [Argon *et al.*, 2004]. Figure 10-2 also shows, however, that after strain softening the deformed nc-Si sample appears to exhibit a gradual elevation of flow stress beginning at about 30% total applied strain. The cause for this elevation is addressed in section 10.4.

The system pressure response shown in figure 10-3 exhibits two peculiarities: an initial drop in system pressure exhibited by the nc-Si system at all three levels of initially applied dilatation and a sudden release of negative pressure at about 15% total strain in the case of plastic deformation of the nc-Si structure with initially high negative pressure. These two phenomena are explained in sections 10.3 and 10.5, respectively.

10.3 Creation of liquidlike atomic environments

Applying the distinction between liquidlike and solidlike atomic environments developed in chapter 6, the evolution of the mass fraction ϕ of liquidlike environments during deformation can be found for all three initial pressures of the investigated quasi-columnar nc-Si structure. Figure 10-4 demonstrates a dramatically rising value of ϕ in all three cases, especially in the regime of total externally applied strain corresponding to strain softening in the system deviatoric stress-total strain dependence (figure 10-2). The increasing proportion of liquidlike atomic environments demonstrated in figure 10-4 explains the initial pressure decrease for all three system pressure-total strain curves shown in figure 10-3. It also agrees with the assertion made in chapter 7 that the mass fraction of liquidlike atomic environments serves as "plasticity carrier" in a-Si.

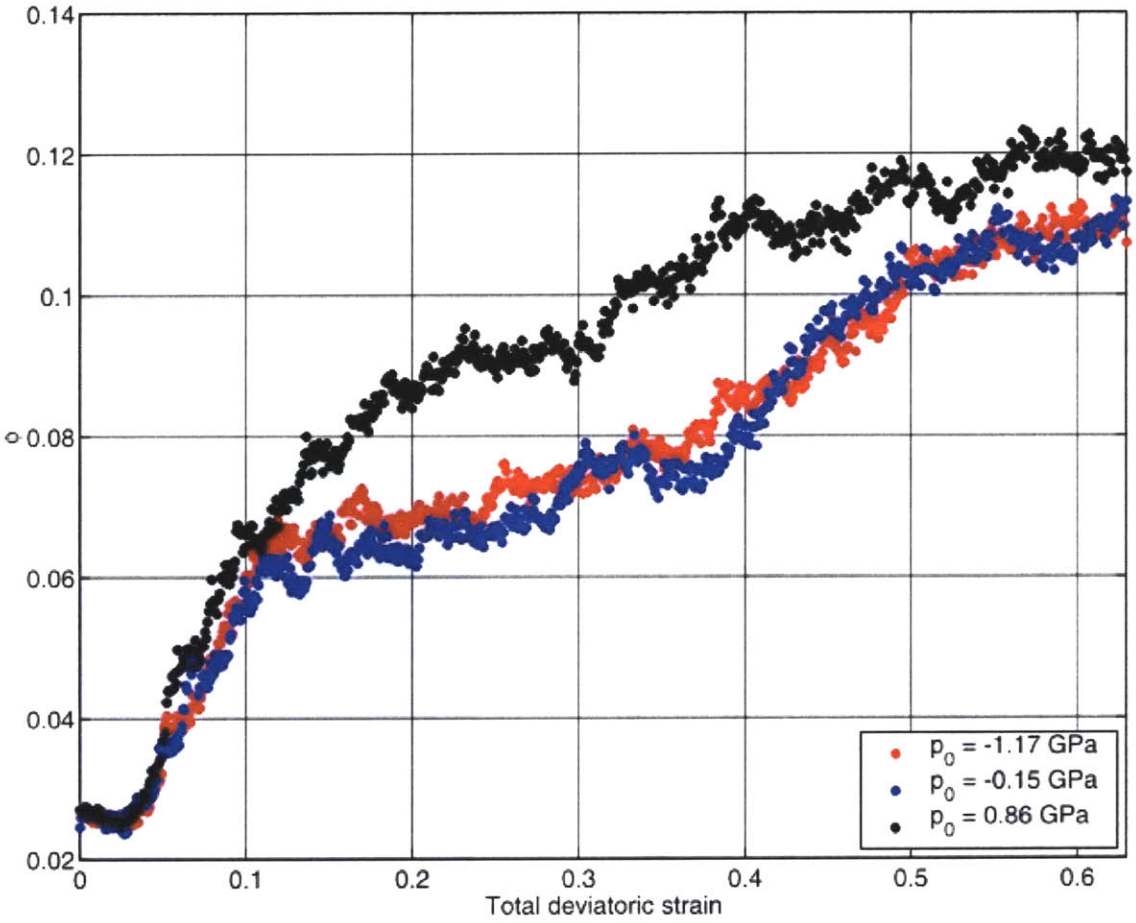

Figure 10-4: The dependence of liquidlike mass fraction ϕ on the total deviatoric strain $\bar{\varepsilon}(\text{å})$ during constant-volume plane strain plastic deformation at 300K of the quasi-columnar SW nc-Si sample described in section 10.1 at differing initial values of externally applied pressure.

Figure 10-5 visualizes the localization of liquidlike atomic environments in a system past the strain-softening stage of its flow behavior, indicating that all such environments are aligned within a single system-spanning zone of intergranular material. This zone is rather narrow, with a typical thickness of about 2 or 3 atomic diameters. Annealing of an nc-Si sample with such a distribution of liquidlike atomic environments at 950K for about 4ns removes the entire excess liquidlike mass fraction accumulated as a result of plastic deformation. This finding confirms that this easily flowing type of a-Si is metastable. Due to time scale constraints, however, the rate of annealing out of liquidlike atomic environments at room temperatures is currently inaccessible to MD simulation, except perhaps through use of the scaling argument summarized in section 2.4.

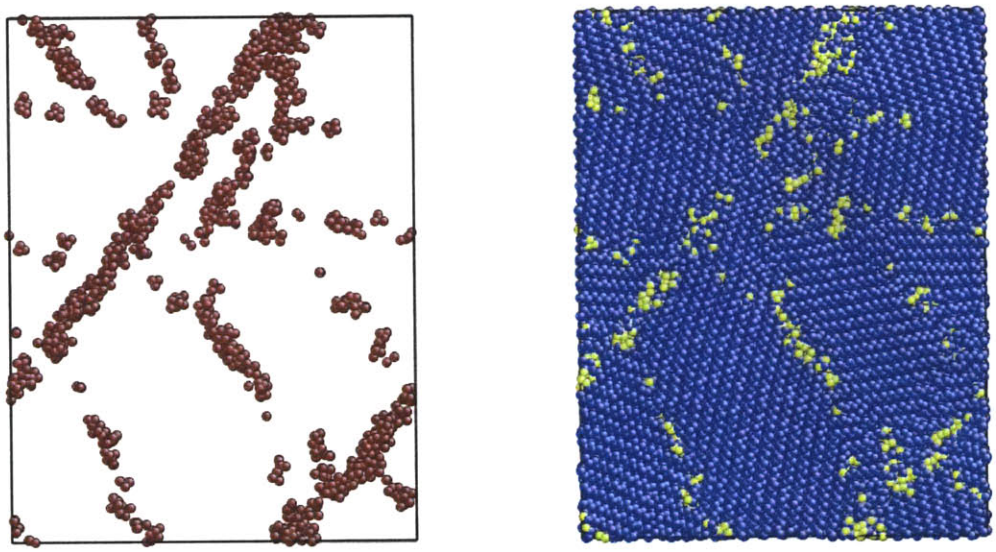

Figure 10-5: Visualization of the distribution of liquidlike atomic environments in a quasi-columnar nc-Si sample initially at a pressure of $p(\hat{\mathbf{o}}) = -0.15$ GPa when plastically deformed to $\bar{\varepsilon}(\mathring{\mathbf{a}}) \approx 0.25$ total deviatoric strain. The visualization at left shows only the atoms with liquidlike environments. The one at right shows the entire system, with atoms that have liquidlike environments colored brightly.

10.4 Plasticity in zones of easy flow

The method of distinguishing between linear elastically deforming matrix and inelastically transforming inclusion introduced in section 4.4.1 can be applied to consecutive configurations of the quasi-columnar nc-Si structures undergoing plastic flow. In this way, portions of nc-Si systems currently undergoing inelastic transformation as well as those that have transformed at some previous time during the course of deformation can be distinguished from those that have only undergone linear elastic flexing. Figures 10-6 through 10-8 show visualizations of the quasi-columnar nc-Si structure with initial pressure of $p(\hat{\mathbf{o}}) = -0.15$ GPa at three stages in the course of its deformation.

At a total strain of $\bar{\varepsilon}(\mathring{\mathbf{a}}) \approx 0.08$ (figure 10-6), inelastic transformation has occurred primarily in a series of mutually parallel or perpendicular intergranular regions such as the ones enclosed in the white ellipses. These transformations have allowed neighboring grains to accommodate the formation of the incipient zone of easy plastic flow visualized previously in figure 10-5 in terms of its concentration of liquidlike atomic environments. In figure 10-7 this zone (indicated by solid white lines) has become fully developed. Note that the thickness of this zone in terms of material that has undergone inelastic transformation at some time during the deformation process (indicated by green atoms) is about 5 to 7 atomic diameters, i.e. about a factor of 2 greater than the liquidlike zone visualized in figure 10-5. This observation indicates that during the course of plastic flow, local inelastic transformations in intergranular regions are aided by cooperative deformation in neighboring crystallites, but that this cooperative deformation does not result in a destruction of crystalline order in these crystallites.

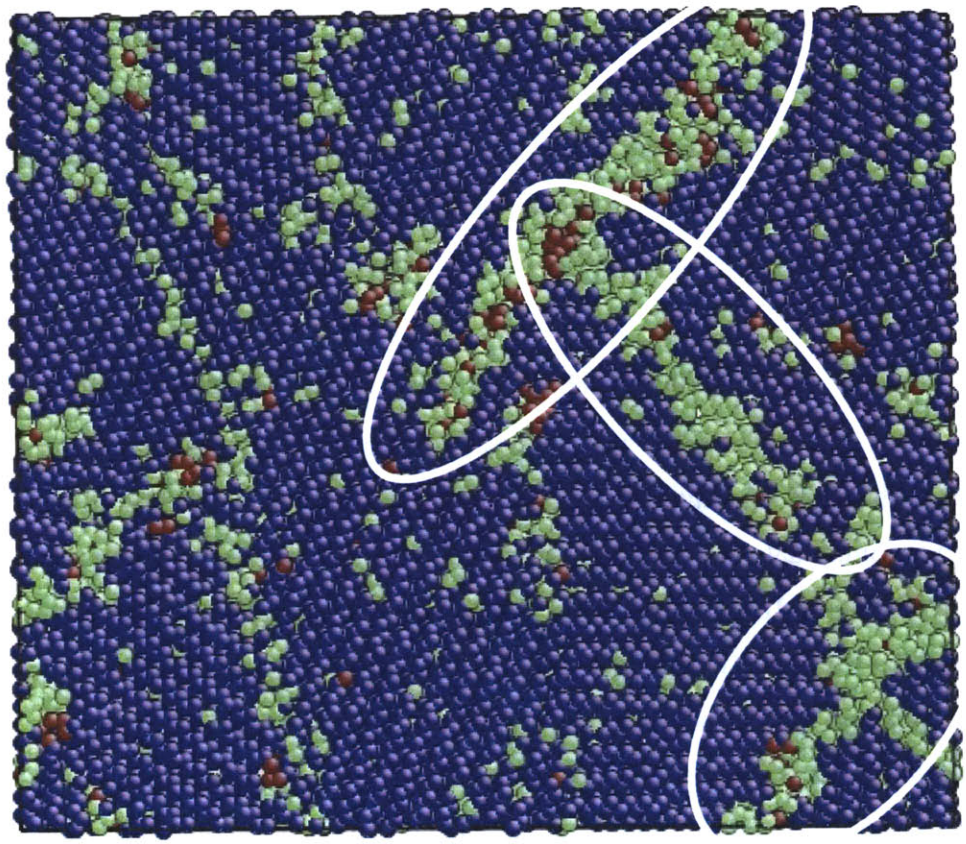

Figure 10-6: Visualization of the quasi-columnar nc-Si sample initially at a pressure of $p(\hat{\mathbf{o}}) = -0.15$ GPa at a stage of plastic deformation corresponding to a total deviatoric strain of $\bar{\varepsilon}(\mathring{\mathbf{a}}) \approx 0.08$. Red atoms denote environments currently undergoing inelastic transformation, green ones indicate those that have transformed at some prior time during the course of deformation, and blue ones represent those environment that have only undergone elastic flexing and have not experienced inelastic transformation. The white ellipses indicate intergranular regions where plastic deformation initially localizes.

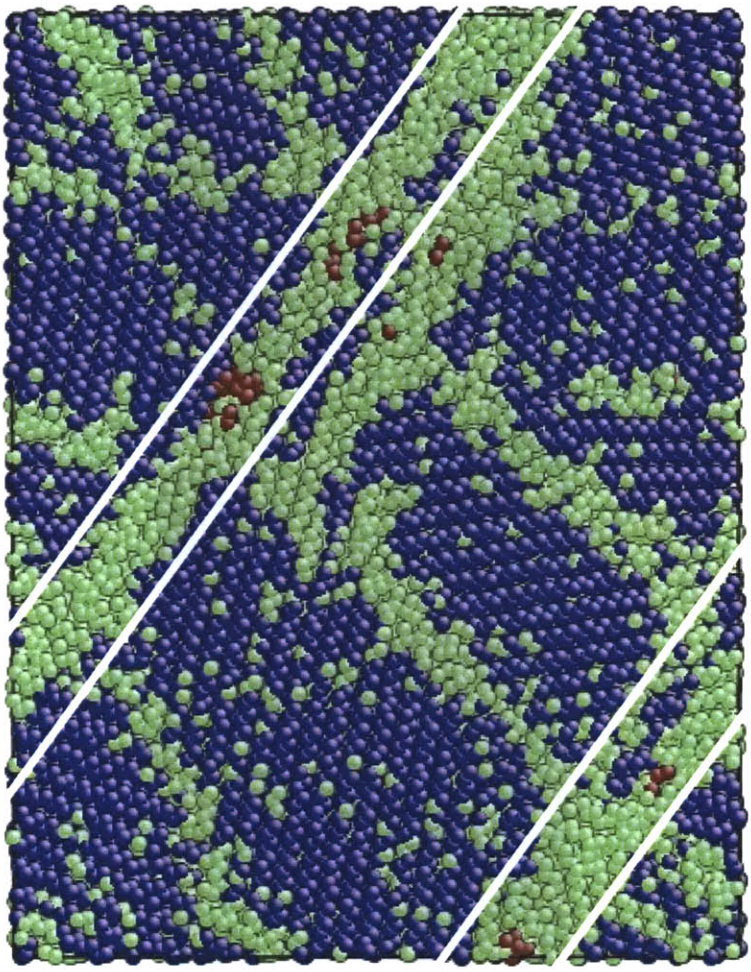

Figure 10-7: Visualization of the quasi-columnar nc-Si sample initially at a pressure of $p(\hat{\mathbf{o}}) = -0.15$ GPa at a stage of plastic deformation corresponding to a total deviatoric strain of $\bar{\varepsilon}(\mathring{\mathbf{a}}) \approx 0.25$. Red atoms denote environments currently undergoing inelastic transformation, green ones indicate those that have transformed at some prior time during the course of deformation, and blue ones represent those environment that have only undergone elastic flexing and have not experienced inelastic transformation. The solid white lines denote a zone of fully developed easy flow.

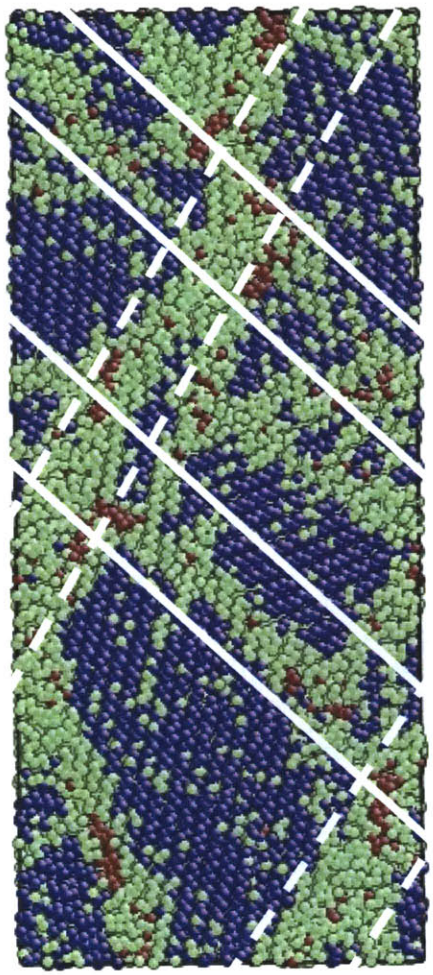

Figure 10-8: Visualization of the quasi-columnar nc-Si sample initially at a pressure of $p(\hat{\mathbf{o}}) = -0.15$ GPa at a stage of plastic deformation corresponding to a total deviatoric strain of $\bar{\varepsilon}(\mathring{\mathbf{a}}) \approx 0.53$. Red atoms denote environments currently undergoing inelastic transformation, green ones indicate those that have transformed at some prior time during the course of deformation, and blue ones represent those environment that have only undergone elastic flexing and have not experienced inelastic transformation. The dashed white lines indicate the zone of easy flow active at the stage of deformation visualized in figure 10-7. The solid white lines denote an emergent new zone of easy flow whose orientation is better aligned with the direction of maximum resolved shear stress.

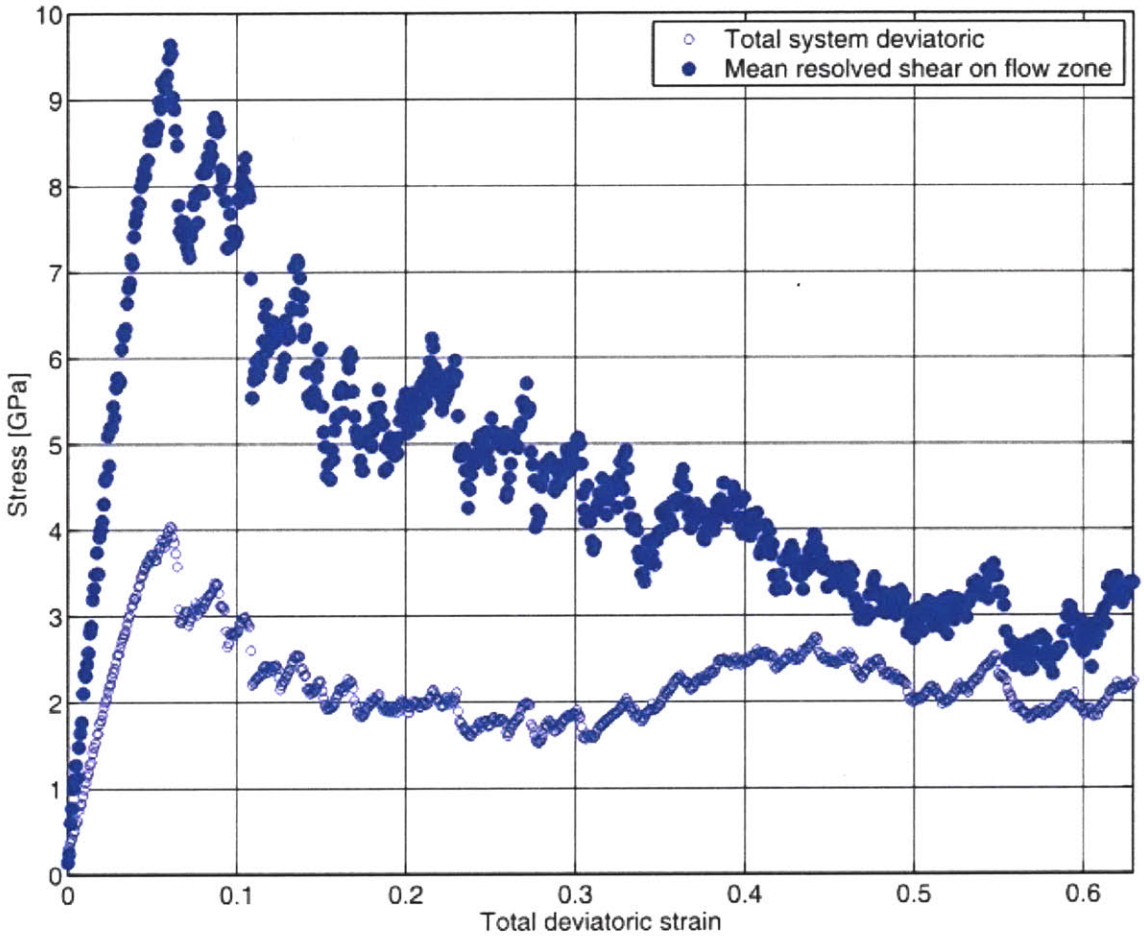

Figure 10-9: Unlike the total system deviatoric stress, the mean resolved shear stress on the initially formed zone of easy plastic flow (shown in figure 10-7) does not exhibit any tendency to increase once a total deviatoric strain of about $\bar{\varepsilon}(\text{å}) = 0.30$ has been reached.

Finally, figure 10-8 visualizes the quasi-columnar nc-Si system at such a high level of deformation that the previously formed zone of easy flow (denoted by dashed white lines) has rotated out of the plan of maximum resolved shear stress. Inelastic transformations at this stage of deformation have begun to localize into a new zone of easy flow (solid white lines) that is better aligned with the maximum resolved shear stress direction. The emergence of this new flow zone suggests an explanation for the rise in flow resistance observed in the composite response of the nc-Si samples plotted in figure 10-2. Namely, this rise can be associated with the necessity of nucleating and building up of a new zone of easy flow after the initial one had rotated out of the maximum resolved shear stress direction.

To confirm the above hypothesis, the mean resolved shear stress on the initially formed zone of easy flow (figure 10-7) was calculated and plotted in figure 10-9. Unlike the dependence of overall system deviatoric stress on total strain, this mean resolved shear stress shows no tendency to increase, indicating that the rise in overall system deviatoric stress is due to the flow geometry and not evolution of the material's intrinsic mechanical properties.

10.5 Release of high negative pressure

Applying the matrix-inclusion analysis of section 4.4.1 in the same way as it was done in section 10.4 above yields insight into the cause of the sudden release of negative pressure during plastic deformation of the quasi-columnar nc-Si structure at an initial (negative) pressure of $p(\hat{\mathbf{o}}) = -1.17$ GPa. Figure 10-10 shows the configuration of the system at the moment of pressure release. It can immediately be seen that a microvoid nucleates at the point in the zone of easy flow (dashed white lines) indicated by the white circle. During the course of later deformation this void elongates into a microcrack along the zone of easy flow. Since the simulation is conducted under constant volume, however, this microcrack does not propagate and closes upon further deformation.

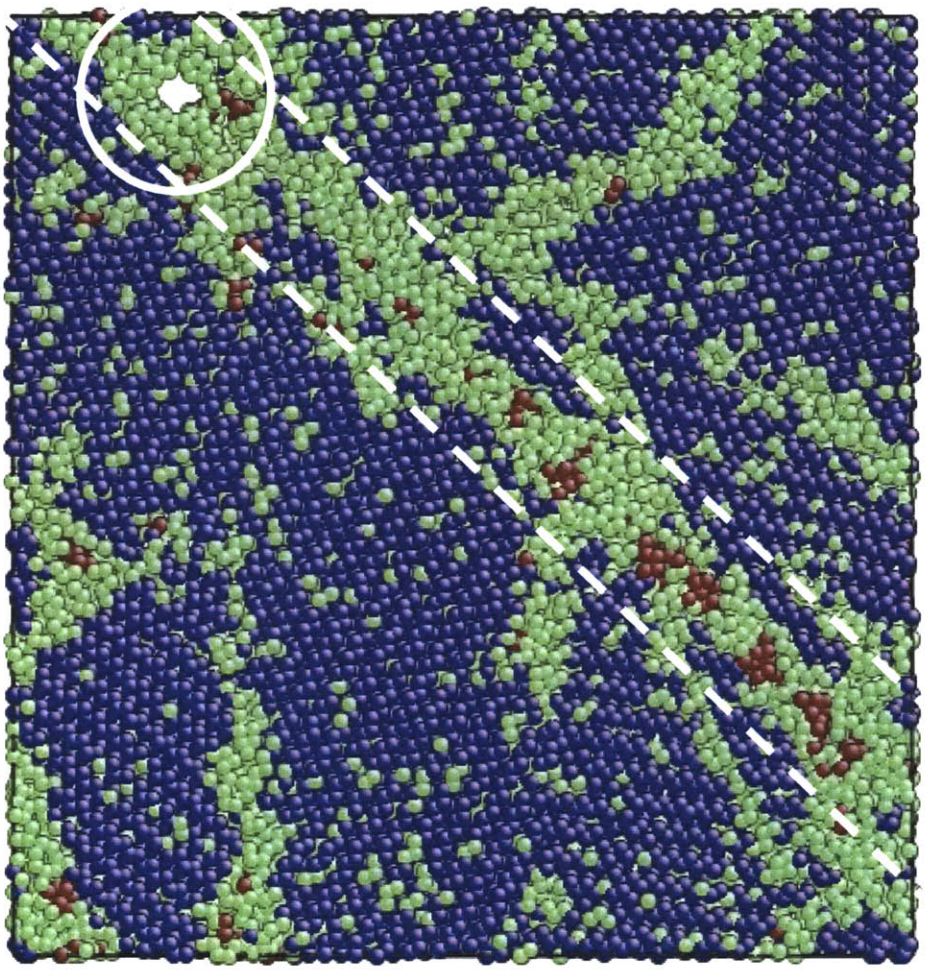

Figure 10-10: Visualization of the quasi-columnar nc-Si sample initially at a (negative) pressure of $p(\hat{\mathbf{o}}) = -1.17$ GPa at a stage of plastic deformation corresponding to a total strain of $\bar{\varepsilon}(\mathring{\mathbf{a}}) \approx 0.16$. Red atoms denote environments currently undergoing inelastic transformation, green ones indicate those that have transformed at some prior time during the course of deformation, and blue ones represent those environment that have only undergone elastic flexing and have not experienced inelastic transformation. Dashed white lines indicate a zone of fully developed easy flow such as the one visualized in figure 10-7. A microvoid has nucleated in the circled region.

The mean tensile stress across the plane of easy flow at the nucleation site of the microvoid was determined for the entire course of deformation and is shown in figure 10-11. Clearly, the release of system negative pressure and nucleation of the microvoid occurs when the mean tensile stress across the zone of easy flow locally reaches a maximum. The reason for the nucleation of the microvoid within the zone of easy flow can be understood in terms of the properties of liquidlike atomic environments listed in Table 6-1. Since these atomic environments are denser than the crystalline and solidlike a-Si ones, their creation during the course of plastic flow is unable to relieve the buildup of negative pressure. Indeed, as discussed in section 10-3, it exacerbates that buildup. The only method of relieving it is through a mechanism not involving plastic flow, such as the observed microvoid nucleation.

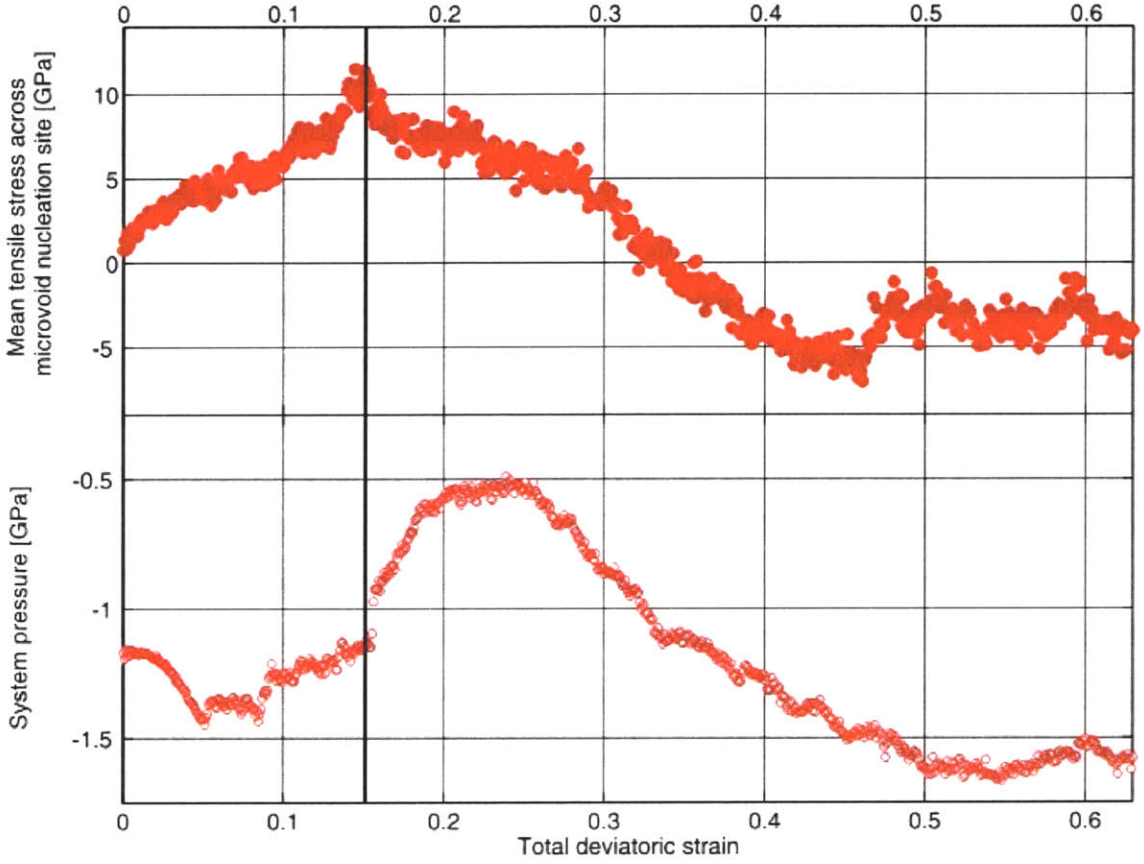

Figure 10-11: Release of system negative pressure during the course of plastic deformation of the quasi-columnar nc-Si structure initially at a pressure of $p(\hat{\mathbf{o}}) = -1.17$ GPa occurred when the mean tensile stress across the region of the zone of easy flow shown in figure 10-8 reached a maximum. The release of negative pressure was achieved by the nucleation of a microvoid.

11. Discussion

It was shown in chapters 6 and 7 that the liquidlike and solidlike atomic environments have well-defined physical properties and that the overall properties of a bulk a-Si sample can be accurately determined from its overall mass fraction of liquidlike atomic environments ϕ by the rule of mixtures. It should therefore be possible to confirm the existence of these two environments by measuring the dependence of the properties of a-Si as a function of the quench rate at which it was created. Because of the fast crystallization kinetics of Si, however, bulk a-Si is typically made by techniques other than quenching [Tanaka *et al.*, 1999], e.g. by ion implantation [Laaziri *et al.*, 1999]. Comparison of the results presented here with the properties of a-Si samples created by those methods is not straightforward since the degree of relaxation of those samples is difficult to correlate to that of a-Si created by fast quenching in the computer.

One possible method of circumventing this obstacle is to gauge the evolution of the properties of thoroughly annealed a-Si (corresponding to the slowest-quenched a-Si samples presented in this study) during large-strain plastic flow. Section 2.3 described the few experiments relevant to this issue. In particular, indentation experiments have shown that a-Si undergoing plastic flow is highly conducting, i.e. metallic. Since liquid Si is metallic and denser than its diamond cubic crystalline form at the melting temperature [Glazov *et al.*, 1969], this finding is consistent with the atomic structure of a-Si under indentation being "liquidlike." Using the same reasoning, it is possible that the metallic a-Si observed in anvil cell pressurization studies (section 2.4) could also be "liquidlike." Indeed, the liquidlike character of high-pressure a-AlGe (section 2.4) has been confirmed to be liquidlike.

Comparing the liquidlike atomic environments found in SW a-Si defines an intriguing contrast with the characteristics of easily flowing material in metallic glasses, whose plastic flow behavior has been studied extensively (section 2.5). Regions of easy flow in metallic glasses are identified as those having a large "free volume" fraction [Deng *et al.*, 1989]. They are sites where atomic motion is less constrained by close packing. The more easily flowing liquidlike a-Si, on the other hand, is denser than

solidlike a-Si (Table 6-1). It should be kept in mind, however, that liquid silicon is denser than diamond cubic c-Si while liquid metals are typically less dense than crystalline metals. Therefore, both liquidlike a-Si and regions of free volume in metallic glasses share the characteristic of being more similar in their local structures to the molten form of their constituent material than solidlike a-Si and the less easily flowing regions of metallic glasses, respectively. This commonality suggests that the liquidlike-solidlike distinction might be a more robust method of identifying easily flowing regions than free volume alone and may prove useful in the study of plasticity in amorphous materials other than a-Si.

The results of PEM deformation investigations of plasticity presented in chapters 8 and 9 can be compared to the study of the mechanisms of viscoelastic stress relaxation in a-Si by Witvrouw and Spaepen discussed in section 2.3. Viscoelasticity and large strain plasticity in a-Si may not at first glance appear to be related, but the results presented in this manuscript indicate the connection: regardless of the extent of inelastic stress relaxation, the underlying structure transformation is describable as an autocatalytic avalanche of unit events. Viscoelasticity therefore involves only small spatially isolated avalanches of such events triggered at low externally applied stresses. Meanwhile fully developed plasticity involves large avalanches triggered at the steady state flow stress that repeatedly percolate through the entire system in close proximity to each other. The characteristics of the local yielding phenomenon that leads to the onset of relaxation, however, were found to be unrelated to the extent of the relaxation or the stress at which it was triggered. As was indicated in section 8, every triggering inclusion contained on average 12 IPBs, a result consistent with the deviation from the predictions of unimolecular relaxation rate theory presented by Witvrouw and Spaepen. The important role of IBBs in inelastic relaxation is also consistent with the possible chemical specificity of "fertile sites" for triggering of viscoelastic relaxations implied by the work of Liu *et al.* (section 2.3).

In the case of a-Si, analysis of the onset of stress relaxations and of the subsequent relaxation processes has shown that the transition state of a grouping of atoms undergoing a unit plastic event is geometrically characterized by the IPB length. Developing a complete theory of structure transitions for these groupings of atoms along

the lines of that used to model the kinetics of plasticity in crystals [Kocks *et al.*, 1975], however, requires a description of the properties of these groupings of atoms in their unloaded, stress-free state, both before and after a transition has taken place. Attempts at such a description, however, have not yielded satisfactory results so far.

Finally, while a-Si has special chemically specific features and is a pure substance, it shares many physical behaviors with other directionally bonded materials such as SiO_2 and other unmodified inorganic glasses [Angell *et al.*, 1996]. The mechanistic features of its plastic relaxations are therefore likely to be present in other directionally bonded pure materials. Indeed, the bond length transitions across the IPB length described in this study (chapter 9) bear a striking resemblance to the two-state mechanism of viscoelastic relaxation [Jackle, Piche, 1976] proposed previously by Stranka for SiO_2 based on ultrasonic attenuation measurements [Stranka, 1961].

12. Conclusions

It has been demonstrated by molecular dynamics simulation that SW a-Si contains two distinct forms of atomic environments. Because of the similarity of their configurations to the structure of silicon in its diamond cubic and molten states, these two environments are referred to as solidlike and liquidlike, respectively. The physical properties of any given a-Si sample can be characterized by the mass fraction ϕ of liquidlike atomic environments in it. In particular, ϕ acts as a plasticity carrier in a-Si. When plastically deformed at low temperatures, samples depleted of liquidlike environments exhibit a pronounced yield phenomenon followed by strain softening due to creation of new liquidlike environments by inelastic structure transformations. Samples with an initially high ϕ do not show any yield phenomenon before steady state plastic flow is attained. When plastically deformed at low temperature under constant externally applied pressure, a-Si samples of differing initial ϕ converge to a single state of steady flow characterized uniquely by a specific average volume and ϕ.

The mechanisms of low-temperature plasticity in SW a-Si were investigated by external straining followed by relaxation using potential energy minimization (PEM). Localized internal atomic rearrangements were found to accompany irreversible relaxations of the system stress. The number of atoms participating in these rearrangements was proportional to the deviatoric component of the corresponding increments of stress relaxation, suggesting that these rearrangements can be described as autocatalytic avalanches of unit shearing events. Investigation of a-Si at the mechanical thresholds for onset of stress relaxations demonstrated the existence of a local yielding criterion that must be satisfied for any given atomic cluster to start undergoing a structure transformation. Further analysis revealed that unit plastic shearing events in a-Si are characterized by the presence of instability-producing bonds (IPBs) whose length corresponds to the trough of the split second nearest neighbor peak in the radial distribution function (RDF) for bulk SW a-Si undergoing stead flow. Inelastic relaxations

consisting of many unit events involve transitions of bond length between these two portions of the split second nearest neighbor peak.

13. Acknowledgements

None of the work presented in this manuscript would have been possible without the profound insight of my thesis advisor and mentor Ali S. Argon. His deep understanding of the physics of solids has shaped me as a researcher. His patience and encouragement was indispensable in helping me to weather the difficult periods of my time in residence at MIT. The strict example of rigor he has set will remain with me throughout my future career.

I would like to thank my thesis committee members—David Parks, Sidney Yip, Nicola Marzari—for the many discussions they held with me at all stages of the work presented here. I am particularly grateful to D. Parks for his insight on the issue of distinguishing between elastically deforming matrix material and an inelastically transforming inclusion. The formalism presented in section 4.4 was inspired by his comments.

I would like to thank the Interfacial Materials Group at Argonne National Laboratory—specifically D. Wolf, P. Keblinski, and V. Yamakov—for making their MD codes available to me as well as for helping me to understand molecular simulation in the initial stages of my research. Special thanks are also due to S. Veprek of the Technical University of Munich whose work led to the creation of the nc-TiN/a-Si_3N_4 ceramic composite coatings that inspired the research presented here.

I am also indebted many researchers for countless useful discussions and insightful feedback: N. Hadjiconstantinou, M. Bazant, J. Li, G. Ceder, H. E. Stanley, A. de Vita, and A. Needleman. My colleagues at MIT R. Sharma and M. Zimmermann have furthermore provided me not only with a constant stream of constructive criticism, but also with support and encouragement.

Although it should go without saying, I will also state that no creative work is possible where there is no group of family and friends to offer support and understanding, especially during the trying periods when constant exertion seems to yield no fruit. I am enormously fortunate—perhaps more than most people—that the group of individuals

who have offered their heartfelt support throughout the years is too long to list here. You know who you are, though, and I thank you.

This manuscript is based upon work supported under an NSF Graduate Fellowship and by the Defense University Research Initiative on NanoTechnology (DURINT) on "Damage- and Failure-Resistant Nanostructured and Interfacial Materials," funded at the Massachusetts Institute of Technology by the Office of Naval Research under grant N00014-01-1-0808. Salary assistance was also provided by the Dean of the Graduate School and the Department of Mechanical Engineering at MIT.

14. References

- Abell, G. C., 1985, Phys. Rev. **B31**, 6184.
- Alexander, H., Haasen, P., 1968, in Solid State Physics **22**, ed. Seitz, F., Academic Press, New York.
- Allen, M. P., Tildesley, D. J., 2000, Computer Simulation of Liquids, Oxford University Press, Oxford, England.
- Anand, L., Gurtin, M. E., 2003, Int. J. Sol. Struct. **40**, 1465.
- Anand, L., Su, C., 2005, J. Mech. Phys. Solids, in press.
- Andersen, H. C., 1980, J. Chem. Phys. **72**, 2384.
- Angell, C. A., Borick, S., Grabow, M., 1996, J. Non-cryst. Sol. **205-207**, 463.
- Argon, A. S., Kuo, H. Y., 1979, Mat. Sci. Eng. **39**, 101.
- Argon, A. S., 1981, in Dislocation Modelling of Physical Systems, ed. Ashby, M. F., Bullough, R., Hartley, C. S., Hirth, J. P., Pergamon Press, Oxford, England, p. 393.
- Argon, A. S., Shi, L. T., 1983, in Amorphous Materials: Modeling of Structure and Properties, ed. Vitek, V., Metallurgical Society of AIME, Warrendale, Pa., 279.
- Argon, A. S., 1996a, "Mechanical Properties of Single-Phase Crystalline Media: Deformation at Low Temperatures," in Physical Metallurgy, Ch. 21, ed. Cahn, R. W., Haasen, P., North-Holland, p. 1957.
- Argon, A. S., 1996b, "Mechanical Properties of Single-Phase Crystalline Media: Deformation in the Presence of Diffusion," in Physical Metallurgy, Ch. 22, ed. Cahn, R. W., Haasen, P., North-Holland.
- Argon, A. S., and Veprek, S., 2002, Mat. Res. Soc. Symp. Proc. Vol. **697**, P1.2.
- Argon, A. S., Demkowicz, M. J., Veprek, S. 2004, in Materials Processing and Design: Modeling, Simulation and Applications, NUMIFORM 2004, edited by S. Ghosh, J. C. Castro and J. K. Lee, American Institute of Physics: New York, vol. **1**, pp. 3-13.
- Balamane, H., Halicioglu, T., Tiller, W. A., 1992, Phys. Rev. **B46**, 2250.

- Barkema, G. T., Mousseau, N., 1996, Phys. Rev. Lett. **77**, 4358.
- Bazant, M. Z., Kaxiras, E., Justo, J. F., 1997, Phys. Rev. **B56**, 8542.
- Bernal, J. D., 1964, Proc. Roy. Soc. Ser. A **280**, 299.
- Bernstein, N., Aziz, M. J., Kaxiras, A., 2000, Phys. Rev. **B61**, 6696.
- Bertsekas, D. P., 1999, Nonlinear Programming, Athena Scientific, Belmont, MA.
- Blinc, R., Zeks, B., 1974, Soft Modes in Ferroelectrics and Antiferroelectrics, North-Holland, Amsterdam.
- Brent, R. P., 1973, Algorithms for Minimization without Derivatives, Prentice-Hall, Englewood Cliffs, NJ.
- Broughton, J. Q., Li, X. P., 1987, Phys. Rev. **B35**, 9120.
- Brown, D., Neyertz, S., 1995, Mol. Phys. **84**, 577.
- Bulatov, V. V., Argon, A. S., 1994, Mod. Simul. Mater. Sc. and Engr. **2**, 167; 185; 203.
- Cai, W., Bulatov, V. V., Justo, J. F., Argon, A. S., Yip, S., 2000, Phys. Rev. Lett. **84**, 3346.
- Cargill, G. S., 1975, in Solid State Physics **30**, ed. Ehrenreich, H., Seitz, F., Turnbull, D., Academic Press, New York.
- Carison, D. E., Wronsky, C. R., 1976, Appl. Phys. Lett. **28**, 671.
- Chaudhari, P., Levi, A., Steinhardt, P., 1979, Phys. Rev. Lett. **43**, 1517.
- Cherns, D., Jenkins, M. L., White, S., 1980, in Electron Microscopy and Analysis 1979, Inst. Phys.: London.
- Chattick, R. C., Alexander, J. H., Sterling, H. F., 1969, J. Electrochem. Soc. **116**, 77.
- Clarke, D. R., Kroll, M. C., Kirchner, P. D., Cook, R. F., 1988, Phys. Rev. Lett. **60**, 2156.
- Cohen, M. H., Turnbull, D., 1959, J. Chem. Phys. **31**, 1164.
- Cohen, M. H., Grest, G. S., 1979, Phys. Rev. B **20**, 1077.
- Conrad, H., 1963, The Relation between the Structure and Mechanical Properties of Metals, Proceedings of the conference held at the National Physical Laboratory, Teddington, Middlesex on the 7th, 8th and 9th January, 1963, Her Majesty's Stationary Office, London.

- Crawford, J. D., 1991, Rev. Mod. Phys. **63**, 991.
- Demkowicz, M. J., 2004a, Phenomenology and kinematics of discrete plastic deformation events in amorphous silicon: atomistic simulation using the Stillinger-Weber potential, MIT S.M. Thesis.
- Demkowicz, M. J., Argon, A. S., 2004b, Phys. Rev. Lett. **93**, 025505.
- Demkowicz, M. J., Argon, A. S., 2005a, submitted.
- Demkowicz, M. J., Argon, A. S., 2005b, submitted.
- Demmel, J. W., 1997, Applied Numerical Linear Algebra, SIAM, Philadelphia.
- Deb, S. K., Wilding, M., Somayazulu, M., McMillan, P. F., 2001, Nature **414**, 528.
- Deng, D., Argon, A. S., Yip, S., 1989, Phil. Trans. Roy. Soc. Lond. **A329**, 549; 575; 595; 613.
- Duff, I. S., Erisman, A. M., and Reid, J. K., 1986, Direct Methods for Sparse Matrices, Oxford University Press, Oxford.
- Ekunwe, N. S. O., Lacks, J. D., 2002, Phys. Rev. **B66**, 212101.
- Elliot, R. S., Shaw, J. A., Triantafyllidis, N., 2002, J. Mech. Phys. Solids **50**, 2463.
- Eshelby, J. D., 1957, Proc. Roy. Soc. A **241**, 376.
- Evans, D. J., and Morriss, G. P., 1983, Phys. Lett. **98A**, 433.
- Evans, D. J., and Morriss, G. P., 1984, Comput. Phys. Rep. **1**, 297.
- Eyring, H., 1936, J. Chem. Phys. **4**, 283.
- Falk, M. L., Langer, J. S., 1998, Phys. Rev. **E57**, 7192.
- Falk, M. L., Langer, J. S., Pechenik, L., 2004, Phys. Rev. **E70**, 011507.
- Furukawa, K., Shimbo, M., Fukuda, K., Tanzawa, K., 1986, Extended Abstracts of the 18th (1986 International) Conference on Solid-State Devices and Materials, Tokyo, B-9-1 (pp.533-536).
- Gilman, J. J., 1968, in Dislocation Dynamics, ed. A. R. Rosenfield *et al.*, McGraw-Hill, New York.
- Glazov, V. M., Chizhevskaya, S. N., Glagoleva, N. N., 1969, Liquid Semiconductors, Plenum, New York (Ch. 3).

- Guckenheimer, J., Holmes, P., 1983, Nonlinear Oscillations, Dynamical Systems, and Bifurcations of Vector Fields, Springer-Verlag, New York.
- Hall, E. O., 1951, Proc. Phys. Soc. London **B64**, 747.
- Hoover, W. G., 1983, A. Rev. Phys. Chem. **34**, 103.
- Horstemeyer, M. F., Baskes, M. I., 2000, Mat. Res. Soc. Symp. Proc. **578**, 15.
- Huang, K., 1987, Statistical Mechanics, John Wiley & Sons, New York.
- Hutnik, M., Gentile, F. T., Ludovice, P. J., Suter, U. W., Argon, A. S., 1991a, Macromolecules **24**, 5962.
- Hutnik, M., Argon, A. S., Suter, U. W., 1991b, Macromolecules **24**, 5970.
- Jackle, J., Piche, L., 1976, J. Non-cryst Sol. **20**, 365.
- Jiang, X., Goranchev, B., Schmidt, K., Grunberg, P., Reichelt, K., 1990, J. Appl. Phys. **67**, 6772.
- Justo, J. F., Bazant, M. Z., Kaxiras, E., Bulatov, V. V., Yip, S., 1998, Phys. Rev. **B58**, 2539.
- Kabla, A., Debregeas, G., 2003, Phys. Rev. Lett. **90**, 258393.
- Kaplan, D., Thomas, P. A., Sol, N., Velasco, G., 1978, Appl. Phys. Lett. **33**, 440.
- Kantor, Y., Webman, I., 1984, Phys. Rev. Lett. **52**, 1891.
- Kauzmann, W., 1948, Chem. Rev. **43**, 219.
- Keating, P. N., 1966, Phys. Rev. **145**, 637.
- Keblinski, P., Phillpot, S. R., Wolf, D., Gleiter, H., 1996, Phys. Rev. Lett. **77**, 2965.
- Keblinski, P., Phillpot, S. R., Wolf, D., Gleiter, H., 1997, Acta. Mater. **45**, 987.
- Keblinski, P., Bazant, M. Z., Dash, R. K., Treacy, M. M., 2002, Phys. Rev. **B66**, 064104.
- Kluge, M. D., Ray, J. R., Rahman, A., 1986, J. Chem. Phys. **85**, 4028.
- Kluge, M. D., Ray, J. R., 1988, Phys. Rev. **B37**, 4132.
- Kocks, U. F., Argon, A. S., Ashby, M. F., 1975, Thermodynamics and Kinetics of Slip, Prog. Mater. Sci. **19**, ed. Chalmers, B., Christian, J. W., Massalski, T. B., Pergamon Press, Oxford.
- Laaziri, K., Kycia, S., Roorda, S., Chicoine, M., Robertson, J. L., Wang, J., Moss, S. C., 1999, Phys. Rev. Lett. **82**, 3460.

- Lacks, D. J., 2002, Phys. Rev. **E66**, 051202.
- Leach, A. R., 2001, Molecular Modelling: Principles and Applications, Prentice Hall, Harlow, England.
- Lehoucq, R. B., Sorensen, D. C., Yang, C., 1998, ARPACK Users' Guide: Solution of Large-Scale Eigenvalue Problems with Implicitly Restarted Arnoldi Methods, SIAM.
- Li, Ju, Van Vliet, K. J., Zhu, T., Yip, S., Suresh, S., 2002, Nature **418**, 307.
- Liu, Xiao, White, B. E. Jr., Pohl, R. O., Iwanizcko, E., Jones, K. M, Mahan, A. H., Nelson, B. N., Crandall, R. S., Veprek, S., 1997, Phys. Rev. Lett. **78**, 4418.
- Liu, Xiao, Pohl, P. O., Crandall, R. S., 1999, Mat. Res. Soc. Symp. Proc. **557**, 323.
- Lu, B., Torquato, S., 1990, J. Chem. Phys. **93**, 3452.
- Luedtke, W. D., Landman, U., 1989, Phys. Rev. **B40**, 1164.
- Lund, A. C., Schuh, C. A., 2004, Mat. Res. Soc. Symp. Proc. Vol. **806**, MM7.4.1.
- Maeda, K., Takeuchi, S., 1981, Philos. Mag. **A44**, 643.
- Maeda, K., Takeuchi, S., 1982, J. Phys. F: Met. Phys. **12**, 2767.
- Malandro, D. L., Lacks, D. J., 1997, J. Chem. Phys. **107**, 5804.
- Malandro, D. L., Lacks, D. J., 1998, J. Chem. Phys. **110**, 4593.
- Maloney, C. Lemaitre, A., 2004, Phys. Rev. Lett. **93**, 016001.
- Marsden, J. E., Tromba, A. J., 1996, Vector Calculus, W. H. Freeman and Company, New York.
- MathWorks, http://www.mathworks.com/.
- McClintock, F. A., Argon, A. S., 1966, Mechanical Behavior of Materials, Addison-Wesley, Reading, MA.
- Mishima, O., Calvert, L. D., Whalley, E., 1985, Nature **314**, 76.
- Mott, P. H., Argon, A. S., Suter, U. W., 1992, J. Comput. Phys. **101**, 140.
- Mott, P. H., Argon, A. S., Suter, U. W., 1993, Philos. Mag. **A67**, 931.
- Nakhmanson, S. M., Mousseau, N., 2002, J. Phys.-Condens. Mat. **14**, 6627.
- Netlib, http://www.netlib.org/.
- Niederhofer, A., Bolom, T., Nesladek, P., Moto, K., Eggs, C., Patil, D. S., Veprek, S., 2001, Surface and Coatings Technology **146**, 183.

- Olmsted, D. L., Hardikar, K. Y., Phillips, R., 2001, Mod. Simul. Mater. Sc. **9**, 215.
- Paige, C. C., Saunders, M. A., 1975, SIAM J. Numer. Anal. **12**, 617.
- Parinello, M., Rahman, A., 1980, Phys. Rev. Lett. **45**, 1196.
- Petch, N. J., 1953, J. Iron Steel Inst. **174**, 25.
- Phillips, J. C., 1979, J. Non-cryst. Solids **34**, 153.
- Phillips, J. C., 1981a, J. Non-cryst. Solids **43**, 37.
- Phillips, J. C., 1981b, J. Non-cryst. Solids **44**, 17.
- Phillpot, S. R., Yip, S., Wolf, D., 1989, Computers in Physics **Nov-Dec**, 20.
- Polak, E. and Ribiere, G., 1969, Revue Francaise Informat. Recherche Operationelle **16**, 35.
- Rasigni, G., Varnier, F., Rasigni, M., Palmari, J. P., Llebaria, A., 1983, Phys. Rev. **B27**, 819.
- Ren, Q., Joos, B., Duesbery, M. S., 1995, Phys. Rev. **B52**, 13223.
- Rose, H., Smith, J. R., Ferrante, J., 1983, Phys. Rev. **B28**, 1835.
- Safarik, D. J., Cady, C. M., Schwarz, R. B., 2005, Acta Mater., in press.
- Sastry, S., Angell, C. A., 2003, Nature Materials **2**, 739.
- Schiotz, J., Di Tolla, F. D., Jacobsen, K. W., 1998, Nature **391**, 561.
- Schiotz, J., and Jacobsen, K. W., 2003, Science **301**, 1357.
- Schiotz, J., 2004, Scripta Mater. **51**, 837-841.
- Shen, T. D., Koch, C. C., McCormick, T. L., Nemanich, R. J., Huang, J. Y., Huang, J. G., 1995, J. Mater. Res. **10**, 139.
- Shimomura, O., Minomura, S., Sakai, N., Asaumi, K., 1974, Phil. Mag. **29**, 547.
- Singleton, R. C., 1969, Communications of the ACM **12**, 185.
- Snell, A. J., MacKenzie, K. D., Spear, W. E., LeComber, P. G., Hughs, A. J., 1981, Appl. Phys. Lett. **24**, 257.
- Srolovitz, D., Vitek, V., Egami, T., 1983, Acta Metall. **31**, 335.
- Staebler, D. L., Wronsky, C. R., 1977, Appl. Phys. Lett **31**, 292.
- Stanley, H. E., Angell, C. A., Essmann, U., Hemmati, M., Poole, P. H., Sciortino, F., 1994, Physica **A205**, 122.
- Stillinger, F. H., Weber, T. A., 1983, Phys. Rev. **A28**, 2408.

- Stillinger, F. H., Weber, T. A., 1985, Phys. Rev. **B31**, 5262.
- Stranka, R. E., 1961, Phys. Rev. **123**, 2020.
- Tanaka, K., Maruyama, E., Shimada, T., Okamoto, H., 1999, Amorphous Silicon, Wiley, New York.
- Tersoff, J., 1986, Phys. Rev. Lett. **56**, 632.
- Theodorou, D. N., Suter, U. W., 1985a, Macromolecules **18**, 1206.
- Theodorou, D. N., Suter, U. W., 1985b, Macromolecules **18**, 1467.
- Theodorou, D. N., Suter, U. W., 1986, Macromolecules **19**, 379.
- Thompson, J. M. T., Hunt, G. W., 1973, A General Theory of Elastic Stability, Wiley, London.
- Thompson, J. M. T., Shorrock, P. A., 1975, J. Mech. Phys. Solids **23**, 21.
- Thompson, M. O., Galvin, G. J., Mayer, J. W., Peercy, P. S., Poate, J. M., Jacobson, D. C., Cullis, A. G., Chew, N. G., 1984, Phys. Rev. Lett. **52**, 2360.
- Thorpe, M. F., Jacobs, D. J., Chubynsky, M. V., Phillips, J. C., 2000, J. Non-cryst. Solids **266-269**, 857.
- Torquato, S., 2002, Random Heterogeneous Materials, Springer-Verlag, New York.
- Trefethen, L. N., Bau, D., 1997, Numerical Linear Algebra, SIAM, Philadelphia.
- Turnbull, D., Cohen, M. H., 1958, J. Chem. Phys. **29**, 1049.
- Turnbull, D., Cohen, M. H., 1961, J. Chem. Phys. **34**, 120.
- Valiquette, F., Mousseau, N., 2003, Phys. Rev. **B68**, 125209.
- Van Vliet, K. J., Suresh, S., 2002, Phil. Mag. **A82**, 1993.
- Veprek, S., Argon, A. S., 2002, J. Vac. Sci. Technol. **B20**, 650.
- Veprek, S., Iqbal, Z., Oswald, H. R., Webb, A. P., 1981, J. Phys. **C14**, 295.
- Veprek, S., Reiprich, S., 1995, Thin Solid Films **268**, 64.
- Veprek, S., 1999, J. Vac. Sci. Technol. **A17**, 2401.
- Vink, R. L. C., Barkema, G. T., van der Weg, W. F., Mousseau, Normand, 2001, J. Non-cryst. Sol. **282**, 248.
- Wallace, D. C., 1972, Thermodynamics of Crystals, John Wiley & Sons, New York.
- Waseda, Y., Suzuki, K., 1975, Z. Physik **B20**, 339.

- Witvrouw, A., Spaepen, F., 1993, J. Appl. Phys. **74**, 7154.
- Wooten, F., Winer, K., Weaire, D., 1985, Phys. Rev. Lett. **54**, 1392.
- Yamakov, V., Wolf, D., Phillpot, S. R., Mukherjee, A. K., Gleiter, H., 2001, Acta. Mater. **49**, 2713.
- Yamakov, V., Wolf, D., Phillpot, S. R., Mukherjee, A. K., Gleiter, H., 2002, Nature Materials **1**, 1.
- Yip, S., 1998, Nature **391**, 532.
- Yip, S., Sylvester, M. F., Argon, A. S., 2000, Computational and Theoretical Polymer Science **10**, 235.
- Young, D. A., 1991, Phase Diagrams of the Elements, University of California Press, Berkeley.
- Yvon, P. J., Schwarz, R. B., Schiferl, D., Johnson, W. L., 1995, Phil. Mag. Lett. **72**, 167.
- Zachariasen, W. H., 1932, J. Am. Chem. Soc. **54**, 3841.
- Zallen, R., 1979, in Fluctuation Phenomena, ed. Montroll, E. W., North-Holland, New York.
- Ziman, J. M., 1995, Principles of the Theory of Solids, Cambridge University Press, Cambridge, England